UNIVERSITY OF CALIFORNIA SAN DIEGO

Observations of Ice-Nucleating Particles Near Marine and Dust Source Regions

A dissertation submitted in partial satisfaction of the
requirements for the degree
Doctor of Philosophy

in

Earth Sciences

by

Charlotte M. DeWald

Committee in charge:

Kimberly A. Prather, Chair
Lihini I. Aluwihare
Paul J. DeMott
Tara Javidi
M. Dale Stokes

2021

The dissertation of Charlotte M. DeWald is approved, and it is acceptable in quality and form for publication on microfilm and electronically.

University of California San Diego

2021

DEDICATION

To my daughter Paidyn

EPIGRAPH

You can make a plan if it makes you feel better, but why don't you just keep and touch and let us know when you are ready to come back?

—Prof. Kimberly Prather, in response to my maternity leave plan

TABLE OF CONTENTS

Dissertation Approval Page iii

Dedication iv

Epigraph v

Table of Contents vi

List of Abbreviations ix

List of Figures xii

List of Tables xvi

Acknowledgements xvii

Vita xxvi

Abstract of the Dissertation xxviii

Chapter 1 1 Introduction 1
1.1 References 12

Chapter 2 2 Automation and Heat Transfer Characterization of Immersion Mode Spectroscopy for Analysis of Ice Nucleating Particles 24
2.1 Abstract 24
2.2 Introduction 25
2.3 Automation of immersion mode ice spectroscopy 29
2.3.1 Theory of operation 29
2.3.2 Physical design of the ice spectrometer 30
2.4 Simulation of heat transfer for immersion mode ice spectroscopy . 35
2.4.1 Model design 35
2.4.2 Setup of the heat transfer simulation 38
2.5 Results 42
2.5.1 Simulation results 42
2.5.2 Automated Ice Spectrometer performance: comparison with six other immersion mode ice nucleation measurement techniques 46
2.6 Discussion 49
2.7 References 52
2.8 Supplement 56

Chapter 3 3 Best practices for precipitation sample storage for offline studies of ice nucleation in marine and coastal environments . . . 59
3.1 Abstract . . . 59
3.2 Introduction . . . 60
3.3 Methods . . . 64
3.3.1 Precipitation sample collection . . . 64
3.3.2 Storage protocols . . . 64
3.3.3 INP analysis . . . 65
3.3.4 Particle size distributions . . . 66
3.4 Results . . . 67
3.4.1 INP concentrations in fresh precipitation samples . . . 67
3.4.2 Effects of sample storage on INP concentration measurements 70
3.5 Discussion . . . 75
3.6 Conclusions . . . 83
3.7 References . . . 85
3.8 Supplement . . . 91

Chapter 4 4 Cultivable halotolerant ice-nucleating bacteria and fungi in coastal precipitation . . . 104
4.1 Abstract . . . 104
4.2 Introduction . . . 105
4.3 Methods . . . 108
4.3.1 Precipitation and aerosol sample collection methods . . . 108
4.3.2 Bacterial and fungal isolation and characterization . . . 110
4.3.3 Storm and aerosol source characterization methods . . . 112
4.3.4 Isolate IN activity measurement and controls . . . 112
4.4 Results and discussion . . . 114
4.4.1 Subtropical coastal storm properties and origins . . . 114
4.4.2 Bacterial and fungal taxonomy . . . 116
4.4.3 Ice-nucleating properties of rain and SSA isolates . . . 120
4.5 Conclusions . . . 125
4.6 References . . . 127
4.7 Supplement . . . 139

Chapter 5 Ice-Nucleating Particles Near Two Major Dust Source Regions . . . 155
5.1 Abstract . . . 155
5.2 Introduction . . . 156
5.3 Methods . . . 160
5.3.1 Project overview . . . 160
5.3.2 Aerosol and trace gas measurements . . . 161
5.3.3 Dust mass concentrations from MERRA . . . 162
5.3.4 Measurement of ice-nucleating particles . . . 163
5.3.5 FLEXPART back trajectories . . . 168

5.4 Results and discussion . . . 169
5.4.1 Characteristics of INPs observed during AQABA . . . 169
5.4.2 Seawater source potential . . . 185
5.5 Conclusions . . . 187
5.6 References . . . 190
5.7 Supplement . . . 203

Chapter 6 Toward Hydrometeor-Phase Evaluation of EAMv1 Arctic Mixed-Phase Cloud Representation Using $(GO)^2$-SIM . . . 216
6.1 Abstract . . . 216
6.2 Introduction . . . 218
6.3 The EAMv1 to $(GO)^2$-SIM pipeline . . . 222
6.3.1 EAMv1 description and configuration . . . 222
6.3.2 $(GO)^2$-SIM description . . . 224
6.3.3 COSP description and configuration . . . 225
6.4 Summary . . . 229
6.5 References . . . 231

Chapter 7 Conclusions . . . 235
7.1 Summary . . . 235
7.2 Directions for future and related research . . . 239
7.3 References . . . 243

LIST OF ABBREVIATIONS

ACI	aerosol-cloud interactions
AI	artificial intelligence
AIS	Automated Ice Spectrometer
AMS	Aerosol Mass Spectrometer
AQABA	Air Quality and climate change around the Arabian BAsin
ATD	Arizona Test Dust
BINARY	Bielefeld Ice Nucleation ARraY
CCN	cloud condensation nuclei
CFDC	continuous flow diffusion chamber
Chl *a*	chlorophyll A
CLD	chemiluminscence monitor
CLUBB	Cloud Layers Unified by Binormals scheme
CNT	classical nucleation theory
CONUS	contiguous United States
COSP	CFMIP Observation Simulator Project
CPC	Condensation Particle Counter
CRAFT	Cryogenic Refrigerator Applied to Freezing Test
CSU-IS	Colorado State University Ice Spectrometer
CU-RMCS	University of Colorado Raman Microscope Cold Stage
CVI	counterflow virtual impactors
DOC	dissolved organic carbon
EAM	DOE Energy Exascale Earth Systems Atmosphere Model
FASW	filtered autoclaved seawater
FLEXPART	FLEXible PARTicle dispersion model

FMPS	Fast Mobility Particle Spectrometer
FRIDGE	Frankfurt Ice Nuclei Deposition FreezinG Experiment
J_{het}	heterogeneous ice nucleation rate coefficient
GCM	global climate model
GOCART	Goddard Chemistry, Aerosol, Radiation and Transport model
H-M	Hallet-Mossop
HR	high resolution
HRRR	High Resolution Rapid Refresh atmospheric model
ICR	ice crystal residuals
IN	ice-nucleating
INA	ice nucleation active
INP	ice-nucleating particle
LES	large-eddy simulations
LINDA	LED-based Ice Nucleation Detection Apparatus
LR	low resolution
MARGA	Monitor for AeRosols and Gases in Ambient Air
MERRA	Modern-Era Retrospective analysis for Research and Applications
MG2	”Morrison and Gettelman version 2” microphysics scheme
ML	machine learning
MLLW	mean lower low water
MOUDI-DFT	MicroOrifice Uniform Deposit Impactor-Droplet Freezing Technique
NC State-CS	North Carolina State Cold Stage
NN	neural network
NSA	ARM Atmospheric Observatory North Slope Alaska
n_s	ice-nucleating surface site density
n_{INP}	INP concentration per volume air

OPC	optical particle counter
POC	particulate organic carbon
RH	relative humidity
SCOPS	Subgrid Cloud Overlap Profile Sampler
SEC	Securities and Exchange Commission
SEM-EDX	scanning electron microscopy with energy dispersive X-Ray
SIO	Scripps Institution of Oceanography
SSA	sea spray aerosol
SSW	sub-surface seawater
SW	seawater
TSPs	total suspended particles
VAE	variational autoencoder
WBF	Wegener-Bergeron-Findeisen
WISDOM	WeIzmann Supercooled Droplets Observation on Microarray

LIST OF FIGURES

Figure 2.1: Schematic of Automated Ice Spectrometer (AIS) showing primary components as indicated by labels. 30
Figure 2.2: Photo of current Automated Ice Spectrometer system. 31
Figure 2.3: Graph of well temperature vs. temperature offset measured between the base of the well and the air above the well as measured with a thermistor probe (orange filled circles). 33
Figure 2.4: A screenshot of the AIS user computer interface, with chiller controls and well temperature readings on the left and video stream of image of wells in the middle. The detected freezing events are highlighted in green and displayed in the well matrix diagram on the right. 34
Figure 2.5: Schematic of cut in well block made for heat transfer simulation and mesh applied. 36
Figure 2.6: Flow chart describing algorithm for detection of freezing events using camera and lights to leverage optical properties of phase change from water to ice. 37
Figure 2.7: Graphical time series of the heat transfer simulation. Top shows isometric view of the well block (top left quarter) at $t = 1638s$. 43
Figure 2.8: Graphical time series of the heat transfer simulation showing the effects of increasing thermal homogeneity in the cooling environment by efficiently cooling headspace gas on performance of the well block. 44
Figure 2.9: Immersion freezing spectra of illite NX particles in terms of $n_{s,BET}(T)$ for comparison of SIO AIS against six other immersion mode techniques reported (see Hiranuma et al., 2015). 48
Figure 2.10: Difference between measured and simulated temperature of the air pocket in the well base. 56
Figure 2.11: Simulated temperature stratification within the sample volume. 57
Figure 2.12: Simulated temperature offset between the sample volume and the well base. 57
Figure 2.13: Spatial temperature gradient in sample volume temperature. 58

Figure 3.1: INP concentrations per liter of precipitation and estimated in-cloud INP concentrations per volume of air in 15 precipitation samples collected at two coastal sites at Scripps Institution of Oceanography (La Jolla, California, USA) between 22 September 2016 and 22 November 2019. 69
Figure 3.2: Ratio of INP concentrations measured in untreated precipitation samples (stored:fresh), calculated in successive 2 °C increments between −19 and −7 °C 70
Figure 3.3: Ratio of INP concentrations measured in heated precipitation samples (stored:fresh), calculated in successive 2 °C increments between −19 and −7 °C. 71
Figure 3.4: Ratio of INP concentrations measured in filtered (0.45μm) precipitation samples (stored : fresh), calculated in successive 2 °C increments between −19 and −7 °C. 72

Figure 3.5: Changes in INP concentration in untreated precipitation samples stored between 1 and 76 days at room temperature (+21-23 °C). 91
Figure 3.6: Changes in INP concentration in untreated precipitation samples stored between 1 and 76 days at +4 °C. 92
Figure 3.7: Changes in INP concentration in untreated precipitation samples stored between 1 and 76 days at -20 °C. 100
Figure 3.8: Changes in INP concentration in untreated precipitation samples stored between 1 and 76 days flash frozen with liquid nitrogen and stored at -20 °C. 101
Figure 3.9: IN spectra of precipitation collected 1/19/2017, fresh and stored samples. IN spectra of stored samples are shown (a) 27 days and (b) 64 days after collection. 102
Figure 3.10: Distribution of total insoluble particle concentration ratios, stored:fresh, for 10 untreated precipitation samples (sampling periods 1-10, see Table 3.1). 102
Figure 3.11: Distribution of total insoluble particle concentration ratios, stored:fresh, for 10 heat-treated precipitation samples (sampling periods 1-10, see Table 3.1). 103
Figure 3.12: IN spectra of untreated and heat-treated precipitation collected 1/11/2017 for (a) a fresh sample and (b) a replicate stored at +4 °C for 22 days. 103

Figure 4.1: INP concentrations per liter precipitation and estimated in-cloud INP concentrations per volume of air in 11 precipitation samples collected at Scripps Institution of Oceanography Ellen Browning Scripps Memorial Pier (32.8662° N, 117.2544° W; La Jolla, California, USA) between March and May 2016. 115
Figure 4.2: The 10 d back trajectories from cloud base, mid-cloud and cloud top during 11 precipitation sampling periods at the SIO pier (32.8662° N, 117.2544° W). 118
Figure 4.3: Maximum likelihood phylogenetic tree based on 420 nucleotides of the 16S rRNA gene sequences showing the phylogenetic relationships of isolates (in bold) related to Gammaproteobacteria reference sequences. 119
Figure 4.4: INP concentrations (g^{-1} biomass) for 14 halotolerant isolates derived from precipitation and aerosol samples. 122
Figure 4.5: INP concentrations at -20 °C in aerosol collected at the Scripps Institution of Oceanography Pier (32°52'01.4"N 117°15'26.5"W) during and between precipitation events. 139
Figure 4.6: Controls of IN measurements. (a) IN activity of 11 ZoBell media blanks. (b) IN activity of selected media–free isolate with a dilution factor of 1 (undiluted). 140
Figure 4.7: IN spectra of the 14 IN isolates and their respective ZoBell media samples, with IN spectra of both ZoBell and isolates scaled by the isolates' dilution factor. 141
Figure 4.8: INP concentrations per liter air sampled for 7 aerosol samples collected at Ellen Browning Scripps Memorial Pier at Scripps Institution of Oceanography (SIO) (32.8662 °N, 117.2544 °W) between March and May 2016. . . 142

Figure 4.9: 10-day back-trajectories from the SIO Pier (32.8662 °N, 117.2544 °W, 8m above MLLW) during the 3 aerosol sampling periods from which IN isolates originated, A1, A2, and A5 (see Tables 1, S1). 143
Figure 4.10: Image of aerosol (red box) and precipitation (yellow box) isolates on agar plates. Isolates derived from cultivation-based isolation. 144
Figure 4.11: Taxonomic distributions of precipitation (a) and aerosol (b) isolates. . . . 145
Figure 4.12: Phylogenetic relationships of isolates (in bold) related to Actinobacteria reference sequences. 146
Figure 4.13: Phylogenetic relationships of isolates (in bold) related to Firmicutes reference sequences. 147
Figure 4.14: INP concentrations observed in 14 halotolerant isolates derived from precipitation and aerosol samples, normalized to culture OD (590 nm). 148
Figure 4.15: Relationship of isolates within the same OTUs using multiple sequence alignments of 16S rRNA gene sequences. 149

Figure 5.1: Map of the sample locations for 26 aerosol samples collected on the RV Kommandor Iona during Air Quality and climate change in the Arabian Basin (AQABA). 169
Figure 5.2: Ice nucleation site densities (n_s) as a function of temperature for 25 of 26 aerosol samples collected during AQABA. 171
Figure 5.3: INP concentrations (a) and ice nucleation site densities (n_s) (b) as a function of temperature for 26 aerosol samples collected during AQABA. 174
Figure 5.4: INPs in select aerosol samples that were treated with heat and H_2O_2 (Methods Sec. 5.2.4) to test for INP heat-lability and organic composition. 176
Figure 5.5: Measured concentrations of INPs in an aerosolized soil dust sample collected 50 km north of Cairo, Egypt, that was treated with heat and peroxide to test for INP heat-lability and organic composition, same as in Fig. 5.4 above (Methods Sect. 5.2.4) to test for INP heat-lability and organic composition. 179
Figure 5.6: Potential ranges of mineral and organic-dominant INP activity observed during AQABA. 184
Figure 5.7: Measured INP concentrations in 10 SSW samples collected during AQABA. 186
Figure 5.8: Locations where each aerosol sample was collected during Leg 1 (Malta to Kuwait). 204
Figure 5.9: Locations where each aerosol sample was collected during Leg 2 (Kuwait to Toulon). 205
Figure 5.10: Time series of dust concentrations estimated from the Ca^+ concentrations measured in the water-soluble fraction of total suspended particles. . . . 206
Figure 5.11: Aerosol sampling set-up on the RV *Kommandor Iona* wheelhouse top. . . 207
Figure 5.12: INP concentrations measured in 8 aerosol samples from which a dilution was performed (10-100X). 208
Figure 5.13: INP concentrations measured in 26 aerosol samples collected during AQABA and in simulated INP concentrations from 7 blank filter samples. 209

Figure 5.14: Linear regressions between total aerosol surface area and concentrations of INPs with freezing temperatures between -10 and -20 °C. 210
Figure 5.15: Aerosol 72-hour back trajectories for Leg 1 simulated by FLEXPART (Methods Sect. 5.2.5). 211
Figure 5.16: Aerosol 72-hour back trajectories for Leg 2 simulated by FLEXPART (Methods Sect. 5.2.5). 212
Figure 5.17: Map of the collection locations of 10 subsurface seawater (SSW) samples. Marker sizes indicate abundance of INPs. 213
Figure 5.18: Average ocean surface chlorophyll a concentration from 1 August to 31 August 2017 (Moderate Resolution Imaging Spectroradiometre.) 214
Figure 5.19: Measured concentrations of INPs in SSW samples that were treated with heat, hydrogen peroxide and a 0.2 μm filter (Methods Sect. 5.2.4). 215

Figure 6.1: Maximum Root-Mean Square Error (RMSE) in COSP subcolumn ensemble stratiform liquid cloud fraction (a-b) and stratiform ice cloud fraction (c-d) from EAMv1 simulation 01-05-2012 00:00 – 23:30 in gridbox centered at 71°30' N 156°30' W. 226
Figure 6.2: Schematic of the data processing pipeline between EAMv1 and $(GO)^2$-SIM (yellow shading). 229

LIST OF TABLES

Table 2.1: Elements and properties used in heat transfer simulation. 40
Table 2.2: Constants used in calculation of heat transfer coefficient h for water in natural convection from −5 to −30 ºC. 41

Table 3.1: Precipitation sampling periods. 67
Table 3.2: Summary of unique and replicate untreated precipitation samples used for INP concentration measurements featured in Fig. 3.2. 68
Table 3.3: Summary of unique and replicate heat-treated precipitation samples used for INP concentration measurements featured in Fig. 3.3. 68
Table 3.4: Estimate of uncertainty associated with storage impacts for INPs with activation temperatures between −9 and −17 °C measured in stored, untreated precipitation samples. 76
Table 3.5: Estimate of uncertainty associated with storage impacts for INPs with activation temperatures between −9 and −17 °C measured in stored, heated precipitation samples. 77
Table 3.6: Estimate of uncertainty associated with storage impacts for INPs with activation temperatures between −11 and −19 °C measured in stored, filtered precipitation samples. 78
Table 3.7: Summary of previously reported precipitation sample storage conditions for offline analysis of INPs. 92

Table 4.1: Identities of 14 cultivable halotolerant IN bacteria and fungi derived from aerosol and precipitation samples. 121
Table 4.2: Identity and characteristics of precipitation and aerosol isolates. Aerosol sampling period labels begin with "A" to distinguish from precipitation sampling periods 1-11 (see Table 4.4 for precipitation and aerosol sampling times). . 150
Table 4.3: Cloud characteristics during 11 precipitation events over the sampling site: SIO Pier (32.8662 °N, 117.2544 °W). 151
Table 4.4: Sampling periods for precipitation and aerosol samples collected on SIO Pier (32.8662 °N, 117.2544 °W). 152
Table 4.5: Results of taxonomic assignment of SILVA Incremental Aligner (SINA) using the SILVA databases determined from 16S rRNA gene sequences. 153
Table 4.6: Summary of ice nucleation behavior of the 9 isolates that were tested for ice nucleation in the absence of media and resuspended in filtered autoclaved seawater (FASW). 154

Table 5.1: Summary of aerosol samples collected during AQABA. "—" indicates where data is missing. 170

Table 6.1: Modification of SCOPS for better agreement with EAMv1 subgrid distributions of stratiform ice and liquid. 227
Table 6.2: Modification of the hydrometeor assumptions used in COSP. 228

ACKNOWLEDGEMENTS

The final three years of my PhD were shaped by life-changing career opportunities, the arrival of my daughter, the abrupt reshuffling of life that ensues and the caregiving crisis of the COVID-19 pandemic. One and a half years into the pandemic with still no vaccine for children under 5, I am still in shock and awe of the support, flexibility and compassion my co-advisors Prof. Kimberly Prather and Dr. Dale Stokes offer their student mentees, colleagues and/or staff. Prof. Prather and Dr. Stokes, your mentorship left an indelible impression on me, and I can only hope to one day be able to support and show up for my future colleagues and mentees in the same you did for me whenever I most needed it. Even now while job hunting and considering my next step, it is empowering to know what I am looking for in a team and its leadership and to also have learned so much about what kind of leader I want to be. Thank you.

I also want to thank the other members of my committee: Prof. Lihini Aluwihare, Prof. Farooq Azam, Prof. Tara Javidi, and Dr. Paul DeMott. I am thankful for the way you have all influenced my experience as a PhD student. Some advice Prof. Aluwihare left on my annual performance review in 2018 when I was a new mom about accepting that you can't do everything and instead "focusing on what things you can do, no matter what happens" became a sort of mantra throughout the remainder of my PhD. I was truly inspired about the marine microbiome after just one or two conversations with Prof. Azam in which he made a few strikingly poetic comments about our fluorescence microscopy images. I felt the enthusiasm he inspired in me was infectious as I began to tell all the members and visitors to our lab about the kinds of things you can learn by looking at the beautiful, otherworldly images of viruses and microbes in seawater. Prof. Javidi, I will always wish that I had more time to collaborate with you during my PhD. Chatting with you just once or twice opened my eyes to the possibilities in AI/ML for measuring and modeling aerosol-cloud interactions. These possibilities are now shaking up the world of research in this field and are also heavily influencing my plans for the next step. Thank you so much for your guidance.

Dr. DeMott, I think the most succinct way to explain how deeply indebted I am to you for all my adventures and accomplishments as a PhD student is to tell you, as I have mentioned to you before, that for a time I had recurring nightmares about you and Dr. Tom Hill announcing your retirement and trekking off to far-flung remote places before I could graduate. This happened because you were the anchors of my experience in science and my subconscious is apparently keenly aware of the extent to which my fantastic experience in grad school was depending on your support. You provided the scientific mentorship I needed to develop my domain knowledge and my professional network. You and Dr. Hill and your colleagues were also the community I needed to celebrate the best times and bear the losses. I have always admired your writing skill and how you apply it to everything from ground-breaking publications to agenda updates for recurring meetings. I will miss reading beautiful, brilliant emails about things like your latest frustrations with mesocosm experiment measurements.

I am also thankful to the many, many other faculty, scientists, postdocs, staff and students who I met throughout my PhD.

Dr. Tom Hill, in addition to my thanks about many things described above, I would like to thank you for reminding me and all the other students you mentor to have fun. I will always look up to you for being both brilliant and having so much fun as you go about doing brilliant things. If it weren't for people like you, I think this field would be missing something terribly important. So many of my best memories in grad school had to do with moments of complete silliness that were often inspired by you.

Dr. Andi Andreae, working with you and your colleagues on the AQABA cruise was one of those life-changing career opportunities I mentioned above. I am really having the best time imaginable in my job interviews because I have the AQABA story to tell. I feel extremely fortunate for having met you, for your support of my participation in AQABA and for having an opportunity to learn from you on a such an extraordinary field campaign. It is experiences like these that strengthen my resolve to give back and help increase access to STEM. I just can't

imagine a more exciting career path.

I am also thankful to Prof. Ian Eisenman, an extraordinary teacher and mentor who was one of the first people who came to mind as part of my SIO network when I realized I didn't know any other students or early career researchers with young children personally and that I would like some introductions. Thank you for your encouragement and assurances that grad school can be a great time to become a parent and that I could find a way to finish grad school. I reflected on your comments many, many times when I was sleep deprived and when doing research activities felt like wading through a muddy bog.

Thank you also to the many people that Prof. Eisenman introduced or re-introduced me to while I was building a support network and for sharing your stories about how you are finding ways to fit your careers with your lives. This includes Prof. Sarah Giddings, thank you for taking me to lunch and reassuring me, as Prof. Eisenman did, that grad school can be a great time to become a parent and sharing your nanny references. Also Prof. Sarah Purkey, I will never forget your story of resilience about interviewing for a faculty position at SIO with a brand-new baby in tow. Dr. Angelica Rodriguez, thank you for the many many chats about life with infants and toddlers. I am so thankful to have had a pal with a child close in age going through many of the same experiences at the same times (and thank you, as always for the hand-me-downs!). There are many, many others I also look up to and remember for their support and leadership for caregivers: Dr. Natalya Gallo, Dr. Alyssa Griffin, Dr. Julia Fieldler, Dr. Tim Wagner, Dr. Alexander Gershunov, and Prof. Katharine Ricke.

SIO Grad Advisor Gilbert Bretado, thank you so much for helping me navigate UCSD and Grad Division policy, for the fun conversations (and SIO Halloween parties) and for all your encouragement over the years. It has always been a great comfort to me to know that whenever I had pressing questions or didn't even know what questions to ask, that you would be there and could help me figure out what was needed. Your support in part enabled me to take all the risks I wanted with e.g., externally supported internships and offsite fellowships to have an extraordinary

experience throughout my PhD. Thank you so much for your leadership of the excellent SIO Peer Mentorship Program. Being a mentor and a mentee in the program was one of my favorite experiences at SIO and one that inspires me to seek out similar opportunities wherever I go.

Dr. Susannah Burrows, thank you so much for encouraging me to apply to an SCGSR fellowship and for teaching me many, many skills and basic background related to modeling. It was through the SCGSR experiences with you and your colleagues that I developed my sense of direction for the next step in my career. I was inspired by many of your publications and talks throughout my PhD.

To all my friends from my time in San Diego and beyond, thank you for the joy and memories and for always being up for celebrating life's important milestones: Kara and Mark Stambaugh, Barbara Thorne-Thomsen, Meredith Fish and Patrick Farrell, Janet Pulido, Paul and Taylor Chamberlain, Alan Seltzer and Kate Durkin, Reuben Demirdjian and Catherine Courtier, Dillon Amaya and Jessica, Bia and Gui Villas-Boas, Ryan and Hannah O'Donnell, Kara Voss and Dan Flanagan, Maya Becker and Drake Singleton, Bonnie Ludka, Austen Michalak, Matthew Pendergraft, Wesley Neely, Luke Johnson, and Victor Minces.

Prof. David Laude, it will always be hard to find the words to thank you. Our conversations throughout my time at UT Austin and what I learned from them shaped the very fabric of my character. Every time one of those pivotal moments in life arises, which seems like all the time these days, I summon up your words about fearlessness and the things that matter most. Our old conversations are the framework through which I continuously discover who I am and who I'd like to be.

Thanks to Dennis Passovoy, for encouraging me to research the relationships between work, wellbeing and health outcomes. It was in part due to these conversations that I felt motivated to take multiple risks to find a career path that I love. Thank you also for helping me discover fascinating questions about leadership. At this point I have so much to learn, but because of you and your colleagues at Catalyzer, I know where to start looking for answers.

To the Prather group members past and present, thank you so much for embarking on this challenging fantastic graduate school experience with me: Matthew Pendergraft, Dr. Jon Sauer, Dr. Kathryn Mayer, Dr. Julie Dinasquet, Dr. Rebecca Simpson, Mitch Santander, Dr. Gavin Cornwell, Dr. Camille Sultana, Hashim Al-Mashat, Ke'La Kimble, Alexia Moore, Brock Mitts, Ben Rico, Clare Morris, Sarah Amiri, Dolan Lucero, Lucia Cancelada, Sabrina Ufer, Raymond Leibensperger, Prof. Doug Collins, Dr. Chris Lee, Dr. Olivia Ryder, Prof. Andy Martin, Prof. Xiaofei Wang, Dr. Louise Kristensen, Dr. Linh Anh Cat, and Dr. Daniel Petras.

Thank you to Joe Mayer for helping us design and fabricate the Automated Ice Spectrometer, the instrument that supported all my work.

A big hug and thankyou to the nannies who helped us care for Paidyn through the first year and half: Roseane Piper, Ali Vasquez, Ariel Hocking, and Phoebe Perry. I simply would not have been able to go back to work had it not been for you and your extraordinary care of Paidyn and sometimes even me. It is said that nannies become a part of the extended family, and looking back at all the rich memories we created together, I really feel this is true. Also thank you to Janet Pulido, who helped us in a pinch over just two weeks between caregivers. You are a natural. I was amazed at how you developed such a rock-solid relationship with Paidyn in just a few days.

Thank you to my family, for whom I am extremely grateful. It is quite a privilege to embark on a PhD program, particularly with a young child in tow, and you are the reason that I managed.

Thank you to Donna, Dan and Dash Ohr. How serendipitous it was that you were living a few blocks away from my first home in La Jolla. I have so much to thank you for: for helping us move and get settled in San Diego, for always welcoming us over for visits, the Thanksgivings and dinners out and for all the fun trips to Big Bear. Knowing you were always a few miles away was like having another home away from home.

To my sister Nonie Hilliard, I will never be able to thank you enough for being up for moving with me and Paidyn across the country when I started my fellowship, even though you

had just graduated yourself. And then, I will never be able to find the right words to thank you for your compassion and understanding when I needed to pull the plug and go home unexpectedly. I really don't know what I did to deserve such support. Thank you for the love and laughter. Nobody in this world makes me laugh as hard as you do.

Prof. Allyson Beall-King, thank you for encouraging me to apply to the NSF Research Experience for Undergraduates in 2013, where I realized how much I loved atmospheric science and field research. Thank you also for being a source of sanity and perspective at times when I was overwhelmed by choices. It was probably some combination of genetics and my admiration of you that led me to choose the earth sciences. To you and Chico, thank you for hosting me in your lovely home the summer of the REU and your wedding! I'm so glad we got to spend that time together.

To my dad, Dr. John Beall. Obviously, I have also followed in your footsteps. It is hard to know where to begin in thanking you. Thank you for convincing me at a young age that I really needed to sleep, exercise, and eat three square meals a day to get through school, for always leaving AAAS Science magazines all over the house because this in part inspired my interest in science, and for following me all over the world to help me live my professional dreams while taking care of Paidyn. Thank you for helping me collect samples at the pier and picking up tacos to-go or whatever I needed during intensive field campaigns, for coming out to Kuwait to see me for just a 1-2 day break in the AQABA cruise, for helping me with electronics projects, for helping Jesse and I keep Paidyn entertained during conferences. Thank you for welcoming us back home to Dallas so that we could weather the pandemic together, and most of all, thank you being the best, most patient grandpa imaginable.

Thanks also to my brother and sister, Otto and Erin Beall. I'm so glad that we got to spend more time together than we would have ever imagined pre-pandemic, and I'm very thankful that Paidyn got to bond with her aunt and uncle during our time here. I also so enjoyed the times swapping stories about our "science projects".

To my mom, Sandy Flippo. Thank you for teaching me the importance of telling a great story, organizing gathering and parties, being a good hostess and for inspiring me to learn foreign languages. These skills have not only taken me far professionally but have enriched my life with friends all over the world. Thank you also for teaching me the importance of manners at a young age and the kinds of things that can happen just by saying "hello", "goodbye", "thank you", listening attentively and expressing interest in another person's experience. Thank you also for demonstrating why it is so important to invest as much energy into all parts of life holistically as it is to invest in a career. Thank you for sharing all this plus joy and wonder with Paidyn. It was much more satisfying and enjoyable to finish my dissertation throughout the past year and half knowing that she had a fun place to go full of people and cats that love her while I worked. Thank you also for the many fabulous hand-me-downs that got me through my first interview season. Thanks also to John Johnson, for welcoming us, hosting and feeding us over the long long days and nights of the pandemic and for your endless patience and loving attentive care of Paidyn. It was immediately apparent how much better life could be for us and Paidyn to have so much family around, and this was a very important silver lining of our pandemic experience.

To my husband Jesse DeWald, who exemplifies why many partners of PhDs also deserve an award at graduation. Thank you for taking a leap, leaving your job and moving to San Diego with me, for helping me build a fantastic community there, for co-hosting the parties to celebrate our milestones and those of our friends, for encouraging me to experience life downtown, to travel and to enjoy my 20s, for driving me out at all hours of the night to collect rainwater at the pier, for coauthoring my first first-author paper with me, for demonstrating assertiveness, for insisting that I also ask for what I need and deserve, for insisting that I attend to my mental health, for indulging me in a wedding that was planned around my participation in a research cruise, for the best maternity leave experience I could ever imagine, and for bearing with me through the reshuffling of our lives upon our daughter's arrival, including the really tough and continuous adjustments and sacrifices. Thank you for moving me and our 6-month-old baby to Tricities, WA

for my fellowship despite the tremendous upheaval, logistics and heartache from be separated for months. Thank you for facing the challenges of setting up our lives there with me, finding a temporary residence and quality child-care. Thank you so much for helping me decide when to pull the plug and then moving us back again and re-establishing our lives and childcare at home when we did so. And thank you for encouraging me to always choose the path that brings me as much joy as this one did and more. I am extremely privileged to have a partner who is willing to endure and co-navigate innumerable challenges for the sake of my education and opportunities.

Finally, thank you to my brave, kind, joyful daughter Paidyn, for helping me rediscover how to play and how to be present. Thank you for coming along on this journey with me, figuratively and literally, and for your affection and patience as we bumble through parenthood. You are a new, powerful motivation to my work in Earth Sciences, just as you are the new, powerful force in my life that is shaping me into the person I want most to be.

Chapter 2, in full, is a reprint of the material as it appears in Atmospheric Measurement Techniques 2017. Beall, C. M., Stokes, M. D., Hill, T. C., DeMott, P. J., DeWald, J. T. and Prather, K. A.: Automation and heat transfer characterization of immersion mode spectroscopy for analysis of ice nucleating particles, Atmos. Meas. Tech., 10(7), 2613–2626, doi:10.5194/amt-10-2613-2017, 2017. The dissertation author was the primary investigator and author of this paper.

Chapter 3, in full, is a reprint of the material as it appears in Atmospheric Measurement Techniques 2020. Beall, C. M., Lucero, D., Hill, T. C., DeMott, P. J., Stokes, M. D. and Prather, K. A.: Best practices for precipitation sample storage for offline studies of ice nucleation in marine and coastal environments, Atmos. Meas. Tech., 13(12), 6473–6486, doi:10.5194/amt-13-6473-2020, 2020. The dissertation author was the primary investigator and author of this paper.

Chapter 4, in full, is a reprint of the material as it appears in Atmospheric Chemistry and Physics 2021. Beall, C. M., Michaud, J. M., Fish, M. A., Dinasquet, J., Cornwell, G. C., Stokes,

M. D., Burkart, M. D., Hill, T. C., DeMott, P. J. and Prather, K. A.: Cultivable halotolerant ice-nucleating bacteria and fungi in coastal precipitation, Atmos. Chem. Phys., 21(11), 9031–9045, doi:10.5194/acp-21-9031-2021, 2021. The dissertation author was the primary investigator and author of this paper.

Chapter 5, in part, has been submitted for publication of the material as it may appear in Atmospheric Chemistry and Physics. Beall, C.M., Hill, Thomas C.J., DeMott, P.J., Könemann, T., Pikridas, M., Drewnick, F., Harder, H., Pöhlker, C., Lelieveld, J., Weber, B., Iakovides, M., Prokes, R., Sciare, J., Andreae, M.O., Stokes, M.D., Prather, K.A. The dissertation author was the primary investigator and author of this material.

Chapter 6, in part, is currently being prepared for submission for publication of the material. Beall, C.M., Lamer, K., Burrows, S.M., Ma, P., Stokes, M.D., Prather, K.A. The dissertation author was the primary investigator and author of this material.

VITA

2011	B.A. in Plan II Honors, *magna cum laude*, University of Texas at Austin
2014-2021	Graduate Student Researcher, Scripps Institution of Oceanography, UCSD
2018	M.S. in Earth Sciences, Scripps Institution of Oceanography, UCSD
2021	P.h. D. in Earth Sciences, Scripps Institution of Oceaongraphy, UCSD

AWARDS

2018 DOE Office of Science Graduate Student Research Program Fellowship

2017 UCSD Friends of the International Center Fellowship

2017 UCSD Frontiers of Innovation Scholars Program Fellowship

2015 SIO Outstanding Mentor of the Year Award

2015 University of California Office of the President UC Carbon Neutrality Fellowship

2014 UCSD San Diego Diversity Fellowship

PATENTS

Stokes, M.D., **Beall, C.M.**, Ice nucleating particle spectrometer, 2020, US Patent 10,557,810.

PUBLICATIONS

Beall, C. M., Michaud, J. M., Fish, M. A., Dinasquet, J., Cornwell, G. C., Stokes, M. D., Burkart, M. D., Hill, T. C., DeMott, P. J. and Prather, K. A.: Cultivable halotolerant ice-nucleating bacteria and fungi in coastal precipitation, *Atmospheric Chemistry and Physics*, (2021); 21(11), 9031–9045, doi:10.5194/acp-21-9031-2021.

Pendergraft, M. A., Grimes, D. J., Giddings, S. N., Feddersen, F., **Beall, C. M.**, Lee, C., Santander, M. V and Prather, K. A.: Airborne transmission pathway for coastal water pollution, edited by J. Collett, *PeerJ*, (2021); 9, e11358, doi:10.7717/peerj.11358.

Mitts, B., Wang, X., Lucero, D., **Beall, C.**, Deane, G., DeMott, P. and Prather, K., Importance of Supermicron Ice Nucleating Particles in Nascent Sea Spray, *Geophysical Research Letters*, (2021); 48, e2020GL089633, doi: 10.1029/2020GL089633.

Beall, C.M., Lucero, D., Hill, T. C., DeMott, P. J., Stokes, M. D., Prather, K. A., Best practices for precipitation sample storage for offline studies of ice nucleation in coastal and marine environments. *Atmospheric Measurement Techniques*, (2020); 13(12), 6473–6486, doi: 10.5194/amt-13-6473-2020.

Martin, A.C., Cornwell, G.C., **Beall, C.M.**, Cannon, F., Reilly, S., Schaap, B., Lucero, D., Creamean, J., Ralph, F.M., Mix, H.T., Prather, K.A., Contrasting local and long-range transported warm ice-nucleating particles during an atmospheric river in coastal California, USA. *Atmospheric Chemistry and Physics*, (2019); 19(7):4193–210, doi: 10.5194/acp-19-4193-2019.

Michaud, J. M., Thompson, L. R., Kaul, D., Espinoza, J. L., Richter, R. A., Xu, Z. Z., Lee, C., Pham, K.M., **Beall, C.M.**, Malfatti, F., Azam, F., Knight, R., Burkart, M. D., Dupont, C. L., Prather, K. A., Taxon-specific aerosolization of bacteria and viruses in an experimental ocean-atmosphere mesocosm. *Nature Communications*, 9, (2018), doi: 10.1038/s41467-018-04409-z.

McCluskey, C.S., Hill, T.C., Sultana, C. M., Laskina, O., Trueblood, J., Santander, M.V., **Beall, C.M.**, Michaud, J.M., Kreidenweis, S.M., Prather, K.A., Grassian, V., DeMott, P.J., A mesocosm double feature: Insights into the chemical make-up of marine ice nucleating particles. *Journal of Atmospheric Science*, JAS-D-17-0155.1 (2018), doi: 10.1175/JAS-D-17-0155.1.

Beall, C.M., Stokes, M.D., Hill, T.C., DeMott, P.J., DeWald, J.T., Prather, K.A., Automation and heat transfer characterization of immersion mode spectroscopy for analysis of ice nucleating particles. *Atmospheric Measurement Techniques*, (2017); 10(7), 2613–2626, doi: 10.5194/amt-10-2613-2017.

Pham, D. Q., O'Brien, R., Fraund, M., Bonanno, D., Laskina, O., **Beall, C.M.**, Moore, K. A., Forestieri, S., Wang, X., Lee, C., Sultana, C., Grassian, V., Cappa, C. D., Prather, K. A. and Moffet, R. C., Biological Impacts on Carbon Speciation and Morphology of Sea Spray Aerosol, *ACS Earth Space Chemistry*, 1(9), 551–561 (2017), doi: 10.1021/acsearthspacechem.7b00069.

Wang, X., Deane, G.B., Moore, K.A., Ryder, O. S., Stokes, M.D., **Beall, C. M.**, Collins, D.B., Santander, M.V., Burrows, S.M., Sultana, C.M., Prather, K.A., The role of jet and film drops in controlling the mixing state of submicron sea spray aerosol particles. *Proceedings of the National Academy of Sciences*, 114, 6978–6983 (2017), doi: 10.1073/pnas.1702420114.

McCluskey, C.S., Hill, T.C., Malfatti, F., Sultana, C.M., Lee, C., Santander, M. V., **Beall, C.M.**, Moore, K. A., Cornwell, G. C., Collins, D.B., Prather, K.A., Jayarathne, T., Stone, E.A., Azam, F., Kreidenweis, S.M., DeMott, P.J., A dynamic link between ice nucleating particles released in nascent sea spray aerosol and oceanic biological activity during two mesocosm experiments. *Journal of Atmospheric Science*, 74, 151–166 (2017), doi: 10.1175/JAS-D-16-0087.1.

Wang, X., Sultana, C.M., Trueblood, J., Hill, T.C., Malfatti, F., Lee, C., Laskina, O., Moore, K.A., **Beall, C.M.**, McCluskey, C. S., Cornwell, G.C., Zhou, Y., Cox, J. L., Pendergraft, M.A., Santander, M.V., Bertram, T.H., Cappa, C.D., Azam, F., DeMott, P.J., Grassian, V.H., Prather, K.A., Microbial Control of Sea Spray Aerosol Composition: A Tale of Two Blooms. *ACS Central Science*, 1 (3), 124-131 (2015), doi: 10.1021/acscentsci.5b00148.

ABSTRACT OF THE DISSERTATION

Observations of Ice-Nucleating Particles Near Marine and Dust Source Regions

by

Charlotte M. DeWald

Doctor of Philosophy in Earth Sciences

University of California San Diego, 2021

Kimberly A. Prather, Chair

Ice-nucleating particles (INPs) are rare aerosols that can have disproportionately large impacts on several climate-relevant properties of clouds, including their contribution to precipitation outcomes and the cooling of the earth's surface. Ice nucleation occurs on scales that are relatively small compared to cloud or climate model resolution (down to nanometers), and thus it is commonly parameterized for representation in simulations. However, critical gaps in knowledge challenge the development of ice nucleation representations. Challenges include the up to five order of magnitude span in observations of INP concentrations at any given temperature, the numerable INP sources of varying strengths, and the fact that little is known about which properties make an aerosol an INP. Of the common INP species, desert dust is thought to be the

most globally important due to its relative abundance and ice nucleating potential, whereas INPs emitted from the ocean surface are implicated in remote ocean regions far from dust sources. Gaps in INP observations near important dust and marine source regions additionally challenge efforts to advance predictive understanding of INPs. Through a synthesis of observational, laboratory and modelling techniques, this dissertation aims to develop INP instrumentation and methods, identify specific marine ice nucleating entities, and provide observations of INPs near major dust sources. Key results include an automated instrument for measurement of immersion-mode INPs, best practices for offline INP analysis of precipitation samples, INP observations from a shipborne campaign over the Red Sea, Indian Ocean, Arabian Gulf and Mediterranean, and identities of 14 ice-nucleating microbes, at least two of which are highly likely marine in origin. Finally, to address challenges that inhibit the implementation of improved INP representation in climate models, a data processing "pipeline" is described that will facilitate hydrometeor phase evaluation of the Department of Energy Exascale Earth System Atmosphere Model (EAMv1). In summary, this dissertation addresses challenges to the development and implementation of improved representations of ice nucleation from both the observational and modeling perspective.

Chapter 1

1 Introduction

Aerosols are tiny particulates (nanometers to several micrometers in diameter) suspended in the atmosphere that affect climate both directly, by absorbing, re-radiating or reflecting incoming solar radiation, and indirectly, by modulating the climate-relevant properties of clouds. Some of the myriad interactions between aerosols and clouds are relatively well understood. For example, it is well known that if aerosol concentrations increase in a liquid cloud, the droplet number will increase, the droplet sizes will decrease (Twomey, 1977), and overall, this process will suppress precipitation and increase the cloud's lifetime (Albrecht, 1989). However, despite decades of research, aerosol-cloud interactions (ACI) have remained the greatest sources of uncertainty in estimates of effective radiative forcing (Table 7.8; IPCC, 2021). The skill with which climate models predict future climate scenarios thus depends upon better constraining the uncertainty associated with ACI.

As the climate becomes less predictable, the need for constraining climate model uncertainty and consequently, advancing predictive understanding of ACI, is becomingly increasingly time critical. By 2030, over 100 million people globally could be pushed into poverty due to climate change (Hallegatte et al., 2017). By 2050, as many as 143 million people may become climate refugees in just three regions (Sub-Saharan Africa, South Asia and Latin America) as

they are forced to seek new, more climate-resilient places to live (Rigaud et al., 2018). Already, extreme weather and climate-related disasters are costing the global economy hundreds of billions in losses each year ($320 billion in 2017 alone) (Löw, 2018). In recognition of the risk climate change poses to the global economy, financial regulatory institutions are beginning to respond. As of the time of writing this chapter, the U.S. Securities and Exchange Commission (SEC) is considering passing regulation that would mandate climate risk disclosures from all domestic publicly traded companies by the end of 2021 (U.S. Securities and Exchange Commission, 2021). Traditionally, catastrophe models are used in the financial sector to estimate physical risks associated with extreme weather events and are designed to provide the asset-level risk information that the SEC may soon require of industry. However, since catastrophe models derive risk estimates from historical climate data, their skillfulness in quantifying risk diminishes quickly with time (i.e., they are less useful on the longer, decadal timescales relevant to climate change). Considering the threat climate change poses to vast, vulnerable populations and the global economy, solutions for quantifying risk based on forward-looking climate model data are urgently needed. However, as the largest source of uncertainty in estimates of radiative forcing, aerosol cloud interactions pose a great challenge to achieving the accuracy and precision needed to derive decision-useful, quantitative information about community or asset-level climate risk from climate models.

ACI challenge climate model cloud representation in part due to the large disparity in spatial scale between many ACI ($\geq$ nanometers) and that of the standard model resolution (50 to 200 km) (e.g., Gettelman et. al, 2015). Other modeling capabilities such as large-eddy simulations (LES) and Cloud Resolving Models (CRM) offer much higher resolution (10s to 100s of meters) (e.g., Eirund et al., 2019; Solomon et al., 2015), yet even these spatial scales are larger than the scale of many ACI. Subgrid-scale ACI processes therefore are commonly parameterized, yet multiple factors challenge the development and evaluation of ACI parameterizations. Besides the challenge of observing ACI *in situ*, it is difficult to untangle their impacts on the radiative

properties of clouds from that of large-scale dynamical or meteorological forces (Fan et al., 2016; Seinfeld et al., 2016). Furthermore, answers to questions about the level of complexity required to accurately represent ACI in climate models remain elusive. For example, how many moments does a cloud microphysics parameterization require to properly represent ACI processes? Does the needed complexity depend on model resolution and the regime of aerosol, clouds and meteorology (Ma et al., 2021)?

Phase changes from vapor to liquid and liquid to ice represent a major pathway through which aerosols affect clouds and their radiative properties. Cloud formation and microphysical properties are modulated by the availability of water vapor and cloud condensation nuclei (CCN), hygroscopic aerosols that nucleate liquid droplets at a given supersaturation. In the absence of CCN, clouds would theoretically require a supersaturation of 300% to form (Pruppacher and Klett, 1997). Ice nucleating particles (INPs) can also influence cloud phase and radiative properties by triggering ice formation at temperatures above the homogenous freezing point of water ($\sim$ -38 °C) and at relative humidities (RH) well below the homogenous freezing RH of aqueous solution droplets.

Both CCN and INPs can affect the number concentration and size distribution of cloud droplets and ice crystals. In a mixed-phase cloud regime, an increase in INPs tends to increase hydrometeor sizes and consequently, the precipitation efficiency of the cloud (e.g., Kanji et al., 2017). For example, through the Wegener-Bergeron-Findeisen (WBF) process, ice crystal sizes increase at the expense of cloud droplets due to the relatively lower vapor-pressure of ice (Bergeron, 1935; Findeisen, 1938; Wegener, 1911). These effects differ from those of CCN, as an increase in CCN in this cloud regime tends to decrease hydrometeor size while increasing droplet number concentrations. Primary ice production (i.e., ice nucleation) can also trigger secondary ice production processes. At high freezing temperatures between $\sim$-3 and -8 °C, fragments of ice are emitted during riming of large droplets onto ice particles through a phenomenon known as the Hallet-Mossop (H-M) ice multiplication process (Hallet and Mossop, 1974). The sedimentation of

ice formed at high altitude via homogenous freezing into supercooled liquid layers in mixed-phase clouds represents another example of a secondary ice production. Secondary ice processes such as these have been suggested as a possible explanation for the discrepancy of up to five orders of magnitude between field measurements of in-cloud ice crystal concentrations and measured or modeled INP concentrations (Auer et al., 1969; DeMott et al., 2011; Heymsfield and Willis, 2014; Lloyd et al., 2015). As most precipitation is initiated in the ice phase (Lau and Wu, 2003; Lohmann and Feichter, 2005), both primary and secondary ice formation processes are important drivers of precipitation and the hydrological cycles, particularly over land (Mülmenstädt et al., 2015). INPs also drive heterogeneous ice nucleation at low temperatures $<$ -38 °C in cirrus clouds where RH_i varies below the RH threshold for homogeneous freezing (140-150 %) (DeMott et al., 2003; Cziczo et al., 2013). In summary, depending on the cloud regime and the meteorological conditions, a small number of INPs can have a disproportionately large impact on cloud phase, lifetime, optical properties and precipitation outcomes.

The following section will outline some outstanding challenges to achieving predictive understanding of INPs, as important contributors to ACI and the focus of this thesis. As mentioned above, ice nucleation occurs on scales that are relatively small compared to model grid cells (down to nanometers) (e.g., Kanji et al., 2017), and thus are commonly parameterized for representation in cloud or climate models. However, multiple factors and critical gaps in knowledge challenge the development of ice nucleation representation, including that observations of INPs at any given temperature span up to five orders of magnitude, INPs have many sources of varying strengths, and little is known about the properties which make an aerosol an INP (Kanji et al., 2017). Natural INP sources include desert dusts, sea spray, volcanic ash and vegetative debris, whereas anthropogenic sources include biomass burning, transportation and industrial processes (e.g., Kanji et al., 2017). The multi-modality of ice nucleation adds further complexity to INP measurements and parameterization. There are at least three distinct modes of ice nucleation, including immersion freezing, in which a freezing event is triggered by an INP immersed in a

supercooled liquid droplet, deposition freezing, in which water vapor simultaneously condenses onto an INP and freezes, and contact freezing, in which an INP triggers freezing by colliding with the droplet at the air-water interface (Pruppacher and Klett, 1997). However, immersion freezing is considered to be the dominant mode of ice nucleation as simulations show it dominates primary freezing in the atmosphere between 1000 and 200 hPa (Hoose and Möhler, 2012) and prior studies have also suggested that immersion mode ice nucleation is the most important primary freezing process in mixed-phase clouds (Ansmann et al., 2008; de Boer et al., 2013; De Boer et al., 2011; Westbrook and Illingworth, 2013).

Ice nucleation parameterizations fall into one of two classes: time-dependent (stochastic) or time-independent (deterministic). The stochastic parameterization framework invokes either nucleation theory or Classical Nucleation Theory (CNT) to derive a heterogeneous ice nucleation rate coefficient (J_{het}, units of m^{-2} s^{-1}) to account for the dependence of nucleation on liquid volume, INP surface area and time (Pruppacher and Klett, 1997). In aqueous solutions, J_{het} also depends on the solute concentration or water activity. Deterministic parameterizations, on the other hand, assume the time-dependent fluctuations of molecules to and from a potential nucleation site do not affect the droplet freezing temperature. Many of these are based upon a concept of ice nucleation active site densities, n_s, in units of m^{-2}, in which each ice nucleation event is assumed to correspond to one ice-active site (Pruppacher and Klett, 1997). The n_s is calculated by normalizing the total number of freezing events by the total INP surface area. Results from studies of dust INPs showing that the "ice embryos" form on preferable crystal surfaces or in surface defects such as steps, cracks and cavities support the surface site density framework for parameterization (Kiselev et al., 2017). Thus, multiple studies have developed mineral dust INP parameterizations used to estimate INP concentrations in aerosolized desert dust, some based exclusively on laboratory measurements (e.g., Niemand et al., 2012; Ullrich et al., 2017), and others derived from a combination of laboratory and field measurements (DeMott et al., 2015). There are, additionally, multiple mineral-specific INP parameterizations including

illite (Broadley et al., 2012), kaolinite (Welti et al., 2012), quartz (Harrison et al., 2019) and K-feldspar (Atkinson et al., 2013). However, n_s-based parameterizations are likely not appropriate for all aerosol species. Some IN-active microbes, for example, are thought to have environment-dependent IN behavior (Beall et al., 2021; Failor et al., 2017). Considering the development effort required to implement a parameterization into a model, one advantage of the deterministic, n_s-based parameterizations is that INP concentrations at a given temperature depend only on the temperature and the total INP surface area. Results from recent studies report evidence both for (Budke and Koop, 2015; Knopf et al., 2020) and against (Vali, 2014; Wright et al., 2013; Wright and Petters, 2013) the relevance of stochastic freezing, and it remains to be seen whether time-dependent parameterizations are required for accurate representation of ice production processes in cloud or climate models.

Alternative solutions to develop, supplement or replace ice production parameterizations altogether using Machine Learning (ML) or Artificial Intelligence (AI) approaches have been proposed. Variational autoencoders (VAE), for example, could be applied to output from high resolution large-eddy simulations (LES) or cloud-resolving models (e.g., 10s of meters) to determine subsets of variables that can be used to parameterize ice production processes (Ma et al., 2021). Neural network (NN)-based emulators developed from LES or simulations could also potentially replace parameterizations by effectively approximating ice production processes. It remains to be seen whether VAE-based parameterizations or NN-based emulators developed from high-resolution, cloud-resolving models that span a relatively small spatial domain can optimize the fidelity of ice process representation in large-scale climate models.

However, whether a parameterization or an ML/AI-based solution designed to replace parameterizations altogether, the development, evaluation and/or validation of each approach depends upon measurements of ice nucleation and the domain knowledge we have derived from them over decades of study. INPs are rare relative to total aerosols (1 in 10^5 at -20 °C) (Rogers et al., 1998), and their rarity poses a great challenge to their measurement. INPs with

high freezing temperatures are exceptionally rare and their detection in the ambient atmosphere demands large sampling volumes, up to hundreds of thousands of liters of air, depending on the INP types and source strengths (e.g., DeMott et al., 2016). A number of online (real-time) and offline (processed post-collection) techniques exist for measurement of each ice nucleation mechanism, including condensation, deposition, immersion and contact freezing. However, as some simulations have shown that immersion mode freezing is the dominant mode of primary freezing in the atmosphere between 1000 and 200 hPa (Hoose et al, 2010), most techniques target immersion freezing. Despite the lack of time resolution, offline techniques enable measurement of INPs at modest supercooling (e.g. up to -5 °C) and temperature regimes where concentrations typically fall below detection limits of online instruments (DeMott et al., 2017). Recent studies that intercompared offline and online instruments designed or operated for measurement of immersion mode INPs showed excellent agreement (i.e., within measurement uncertainty) in measurements of standardized dust and biological samples (DeMott et al., 2018) and when co-sampling ambient aerosol (DeMott et al., 2017). DeMott et al. (2017) and DeMott et al. (2018) also reported some exceptions in co-sampling or standard samples which resulted in discrepancies of up to or exceeding 2 orders of magnitude, implicating measurement or sampling artifacts and sensitive properties of the standard used for comparison, respectively. While instruments measuring immersion mode INPs have been rigorously intercompared over the years (DeMott et al., 2017, 2018; Hiranuma et al., 2014; Wex et al., 2015), relatively little is known regarding how the variable storage practices applied to samples collected for offline analysis of INPs affect measurements and reproducibility of results (Beall et al., 2020; Petters, Markus. Wright, 2015; Wex et al., 2019), and there is no standard protocol.

The rarity of INPs relative to ambient aerosols additionally challenges INP identification and source attribution. In effort to probe INP identities or composition, prior aircraft-based studies used counterflow virtual impactors (CVIs) to sample ice crystal residuals (ICR), or the particles remaining from ice in hydrometeors (Cziczo et al., 2017 and references therein). However,

identifying INPs present in ICRs has proven challenging due to shattering of ice crystals in the CVI and the fact that the INPs are often mixed with other aerosols due to in-cloud and atmospheric processing. More recently, scanning electron microscopy combined with energy dispersive X-ray (SEM-EDX) has been used to image and determine the chemical composition of INPs in ICRs collected from online instruments such as the Continuous Flow Diffusion Chamber (CFDC) (e.g., Suski et al., 2018). INP composition can also be inferred by testing samples for sensitivity to various chemical treatments (e.g., McCluskey et al., 2018a; Pummer et al., 2015; Suski et al., 2018). For example, sensitivity to digestion by lysozyme or hydrogen peroxide is indicative of cellular (microbial) or organic composition, respectively (Christner et al., 2008; Hill et al., 2016; McCluskey et al., 2018a; Suski et al., 2018). Prior studies have identified IN-active microbes by cultivating microbes derived from environmental samples and testing isolates for IN activity (e.g., Failor et al., 2017; Morris et al., 2008; Sands et al., 1982). Some microbes and fungi ice nucleate by expressing IN-active proteins, a few of which have been identified (e.g., Fröhlich-Nowoisky et al., 2015; O'Sullivan et al., 2015; Warren and Corotto, 1989). Recent innovations that aim to support studies of INP identities and chemical composition include a microfluidics device for INP detection and a Raman spectrometer coupled with a temperature and RH-controlled cell (Mael et al., 2019; Roy et al., 2021). The microfluidics device enables high-throughput IN analysis of picoliter droplets at a rate of 1500 min^{-1} and supports downstream biological and chemical analysis of INPs by sorting droplets and ice crystals (Roy et al., 2021), whereas the Mael et al. (2019) instrument enables characterization of the INP phase state and chemical composition.

Advancing predictive understanding of INPs is further challenged by the fact that aerosols often undergo heterogeneous, photochemical and multiphase reactions throughout their lifetime in the atmosphere, referred to as chemical aging. Prior studies of the effects of chemical aging on the hygroscopicity and IN efficiency of dust particles have demonstrated that the impacts depend on multiple factors including size, minerology, chemical mixing state, and the transport timeline (e.g., Andreae and Rosenfeld, 2008; Sullivan et al., 2007; 2009; 2010a; 2010b). Chemical aging

has been shown to significantly increase a dust particle's hygroscopicity if the aging processes result in mixing with soluble hygroscopic material (Fan et al., 2004; Andreae and Rosenfeld, 2008; Sullivan et al., 2009). A classic example is the reaction of calcite-rich dust particles with nitrate or chloride precursors such as NO_x, HNO_3, or HCl, which results in calcium nitrate and chloride salts that are highly hygroscopic compared to nascent dust (Sullivan et al., 2009). However, a study of single particle measurements of reactions of calcite-rich dust with oxalic acid, a typically dominant component of water-soluble organic aerosol mass, showed little to no impact on hygroscopicity, likely due to low solubility complexes with divalent cations such as Ca^{2+} (Sullivan et al., 2009). Sullivan et al. (2007) also found that uptake of secondary acids differed submicron and supermicron dust particles, and that mixing state also depended upon the transport timeline (i.e., the order in which the particles encountered secondary acids in the atmosphere). Many questions regarding the effect of aging on the hygroscopicity of dust remain open, including: 1.) to what extent do the various multiphase and heterogenous reactions increase hygroscopicity? and 2.) how sensitivity to aging relates to nascent dust minerology and composition (Gaston, 2020)? The effects of chemical aging on IN-efficiency are also complex, and as for CCN, most studies have primarily focused on dust particles. Prior studies of field observations of INP concentrations demonstrated that aging increased the IN efficiency of desert dust immersion-mode INPs (Boose et al., 2016; Conen et al. 2015). However, laboratory-based studies of the effects of aging on mineral dust INPs have yielded mixed and sometimes contradictory results, indicating that the impact of aging on IN properties likely depends on multiple factors including the ice nucleation pathway, temperature regime, the type of aging process, surface morphology and mineralogy (Perkins et al., 2020 and references therein). Multiple studies have investigated the effects of various aging processes on Arizona Test Dust (ATD) as a proxy for diverse natural dust samples, including exposure to sulfuric acid, nitric acid vapor, and solution-phase processes (Sullivan et al., 2010a, b; Salam et al., 2007; Eastwood et al., 2009; Knopf and Koop, 2006; Cziczo et al., 2009). Sullivan et al. (2010b) demonstrated that exposure to nitric acid promoted

immersion freezing of dust particles at -20 °C, but reduced the fraction of particles nucleating via the deposition freezing relative to unreacted dust. Exposure to sulfuric acid has been shown in multiple studies to dramatically decrease IN activity in both the deposition and immersion mode, yet this result was also contradicted by Knopf and Koop (2006) which found no significant impact for deposition freezing. Perkins et al. (2020) demonstrated the immersion-mode INP lability in ATD through multiple solution-phase aging processes (e.g., acid, salt), with up to 1000-fold reductions in IN abundance at freezing temperatures $>$ 10 °C. This result contrasts with the increase in IN activity attributed to aging reported in Boose et al. (2016) and Conen et al. (2015). Perkins et al. (2020) additionally reported that the lability of IN activity in ATD is temperature dependent, with large reductions evident at freezing temperature $>$ 10 °C, yet little to no change at temperatures below -15 °C. The decreased lability to heat and solution-phase processes with decreasing temperature was also reported in soil dust samples (Paramonov et al., 2018). In summary, it has proven difficult to determine any consistent impact of atmospheric processing on the IN activity of dust.

Gaps in INP observations near important sources additionally challenge development or evaluation of INP representations. Desert dust is likely the most abundant aerosol type by mass (Kinne et al., 2006; Kok et al., 2021) and multiple studies have demonstrated that mineral (i.e., desert) dust is the dominant IN species in many parts of the world based on observations (Ardon-Dryer and Levin, 2014; Boose et al., 2016; DeMott et al., 2015a; Price et al., 2018) and modeling of global INP distributions (Burrows et al., 2013; Hoose et al., 2010; Murray et al., 2012; Vergara-Temprado et al., 2017). There are multiple existing mineral dust INP parameterizations used to estimate INP concentrations in aerosolized desert dust, some based exclusively on laboratory measurements (e.g., Niemand et al., 2012; Ullrich et al., 2017), and others derived from a combination of laboratory and field measurements (DeMott et al., 2015). Yet few studies report INP measurements near (e.g., within 1 day of transport) a major dust source, and the lack of observations near dust sources inhibits evaluation of existing dust INP

parameterizations in nascent dust populations (Boose et al., 2016; Gong et al., 2020; Price et al., 2018).

Though mineral dust is considered to be the dominant INP source in many regions, multiple modeling and observational studies suggest that marine INPs are frequently dominant in remote ocean regions or in air masses with low concentrations of terrestrial aerosol (McCluskey et al., 2018b, 2018c; Vergara-Temprado et al., 2017; Wilson et al., 2015; DeMott et al., 2016). Recently, multiple studies provided much-needed INP measurements in nascent sea spray aerosol (SSA) as well as observations of ambient atmospheric INPs in marine environments (DeMott et al., 2016; Hartmann et al., 2020; McCluskey et al., 2018a, 2018b; Yang et al., 2020) where data was historically lacking and consequently, an impediment to achieving predictive understanding of global INP distributions (Burrows et al., 2013). There are now two parameterizations available for the estimation of atmospheric concentrations of marine INPs emitted from the ocean surface: Wilson et al. (2015), which derives estimates of cumulative INPs from total organic carbon concentrations, and McCluskey et al. (2018), which estimates ice nucleation site density (n_s) from aerosol surface area.

In response to the challenges to improving representation of INPs and cloud ice processes described above, the objective of this dissertation is to address critical gaps in INP instrumentation, methods and observations of marine and dust INPs to advance predictive understanding of INPs. As the implementation of INP parameterizations require significant model development effort, this dissertation also aims to provide hydrometeor phase evaluation tools needed to motivate the implementation of improved INP or ice process representation. In Chapter 2, an automated droplet assay for measurement of immersion-mode INPs is presented. We demonstrate how finite-element-analysis based heat transfer simulations can be used to quantify uncertainty in measurements of INP freezing temperature and how this can facilitate more meaningful measurement intercomparison between droplet assay instruments. In Chapter 3, we provide best practices for storage of precipitation samples for offline analysis of immersion-mode INPs,

demonstrate how storage practices can cause measurement artifacts and quantify the impacts of various common storage practices on measurements of INP concentrations. In Chapter 4, the identities and IN-activity of 14 cultivable halotolerant ice-nucleating microbes and fungi derived from precipitation and aerosol samples are reported, at least two of which are highly likely marine. Chapter 5 provides INP observations near the two greatest sources of dust emissions globally: the Sahara and the Arabian Peninsula (Kok et al., 2021). This study demonstrates that INPs observed $>$ -15 °C were organic in composition and that the existing n_s-based dust parameterizations alone would not skillfully represent the n_s observed, despite proximity (within 1 day of transport) to major dust sources and dominance of dust in air masses sampled. In Chapter 6, we present a capability to evaluate the Department of Energy's Energy Exascale Earth System Atmosphere Model (EAMv1) representation of hydrometeor phase using a forward instrument simulator that facilitates comparison between model output and ground-based cloud observations from Doppler radar and micropulse lidar (Lamer et al., 2018). The evaluation pipeline presented here will support studies of the sensitivity of simulated mixed-phase clouds to the representation of microphysical parameters such as INPs.

Finally, Chapter 7 offers reflections on how the innovations and results described in Chapters 2-5 will support efforts to develop improved representations of ice nucleation in models and how the hydrometeor phase evaluation capability in Chapter 6 can address barriers to the implementation of the improved representations of ice nucleation or other cloud ice production processes.

1.1 References

Albrecht, B. A.: Aerosols, Cloud Microphysics, and Fractional Cloudiness, Science (80), 245(4923), 1227–1230, doi:10.1126/science.245.4923.1227, 1989.

Andreae, M O and Rosenfeld, D: Aerosol–cloud–precipitation interactions. Part 1. The nature and sources of cloud-active aerosols, Earth-Science Rev., 89, 13–41,

https://doi.org/https://doi.org/10.1016/j.earscirev.2008.03.001, 2008.

Ansmann, A., Tesche, M., Althausen, D., Müller, D., Seifert, P., Freudenthaler, V., Heese, B., Wiegner, M., Pisani, G., Knippertz, P. and Dubovik, O.: Influence of Saharan dust on cloud glaciation in southern Morocco during the Saharan Mineral Dust Experiment, J. Geophys. Res. Atmos., 113(D4), doi:https://doi.org/10.1029/2007JD008785, 2008.

Ardon-Dryer, K. and Levin, Z.: Ground-based measurements of immersion freezing in the eastern Mediterranean, Atmos. Chem. Phys., 14(10), 5217–5231, doi:10.5194/acp-14-5217-2014, 2014.

Atkinson, J. D., Murray, B. J., Woodhouse, M. T., Whale, T. F., Baustian, K. J., Carslaw, K. S., Dobbie, S., O'Sullivan, D. and Malkin, T. L.: The importance of feldspar for ice nucleation by mineral dust in mixed-phase clouds, Nature, 498(7454), 355–358, doi:10.1038/nature12278, 2013.

Auer, A. H., Veal, D. L. and Marwitz, J. D.: Observations of Ice Crystal and Ice Nuclei Concentrations in Stable Cap Clouds, J. Atmos. Sci., 26(6), 1342–1343, doi:10.1175/1520-0469(1969)026¡1342:OOICAI¿2.0.CO;2, 1969. Beall, C. M., Lucero, D., Hill, T. C., DeMott, P. J., Stokes, M. D. and Prather, K. A.: Best practices for precipitation sample storage for offline studies of ice nucleation in marine and coastal environments, Atmos. Meas. Tech., 13(12), 6473–6486, doi:10.5194/amt-13-6473-2020, 2020.

Beall, C. M., Michaud, J. M., Fish, M. A., Dinasquet, J., Cornwell, G. C., Stokes, M. D., Burkart, M. D., Hill, T. C., Demott, P. J. and Prather, K. A.: Cultivable halotolerant ice-nucleating bacteria and fungi in coastal precipitation, Atmos. Chem. Phys., 21(11), 9031–9045, doi:10.5194/acp-21-9031-2021, 2021.

Bergeron, T.: On the physics of clouds and precipitation, in Proces Verbaux de l'Association de Météorologie, edited by International Union of Geodesy and Geophysics, pp. 156–178., 1935.

de Boer, G., Hashino, T., Tripoli, G. J. and Eloranta, E. W.: A numerical study of aerosol influence on mixed-phase stratiform clouds through modulation of the liquid phase, Atmos. Chem. Phys., 13(4), 1733–1749, doi:10.5194/acp-13-1733-2013, 2013.

de Boer, G., Morrison, H., Shupe, M. D. and Hildner, R.: Evidence of liquid dependent ice nucleation in high-latitude stratiform clouds from surface remote sensors, Geophys. Res. Lett., 38(1), 1–5, doi:10.1029/2010GL046016, 2011.

Boose, Y., Sierau, B., Isabel García, M., Rodríguez, S., Alastuey, A., Linke, C., Schnaiter, M., Kupiszewski, P., Kanji, Z. A. and Lohmann, U.: Ice nucleating particles in the Saharan Air Layer, Atmos. Chem. Phys., 16(14), 9067–9087, doi:10.5194/acp-16-9067-2016,

2016.

Boose, Yvonne, Sierau, Berko, Isabel García, M., Rodríguez, Sergio, Alastuey, Andrés, Linke, Claudia, Schnaiter, Martin, Kupiszewski, Piotr, Kanji, Zamin A., and Lohmann, Ulrike: Ice nucleating particles in the Saharan Air Layer, Atmos. Chem. Phys., 16, 9067–9087, https://doi.org/10.5194/acp-16-9067-2016, 2016.

Broadley, S. L., Murray, B. J., Herbert, R. J., Atkinson, J. D., Dobbie, S., Malkin, T. L., Condliffe, E. and Neve, L.: Immersion mode heterogeneous ice nucleation by an illite rich powder representative of atmospheric mineral dust, Atmos. Chem. Phys., 12(1), 287–307, doi:10.5194/acp-12-287-2012, 2012.

Budke, C. and Koop, T.: BINARY: An optical freezing array for assessing temperature and time dependence of heterogeneous ice nucleation, Atmos. Meas. Tech., 8(2), 689–703, doi:10.5194/amt-8-689-2015, 2015.

Burrows, S. M., Hoose, C., Pöschl, U. and Lawrence, M. G.: Ice nuclei in marine air: biogenic particles or dust?, Atmos. Chem. Phys., 13(1), 245–267, doi:10.5194/acp-13-245-2013, 2013.

Christner, B. C., Cai, R., Morris, C. E., McCarter, K. S., Foreman, C. M., Skidmore, M. L., Montross, S. N. and Sands, D. C.: Geographic, seasonal, and precipitation chemistry influence on the abundance and activity of biological ice nucleators in rain and snow., Proc. Natl. Acad. Sci. U. S. A., 105(48), 18854–18859, doi:10.1073/pnas.0809816105, 2008.

Conen, Franz, Rodríguez, Sergio, Hüglin, Christoph, Henne, Stephan, Herrmann, Erik, Bukowiecki, Nicolas, and Alewell, Christine: Atmospheric ice nuclei at the high-altitude observatory Jungfraujoch, Switzerland, Tellus, Ser. B Chem. Phys. Meteorol., 67, 1–10, https://doi.org/10.3402/tellusb.v67.25014, 2015.

Cziczo, Daniel J, Froyd, Karl D, Gallavardin, Stephane J, Moehler, Ottmar, Benz, Stefan, Saathoff, Harald, and Murphy, Daniel M: Deactivation of ice nuclei due to atmospherically relevant surface coatings, Environ. Res. Lett., 4, 44013, https://doi.org/10.1088/1748-9326/4/4/044013, 2009.

Cziczo, Daniel J, Froyd, Karl D, Hoose, Corinna, Jensen, Eric J, Diao, Minghui, Zondlo, Mark a, Smith, Jessica B, Twohy, Cynthia H, and Murphy, Daniel M: Clarifying the Dominant Sources and Mechanisms of Cirrus Cloud Formation., 1–8, https://doi.org/10.1126/science.1234145, 2013.

Cziczo, D. J., Ladino, L., Boose, Y., Kanji, Z. A., Kupiszewski, P., Lance, S., Mertes, S. and Wex, H.: Measurements of Ice Nucleating Particles and Ice Residuals, Meteorol. Monogr., 58,

8.1-8.13, doi:10.1175/AMSMONOGRAPHS-D-16-0008.1, 2017.

DeMott, P J, Cziczo, D J, Prenni, A J, Murphy, D M, Kreidenweis, S M, Thomson, D S, Borys, R, and Rogers, D C: Measurements of the concentration and composition of nuclei for cirrus formation., Proc. Natl. Acad. Sci. U. S. A., 100, 14655–60, https://doi.org/10.1073/pnas.2532677100, 2003.

DeMott, P. J., Möhler, O., Stetzer, O., Vali, G., Levin, Z., Petters, M. D., Murakami, M., Leisner, T., Bundke, U., Klein, H., Kanji, Z. A., Cotton, R., Jones, H., Benz, S., Brinkmann, M., Rzesanke, D., Saathoff, H., Nicolet, M., Saito, A., Nillius, B., Bingemer, H., Abbatt, J., Ardon, K., Ganor, E., Georgakopoulos, D. G. and Saunders, C.: Resurgence in Ice Nuclei Measurement Research, Bull. Am. Meteorol. Soc., 92(12), 1623–1635, doi:10.1175/2011BAMS3119.1, 2011.

DeMott, P. J., Prenni, A. J., Mcmeeking, G. R., Sullivan, R. C., Petters, M. D., Tobo, Y., Niemand, M., Möhler, O., Snider, J. R., Wang, Z. and Kreiden: Integrating laboratory and field data to quantify the immersion freezing ice nucleation activity of mineral dust particles, , 393–409, doi:10.5194/acp-15-393-2015, 2015.

DeMott, P. J., Hill, T. C. J., McCluskey, C. S., Prather, K. A., Collins, D. B., Sullivan, R. C., Ruppel, M. J., Mason, R. H., Irish, V. E., Lee, T., Hwang, C. Y., Rhee, T. S., Snider, J. R., McMeeking, G. R., Dhaniyala, S., Lewis, E. R., Wentzell, J. J. B., Abbatt, J., Lee, C., Sultana, C. M., Ault, A. P., Axson, J. L., Diaz Martinez, M., Venero, I., Santos-Figueroa, G., Stokes, M. D., Deane, G. B., Mayol-Bracero, O. L., Grassian, V. H., Bertram, T. H., Bertram, A. K., Moffett, B. F. and Franc, G. D.: Sea spray aerosol as a unique source of ice nucleating particles, Proc. Natl. Acad. Sci., 113(21), 5797–5803, doi:10.1073/pnas.1514034112, 2016.

DeMott, P. J., Hill, T. C. J., Petters, M. D., Bertram, A. K., Tobo, Y., Mason, R. H., Suski, K. J., Mccluskey, C. S., Levin, E. J. T., Schill, G. P., Boose, Y., Rauker, A. M., Miller, A. J., Zaragoza, J., Rocci, K., Rothfuss, N. E., Taylor, H. P., Hader, J. D., Chou, C., Huffman, J. A., Pöschl, U., Prenni, A. J. and Kreidenweis, S. M.: Comparative measurements of ambient atmospheric concentrations of ice nucleating particles using multiple immersion freezing methods and a continuous flow diffusion chamber, Atmos. Chem. Phys., 17(18), 11227–11245, doi:10.5194/acp-17-11227-2017, 2017.

DeMott, P. J., Möhler, O., Cziczo, D. J., Hiranuma, N., Petters, M. D., Petters, S. S., Belosi, F., Bingemer, H. G., Brooks, S. D., Budke, C., Burkert-Kohn, M., Collier, K. N., Danielczok, A., Eppers, O., Felgitsch, L., Garimella, S., Grothe, H., Herenz, P., Hill, T. C. J., Höhler, K., Kanji, Z. A., Kiselev, A., Koop, T., Kristensen, T. B., Krüger, K., Kulkarni, G., Levin, E. J. T., Murray, B. J., Nicosia, A., O'Sullivan, D., Peckhaus, A., Polen, M. J., Price, H. C., Reicher, N., Rothenberg, D. A., Rudich, Y., Santachiara, G., Schiebel, T., Schrod, J., Seifried, T. M., Stratmann, F., Sullivan, R. C., Suski, K. J., Szakáll, M., Taylor, H. P.,

Ullrich, R., Vergara-Temprado, J., Wagner, R., Whale, T. F., Weber, D., Welti, A., Wilson, T. W., Wolf, M. J. and Zenker, J.: The Fifth International Workshop on Ice Nucleation phase 2 (FIN-02): laboratory intercomparison of ice nucleation measurements, Atmos. Meas. Tech., 11(11), 6231–6257, doi:10.5194/amt-11-6231-2018, 2018.

Eastwood, Michael L, Cremel, Sebastien, Wheeler, Michael, Murray, Benjamin J, Girard, Eric, and Bertram, Allan K: Effects of sulfuric acid and ammonium sulfate coatings on the ice nucleation properties of kaolinite particles, Geophys. Res. Lett., 36, https://doi.org/https://doi.org/10.1029/2008GL035997, 2009.

Eirund, G. K., Possner, A. and Lohmann, U.: Response of Arctic mixed-phase clouds to aerosol perturbations under different surface forcings, Atmos. Chem. Phys., 19(15), 9847–9864, doi:10.5194/acp-19-9847-2019, 2019.

Failor, K. C., Schmale, D. G., Vinatzer, B. A. and Monteil, C. L.: Ice nucleation active bacteria in precipitation are genetically diverse and nucleate ice by employing different mechanisms, ISME J., 11(12), 2740–2753, doi:10.1038/ismej.2017.124, 2017.

Fan, J., Wang, Y., Rosenfeld, D. and Liu, X.: Review of Aerosol-Cloud Interactions: Mechanisms, Significance, and Challenges, J. Atmos. Sci., 73(11), 4221–4252, doi:10.1175/JAS-D-16-0037.1, 2016.

Fan, Song-Miao, Horowitz, Larry W, Levy II, Hiram, and Moxim, Walter J: Impact of air pollution on wet deposition of mineral dust aerosols, Geophys. Res. Lett., 31, https://doi.org/https://doi.org/10.1029/2003GL018501, 2004.

Findeisen, W.: Kolloid?meteorologische Vorgange bei Neiderschlagsbildung, Meteor. Z., 55, 121–133, 1938.

Fröhlich-Nowoisky, J., Hill, T. C. J., Pummer, B. G., Yordanova, P., Franc, G. D. and Pöschl, U.: Ice nucleation activity in the widespread soil fungus Mortierella alpina, Biogeosciences, 12(4), 1057–1071, doi:10.5194/bg-12-1057-2015, 2015.

Gaston, Cassandra J: Re-examining Dust Chemical Aging and Its Impacts on Earth's Climate, Acc. Chem. Res., 53, 1005–1013, https://doi.org/10.1021/acs.accounts.0c00102, 2020.

Gettelman, A., Morrison, H., Santos, S., Bogenschutz, P. and Caldwell, P. M.: Advanced Two-Moment Bulk Microphysics for Global Models. Part II: Global Model Solutions and Aerosol-Cloud Interactions, J. Clim., 28(3), 1288–1307, doi:10.1175/JCLI-D-14-00103.1, 2015.

Gong, X., Wex, H., van Pinxteren, M., Triesch, N., Fomba, K. W., Lubitz, J., Stolle, C., Robinson, T.-B., Müller, T., Herrmann, H. and Stratmann, F.: Characterization of aerosol particles

at Cabo Verde close to sea level and at the cloud level – Part 2: Ice-nucleating particles in air, cloud and seawater, Atmos. Chem. Phys., 20(3), 1451–1468, doi:10.5194/acp-20-1451-2020, 2020.

Hallegatte, S., Vogt-Schilb, A., Bangalore, M. and Rozenberg, J.: Unbreakable: Building the Resilience of the Poor in the Face of Natural Disasters, Climate Ch., World Bank, Washington, D.C. [online] Available from: http://documents.worldbank.org/curated/%0Aen/512241480487839624/Unbreakable-building-the-resilience-of-the-poor-in-the-face-of-natural-disasters (last access 14 Oct 2021), 2017.

Hallet, J. and Mossop, S. C.: Production of secondary ice particles during the riming process, Nature, 249(5452), 26–28, doi:10.1038/249026a0, 1974.

Harrison, A. D., Lever, K., Sanchez-Marroquin, A., Holden, M. A., Whale, T. F., Tarn, M. D., McQuaid, J. B. and Murray, B. J.: The ice-nucleating ability of quartz immersed in water and its atmospheric importance compared to K-feldspar, Atmos. Chem. Phys., 19(17), 11343–11361, doi:10.5194/acp-19-11343-2019, 2019.

Hartmann, M., Adachi, K., Eppers, O., Haas, C., Herber, A., Holzinger, R., Hünerbein, A., Jäkel, E., Jentzsch, C., van Pinxteren, M., Wex, H., Willmes, S. and Stratmann, F.: Wintertime Airborne Measurements of Ice Nucleating Particles in the High Arctic: A Hint to a Marine, Biogenic Source for Ice Nucleating Particles, Geophys. Res. Lett., 47(13), e2020GL087770, doi:https://doi.org/10.1029/2020GL087770, 2020.

Heymsfield, A. and Willis, P.: Cloud Conditions Favoring Secondary Ice Particle Production in Tropical Maritime Convection, J. Atmos. Sci., 71(12), 4500–4526, doi:10.1175/JAS-D-14-0093.1, 2014.

Hill, T. C. J., DeMott, P. J., Tobo, Y., Fröhlich-Nowoisky, J., Moffett, B. F., Franc, G. D. and Kreidenweis, S. M.: Sources of organic ice nucleating particles in soils, Atmos. Chem. Phys., 16(11), 7195–7211, doi:10.5194/acp-16-7195-2016, 2016.

Hiranuma, N., Bingemer, H., Budke, C., Curtius, J., Danielczok, A., Diehl, K., Dreischmeier, K., Ebert, M., Frank, F., Hoffmann, N., Kandler, K., Kiselev, A., Koop, T., Leisner, T., Peckhous, A., Rose, D., Weinbruch, S., Wex, H., Boose, Y., DeMott, P. J., Hader, J. D., Hill, T. C. J., Kanji, Z. a, Kulkarni, G., Levin, E. J. T., Mccluskey, C. S., Murakami, M., Murray, B. J., Niedermeier, D., Petters, M. D., Saito, A., Schill, G. P., Tajiri, T., Tolbert, M. a, Whale, T. F., Wright, T. P. and Yamashita, K.: A comprehensive laboratory study on the immersion freezing behavior of illite NX particles: a comparison of seventeen ice nucleation measurement techniques, Atmos. Chem. Phys., 14, doi:10.5194/acpd-14-22045-2014, 2014.

Hoose, C. and Möhler, O.: Heterogeneous ice nucleation on atmospheric aerosols: A review of

results from laboratory experiments., 2012.

Hoose, C., Kristjánsson, J. E., Chen, J.-P. and Hazra, A.: A Classical-Theory-Based Parameterization of Heterogeneous Ice Nucleation by Mineral Dust, Soot, and Biological Particles in a Global Climate Model, J. Atmos. Sci., 67(8), 2483–2503, doi:10.1175/2010JAS3425.1, 2010.

IPCC: Climate Change 2021: The Physical Science Basis, Cambridge Univ. Press. Press., 2021.

Kanji, Z. A., Ladino, L. A., Wex, H., Boose, Y., Burkert-Kohn, M., Cziczo, D. J. and Krämer, M.: Overview of Ice Nucleating Particles, Meteorol. Monogr., 58, 1.1-1.33, doi:10.1175/amsmonographs-d-16-0006.1, 2017.

Kinne, S., Schulz, M., Textor, C., Guibert, S., Balkanski, Y., Bauer, S. E., Berntsen, T., Berglen, T. F., Boucher, O., Chin, M., Collins, W., Dentener, F., Diehl, T., Easter, R., Feichter, J., Fillmore, D., Ghan, S., Ginoux, P., Gong, S., Grini, A., Hendricks, J., Herzog, M., Horowitz, L., Isaksen, I., Iversen, T., Kirkevåg, A., Kloster, S., Koch, D., Kristjansson, J. E., Krol, M., Lauer, A., Lamarque, J. F., Lesins, G., Liu, X., Lohmann, U., Montanaro, V., Myhre, G., Penner, J., Pitari, G., Reddy, S., Seland, O., Stier, P., Takemura, T. and Tie, X.: An AeroCom initial assessment – optical properties in aerosol component modules of global models, Atmos. Chem. Phys., 6(7), 1815–1834, doi:10.5194/acp-6-1815-2006, 2006.

Kiselev, A., Bachmann, F., Pedevilla, P., Cox, S. J., Michaelides, A., Gerthsen, D. and Leisner, T.: Active sites in heterogeneous ice nucleation–the example of K-rich feldspars, Science (80-.)., 355(6323), 367–371, doi:10.1126/science.aai8034, 2017.

Knopf, Daniel A and Koop, Thomas: Heterogeneous nucleation of ice on surrogates of mineral dust, J. Geophys. Res. Atmos., 111, https://doi.org/https://doi.org/10.1029/2005JD006894, 2006.

Knopf, D. A., Alpert, P. A., Zipori, A., Reicher, N. and Rudich, Y.: Stochastic nucleation processes and substrate abundance explain time-dependent freezing in supercooled droplets, npj Clim. Atmos. Sci., 3(1), 2, doi:10.1038/s41612-020-0106-4, 2020.

Kok, J. F., Adebiyi, A. A., Albani, S., Balkanski, Y., Checa-Garcia, R., Chin, M., Colarco, P. R., Hamilton, D. S., Huang, Y., Ito, A., Klose, M., Li, L., Mahowald, N. M., Miller, R. L., Obiso, V., Pérez García-Pando, C., Rocha-Lima, A. and Wan, J. S.: Contribution of the world's main dust source regions to the global cycle of desert dust, Atmos. Chem. Phys., 21(10), 8169–8193, doi:10.5194/acp-21-8169-2021, 2021.

Lamer, K., Fridlind, A. M., Ackerman, A. S., Kollias, P., Clothiaux, E. E. and Kelley, M.: $(GO)^2$-SIM: a GCM-oriented ground-observation forward-simulator framework for objective

evaluation of cloud and precipitation phase, Geosci. Model Dev., 11(10), 4195–4214, doi:10.5194/gmd-11-4195-2018, 2018.

Lau, K. M. and Wu, H. T.: Warm rain processes over tropical oceans and climate implications, Geophys. Res. Lett., 30(24), doi:https://doi.org/10.1029/2003GL018567, 2003.

Lee, A. (U. S. S. and E. C.: Public Input Welcomed on Climate Change Disclosures. [online] Available from: https://www.sec.gov/news/public-statement/lee-climate-change-disclosures#˙ftn4 (last access 14 Oct 2021), 2021.

Lloyd, G., Choularton, T. W., Bower, K. N., Gallagher, M. W., Connolly, P. J., Flynn, M., Farrington, R., Crosier, J., Schlenczek, O., Fugal, J. and Henneberger, J.: The origins of ice crystals measured in mixed phase clouds at High-Alpine site Jungfraujoch., 2015.

Lohmann, U. and Feichter, J.: Global indirect aerosol effects: a review, Atmos. Chem. Phys., 5(3), 715–737, doi:10.5194/acp-5-715-2005, 2005.

Löw, P.: Hurricanes cause record losses in 2017 - The year in figures, Munich RE, Munich, Germany, 2018, https://www.munichre.com/topics-online/en/climate-change-and-natural-disasters/natural-disasters/2017-year-in-figures.html (last access 14 Oct. 2021).

Ma, P.-L., Bretherton, C., Stinis, P., Larson, V., Barnes, E., Silva, S., Hardin, J., Pritchard, M., Harrop, B., Pressel, K., Kaul, C., Wang, H., Muelmenstaedt, J. and Singh, B.: Facilitating better and faster simulations of aerosol-cloud interactions in Earth system models., 2021.

Mael, L. E., Busse, H. and Grassian, V. H.: Measurements of Immersion Freezing and Heterogeneous Chemistry of Atmospherically Relevant Single Particles with Micro-Raman Spectroscopy, Anal. Chem., 91(17), 11138–11145, doi:10.1021/acs.analchem.9b01819, 2019.

Mayer, Kathryn J, Wang, Xiaofei, Santander, Mitchell V, Mitts, Brock A, Sauer, Jonathan S, Sultana, Camille M, Cappa, Christopher D, and Prather, Kimberly A: Secondary Marine Aerosol Plays a Dominant Role over Primary Sea Spray Aerosol in Cloud Formation, ACS Cent. Sci., 6, 2259–2266, https://doi.org/10.1021/acscentsci.0c00793, 2020.

McCluskey, C. S., Ovadnevaite, J., Rinaldi, M., Atkinson, J., Belosi, F., Ceburnis, D., Marullo, S., Hill, T. C. J., Lohmann, U., Kanji, Z. A., O'Dowd, C., Kreidenweis, S. M. and DeMott, P. J.: Marine and Terrestrial Organic Ice-Nucleating Particles in Pristine Marine to Continentally Influenced Northeast Atlantic Air Masses, J. Geophys. Res. Atmos., 123(11), 6196–6212, doi:10.1029/2017JD028033, 2018a.

McCluskey, C. S., Hill, T. C. J., Humphries, R. S., Rauker, A. M., Moreau, S., Strutton, P. G., Chambers, S. D., Williams, A. G. and McRobert, I.: Observations of Ice Nucleating

Particles Over Southern Ocean Waters, Geophys. Res. Lett., 989–997, doi:10.1029/2018GL079981, 2018b.

Morris, C. E., Sands, D. C., Vinatzer, B. A., Glaux, C., Guilbaud, C., Buffière, A., Yan, S., Dominguez, H. and Thompson, B. M.: The life history of the plant pathogen Pseudomonas syringae is linked to the water cycle, ISME J., 2(3), 321–334, doi:10.1038/ismej.2007.113, 2008.

Mülmenstädt, J., Sourdeval, O., Delanoë, J. and Quaas, J.: Frequency of occurrence of rain from liquid-, mixed-, and ice-phase clouds derived from A-Train satellite retrievals, Geophys. Res. Lett., 42(15), 6502–6509, doi:https://doi.org/10.1002/2015GL064604, 2015.

Murray, B. J., O'Sullivan, D., Atkinson, J. D. and Webb, M. E.: Ice nucleation by particles immersed in supercooled cloud droplets., Chem. Soc. Rev., 41(19), 6519–54, doi:10.1039/c2cs35200a, 2012.

Niemand, M., Möhler, O., Vogel, B., Vogel, H., Hoose, C., Connolly, P., Klein, H., Bingemer, H., Demott, P., Skrotzki, J. and Leisner, T.: A particle-surface-area-based parameterization of immersion freezing on desert dust particles, J. Atmos. Sci., 69(10), 3077–3092, doi:10.1175/JAS-D-11-0249.1, 2012.

O'Sullivan, D., Murray, B. J., Ross, J. F., Whale, T. F., Price, H. C., Atkinson, J. D., Umo, N. S. and Webb, M. E.: The relevance of nanoscale biological fragments for ice nucleation in clouds., Sci. Rep., 5, 8082, doi:10.1038/srep08082, 2015.

Paramonov, M, David, R O, Kretzschmar, R, and Kanji, Z A: A laboratory investigation of the ice nucleation efficiency of three types of mineral and soil dust, Atmos. Chem. Phys., 18, 16515–16536, https://doi.org/10.5194/acp-18-16515-2018, 2018.

Perkins, Russell J, Gillette, Samantha M, Hill, Thomas C J, and DeMott, Paul J: The Labile Nature of Ice Nucleation by Arizona Test Dust, ACS Earth Sp. Chem., 4, 133–141, https://doi.org/10.1021/acsearthspacechem.9b00304, 2020.

Petters, Markus. Wright, T. P.: Revisiting ice nucleation from precipitation samples, Geophys. Res. Lett., 8758–8766, doi:10.1002/2015GL065733.

Price, H. C., Baustian, K. J., McQuaid, J. B., Blyth, A., Bower, K. N., Choularton, T., Cotton, R. J., Cui, Z., Field, P. R., Gallagher, M., Hawker, R., Merrington, A., Miltenberger, A., Neely III, R. R., Parker, S. T., Rosenberg, P. D., Taylor, J. W., Trembath, J., Vergara-Temprado, J., Whale, T. F., Wilson, T. W., Young, G. and Murray, B. J.: Atmospheric Ice-Nucleating Particles in the Dusty Tropical Atlantic, J. Geophys. Res. Atmos., 123(4), 2175–2193, doi:https://doi.org/10.1002/2017JD027560, 2018.

Pruppacher, H. R. and Klett, J. D.: Microphysics of Clouds and Precipitation, Atmopsheri., Kluwer Academic Publishers, Dordrecht, the Netherlands., 1997.

Pummer, B. G., Budke, C., Augustin-Bauditz, S., Niedermeier, D., Felgitsch, L., Kampf, C. J., Huber, R. G., Liedl, K. R., Loerting, T., Moschen, T., Schauperl, M., Tollinger, M., Morris, C. E., Wex, H., Grothe, H., Pöschl, U., Koop, T. and Fröhlich-Nowoisky, J.: Ice nucleation by water-soluble macromolecules, Atmos. Chem. Phys., 15(8), 4077–4091, doi:10.5194/acp-15-4077-2015, 2015.

Rigaud, K. K., de Sherbinin, A., Jones, B., Bergmann, J., Clement, V., Ober, K., Schewe, J., Adamo, S., McCusker, B., Heuser, S. and Midgley, A.: Groundswell: Preparing for Internal Climate Migration, World Bank, Washington, D.C. [online] Available from: https://openknowledge.worldbank.org/handle/10986/29461, 2018.

Rogers, D. C., DeMott, P. J., Kreidenweis, S. M. and Chen, Y.: Measurements of ice nucleating aerosols during SUCCESS, Geophys. Res. Lett., 25(9), 1383, doi:10.1029/97GL03478, 1998.

Roy, P., House, M. L. and Dutcher, C. S.: A Microfluidic Device for Automated High Throughput Detection of Ice Nucleation of Snomax(®), Micromachines, 12(3), 296, doi:10.3390/mi12030296, 2021.

Salam, A, Lohmann, U, and Lesins, G: Ice nucleation of ammonia gas exposed montmorillonite mineral dust particles, Atmos. Chem. Phys., 7, 3923–3931, https://doi.org/10.5194/acp-7-3923-2007, 2007.

Sands, D., Langhans, V. E., Scharen, A. L. and Smet, G.: The association between bacteria and rain and possible resultant meteorological implications, J. Hungarian Meteorol. Serv., 86, 148–152, 1982.

Seinfeld, J. H., Bretherton, C., Carslaw, K. S., Coe, H., DeMott, P. J., Dunlea, E. J., Feingold, G., Ghan, S., Guenther, A. B., Kahn, R., Kraucunas, I., Kreidenweis, S. M., Molina, M. J., Nenes, A., Penner, J. E., Prather, K. A., Ramanathan, V., Ramaswamy, V., Rasch, P. J., Ravishankara, A. R., Rosenfeld, D., Stephens, G. and Wood, R.: Improving our fundamental understanding of the role of aerosol-cloud interactions in the climate system, Proc. Natl. Acad. Sci., 113(21), 5781–5790, doi:10.1073/pnas.1514043113, 2016.

Solomon, A., Feingold, G. and Shupe, M. D.: The role of ice nuclei recycling in the maintenance of cloud ice in Arctic mixed-phase stratocumulus, Atmos. Chem. Phys., 15(18), 10631–10643, doi:10.5194/acp-15-10631-2015, 2015.

Sullivan, R C, Guazzotti, S A, Sodeman, D A, and Prather, K A: Direct observations of the atmospheric processing of Asian mineral dust, Atmos. Chem. Phys., 7, 1213–1236,

https://doi.org/10.5194/acp-7-1213-2007, 2007.

Sullivan, R C, Moore, M J K, Petters, M D, Kreidenweis, S M, Roberts, G C, and Prather, K A: Effect of chemical mixing state on the hygroscopicity and cloud nucleation properties of calcium mineral dust particles, Atmos. Chem. Phys., 9, 3303–3316, https://doi.org/10.5194/acp-9-3303-2009, 2009.

Sullivan, R C, Petters, M D, DeMott, P J, Kreidenweis, S M, Wex, H, Niedermeier, D, Hartmann, S, Clauss, T, Stratmann, F, Reitz, P, Schneider, J, and Sierau, B: Irreversible loss of ice nucleation active sites in mineral dust particles caused by sulphuric acid condensation, Atmos. Chem. Phys., 10, 11471–11487, https://doi.org/10.5194/acp-10-11471-2010, 2010a.

Sullivan, Ryan C, Miñambres, Lorena, DeMott, Paul J, Prenni, Anthony J, Carrico, Christian M, Levin, Ezra J T, and Kreidenweis, Sonia M: Chemical processing does not always impair heterogeneous ice nucleation of mineral dust particles, Geophys. Res. Lett., 37, https://doi.org/https://doi.org/10.1029/2010GL045540, 2010b.

Suski, K. J., Hill, T. C. J., Levin, E. J. T., Miller, A., DeMott, P. J. and Kreidenweis, S. M.: Agricultural harvesting emissions of ice-nucleating particles, Atmos. Chem. Phys., 18(18), 13755–13771, doi:10.5194/acp-18-13755-2018, 2018.

Twomey, S.: The Influence of Pollution on the Shortwave Albedo of Clouds, J. Atmos. Sci., 34(7), 1149–1152, doi:10.1175/1520-0469(1977)034¡1149:TIOPOT¿2.0.CO;2, 1977.

Ullrich, R., Hoose, C., Möhler, O., Niemand, M., Wagner, R., Höhler, K., Hiranuma, N., Saathoff, H. and Leisner, T.: A new ice nucleation active site parameterization for desert dust and soot, J. Atmos. Sci., 74(3), 699–717, doi:10.1175/JAS-D-16-0074.1, 2017. Vali, G.: Interpretation of freezing nucleation experiments: Singular and stochastic; Sites and surfaces, Atmos. Chem. Phys., 14(11), 5271–5294, doi:10.5194/acp-14-5271-2014, 2014.

Vergara-Temprado, J., Murray, B. J., Wilson, T. W., O'Sullivan, D., Browse, J., Pringle, K. J., Ardon-Dryer, K., Bertram, A. K., Burrows, S. M., Ceburnis, D., Demott, P. J., Mason, R. H., O'Dowd, C. D., Rinaldi, M. and Carslaw, K. S.: Contribution of feldspar and marine organic aerosols to global ice nucleating particle concentrations, Atmos. Chem. Phys., 17(5), 3637–3658, doi:10.5194/acp-17-3637-2017, 2017.

Warren, G. and Corotto, L.: The consensus sequence of ice nucleation proteins from Erwinia herbicola, Pseudomonas fluorescens and Pseudomonas syringae, Gene, 85(1), 239–242, doi:https://doi.org/10.1016/0378-1119(89)90488-5, 1989.

Wegener, A.: Thermodynamik der Atmosphäre, edited by J. A. Barth., 1911.

Welti, A., Lüönd, F., Kanji, Z. A., Stetzer, O. and Lohmann, U.: Time dependence of immersion freezing: an experimental study on size selected kaolinite particles, Atmos. Chem. Phys., 12(20), 9893–9907, doi:10.5194/acp-12-9893-2012, 2012.

Westbrook, C. D. and Illingworth, A. J.: The formation of ice in a long-lived supercooled layer cloud, Q. J. R. Meteorol. Soc., 139(677), 2209–2221, doi:https://doi.org/10.1002/qj.2096, 2013.

Wex, H., Augustin-Bauditz, S., Boose, Y., Budke, C., Curtius, J., Diehl, K., Dreyer, A., Frank, F., Hartmann, S., Hiranuma, N., Jantsch, E., Kanji, Z. A., Kiselev, A., Koop, T., Möhler, O., Niedermeier, D., Nillius, B., Rösch, M., Rose, D., Schmidt, C., Steinke, I. and Stratmann, F.: Intercomparing different devices for the investigation of ice nucleating particles using Snomax as test substance, Atmos. Chem. Phys., 15(3), 1463–1485, doi:10.5194/acp-15-1463-2015, 2015.

Wex, H., Huang, L., Zhang, W., Hung, H., Traversi, R., Becagli, S., Sheesley, R. J., Moffett, C. E., Barrett, T. E., Bossi, R., Skov, H., Hünerbein, A., Lubitz, J., Löffler, M., Linke, O., Hartmann, M., Herenz, P. and Stratmann, F.: Annual variability of ice-nucleating particle concentrations at different Arctic locations, Atmos. Chem. Phys., 19(7), 5293–5311, doi:10.5194/acp-19-5293-2019, 2019.

Wilson, T. W., Ladino, L. a., Alpert, P. a., Breckels, M. N., Brooks, I. M., Browse, J., Burrows, S. M., Carslaw, K. S., Huffman, J. A., Judd, C., Kilthau, W. P., Mason, R. H., McFiggans, G., Miller, L. a., Nájera, J. J., Polishchuk, E., Rae, S., Schiller, C. L., Si, M., Temprado, J. V., Whale, T. F., Wong, J. P. S., Wurl, O., Yakobi-Hancock, J. D., Abbatt, J. P. D., Aller, J. Y., Bertram, A. K., Knopf, D. a. and Murray, B. J.: A marine biogenic source of atmospheric ice-nucleating particles, Nature, 525(7568), 234–238, doi:10.1038/nature14986, 2015.

Wright, T. P. and Petters, M. D.: The role of time in heterogeneous freezing nucleation, J. Geophys. Res. Atmos., 118(9), 3731–3743, doi:https://doi.org/10.1002/jgrd.50365, 2013.

Wright, T. P., Petters, M. D., Hader, J. D., Morton, T. and Holder, A. L.: Minimal cooling rate dependence of ice nuclei activity in the immersion mode, J. Geophys. Res. Atmos., 118(18), 10535–10543, doi:10.1002/jgrd.50810, 2013.

Yang, J., Wang, Z., Heymsfield, A. J., DeMott, P. J., Twohy, C. H., Suski, K. J. and Toohey, D. W.: High ice concentration observed in tropical maritime stratiform mixed-phase clouds with top temperatures warmer than −8°C, Atmos. Res., 233, 104719, doi:https://doi.org/10.1016/j.atmosres.2019.104719, 2020.

Chapter 2

2 Automation and Heat Transfer Characterization of Immersion Mode Spectroscopy for Analysis of Ice Nucleating Particles

2.1 Abstract

Ice-nucleating particles (INPs) influence cloud properties and can affect the overall precipitation efficiency. Developing a parameterization of INPs in global climate models has proven challenging. More INP measurements, including studies of their spatial distribution, sources and sinks, and fundamental freezing mechanisms, must be conducted in order to further improve INP parameterizations. In this paper, an immersion mode INP measurement technique is modified and automated using a software-controlled, real-time image stream designed to leverage optical changes of water droplets to detect freezing events. For the first time, heat transfer properties of the INP measurement technique are characterized using a finite-element analysis

based heat transfer simulation to improve accuracy of INP freezing temperature measurement. The heat transfer simulation is proposed as a tool that could be used to explain the sources of bias in temperature measurements in INP measurement techniques, and ultimately explain the observed discrepancies in measured INP freezing temperatures between different instruments. The simulation results show that a difference of +8.4 ºC between the well base temperature and the headspace gas results in an up to 0.6 ºC stratification of the aliquot, whereas a difference of +4.2 ºC or less results in a thermally homogenous water volume within the error of the thermal probe, ±0.2 ºC. The results also show that there is a strong temperature gradient in the immediate vicinity of the aliquot, such that without careful placement of temperature probes, or characterization of heat transfer properties of the water and cooling environment, INP measurements can be biased toward colder temperatures. Using the modified immersion mode technique, the Automated Ice Spectrometer (AIS), measurements of the standard test dust illite NX are reported and compared against 6 other immersion mode droplet assay techniques featured in Hiranuma et al. (2015) that used wet suspensions. AIS measurements of illite NX INP freezing temperatures compare reasonably with others, falling within the 5 ºC spread in reported spectra. The AIS and its characterization of heat transfer properties allows higher confidence in accuracy of freezing temperature measurement, higher throughput of sample analysis, and enables disentanglement of the effects of heat transfer rates on sample volumes from time dependence of ice nucleation.

2.2 Introduction

Ice-nucleating particles (INPs) induce freezing of cloud droplets at temperatures above their homogeneous freezing-point (-38 °C), and at a relative humidity (RH) below the homogeneous freezing RH of aqueous solution droplets at lower temperatures, influencing cold cloud lifetime, phase, as well as their optical and microphysical properties. INPs are comprised of a diverse population of particles, some species of which have complex sources and sinks; devel-

oping a parameterization of INPs in global climate models (GCMs) that results in a credible representation of global cloud coverage and the radiative balance remains a challenge (DeMott et al., 2010; Seinfeld et al., 2016; Burrows et al., 2013). In situ observations to close critical knowledge gaps such as the vertical distribution of INPs in the air column, the complex sources and sinks of biological INPs, and INP influence on cloud microphysics are identified as a high priority for the improvement of INP representation in GCMs (Seinfeld et al., 2016; Burrows et al., 2013). One of the largest biases in shortwave reflectivity exists over the Southern Ocean, and this bias may be influenced by poor representation of INPs over primarily oceanic regions (Trenberth and Fasullo, 2010; DeMott et al., 2010). Measurements of INP number concentrations, particularly in remote ocean regions are needed to help develop parameterizations of ice nucleation for use in cloud resolving models and GCMs. To further improve the parameterization of INPs, both field and laboratory measurements are needed to identify drivers of ice nucleation in clouds. Accurately defining the activation temperature of INPs is critical to understanding the influence of INPs on clouds and improving representation of INPs in GCMs because INP freezing temperatures influence cloud phase and lifetime in mixed-phase clouds, or the supersaturation or temperature conditions in which ice clouds can form (DeMott et al., 2003, Cziczo et al., 2013). INP concentrations applied in cloud and climate models must be accurate to within a factor of 10 to avoid biases that lead to significant differences in cloud radiative and microphysical properties (Phillips et al., 2003).

Several instruments and techniques exist, utilizing both online (real-time) and offline (processed post-collection) approaches, for the measurement of INP number concentration and activation temperature across the range of ice nucleation mechanisms. Ice nucleation mechanisms include deposition nucleation, immersion, contact and condensation freezing. However, some simulations find immersion freezing is the dominant ice nucleation mechanism globally from 1000 to 200 hPa (Hoose et al., 2010) hence, most INP measurement techniques target immersion mode freezing. In Hiranuma et al. (2015), 17 online and offline immersion mode instruments were

compared using illite NX as the dust standard. The major differences between the 17 instruments studied are described in detail therein, however in brief, all of the instruments fall into one of two categories: droplet assay techniques, in which INPs are immersed in water and distributed among an array of pico to microliter scale droplets on a substrate and then cooled until frozen, or chamber techniques, in which droplets are passed through a temperature and humidity controlled chamber, where the freezing of droplets and their associated size change is detected with optical particle counters. Each of these techniques pose significant INP measurement challenges due to the rarity of INPs, which represent 1 in 10^6 or fewer of total aerosol particles (Rogers et al., 1998), and mitigation requires large air sample volumes which both limits the temporal sampling resolution, and increases the chance of contamination, which can overwhelm subtle INP signals in the data. Making INP freezing temperature measurements can also present challenges, because sample droplets or crystals cannot be directly probed with thermal sensors throughout the cooling process without altering the fundamental shape or content of the droplet, and most thermal probes are not small enough to access nano to microliter sized droplets.

In this paper, an offline freezing assay technique for measurement of immersion mode INPs (Hill et al., 2014; Hiranuma et al., 2015) is automated using a software-controlled real-time image stream designed to leverage optical changes of water volume arrays to detect freezing events. The offline freezing assay is an immersion mode technique that is similar to the immersion mode droplet assay, with a difference in the type of substrate used. In both techniques, multiple water volumes are supported on a substrate which is cooled until the water volumes are frozen, and concentrations of INPs as a function of freezing temperature are calculated from fractions of unfrozen droplets per temperature (see Sec. 2.1). In droplet assays, water volumes are distributed on a cold-stage as droplets during measurements. However, in the freezing assay, small aliquots of water, typically around 50 μL each, are distributed in 1.2 mL wells within disposable polypropylene trays. The trays are mounted in aluminum blocks that are cooled during measurements (see Sec. 2.2). Albeit with significant loss of time resolution, droplet or freezing

assays provide an offline alternative for INP measurement with fewer aerosol size limitations than online chamber techniques. For regular sampling on any surface site, INP samples may be collected on open-face filters, which reduce sample inlet particle size biases and particle losses.

There are ten current instruments for measuring immersion mode INP concentrations using picoliter to nanoliter droplet or liquid volume arrays on or within cooled surfaces: the Leeds Nucleation by Immersed Particles instrument (NIPI) (Whale et al., 2015), the Bielefeld Ice Nucleation ARraY (BINARY) (Budke and Koop, 2015), the North Carolina State Cold Stage (NC State-CS) (Wright et al., 2013), the University of Colorado Raman Microscope Cold Stage (CU-RMCS) (Baustian et al., 2010; Wise et al. 2010), the Frankfurt Ice Nuclei Deposition FreezinG Experiment (FRIDGE) (Klein et al., 2010), the Colorado State University Ice Spectrometer (CSU-IS) (Hiranuma et al. 2015, SI), the LED-based Ice Nucleation Detection Apparatus (LINDA) (Stopelli et al., 2014), the Cryogenic Refrigerator Applied to Freezing Test (CRAFT) (Tobo, 2016), WISDOM (WeIzmann Supercooled Droplets Observation on Microarray) (Y. Rudich, personal communication), and the MicroOrifice Uniform Deposit Impactor-Droplet Freezing Technique (MOUDI-DFT) (Mason et al., 2015). Differences between the techniques include: a variety of strategies to minimize the Wegener-Bergeron-Findeisen process, in which frozen droplets near liquid droplets take up water vapour as the liquid droplets shrink, the degree to which RH or evaporation is controlled, number and size of droplets (or samples) accommodated, measurable freezing temperature range, and how freezing events are detected. Almost all of the ten techniques, with the exception of the CSU-IS, use a camera to image the droplets. The NIPI, FRIDGE, and NC-State CS save images at a frequency on the order of 1 image per second, and post-process a stream of images of the droplets with varying levels of automation in the determination of freezing events. BINARY and LINDA report the use of an algorithm similar to the one described here (see Sec. 2.2) in which changes in the 8-bit mean grey value of a monochrome image, or the intensity of LED light transmitted, respectively, are used to detect the droplet's phase change. Additionally, the heat transfer properties of the new SIO-AIS (Scripps

Institution of Oceanography – Automated Ice Spectrometer) instrument are also characterized through a finite element analysis heat transfer simulation to evaluate the homogeneity of INP sample temperatures and identify optimal locations for the thermal probes. Finally, the standard test dust used in Hiranuma et al. (2015) was tested using the instrument, and was compared against the 6 other droplet array immersion mode INP measurement techniques that reported wet suspension measurements of illite NX.

2.3 Automation of immersion mode ice spectroscopy

2.3.1 Theory of operation

Immersion mode ice spectroscopy measures INP concentrations at specific temperatures of a liquid sample. INP measurements of air samples are made by collecting particles on a filter (or via impinging particles into liquid), immersing the filter in ultrapure water, and shaking particles off of the filter by hand or via an automated rotator (DeMott et al., 2016). The liquid sample is then distributed in microliter aliquots into a clean 96-well disposable polypropylene sample tray. An equal number and volume of aliquots of ultrapure water accompany each sample in the disposable tray as a control for contamination from the loading and/or ultrapure water. The sample trays are then inserted into an aluminum block that is cooled until the samples are frozen. The homogenous freezing point of water is −38 ºC, but either the 96-well sample tray surface or impurities present in the water induce freezing at higher temperatures, typically starting at −25 to −27 ºC, which limits the lower temperatures for which INP number concentrations may be assessed. Cumulative INP number concentrations per temperature per volume are calculated using the fraction of unfrozen wells f per given temperature interval:

$$INP = \frac{-ln(f)}{V} \tag{2.1}$$

where V is the volume of the sample in each well (Vali, 1971). The fraction of unfrozen wells f is adjusted for contamination by subtracting the number of frozen ultrapure water wells per temperature interval from both the total number of unfrozen wells and total wells of the sample.

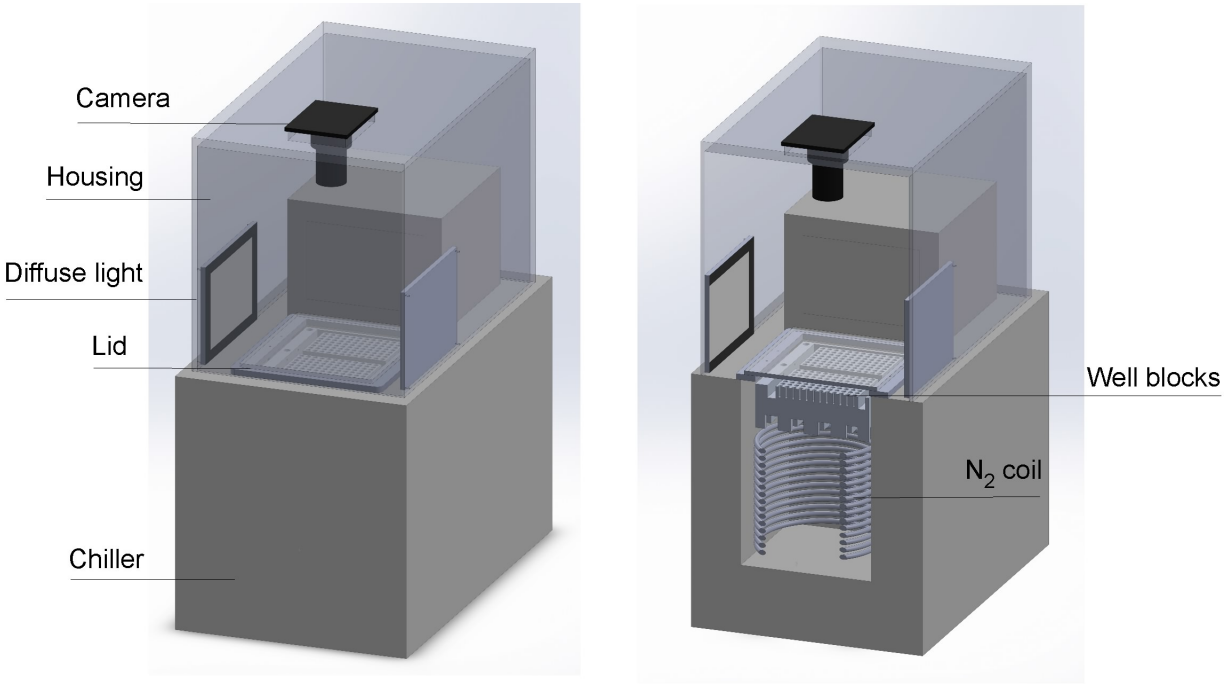

Figure 2.1: Schematic of Automated Ice Spectrometer (AIS) showing primary components as indicated by labels. Shown on the left is a camera, insulated housing for the camera and lights, LED diffuse lighting, a lid placed over the well blocks, and the chiller unit. Lid refers to the optically clear plexiglass cover, beneath which cold nitrogen gas is injected. Cutaway shows copper coil submerged in coolant that provides pre-chilled nitrogen gas to the space beneath plexiglass lid.

2.3.2 Physical design of the ice spectrometer

In previous ice spectrometer INP studies, observation of each well-freezing event was conducted manually by an operator, which limited the number of samples and wells per sample that could be processed and required a cooling rate slow enough to accurately observe and manually record each freezing event. In order to increase sample throughput and improve accuracy of INP freezing temperature measurement, the immersion mode ice spectrometer (Hill

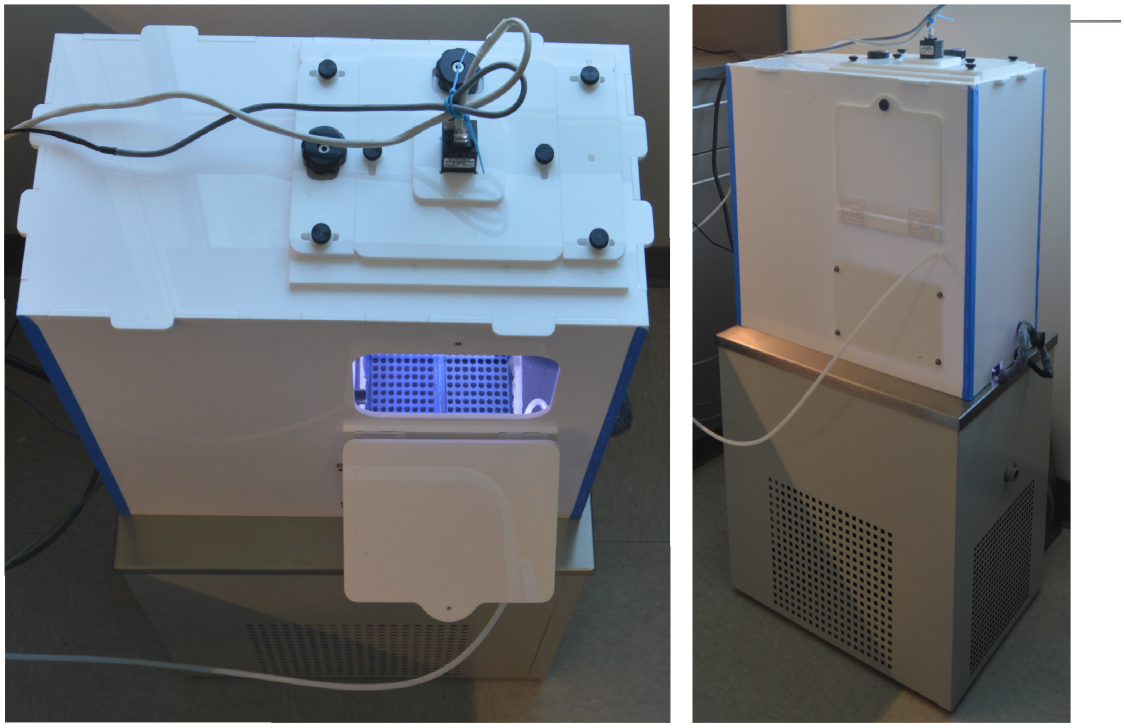

Figure 2.2: Photo of current Automated Ice Spectrometer system. Housing is manufactured from white cast acrylic. **(a)** Top–side view indicating camera and its adjustable cradle and access door open, showing cooled well plate within. **(b)** Oblique front view showing AIS housing sitting atop commercial chiller unit (Fisher Scientific Isotemp® circulator). Tubing shown is the nitrogen gas input line.

et al., 2014; Hiranuma et al., 2015) was redesigned to increase sample cooling rates (see Figs. 2.1 and 2.2) and automated using a software-controlled camera that monitors changes in optical properties of water droplets during freezing. In this paper, the new instrument's maximum average cooling rate of −0.87 ºC min^{-1}, as measured in the coolant bath from room temperature to −33 ºC, was used for all measurements and simulations. For the same temperature range, the average cooling rate as measured at the base of the well is the same. We do not investigate the role of cooling rate on freezing, known to influence freezing activation spectra to a much smaller extent than temperature alone (Vali, 2014).

In the new instrument, the Automated Ice Spectrometer (AIS), two aluminum well blocks are fixed inside the coolant bath cavity of a Fisher™ Isotemp™ refrigerated bath circulator and fitted with a sealed splash guard to prevent contamination of the well region by contact with the coolant. Each of the two aluminum blocks has a machined indentation cavity in which the 96-well disposable sample tray is tightly fitted. A plexiglass lid caps the well region to insulate and isolate the air above the wells from room temperature air. A 1.8 mm long, 0.64 cm diameter coiled copper tube, connected to an external dry-nitrogen supply, lies in the coolant bath beneath the well block in order to cool nitrogen gas that is pumped over the well region at 0.25 L min^{-1}. The cold nitrogen gas purges room temperature air away from the well region to decrease stratification of temperature within the sample volumes. A flow rate of 0.25 L min^{-1} was chosen because it was found empirically to most effectively cool the air above the well region. The nitrogen gas enters the well region significantly warmer than the chilled bath temperature (about +11 ºC; see Fig. 2.3) because the gas flows through approximately 15 cm of rubber tubing exposed to the ambient room temperature before being injected beneath the plexiglass cover, and the headspace gas is not perfectly isolated from room air heat. At flow rates less than 0.25 L min^{-1}, room temperature air leaks into the well region, but at significantly higher flow rates the fast-flowing nitrogen gas lifts the acrylic plate, causing additional leakage.

A 0.5-megapixel monochrome camera (Point Grey Blackfly 0.5 MP Mono GigE POE) is used to image the wells throughout the cooling process. As depicted in Fig. 2.6, the camera is controlled with custom National Instruments LabVIEW software, which allows the user to adjust imaging parameters including brightness, exposure, gain, and rotation via a graphical user interface control panel shown in Fig. 2.4. The refrigerated bath circulator is also controlled by the software and allows the user either to ramp the temperature of the coolant from room temperature to the input target temperature at a constant rate or to "stair-step" the coolant bath temperature at adjustable, incremented time and temperature steps (with the tolerance of the bath circulator thermostat and the starting and stopping temperature as additional input options).

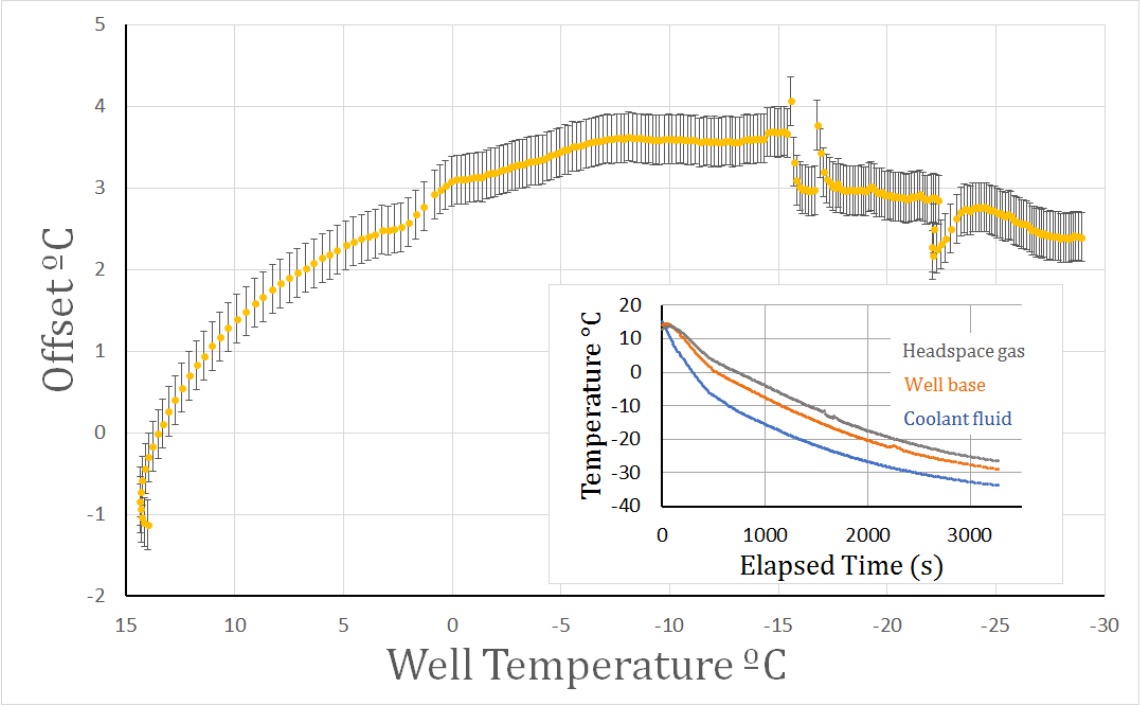

Figure 2.3: Graph of well temperature vs. temperature offset measured between the base of the well and the air above the well as measured with a thermistor probe (orange filled circles). The error bars in the larger plot show the range of temperature offsets corresponding to the ±0.3 ºC calibration error of the temperature standard. From room temperature to −33 ºC as measured at the base of the well, the average cooling rate is −0.87 ºC min^{-1}. Inset shows cooling performance of the bath coolant and the temperature within the well and gas above well over 3276 s measured by thermistor probes. The average cooling rate at the base of the well during the time period from 0 to −27 ºC, however, is −0.69 ºC min^{-1} because the cooling rate slows as the refrigerated cooling bath approaches its minimum temperature.

As shown in Figs. 2.1 and 2.2, the camera is fixed above the well region at the top of a plastic housing fabricated from white cast acrylic sheet (0.64 cm thick). An adjustable cradle holds the camera and allows aligning of the camera lens (2.8– 12 mm Focal Length, Varifocal Video Lens, Edmund Optics) over the center of the well block. Also fixed within the white housing are two white LED backlights (Edmund Optics), one on either side of the well region, which together provide a stable lighting environment for imaging of the wells and the liquid samples. Once the camera is aligned using the adjustable cradle, the video image is live-streamed via the control software so that two 8×12 grids of 15×15 pixel squares are aligned over all 192 wells. Each 15×15 pixel box corresponds to an individual sample well, and the mean intensity of

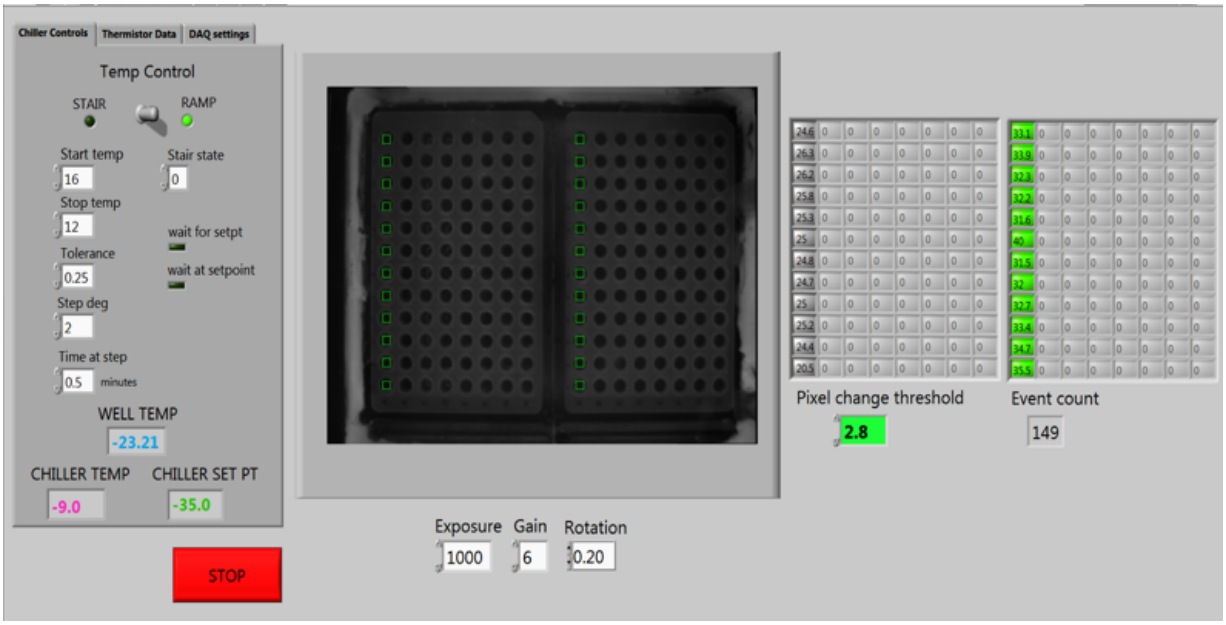

Figure 2.4: A screenshot of the AIS user computer interface, with chiller controls and well temperature readings on the left and video stream of image of wells in the middle. The detected freezing events are highlighted in green and displayed in the well matrix diagram on the right.

light reflected from each well is recorded.

When droplets freeze, the intensity of the light reflected back to the camera decreases due to the dark background of the inner well block. As in the flowchart depicted in Fig. 2.6, at each new time step t_i, if the difference between the mean intensity I of the well at t_i and the mean intensity of the well at t_{i-1} is greater than the set pixel change threshold η such that $|I(t_i) - I(t_{i-1})| > \eta$, a freezing event is detected, and time, freezing temperature, and location of the well are recorded. The exposure, gain, and pixel change threshold η can be adjusted in the control panel to increase the signalto-noise ratio by emphasizing the decrease in mean intensity due to freezing and minimizing the background variation in mean intensity due any oscillation of the chiller unit when the coolant circulator is running. Temperature measurements are made with a thermistor imbedded at the base of a well in the sample tray after threading the sensor leads through a small hole drilled in the aluminum block.

2.4 Simulation of heat transfer for immersion mode ice spectroscopy

2.4.1 Model design

In order to accurately measure the freezing temperature of INPs in immersion mode spectroscopy, the temperature of each well must be quantified, and the temperature of the sample throughout the volume itself must be homogenous (unstratified). Placing thermistors directly in the sample volume would be ineffective for several reasons, including that (1) the probe itself disrupts the structure of the surface of the droplet and could provide a surface for nucleation, (2) heat conducts through the probe into the sample volume, and (3) probes can introduce contamination. Also, if a probe is placed in a sacrificial sample well, once the well freezes, latent heat is released, and because the thermal properties of ice are different from those of water, the temperature of the frozen well may not be representative of the supercooled liquid wells. Thus, the probe must be placed outside the well volume but in a region of the well block that is thermally homogenous with the sample. Alternatively, if the heat transfer characteristics of the system are resolved, the thermal probe could be placed anywhere in the block where the offset in temperature between the probe's location and the sample well volume is quantified. The sample volume itself must be thermally homogenous because, if the sample volumes were stratified, a freezing event could be triggered in any of the stratified well layers depending on its temperature and the buoyancy of the ice nucleating entity. In order to address the thermal properties of the aluminum block and well-plate system, a finite-element-analysis-based heat transfer simulation was developed using the 3-D design software SOLIDWORKS to investigate the homogeneity of temperature within the 50 μL sample volumes throughout the cooling process and to determine the optimal placement and number of thermistors needed to resolve the temperature of each well.

As shown in Fig. 2.5, a 3-D model of the AIS was designed using the dimensions

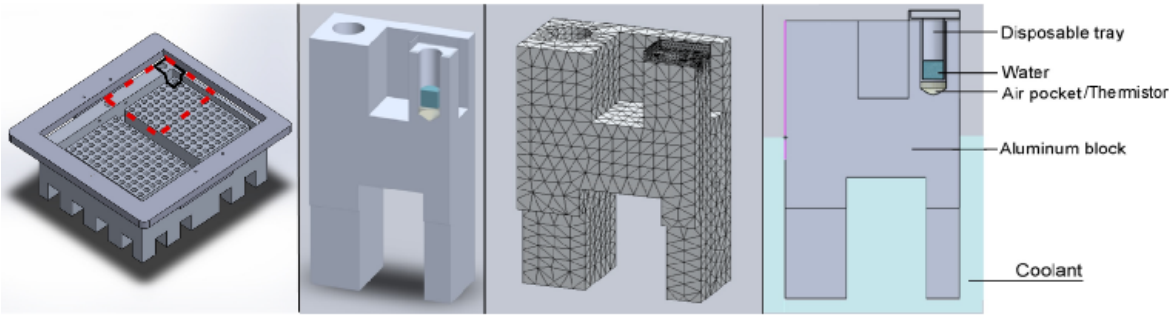

Figure 2.5: Schematic of cut in well block made for heat transfer simulation and mesh applied. **(a)** Well block and cover with red dashed line to indicate where simplifying cut (see Figs. 2.7 and 2.8) in assembly was made for the heat transfer simulations. Black line indicates the section of well block that is featured in **(b)**, **(c)**, and **(d)** to show all components modeled in the simulations. **(b)** Isometric, sectional view of the block corner. **(c)** Image of mesh applied using SOLIDWORKS standard mesh solver (see Sect. 2.4.1 for details). **(d)** Isometric, flat sectional view of the block corner with labels to indicate materials parameterized in the heat transfer simulations shown in Figs. 2.6 and 2.7

and material properties of the actual instrument components. In finite-element-analysis heat transfer simulations, a mesh is applied to the modeled object such that, with a given initial temperature and/or heat source at the boundaries, rates of heat transfer and temperature are computed iteratively until solutions converge on the user-defined mesh. Meshing becomes more computationally expensive over curved or complex surfaces, and because the AIS well blocks contain 192 wells each with a curved inner surface, a cut of the upper left quadrant shown in Fig. 2.5a was made in the 3-D model to reduce computation time. In Fig. 2.5a, the two aluminum 96-well blocks are shown with the PVC splash guard, and the dashed red line in the upperleft corner represents the modeled cut in the well block. Figure 2.5b and d show a close-up of the well block quadrant featured in the model, including the aluminum well block, the polypropylene sample tray, and a 50 μL sample of water. A pocket of gas between the sample tray and the well block is also modeled due to the slightly imperfect fit of the tray to the well block in the actual instrument. The simplifying modeling cut was justified by making measurements of the horizontal

distribution of temperature through the two boundaries of the well region: the nitrogen gas above the well region and the coolant bath, which by design maintains a homogenous temperature throughout the coolant volume. The homogeneity of temperature in the coolant bath was verified using a calibrated thermometer (Checktemp Pocket Thermometer, Hanna Instruments, accuracy ±0.3 ºC from −20 to 90 ºC).

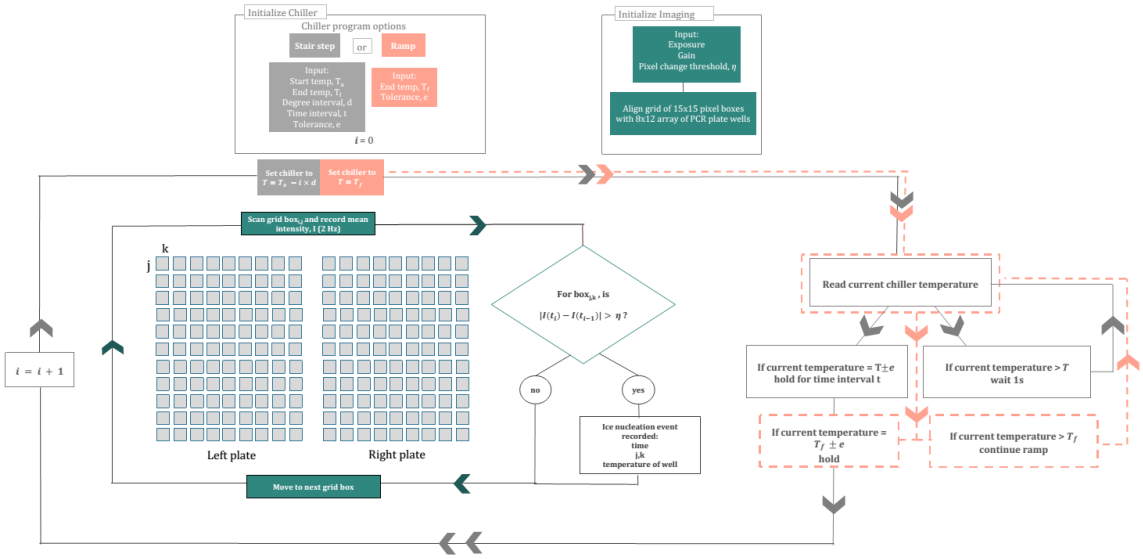

Figure 2.6: Flow chart describing algorithm for detection of freezing events using camera and lights to leverage optical properties of phase change from water to ice. Grey and pink are used to indicate the "stair step" and "ramp" temperature control of the chiller (for details see main text). Green is used to indicate imaging section of the algorithm for detection of freezing events.

To investigate the horizontal distribution of the temperature of gas across the surface of the well block, four thermistors were placed in the 5 cm headspace between the well block surface and the plexiglass lid during repeated cooling processes, and the thermistor temperature was monitored while systematically moving the thermistors through the headspace. The temperature of the nitrogen gas in the headspace was found to be homogenous across the plate within ±0.3 °C (within the error of the calibrated temperature probe). The horizontal gradient of temperature is constrained by the homogenous temperature across the bottom surface of the well block and a temperature difference of max ±0.3 °C across the top surface. The vertical gradient of temperature

through the well block, disposable sample tray, and sample volume is not practically measurable and requires resolution through heat transfer simulations in order to determine where probes should be placed to measure temperature of the wells. The larger hole on the left side of the sample well in Fig. 6a and b is where the thermal probes were placed in the original AIS design.

The mesh used is shown in Fig. 6c and was applied using the SOLIDWORKS standard mesh solver. It is composed of discrete, tetrahedral elements that are connected at the three nodes such that they converge through all components in the modeled system. Generally, an aspect ratio around 1 for each element is ideal; for the mesh applied in the heat transfer simulations, 99.1 % of the mesh elements have an aspect ratio of less than 3, and 0.00 % of mesh elements have an aspect ratio greater than 10. Four Jacobian points, or nodes at the midpoint of element sides, were applied to each element to align with curvature more effectively with linear elements, and the mesh took 1 min, 56 s to converge.

2.4.2 Setup of the heat transfer simulation

The nitrogen and coolant fluid in thermal contact with the sample volumes and well block, respectively, form the thermal boundaries of the simulation. Thus, to quantify the boundary conditions for the heat transfer simulation, temperature measurements were made of the gas temperature above the sample volumes and the coolant temperature during a ramp cooling process, in which the refrigerated bath circulator ran from room temperature to −33 ºC at an average cooling rate of −0.87 ºC min^{-1} (see Fig. 2.3. In addition, a hole was drilled into the aluminum block so that a thermistor could be placed directly underneath a sample well.

Once the thermistor was placed in the block, the hole was sealed with acrylic caulk to prevent coolant fluid from entering the well region, and heat sink compound was applied to the thermistor so that it was in thermal contact with the aluminum block and the disposable sample tray. In Fig. 2.3, the temperature at three locations within the AIS is shown after measurement throughout a “ramp” cooling process from 15 to −33 ºC: (1) the coolant in contact with the

bottom surface of the well block; (2) the gas above the sample volume, or headspace gas; and (3) directly below the sample well. The measurements of temperature of the gas above the sample volume and coolant over 3276 s of cooling are applied as boundary conditions in the heat transfer simulation. The larger plot in Fig. 2.3 shows the warm temperature offset of the headspace gas from the measured temperature at the well base, and the inset plot shows temperature changes in time, at the three locations over the ramp cooling cycle. The headspace gas and coolant temperature data are applied as boundary conditions in the simulation. Figure 3 shows that the air above the well region is a maximum of +4.19 ºC warmer than the well base, despite the chilled nitrogen pumped over the well region, because the system is imperfectly insulated from the room temperature environment and because there is a slight warming of the gas before it enters the headspace (as described in Sect. 2.3.2. An acrylic plate covers the wells as shown in Fig. 2.1, but the system is not thermally isolated from the environment. Figure 2.5d shows each of the components considered in the model: the aluminum well block, the disposable sample tray, the gas pocket in the gap between bottom of the sample tray and the well block, and the 50 μL sample water volume. The coolant and the headspace gas were considered as variable thermal loads to the system rather than included as components. Two types of heat transfer were considered during the model analysis: conductive and convective. All of the components shown in Fig. 2.5d are considered to be bonded, or treated as if heat transfer by conduction occurs in a continuous manner. Heat transfer by conduction is computed at each element of the mesh by the following equation:

$$Q_{conduction} = kA(T_{hot} - T_{cold}), \tag{2.2}$$

where $Q_{conduction}$ is the rate of heat transfer in watts, k is thermal conductivity of the component, A is the heat transfer area defined by the mesh, and (T_{hot} - T_{cold}) is the temperature difference between the two mesh elements considered. Thermal conductivity, k, is determined by the material of the component. Values of k used in the simulation are shown in Table 2.1.

Table 2.1: Elements and properties used in heat transfer simulation.

Components	Material	k^a (W mK^{-2})	h^b (W m^{-2} K)
Well block	Aluminum 1060 alloy	200	25
Disposable sample tray	Polypropylene	0.117	25
Gas pocket	Air	0.027	n/a
Liquid INP sample	Water	0.5	191

At all interfaces where the model is in contact with headspace gas, heat transfer by convection is considered. For heat transfer by convection, Eq. (2.3) is applied at each element:

$$Q_{convection} = hA(T_s - T_t), \tag{2.3}$$

where $Q_{convection}$ is the rate of heat transfer from a body to a fluid in watts, h is the heat transfer coefficient in W m^{-2} K, and $(T_s - T_f)$ is the difference in temperature between the surface of the body and the fluid. A is the same as above in 4.2. The convection of both the gas and the water in the model was considered natural convection rather than forced. Typical ranges for the heat transfer coefficient h for natural convection of air are 5-25 W m^{-2} K (Yousef et al., 1982). The model output was insensitive to this range of coefficient variability, and a value of 25 W m^{-2} K was used. The range of h for natural convection of water, however, is much larger: 2-3000 W m^{-2} K (VDI-Gesellschaft Energietechnik, 2013), so h was estimated by approximating the wells as two vertical plates; calculating the Nusselt number N; and using $h = Nk/H$, where H is the height of the plates. N was calculated using Eq. (2.4) for laminar flow (Churchill and Chu, 1975):

$$N = 0.68 + \frac{0.670Ra^{1/4}}{(1 + (\frac{0.492}{Pr})^{9/16})^{4/9}} \tag{2.4}$$

Ra and Pr are the Rayleigh and Prandtl number (Holman, 2009), respectively, where

$$Ra = \frac{g\beta(T - T_\infty)D^3}{v^2} \cdot Pr \tag{2.5}$$

and $Pr = v/\alpha$. β is the coefficient of thermal expansion, g is the acceleration due to gravity, T is the temperature of the water volume, T_∞ is the temperature of the iar at the surface of the water volume, D is the diameter of the well as measured at the top of the well of the disposable sample tray, v is dynamic viscosity, and α is the thermal diffusivity.

Table 2.2: Constants used in calculation of heat transfer coefficient h for water in natural convection from −5 to −30 ºC.

Water temperature T (ºC)	Gas temperature T_∞ (ºC)	β^a (K^{-1}) $x10^{-6}$	v^b (m^2 s^{-1}) $x10^{-6}$	α^c (m^2 s^{-1}) $x10^{-7}$	k^d W mK^{-1}	h W $m^{-2}K$
−5.0	−1.6	−168.6	2.0026	1.30	0.520	160.8
−15.0	−10.3	−450.3	3.0707	1.20	0.500	191.0
−30.0	−23.4	−1400.0	7.9703	1.05	0.450	201.6

[a] Kell (1972). [b] Dehaoui (2015). [c] Benchikh (1985). [d] Biddle (2015).

Since β, v, α, and k are temperature-dependent properties, and h is of interest over the supercooled range from 0 to −25 ºC, N and h were calculated at −5, −15, and −25 ºC, using corresponding values of β, v, α, and k (Kell, 1975; Dehaoui et al., 2015; Benchikh et al., 1985; Biddle et al., 2013), which are shown in Table 2.2. Thus, h was estimated to be 161, 191, and 202 W $m^{-2}K$, the model was insensitive, and a constant value of 191 W $m^{-2}K$ was used throughout the simulations.

The simulation was run over 3276 s with two different sets of boundary conditions representing the coolant fluid and headspace gas temperatures. In the first simulation, the coolant

fluid temperatures from Fig. 2.3 were applied, but the difference between the temperature of the headspace gas and that of the well base was multiplied by 2 in order to approximate inefficient cooling of headspace gas. In the second simulation, the gas and coolant temperatures were applied directly from the coolant fluid and headspace gas temperature in Fig. 2.3. The first condition has warmer headspace gas temperatures than those that were measured during the cooling process on the actual instrument in Fig. 2.3.

2.5 Results

2.5.1 Simulation results

The results of the heat transfer simulation for the warmer headspace gas condition and the measured gas and coolant temperature conditions are shown in Figs. 2.7 and 2.8. Figure 2.7 shows a graphical time series of the heat transfer simulation with the doubling of the offset between the well base and the warmer gas above the well region. The heat distribution is shown in 12 time steps at 273 s intervals over a 3276 s simulation, with the coolant fluid cooling from 15 to −33 ºC over that period (i.e., −0.87 ºC min^{-1}). At the top of Fig. 2.7, an isometric view of the well block at 1638 s is shown, and to the right is a detailed view of the well. The results show the stratification of temperature in the sample volume itself, ranging from −13.8 ºC at the skin of the sample volume to −14.3 ºC at the bottom of the sample volume. These results demonstrate that the temperature difference of +6 ºC between the well and the headspace gas is too large to maintain homogenous temperature within the liquid sample volume, which then becomes stratified by 0.5 ºC. The degree of stratification through the duration of the simulation is shown in Fig. 2.11 in the Supplement, reaching a maximum of 0.6 ºC.

Figure 2.8 shows a graphical time series of the heat transfer simulation with the measured AIS headspace gas temperature and coolant bath temperature conditions from Fig. 2.3. With an offset between the base of the well and the headspace gas temperature of +3.0 ºC, stratification

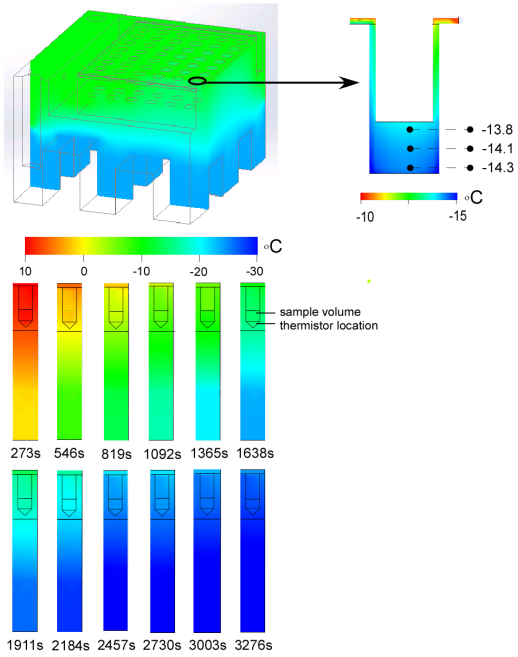

Figure 2.7: Graphical time series of the heat transfer simulation. Top shows isometric view of the well block (top left quarter) at $t = 1638s$. Top right shows detailed plane view of well at $t = 1638s$. Dashed lines indicate temperature of water in the well at three points. Colors indicate temperature referenced by the scale below. Twelve time steps at 273 s intervals show temperature distribution within the well block shown below. The average cooling rate over this time period is –0.87 ºC min^{-1}. Results show the stratification of temperature in the sample volume due to warmer air above the well region (see Sect. 2.4.2 for details).

has significantly decreased to 0.1 ºC from top to bottom of the sample volume, which is within the error of the thermal probe (see Fig. 2.11). The results also show that the distribution of heat throughout the well block requires careful placement of the temperature probe such that the temperature of the probe location is accurately indicating the temperature of the sample volume. In each of the simulations, the sample water volume comprises the warmest body in the model assembly. Throughout the modeled assembly, the temperature in the gas pocket underneath the well of the polypropylene disposable tray was the region closest in temperature to the sample volume, albeit still colder by as much as –1.8 ºC. Due to strong temperature gradients between

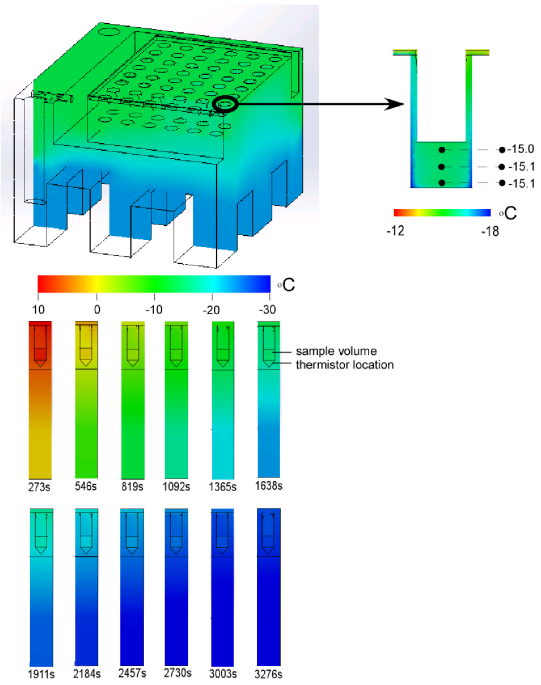

Figure 2.8: Graphical time series of the heat transfer simulation showing the effects of increasing thermal homogeneity in the cooling environment by efficiently cooling headspace gas on performance of the well block. As in Fig. 2.7, the top shows isometric view of the well block at $t = 1638s$. Dashed lines indicate temperature of water in the well at three points. Colors indicate temperature referenced by the scale below. Twelve time steps at 273 s intervals showing temperature distribution within the well block shown below. The average cooling rate over this time period is −0.87 ºC min^{-1}. Results show the decreased stratification of temperature in the well due to cooler air above the well region (air temperature offset varied approximately +2-4 ºC from the bath coolant temperature as shown in Fig. 2.3).

the water sample and the immediately surrounding aluminum block, small variations in probe location can result in disproportionately large temperature offsets from the sample volume. At 1638 s in the second simulation, which applies the gas and coolant temperature conditions as measured on the AIS (Fig. 2.3), the temperature decreases 1.8 ºC from base of the well of the polypropylene disposable tray through the gas pocket to the aluminum surface of the well block over a distance of 2.5 mm, resulting in an offset of −1.6 ºC between the average temperature of the air pocket and that of the sample volume. This could be caused by the high specific heat of the

water volume relative to the aluminum, and the insulating thermal properties of the polypropylene tray could be responsible for the strong temperature gradient. In the current design of the AIS, the thermal probe is located in this gas pocket, and the simulation results suggest that at this location there could be up to a −1.8 ºC cold bias in the INP freezing temperature measurements. Thus, during ramping of the coolant bath from room temperature to num-33 ºC at about −0.87 ºC min^{-1}, there is nowhere to place a probe in the aluminum block where the temperature perfectly matches that of the liquid sample volume (within $\ll 1$ ºC). The offset in temperature between the probe and the sample temperature was quantified so that recorded temperatures can be adjusted accordingly.

In order to verify the simulation output so that offsets found can be applied quantitatively to freezing temperature measurements, simulated temperatures were checked against measurements that were independent of the simulation. Since the entire surface of the system was constrained by boundary conditions in the simulation, the measurements from inside of the well block at the well base (shown in Fig. 2.3) were used for comparison with the simulation output at the same location. Results of the comparison over the 12 time steps of the simulation are shown in Fig. 2.10. At subzero temperatures, the maximum difference between the measured and simulated temperatures was 0.6 ºC at $t = 819s$, decreasing to values below the error of the thermistor for most of the simulation. $\pm$0.6 ºC is assumed to be the uncertainty of the simulation. The measured temperature was consistently slightly warmer than the simulated temperature, possibly because the hole drilled into the aluminum well block was not modeled. In the second simulation using measured boundary conditions, the average temperature of the sample volume was compared with the average temperature of the air pocket in which the thermistor is placed throughout the 3276 s simulation (see Fig. 2.11), in order to quantify the offset between the thermistor and the sample. The air pocket temperatures are consistently colder than the sample volume temperatures, ranging from −1.8 to −1.2 ºC over the 3276 s simulation. Offsets in temperature between the 192 wells also exist in the AIS and are shown in Fig. 2.13. Sample volumes in wells near the

outer perimeter are up to +2.2 ºC warmer than sample volumes near the center of the well block. Detailed analyses of the offsets along the *x* and *y* axis over the 3276 s simulation are not shown because there is currently only one thermistor embedded in the well block, so verification of the simulation's temperature gradient in *x* and *y* was not possible without further modifications to the well block. In the future, additional thermistors embedded within the well block can be used to verify the simulation output so that measurements can be adjusted with offsets due to the gradient in *x* and *y* as well as *z*. However, the maximum offset found between wells in *x* and *y*, +2.2º, will be represented as the uncertainty associated with the measurements reported in the following sections.

2.5.2 Automated Ice Spectrometer performance: comparison with six other immersion mode ice nucleation measurement techniques

The accuracy of the AIS INP concentration measurements were evaluated using a standard, well-characterized test dust that has previously been used to compare immersion mode ice nucleation measurement techniques, illite NX (Arginotech, NX nanopowder) (Hiranuma et al., 2015). A suspension of dust and Milli-Q ultrapure water was prepared in a sterile 50 mL centrifuge tube (Corning) using a sample from the same batch of illite NX used in Hiranuma et al. (2015), a study of 17 immersion mode ice nucleation measurement techniques. Twenty milligrams of illite NX was immersed in 500 mL of ultrapure water, resulting in a 4.0×10^{-3} wt % solution. Two more dilutions were made by immersing 25 mg of illite NX in 50 mL of ultrapure water and diluting again by factors of 1/10 and 1/100, resulting in solutions of 5.0×10^{-2} and 5.0×10^{-3} wt %, respectively. A final solution was prepared by starting with 300 mg in 50 mL of ultrapure water and then diluting by factors of 1/100 and 1/1000, resulting in a solution of 6.0×10^{-6} wt %. For comparison, in Hiranuma et al. (2015), droplet assays were intercompared using illite NX suspensions of varying dilutions within the range of 3.1×10^{-6} wt % to 1.0 wt %. Higher concentrations of illite NX solution were not measured using the AIS because the automation

software requires an optically clear solution to detect freezing events. Fifty-microliter aliquots of the suspension were loaded into 24 wells of the disposable sample tray (Life Science Products™ 96-well PCR plates), and 24 adjacent wells were filled with 50 μL aliquots of Milli-Q water. Prior to loading, the plexiglass lid was cleaned with an isopropyl-alcohol-based surface cleaner, rinsed three times with Milli-Q, and dried with clean compressed air, and nitrogen was pumped over the well region at 0.25 L min^{-1} for 20 min to purge the lines of any dust. The loaded and covered sample was then cooled from room temperature to −27 ºC (with an average cooling rate of −0.87 ºC min^{-1}, at which point the Milli-Q water had frozen in all wells. The experiment was repeated four times. Freezing events were detected using the automation software and, the time of freezing, well temperature, and sample number were recorded into an ASCII file for further analysis. Cumulative concentration of INPs per volume per 0.25 ºC were calculated using Eq. (4.1) (Vali, 1971). In order to compare directly with Hiranuma et al. (2015), cumulative concentrations of INPs were converted into a surface site density, $n_{s,BET}$. The specifics of the parameterization are in Hiranuma et al. (2014), but briefly, the parameterizations are based on BET (Brunauer–Emmet–Teller) (Brunauer et al., 1938) N_2- adsorption-based specific surface area (SSA) in which the particle surface area is measured based on the quantities of a variety of gases that form monolayers on the surface of the particle. The SSA of the illite NX sample used in Hiranuma et al. (2015) was 124 m^2 g^{-1}, and the mass concentration (m/ of the four illite NX solutions processed n the AIS ranged from 6.0×10^{-6} to 5.0×10^{-2} g mL^{-1}. The AIS measurement results in terms of cumulative INPs per volume were converted to the surface site density, $n_{s,BET}$, using the mass concentration and specific site density as follows:

$$n_{s,BET} = \frac{(\frac{INPs}{mL})}{SSA \cdot m} \tag{2.6}$$

In Fig. 2.9, the measured illite NX spectra are shown with 6 of the 17 total ice nucleation measurement techniques from Hiranuma et al. (2015). These were similar freezing or droplet

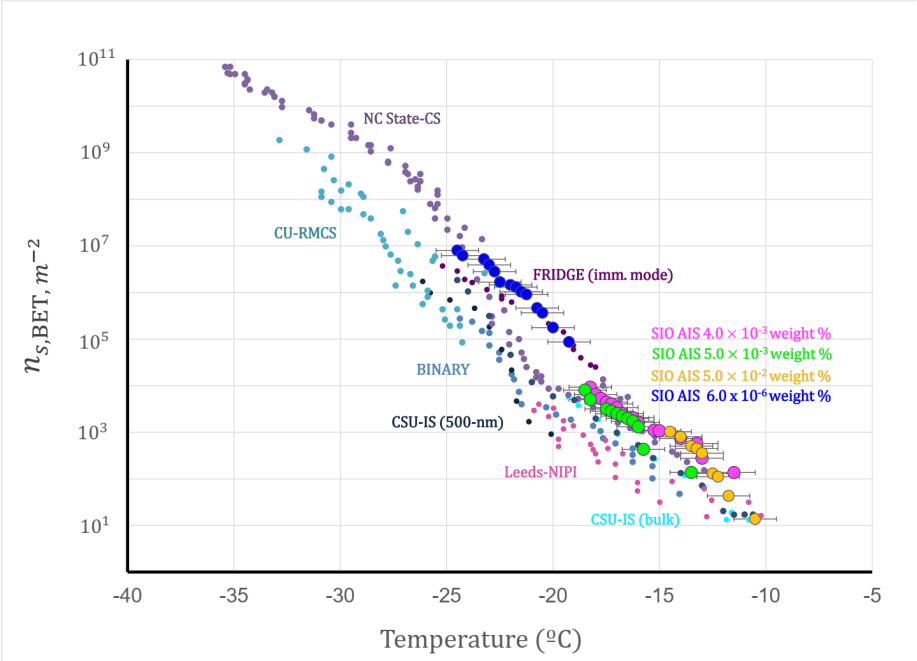

Figure 2.9: Immersion freezing spectra of illite NX particles in terms of $n_{s,BET}(T)$ for comparison of SIO AIS against six other immersion mode techniques reported (see Hiranuma et al., 2015). $n_{s,BET}$ is used to estimate ice nucleation surface site density from an N_2-adsorption-based specific surface area (Hiranuma et al., 2015). CSU-IS (500 nm) represents measurements made on illite NX particles that were mobility-diameter-size-selected, whereas all other measurements reported were of bulk illite NX samples. Four different dilutions of illite NX suspensions were measured by the SIO AIS: $4.0 \times 10^{-3} wt\%$, $5.0 \times 10^{-3} wt\%$, $5.0 \times 10^{-2} wt\%$, and $6.0 \times 10^{-6} wt\%$. SIO AIS measurements fall on the warm side of the spectra.

assay techniques: the CSU-IS, the NIPI, FRIDGE (in immersion mode), NC-State CS, BINARY, and the CU-RMCS. The six instruments made wet-suspension-based measurements of illite NX in ultrapure water rather than dry-particle-based measurements and thus should more directly compare to those of the AIS. Temperature offsets between the thermistor and the sample volumes due to the consistently colder location of the thermistor, ± 1.8 ºC, and the warmer wells near the perimeter of the well block, ± 2.2 ºC (see Sect. 4.1), are represented in the error bars on the AIS measurements. The ice nucleation surface site density spectra of the six measurements fall within a range of about 5 ºC, and the Automated Ice Spectrometer measurements compare favorably to those of the other six techniques through its final temperature of −25 ºC. However, the AIS measurements fall on the warmer side of the temperature spectrum from −10 to −25 ºC.

Based on the results of the heat transfer simulations in Sect. 2.5.1, differences in the cooling process type (stair step or ramp), location of temperature probe or method of freezing temperature measurement could have strong influences on reported freezing temperatures. These factors might account for some of the 8 ºC (or 5 ºC for wet-suspension droplet assay techniques) spread in spectra reported in Hiranuma et al. (2015).

2.6 Discussion

The immersion mode ice spectrometer (original configuration in Hill et al., 2014 and latest design described in Hiranuma et al., 2015) was modified to fit inside a refrigerated circulating coolant bath and automated using a software controlled camera. Older versions of the immersion mode ice pectrometer were designed with the aluminum well blocks external to the refrigerated circulator bath, and the coolant fluid was pumped through heat exchange plates encasing the aluminum well blocks for cooling via external copper tube plumbing. The operator observed and recorded well freezing manually. Modifications to the instrument increased thermal homogeneity across the well block by immersing well blocks directly in the coolant bath. Automation enables more objective and instantaneous recording of well-freezing events and frees the operator from having to constantly monitor sample processing.

The heat transfer properties of the AIS were characterized using finite-element-analysis heat transfer simulations, with measured temperatures of the well block headspace gas and the coolant bath applied as boundary conditions. Heat transfer by conduction and convection was considered.

The results of the simulations showed that efficient cooling of the well block headspace, with a maximum +4 ºC offset between the base of the well and the headspace gas or +11 ºC between the coolant bath and the headspace gas, is necessary to ensure that the liquid sample volume is unstratified within the error of the thermal probe, $\pm$0.2 ºC, so that the well-freezing

temperature is representative of the population INPs in the well. The results also demonstrate a strong temperature gradient from the sample volume to the polypropylene and aluminum immediately surrounding the sample, of up to −1.8 ºC in the 2.5 mm gap. Thus the temperature measurement in the AIS is highly sensitive to the location of the thermal probe. In the simulation, the only region with a temperature consistent with the sample volume was the top of the gas pocket between the bottom of the polypropylene disposable tray and the aluminum block. However, a thermistor probe cannot physically fit in this small region, so INP freezing temperature measurements are likely biased by the thermistors contact with the aluminum block. An offset between the thermistor location and the sample volume was quantified, first by verifying the simulation output using a thermistor embedded in the well block (see Fig. S1), then using the simulation output to determine the offset to apply to the recorded measurements. For other immersion mode droplet assay INP measurement techniques, variation in heat transfer properties and thermal probe placements may result in higher or lower accuracy of INP freezing temperature measurement, but the sensitivity of the temperature gradient within the droplet to the thermal heterogeneity of its cooling environment, as well as that of the temperature measurement to thermal probe placement, motivates careful study of the effect of heat transfer properties of the various techniques. The heat transfer simulations applied here could support investigations of bias in temperature measurement for INP measurement techniques, enable higher accuracy in INP freezing temperature measurements, and ultimately help decrease disparities between various instruments. INP concentrations applied in cloud and climate models must be accurate within an order of 10 to avoid propagation of error leading to significantly different cloud properties (Phillips et al., 2003), and as measurements typically show INP concentrations increasing with decreasing temperature in complex multi-exponential functions (Hiranuma et al., 2015), an 8 ºC uncertainty in freezing temperature measurement could result in vast differences in model output. Heat transfer simulations could prove particularly useful in studies of the role of varied cooling rates on assessment of ice nucleation activity in different devices due to the stochastic or

time-dependent nature of droplet freezing at a given temperature. In such an investigation, it is important to separate the impact of time dependence of the ice nucleating entity from variations due to temperature gradients between the location of the thermal probe and the sample volume.

Fast cooling of samples ($>$ 1 ºC min^{-1}) has been discussed as a potential source of stratification of temperature between the substrate and the droplets, or within the droplets; conversely, that chilled nitrogen in the headspace might not be necessary to avoid stratification (Tobo, 2016). However, the heat transfer simulation results below show that, even with cooling rates below 1 ºC min^{-1}, stratification within the sample volume can occur and that the temperature of nitrogen gas in the headspace may play a significant role in controlling temperature stratification within the droplets.

The performance of the Automated Ice Spectrometer was evaluated using measurements of illite NX, a wellcharacterized test dust that has been used to intercompare 17 immersion mode INP measurement techniques. Four different dilutions of illite NX suspension were measured: 4.0×10^{-3} wt %, 5.0×10^{-3} wt %, 5.0×10^{-2} wt %, and 6.0×10^{-6} wt %. These concentrations fall in the middle to the lower end of the range of suspension concentrations (3.0×10^{-6} to 1.0 wt %) measured by the six selected droplet assay INP measurement techniques in Hiranuma et al. (2015) (see Fig. 2.9). Measurements of specific site density compare well with the six droplet assay techniques from the intercomparison study (Hiranuma et al., 2015), falling on the warmer side of the 5 ºC spread in the reported spectra from −10 to −25 ºC.

In summary, the Automated Ice Spectrometer

1. enables entirely autonomous measurement of INP concentrations;

2. can measure concentrations of INPs with activation temperatures in the range 0 to −25 ºC;

3. can process up to seven samples per hour using 24 wells per sample (including time for loading samples);

4. has characterized heat transfer properties so that stratification, temperature offsets from well to well, and offsets between temperature probes and the sample volume can be studied.

Data availability. Data collected for the AIS heat transfer simulations, results, and intercomparison using illite NX are available on https://doi.org/10.6075/J0ZC80S8.

Acknowledgements. We would like to thank Joe Mayer for his invaluable help in constructing the AIS housing and camera mount. Funding to support this research was provided by the Center for Aerosol Impacts on Climate and Environment (CAICE), an National Science Foundation (NSF) Center for Chemical Innovation (CHE-1305427).

Chapter 2, in full, is a reprint of the material as it appears in Atmospheric Measurement Techniques 2017. Beall, C. M., Stokes, M. D., Hill, T. C., DeMott, P. J., DeWald, J. T. and Prather, K. A.: Automation and heat transfer characterization of immersion mode spectroscopy for analysis of ice nucleating particles, Atmos. Meas. Tech., 10(7), 2613–2626, doi:10.5194/amt-10-2613-2017, 2017. The dissertation author was the primary investigator and author of this paper.

2.7 References

Baustian, K. J., Wise, M. E., and Tolbert, M. A.: Depositional ice nucleation on solid ammonium sulfate and glutaric acid particles, Atmos. Chem. Phys., 10, 2307–2317, https://doi.org/10.5194/acp-10-2307-2010, 2010.

Benchikh, O., Fournier, D., and Boccara, A. C.: Photothermal measurement of the thermal conductivity of supercooled water, Sci. York, 46, 727–731, 1985.

Biddle, J. W., Holten, V., Sengers, J. V., and Anisimov, M. A.: Thermal conductivity of supercooled water, Phys. Rev. E, 87, 1–7, https://doi.org/10.1103/PhysRevE.87.042302, 2013.

Brunauer, S., Emmett, P. H., and Teller, E.: Adsorption of Gases in Multimolecular Layers, J. Am. Chem. Soc., 60, 309–319, https://doi.org/10.1021/ja01269a023, 1938.

Budke, C. and Koop, T.: BINARY: an optical freezing array for assessing temperature and time dependence of heterogeneous ice nucleation, Atmos. Meas. Tech., 8, 689–703,

https://doi.org/10.5194/amt-8-689-2015, 2015.

Burrows, S. M., Hoose, C., Pöschl, U., and Lawrence, M. G.: Ice nuclei in marine air: biogenic particles or dust?, Atmos. Chem. Phys., 13, 245–267, https://doi.org/10.5194/acp-13-245-2013, 2013.

Churchill, S. and Chu, H.: Correlating equations for laminar and turbulent free convection from a vertical plate, Int. J. Heat Mass Tran., 18, 1323–1329, https://doi.org/10.1016/0017-9310(75)90222-7, 1975.

Cziczo, D. J., Froyd, K. D., Hoose, C., Jensen, E. J., Diao, M., Zondlo, M. A., Smith, J. B., Twohy, C. H., and Murphy, D. M.: Clarifying the Dominant Sources and Mechanisms of Cirrus Cloud Formation, Science, 340, 1–8, https://doi.org/10.1126/science.1234145, 2013.

Davis, J. R. (Ed.): Metals Handbook, 2nd Edn., ASM International, Materials Park, Ohio, USA, 1521 pp., 1998.

Dehaoui, A., Issenmann, B., and Caupin, F.: Viscosity of deeply supercooled water and its coupling to molecular diffusion, P. Natl. Acad. Sci. USA, 112, 12020–12025, https://doi.org/10.1073/pnas.1508996112, 2015.

DeMott, P. J., Cziczo, D. J., Prenni, A. J., Murphy, D. M., Kreidenweis, S. M., Thomson, D. S., Borys, R., and Rogers, D. C.: Measurements of the concentration and composition of nuclei for cirrus formation, P. Natl. Acad. Sci. USA, 100, 14655–14660, https://doi.org/10.1073/pnas.2532677100, 2003.

DeMott, P. J., Prenni, A. J., Liu, X., Kreidenweis, S. M., Petters, M. D., Twohy, C. H., Richardson, M. S., Eidhammer, T., and Rogers, D. C.: Predicting global atmospheric ice nuclei distributions and their impacts on climate, P. Natl. Acad. Sci. USA, 107, 11217– 11222, https://doi.org/10.1073/pnas.0910818107, 2010.

DeMott, P. J., Hill, T. C. J., McCluskey, C. S., Prather, K. A., Collins, D. B., Sullivan, R. C., Ruppel, M. J., Mason, R. H., Irish, V. E., Lee, T., Hwang, C. Y., Rhee, T. S., Snider, J. R., McMeeking, G. R., Dhaniyala, S., Lewis, E. R., Wentzell, J. J. B., Abbatt, J., Lee, C., Sultana, C. M., Ault, A. P., Axson, J. L., Diaz Martinez, M., Venero, I., Santos-Figueroa, G., Stokes, M. D., Deane, G. B., Mayol-Bracero, O. L., Grassian, V. H., Bertram, T. H., Bertram, A. K., Moffett, B. F., and Franc, G. D.: Sea spray aerosol as a unique source of ice nucleating particles, P. Natl. Acad. Sci. USA, 113, 5797–5803, https://doi.org/10.1073/pnas.1514034112, 2016.

Hill, T. C. J., Moffet, B. F., DeMott, P. J., Georgakopoulos, D. G., Stump, W. L., and Franc, G. D.: Measurement of ice nucleation-active bacteria on plants and in precipitation by quantitative

PCR, Appl. Environ. Microbiol., 80, 1256–1267, https://doi.org/10.1128/AEM.02967-13, 2014.

Hiranuma, N., Hoffmann, N., Kiselev, A., Dreyer, A., Zhang, K., Kulkarni, G., Koop, T., and Möhler, O.: Influence of surface morphology on the immersion mode ice nucleation efficiency of hematite particles, Atmos. Chem. Phys., 14, 2315–2324, https://doi.org/10.5194/acp-14-2315-2014, 2014.

Hiranuma, N., Augustin-Bauditz, S., Bingemer, H., Budke, C., Curtius, J., Danielczok, A., Diehl, K., Dreischmeier, K., Ebert, M., Frank, F., Hoffmann, N., Kandler, K., Kiselev, A., Koop, T., Leisner, T., Möhler, O., Nillius, B., Peckhaus, A., Rose, D., Weinbruch, S., Wex, H., Boose, Y., DeMott, P. J., Hader, J. D., Hill, T. C. J., Kanji, Z. A., Kulkarni, G., Levin, E. J. T., McCluskey, C. S., Murakami, M., Murray, B. J., Niedermeier, D., Petters, M. D., O'Sullivan, D., Saito, A., Schill, G. P., Tajiri, T., Tolbert, M. A., Welti, A., Whale, T. F., Wright, T. P., and Yamashita, K.: A comprehensive laboratory study on the immersion freezing behavior of illite NX particles: a comparison of 17 ice nucleation measurement techniques, Atmos. Chem. Phys., 15, 2489–2518, https://doi.org/10.5194/acp-15-2489-2015, 2015.

Holman, J. P.: Heat transfer, McGraw-Hill series in mechanical engineering, 10, McGraw-Hill Education, 2009. Hoose, C., Kristjánsson, J. E., Chen, J.-P., and Hazra, A.: A Classical-Theory-Based Parameterization of Heterogeneous Ice Nucleation by Mineral Dust, Soot, and Biological Particles in a Global Climate Model, J. Atmos. Sci., 67, 2483–2503, https://doi.org/10.1175/2010JAS3425.1, 2010.

Kell, G. S.: Density, Thermal Expansivity, and Compressibility of Liquid Water from 0" to 150 °C: Correlations and Tables for Atmospheric Pressure and Saturation Reviewed and Expressed on 1968 Temperature Scale, J. Chem. Eng. Data, 20, 97–105, https://doi.org/10.1021/je60064a005, 1975.

Klein, H., Haunold, W., Bundke, U., Nillius, B., Wetter, T., Schallenberg, S., and Bingemer, H.: A new method for sampling of atmospheric ice nuclei with subsequent analysis in a static diffusion chamber, Atmos. Res., 96, 218–224, https://doi.org/10.1016/j.atmosres.2009.08.002, 2010.

Mason, R. H., Chou, C., McCluskey, C. S., Levin, E. J. T., Schiller, C. L., Hill, T. C. J., Huffman, J. A., DeMott, P. J., and Bertram, A. K.: The micro-orifice uniform deposit impactor–droplet freezing technique (MOUDI–DFT) for measuring concentrations of ice nucleating particles as a function of size: improvements and initial validation, Atmos. Meas. Tech., 8, 2449– 2462, https://doi.org/10.5194/amt-8-2449-2015, 2015.

Phillips, V. T. J., Choularton, T. W., Illingworth, A. J., Hogan, R. J. and Field, P. R.: Simulations of the glaciation of a frontal mixed-phase cloud with the Explicit Microphysics Model, Q.

J. Roy. Meteor. Soc., 129, 1351–1371, https://doi.org/10.1256/qj.02.100, 2003.

Rogers, D. C., DeMott, P. J., Kreidenweis, S. M., and Chen, Y.: Measurements of ice nucleating aerosols during SUCCESS, Geophys. Res. Lett., 25, 1383–1386, https://doi.org/10.1029/97GL03779, 1998.

Seinfeld, J. H., Bretherton, C., Carslaw, K. S., Coe, H., DeMott, P. J., Dunlea, E. J., Feingold, G., Ghan, S., Guenther, A. B., Kahn, R., Kraucunas, I., Kreidenweis, S. M., Molina, M. J., Nenes, A., Penner, J. E., Prather, K. A., Ramanathan, V., Ramaswamy, V., Rasch, P. J., Ravishankara, A. R., Rosenfeld, D., Stephens, G., and Wood, R.: Improving our fundamental understanding of the role of aerosol-cloud interactions in the climate system, P. Natl. Acad. Sci. USA, 113, 5781–5790, https://doi.org/10.1073/pnas.1514043113, 2016.

Stopelli, E., Conen, F., Zimmermann, L., Alewell, C., and Morris, C. E.: Freezing nucleation apparatus puts new slant on study of biological ice nucleators in precipitation, Atmos. Meas. Tech., 7, 129–134, https://doi.org/10.5194/amt-7-129-2014, 2014.

Tobo, Y.: An improved approach for measuring immersion freezing in large droplets over a wide temperature range, Sci. Rep., 6, 32930, https://doi.org/10.1038/srep32930, 2016.

Trenberth, K. E. and Fasullo, J. T.: Simulation of present-day and twenty-first-century energy budgets of the southern oceans, J. Climate, 23, 440–454, https://doi.org/10.1175/2009JCLI3152.1, 2010.

Vali, G.: Quantitative Evaluation of Experimental Results an the Heterogeneous Freezing Nucleation of Supercooled Liquids, J. Atmos. Sci., 28, 402–409, https://doi.org/10.1175/1520-0469(1971)028¡0402:QEOERA¿2.0.CO;2, 1971.

Vali, G.: Interpretation of freezing nucleation experiments: singular and stochastic; sites and surfaces, Atmos. Chem. Phys., 14, 5271–5294, https://doi.org/10.5194/acp-14-5271-2014, 2014.

VDI-Gesellschaft Energietechnik (Eds.): Engineering reference book on energy and heat, Springer Science, and Business Media, Düsseldorf, 2013.

Whale, T. F., Murray, B. J., O'Sullivan, D., Wilson, T. W., Umo, N. S., Baustian, K. J., Atkinson, J. D., Workneh, D. A., and Morris, G. J.: A technique for quantifying heterogeneous ice nucleation in microlitre supercooled water droplets, Atmos. Meas. Tech., 8, 2437–2447, https://doi.org/10.5194/amt-8-2437-2015, 2015.

Wise, M. E., Baustian, K. J., and Tolbert, M. A.: Internally mixed sulfate and organic particles as potential ice nuclei in the tropical tropopause region, P. Natl. Acad. Sci. USA, 107,

6693–6698, https://doi.org/10.1073/pnas.0913018107, 2010.

Wright, T. P., Petters, M. D., Hader, J. D., Morton, T., and Holder, A. L.: Minimal cooling rate dependence of ice nuclei activity in the immersion mode, J. Geophys. Res.-Atmos., 118, 10535–10543, https://doi.org/10.1002/jgrd.50810, 2013.

Yousef, W. W., Tarasuk, J. D., and McKeen, W. J.: Free Convection Heat Transfer From Upward-Facing Isothermal Horizontal Surfaces, J. Heat Transf., 104, 493, https://doi.org/10.1115/1.3245120, 1982.

2.8 Supplement

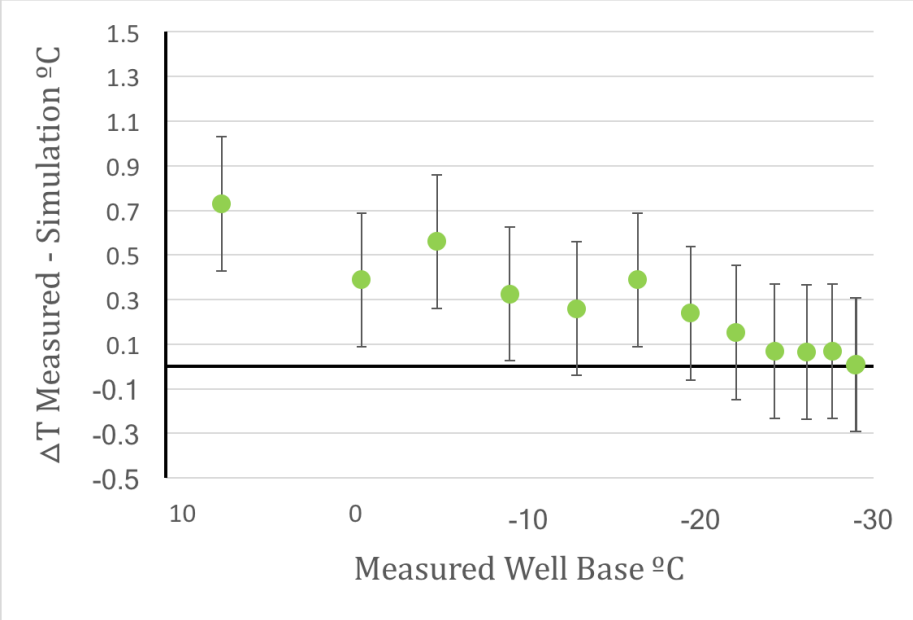

Figure 2.10: Difference between measured and simulated temperature of the air pocket in the well base.The maximum difference between the predicted temperature and the measured temperature over the twelve time steps of the 3276s simulation was 0.6 ºC at subzero temperatures. The error bars shown represent the uncertainty of the thermal probe at the well base, ±0.3 ºC.

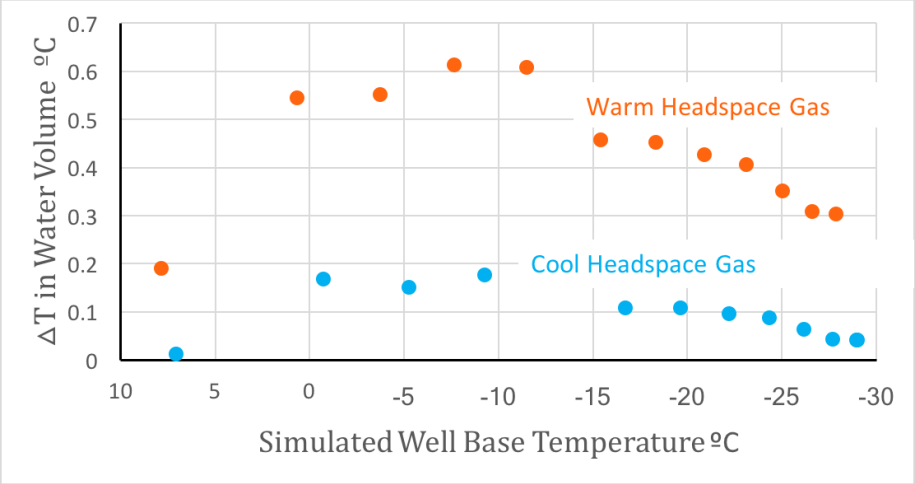

Figure 2.11: Simulated temperature stratification within the sample volume. The difference in simulated temperature between the top and bottom of the 50 μL sample volume is shown for the two simulations. Stratification of the sample volume under normal conditions as measured in the AIS reaches a maximum of 0.2 ºC. Under the warmer headspace gas conditions as described in Sec. 2.4.2, stratification increases to a maximum of 0.6 ºC.

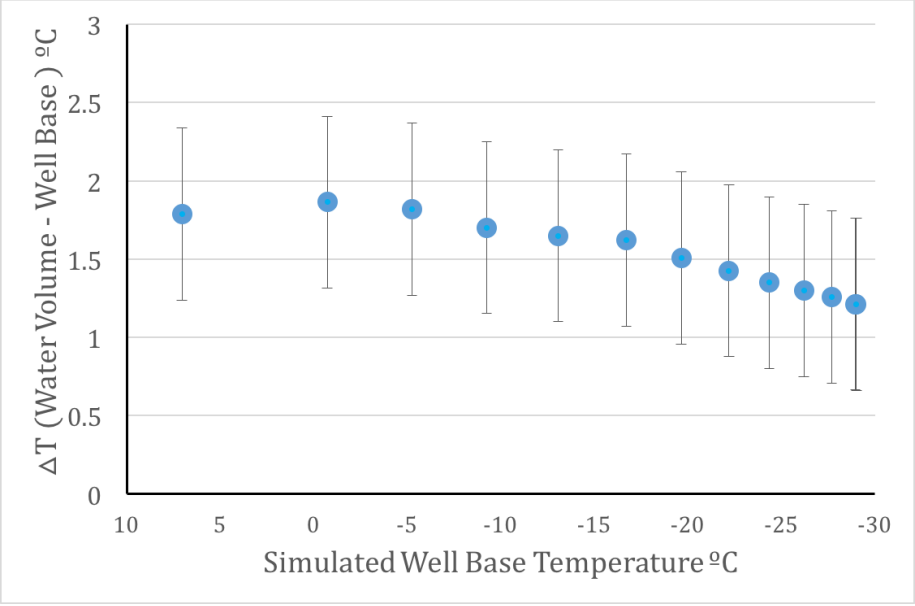

Figure 2.12: Simulated temperature offset between the sample volume and the well base. The average sample volume temperature is warmer than the air pocket in the well base throughout the 3276s simulation. Error bars reflect the uncertainty of the simulation based on the difference between measured and simulated temperature of the well base (see Fig. 2.10).

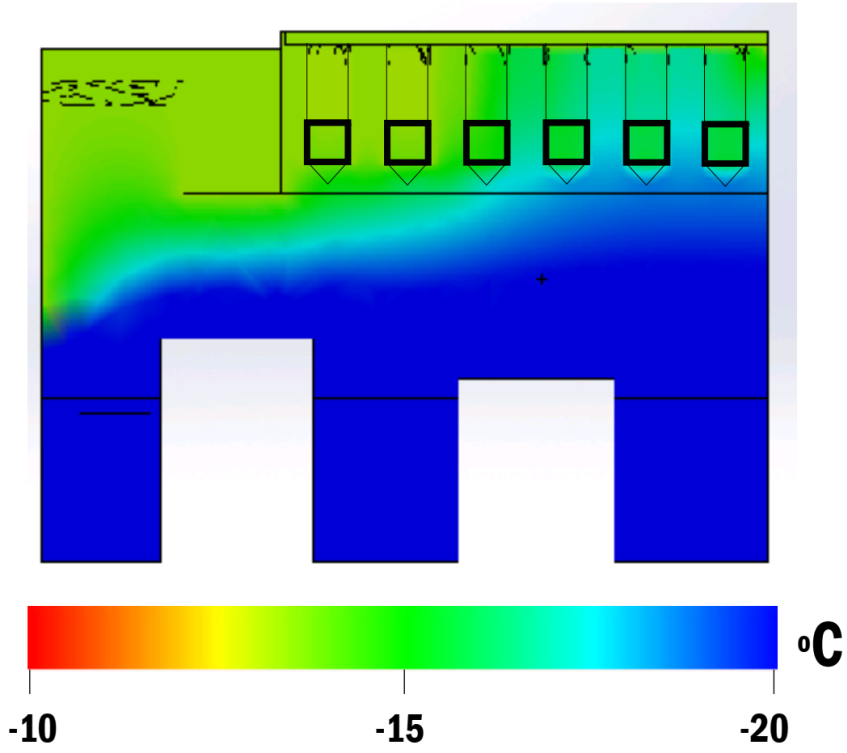

Figure 2.13: Spatial temperature gradient in sample volume temperature. Cross-section of top left quadrant of the well block (see Sec. 2.4.2 for details) at 1638 s. The sample volumes are outlined by the thick black rectangles. The leftmost sample volumes are closer to the outer edges of the well block, whereas the rightmost sample volumes are closer to the interior of the block. Thus, the leftmost sample volumes that are closer to the outer edges of the well block are warmer than the sample volumes along the interior of the well block, with a maximum difference of 2.2ºC.

Chapter 3

3 Best practices for precipitation sample storage for offline studies of ice nucleation in marine and coastal environments

3.1 Abstract

Ice-nucleating particles (INPs) are efficiently removed from clouds through precipitation, a convenience of nature for the study of these very rare particles that influence multiple climate-relevant cloud properties including ice crystal concentrations, size distributions and phase-partitioning processes. INPs suspended in precipitation can be used to estimate in-cloud INP concentrations and to infer their original composition. Offline droplet assays are commonly used to measure INP concentrations in precipitation samples. Heat and filtration treatments are also used to probe INP composition and size ranges. Many previous studies report storing samples prior to INP analyses, but little is known about the effects of storage on INP concentration or their sensitivity to treatments. Here, through a study of 15 precipitation samples collected at a coastal location in La Jolla, CA, USA, we found INP concentration changes up to $>$ 1 order of magnitude

caused by storage to concentrations of INPs with warm to moderate freezing temperatures (−7 to −19 °C). We compared four conditions: (1) storage at room temperature (+21–23 °C), (2) storage at +4 °C, (3) storage at −20 °C and (4) flash-freezing samples with liquid nitrogen prior to storage at −20 °C. Results demonstrate that storage can lead to both enhancements and losses of greater than 1 order of magnitude, with non-heat-labile INPs being generally less sensitive to storage regime, but significant losses of INPs smaller than 0.45 μm in all tested storage protocols. Correlations between total storage time (1-166 d) and changes in INP concentrations were weak across sampling protocols, with the exception of INPs with freezing temperatures $\geq$ −9 °C in samples stored at room temperature. We provide the following recommendations for preservation of precipitation samples from coastal or marine environments intended for INP analysis: that samples be stored at −20 °C to minimize storage artifacts, that changes due to storage are likely an additional uncertainty in INP concentrations, and that filtration treatments be applied only to fresh samples. At the freezing temperature −11 °C, average INP concentration losses of 51 %, 74 %, 16 % and 41 % were observed for untreated samples stored using the room temperature, +4, −20 °C, and flash-frozen protocols, respectively. Finally, the estimated uncertainties associated with the four storage protocols are provided for untreated, heat-treated and filtered samples for INPs between −9 and −17 °C.

3.2 Introduction

In-cloud ice crystals and their formation processes are critical features of Earth's radiative and hydrological balance, affecting multiple climate-relevant cloud properties including cloud lifetime, reflectivity and precipitation efficiency (DeMott et al., 2010; Lohmann, 2002; Lohmann and Feichter, 2005; Tan et al., 2016; Creamean et al., 2013). Ice-nucleating particles (INPs) impact ice crystal concentrations and size distributions in clouds by triggering the freezing of droplets at temperatures above the homogeneous freezing point of water (−38 °C).

INPs have been sampled in clouds and precipitation for decades (e.g., Rogers et al., 1998; Vali, 1971, 1966) to measure abundances, probe their compositions and investigate the extent to which they impact the properties of clouds. There are several caveats to consider when inferring in-cloud INP concentrations or properties from precipitation samples (Petters and Wright, 2015), including sweep-out of additional INPs as the hydrometeor traverses the atmosphere below the cloud (Vali, 1974) and heterogeneous chemistry due to adsorption or absorption of gases (Hegg and Hobbs, 1982; Kulmala et al., 1997; Lim et al., 2010). However, assessing the composition of INPs in precipitation samples is more straightforward than cloud particles. Thus, the number of publications reporting measurements of INP concentrations in precipitation has increased over the past decade. Numerable insights have been obtained in previous precipitationbased INP studies, including the efficient depletion of INPs relative to other aerosols of similar size in precipitating clouds (Stopelli et al., 2015); constraints on minimum enhancement factors for secondary ice formation processes (Petters and Wright, 2015); and the identification, characteristics and distribution of various INP populations (e.g., Christner et al., 2008; Hader et al., 2014; Stopelli et al., 2017). INP concentrations in precipitation have been used to estimate in-cloud concentrations, based on assumptions that the majority of particles (86 %) in precipitation originate from the cloud rather than the atmospheric column through which the hydrometeor descended (Wright et al., 2014). Along the same line of reasoning, INPs in precipitation have also been used to infer sources and composition of in-cloud INP populations (e.g., Martin et al., 2019; Michaud et al., 2014, respectively).

A number of online (real-time) and offline (processed postcollection) techniques exist for measurement of INPs for each ice nucleation mechanism, including condensation, deposition, immersion and contact freezing. However, as some simulations have shown that immersion mode freezing is the dominant mode of primary freezing in the atmosphere between 1000 and 200 hPa (Hoose et al., 2010), most techniques target immersion freezing. Despite the lack of time resolution, offline techniques enable measurement of INPs at modest supercooling (e.g., up to

−5 °C) and temperature regimes where concentrations typically fall below detection limits of online instruments (DeMott et al., 2017). Offline instruments capable of immersion mode INP measurement include a number of droplet assays, in which sample suspensions are distributed among an array of droplets that are then cooled and frozen (e.g., Budke and Koop, 2015; Harrison et al., 2018; Hill et al., 2014; Whale et al., 2015) as well as other systems in which water is condensed onto particles collected on substrates prior to cooling and freezing (e.g., Mason et al., 2015). As they are designed for analysis of liquid suspensions, droplet freezing assay techniques are commonly used for measurement of INPs suspended in precipitation (e.g., Creamean et al., 2019; Rangel-Alvarado et al., 2015; Michaud et al., 2014; Stopelli et al., 2014; Wright et al., 2014).

Many studies report results from samples stored prior to processing. Storage protocols vary widely, including total storage time; time between collection and storage; and temperature fluctuations between collection, shipment and storage (if these details are provided at all; see summary Table 3.8 in the Supplement). Storage temperatures range from −80 °C (Vali et al., 1971) to +4 °C (e.g., Petters and Wright, 2015; Failor et al., 2017; Joyce et al., 2019), yet generally samples are stored between +4 and −20 °C. Reported storage intervals range between hours (Schnell et al., 1977; Christner et al., 2008) to 48 years (Vasebi et al., 2019). The understanding of storage effects on INPs suspended in precipitation is limited (Petters and Wright, 2015), and the understanding of storage effects on INPs collected on filters is similarly lacking (Wex et al., 2019). Stopelli et al. (2014) studied INP concentrations in a snow sample stored at +4 °C and observed a decrease in the concentration of INPs active at −10 °C over 30 d by a factor of ~ 2. Schnell (1977) reported significant losses in fog and seawater samples after storage at room temperature for short periods (6-11 h). Several studies have reported on the lability of commercially available dust and biological IN entities in storage above 0 °C or under freezing conditions, including Arizona test dust and Snomax® (Perkins et al., 2020; Polen et al., 2016; Wex et al., 2015), and similar labilities could affect the INPs of similar composition in precipitation samples (Creamean et al.,

2013; Martin et al., 2019). Considering the abundance of precipitation-based INP studies, the lack of bounds on potential impacts of storage on INP concentration measurements represents a critical uncertainty in conclusions derived from data on stored samples. Furthermore, to determine INP activation mechanisms and composition, previous studies have applied treatments to precipitation samples, including heat, filtration, enzymes and peroxide (e.g., Hill et al., 2016), but it is unknown to what extent storage affects the results of such experiments.

Here we investigate the effects of four storage protocols on INPs using 15 precipitation samples collected between 22 September 2016 and 22 November 2019 at two coastal sites at Scripps Institution of Oceanography, La Jolla, CA, USA: (1) storage at room temperature (+21-23 °C), (2) storage at +4 °C ("refrigerated"), (3) storage at −20 °C ("frozen") and (4) flash-freezing samples with liquid nitrogen prior to storage at −20 °C ("flash frozen"). The abundance of previous studies that report storage between +4 and −20 °C motivated the choice of techniques 2 and 3 (see Table 3.8). Room temperature storage was chosen to provide context as a worst-case scenario, and the flash-freezing technique was chosen to investigate whether any changes of INP concentrations could be mitigated by instantaneous freezing prior to storage. The 15 precipitation samples in this study were divided into several replicates so that the concentration of INPs could be measured in untreated, heated and filtered samples when fresh and again after storage using the four techniques described above. Sample replicates were additionally processed at two different points in time to investigate the effects of total storage time on INP concentration measurements. Enhancements and losses of INPs according to storage protocol and treatment are reported, as well as recommendations for storage protocols that best preserve INPs in untreated, heated and filtered precipitation samples from marine or coastal environments.

3.3 Methods

3.3.1 Precipitation sample collection

Precipitation samples were collected at two coastal locations at Scripps Institution of Oceanography (32.87° N 177.25° W): the rooftop of the Ellen Browning Scripps Memorial Pier laboratory (32.8662° N, 117.2544° W) (10 m above sea level) and the rooftop of a storage container next to Isaacs Hall (32.8698° N, 117.2522° W, 58 m above sea level, 500 m inland). Collection technique varied based on location. At the SIO pier, the Teledyne ISCO model 6712 commercial water sampler (Teledyne ISCO, Inc., US) was used. A plastic funnel, 27 cm in diameter, and Tygon tubing, connected the sampler inlet to the water sampler's distributor arm. The samples were distributed via the distributor arm into one of twenty-four 1 L polypropylene bottles on an hourly time interval. Bottles corresponding to consecutive 1 h time intervals were combined when the hourly precipitation volume was insufficient for sample separation and analysis ($<$ 50 mL per bottle). At the Isaacs Hall location, an ISO 6706 plastic graduated cylinder and plastic funnel, 27 cm in diameter, were used for precipitation collection. At both sites, ring stands supported the collection funnels approximately 60 cm above the rooftop. All funnels, tubing, cylinders and bottles were cleaned with 10 % hydrogen peroxide for 10 min and rinsed with Milli-Q purified water three times immediately before each sampling event. Satellite composites from the National Weather Service Weather Prediction Center's North American Surface Analysis Products were used for synoptic weather analysis to generally characterize each rain event (see Table 3.1). Atmospheric river (AR) events were identified using the global AR dataset that was developed by Guan and Waliser (2015) and further refined in Guan et al. (2018).

3.3.2 Storage protocols

The following sample storage protocols were used: frozen at −20 °C, refrigerated at 4 °C, room temperature (21-23 °C), and flash freezing, or flashing with liquid nitrogen (−196

°C) before frozen at −20 °C. All techniques except storage at room temperature are commonly used for offline INP analysis (see Table 3.8). Excluding the samples that were flash frozen, all samples were stored in 50 mL sterile plastic Falcon® tubes (Corning Life Sciences, Corning, NY, USA). Flash-frozen samples were stored in polypropylene 5 mL cryovials. Prior to storage, 25-50 mL bulk sample aliquots were distributed from collection bottles into Falcon® tubes, shaking bottles $\sim$ 10 s between each distribution. Not all samples were stored using all four of the storage protocols due to limited volume for some samples. See Tables 3.2-3.4 for a summary of the number of samples studied for each storage protocol. Precipitation samples were stored for varying intervals between 1 and 166 d to investigate effects of storage time on INP concentrations. INP measurements were made in two or three time steps: within 2 h of collection, and once or twice after storing using one of four storage protocols described above, depending on volume. Stored and fresh samples were analyzed in three treatment conditions: (1) raw untreated precipitation, (2) heated over a 95 °C water bath for 20 min and (3) filtered through a 0.45 μm surfactant-free cellulose acetate syringe filter (Thermo Scientific™ Nalgene™, Waltham, MA, USA). Heat treatments and filters were applied to samples just prior to processing (i.e., treatments were not applied to samples prior to storage).

3.3.3 INP analysis

The automated ice spectrometer (AIS) is an offline immersion-mode freezing assay which is described elsewhere (Beall et al., 2017). Briefly, 50 μL aliquots of sample are pipetted into two sterile 96-well polypropylene PCR plates. The plates are inserted into an aluminum block, machined to hold PCR plates, that sits in the coolant bath of a Fisher Scientific Isotemp® Circulator. A thermistor placed atop the left side of the aluminum block, below the PCR plate, recorded temperature. An acrylic plate separated the PCR plates from the ambient lab air. In the headspace between the acrylic plate and the PCR plates, nitrogen gas flowed at a flow rate of 14 L min^{-1} to reduce temperature stratification in the samples (Beall et al., 2017). The nitrogen gas was

cooled before emission by passing through the chiller via copper tubing. A 0.5 MP monochrome camera (Point Grey Blackfly 0.5 MP Mono GigE POE) performed the image capture. Custom LabVIEW software controlled the camera settings, controlled the rate at which the chiller cooled and displayed the temperature of the thermistor.

A control Milli-Q water sample is used, typically in the first 30 wells of each sample run, to detect contamination and for subsequent INP concentration calculations. Thirty wells were used per sample to achieve a limit of detection of 0.678 IN mL^{-1}. For each run, the chiller was cooled to -35 °C. As the chiller cools the sample plates (1 °C min^{-1}), the custom LabVIEW virtual instrument records the location and temperature of the freezing event as they occur. Freezing events are detected by the change in pixel intensity of the sample as it changes from liquid to solid.

3.3.4 Particle size distributions

Size distributions of insoluble particles suspended in the fresh and stored precipitation samples were measured using the Multi-sizing Advanced Nanoparticle Tracking Analysis (MANTA) ViewSizer 3000 (Manta Instruments Inc.). The Manta ViewSizer 3000 applies multispectral particle tracking analysis (m-PTA) to obtain size distributions of particles of sizes between 10 and 2000 nm with three solid-state lasers with wavelengths of 450, 520 and 650 nm. m-PTA has been shown to outperform traditional dynamic light scattering (DLS) techniques when measuring polydisperse particles in suspension (McElfresh et al., 2018). For analysis, 300 videos of the illuminated particles in suspension are recorded, each 10 s in length. The software tracks each particle individually, obtaining particle size and number concentration from their Brownian motion and the imaged sample volume.

Table 3.1: Precipitation sampling periods.

Sampling period	UTC date (mm/dd/yyyy)	UTC time start	UTC time end	Meteorological conditions
1	09/22/2016	19:20	21:13	scattered, low coastal clouds, lack of dynamical system
2	09/22/2016	19:42	21:13	scattered, low coastal clouds, lack of dynamical system
3	12/31/2016	04:53	07:52	warm, low cloud rain
4	01/01/2017	07:53	10:52	postfrontal rain, mesoscale system
5	01/05/2017	21:02	22:01	prefrontal rain, mesoscale system
6	01/09/2017	15:51	19:50	decaying atmospheric river
7	01/11/2017	19:00	23:30	frontal rain
8	01/14/2017	02:03	06:00	warm, low cloud rain
9	01/19/2017	12:30	17:30	prefrontal rain, mesoscale system
10	01/20/2017	14:15	02:20 (next day)	weak atmospheric river
11	11/19/2019	22:34	22:45	prefrontal rain, mesoscale system
12	11/22/2019	04:43	05:42	scattered, low coastal clouds, lack of dynamical system
13	11/22/2019	06:43	07:42	scattered, low coastal clouds, lack of dynamical system
14	11/23/2019	07:42	08:41	convective, local updraft rain
15	11/23/2019	08:42	09:41	convective, local updraft rain

3.4 Results

3.4.1 INP concentrations in fresh precipitation samples

Figure 3.1 shows INP concentrations of 15 coastal rain samples, collected in a variety of meteorological conditions including scattered, low coastal rain clouds, frontal rain and atmospheric river events (see Table 3.1). Observations generally fall within bounds of previously reported INP concentrations from precipitation and cloud water samples (grey shaded region, adapted from Petters and Wright, 2015). Observed freezing temperatures ranged from −4.0 to −18.4 °C, with concentrations up to the limit of testing at 10^5 INP L^{-1} precipitation. AIS

Table 3.2: Summary of unique and replicate untreated precipitation samples used for INP concentration measurements featured in Fig. 3.2.

Storage technique	No. of unique samples	No. of stored samples measured at two time steps
Room temperature (19-23 °C)	8	6
Refrigeration (+4 °C)	8	8
Freezing (−20 °C)	9	9
Flash freezing (−20 °C)	8	4

Table 3.3: . Summary of unique and replicate heat-treated precipitation samples used for INP concentration measurements featured in Fig. 3.3

Storage technique	No. of unique samples	No. of stored samples measured at two time steps
Room temperature (19-23 °C)	8	6
Refrigeration (+4 °C)	8	8
Freezing (−20 °C)	8	7
Flash freezing (−20 °C)	8	4

measurement uncertainties are represented with 95 % binomial sampling intervals (Agresti and Coull, 1998).

Following the assumptions in Wright and Petters (2015) to estimate in-cloud INP concentrations from precipitation samples (i.e., condensed water content of 0.4 g m^{-3} air), observations of INP concentrations in fresh precipitation samples are additionally compared to studies of field measurements conducted in marine and coastal environments. Figure 3.1 shows that atmospheric INP concentration estimates compare with INP concentrations observed in a range of marine and coastal environments, including the Caribbean, east Pacific, and Bering Sea, as well as laboratory-generated nascent sea spray aerosol (DeMott et al., 2016). However, two of the warmest-freezing INP observations in Fig. 1 (at −4.0 and −4.75 °C) exceed temperatures commonly observed in marine-influenced atmospheres, precipitation and cloud water samples.

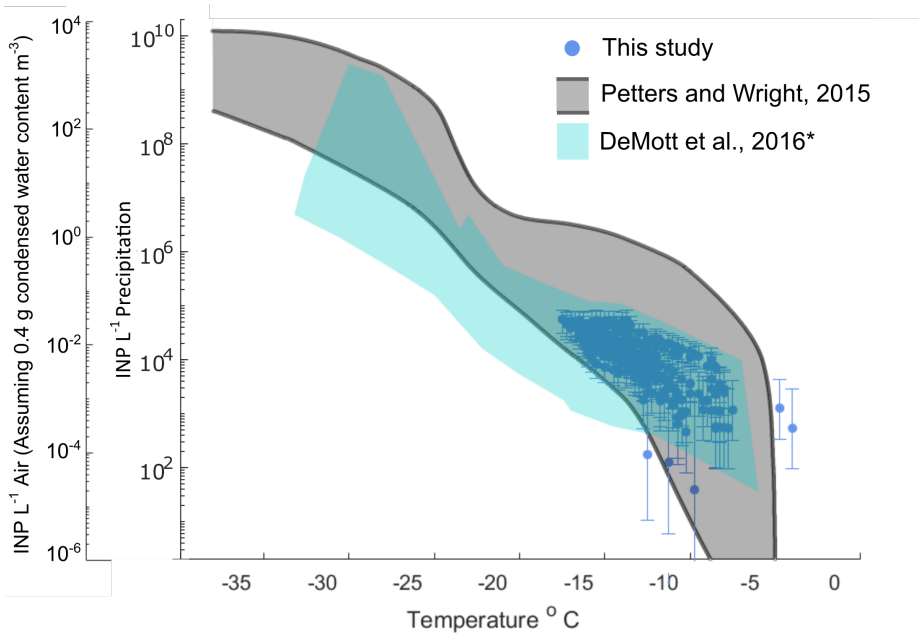

Figure 3.1: INP concentrations per liter of precipitation and estimated in-cloud INP concentrations per volume of air in 15 precipitation samples collected at two coastal sites at Scripps Institution of Oceanography (La Jolla, California, USA) between 22 September 2016 and 22 November 2019. Grey shaded region indicates the spectrum of INP concentrations reported in nine previous studies of precipitation and cloud water samples collected from various seasons and locations worldwide, adapted from Fig. 1 in Petters and Wright (2015). The blue shaded region denotes the composite spectrum of INP concentrations observed in a range of marine and coastal environments including the Caribbean, east Pacific, and Bering Sea as well as laboratory-generated nascent sea spray (DeMott et al., 2016). * DeMott et al. (2016) data have been updated with a completed dataset for the ICE-T study, as shown in Yang et al. (2020).

In 5 of the 15 heat-treated samples, INP concentrations were increased by 1.9-13 times between −9 and −11 °C (see Discussion). Excluding these five samples, the fraction of heat-resilient INPs varied between samples and generally increased with decreasing temperature. Geometric means and standard deviations of heat-treated: untreated INP ratios were 0.40 $\times/\div$ 1.9, 0.51 $\times/\div$ 2.0 and 0.62 $\times/\div$ 2.1 at −11, −13 and −15 °C respectively.

Fractions of INPs < 0.45 μm also varied between samples, with geometric means and standard deviations of 0.48 $\times/\div$ 1.73, 0.30 $\times/\div$ 3.4 and 0.37 $\times/\div$ 1.9 at −11, −13 and −15 °C respectively. Mean values of heat-resilient INP fractions and INPs < 0.45 μm were calculated using the geometric mean, which is more appropriate than the arithmetic mean for describing a

distribution of ratios (Fleming and Wallace, 1986).

3.4.2 Effects of sample storage on INP concentration measurements

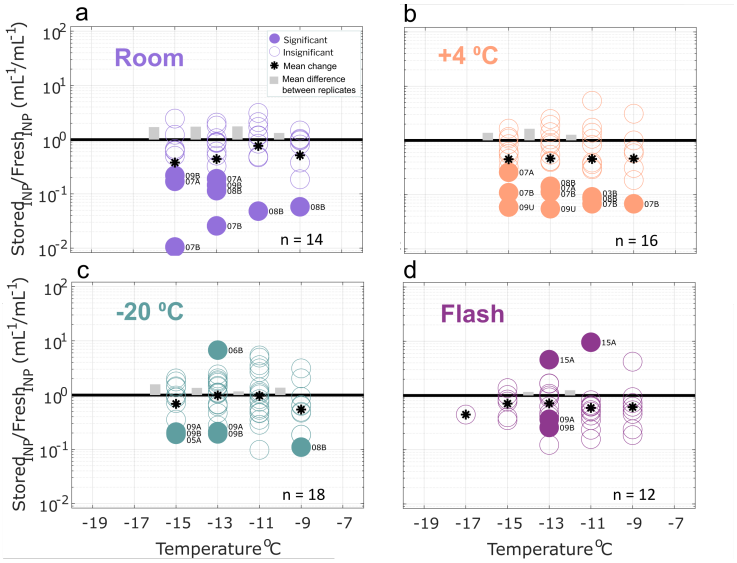

Figure 3.2: Ratio of INP concentrations measured in untreated precipitation samples (stored:fresh), calculated in successive 2 °C increments between −19 and −7 °C. Four storage protocols were applied: (a) room temperature (21-23 °C), (b) refrigerated (+4 °C), (c) frozen (−20 °C) and (d) flash frozen in liquid nitrogen before storing frozen (−20 °C). All samples were processed at one or two time intervals between 1 and 166 d postcollection (see Supplementary Figs. 3.5-3.9). For samples processed at two intervals, both replicate samples are represented in the figure for a total of 14, 16, 18 and 12 samples in panels (a), (b), (c) and (d), respectively (see Table 2 for summary of sample and replicate numbers). Markers above the black 1 : 1 line indicate enhancement of INP concentrations in stored samples, and markers below indicate losses. In temperature intervals containing stored:fresh ratios from at least two sets of replicate samples, grey bars represent the average difference between replicates. Stored sample frozen well fractions that passed Fisher's exact test ($p < 0.01$) for significant differences from original fresh sample frozen well fractions at each of the five temperatures are indicated with filled markers, and the mean change in each temperature interval is marked with a star. Significant data are also labeled to indicate the sample number (01-15; see Table 1) and replicate ("A" or "B", and "U" indicates there were no replicates for the sample). Results show that, on average, INP concentrations decrease in stored samples and that both room temperature storage and refrigeration result in significant INP losses. Frozen and flash-frozen storage show comparable results, with fewer (3-4) of the observations exhibiting significant losses and enhancements in INP concentrations.

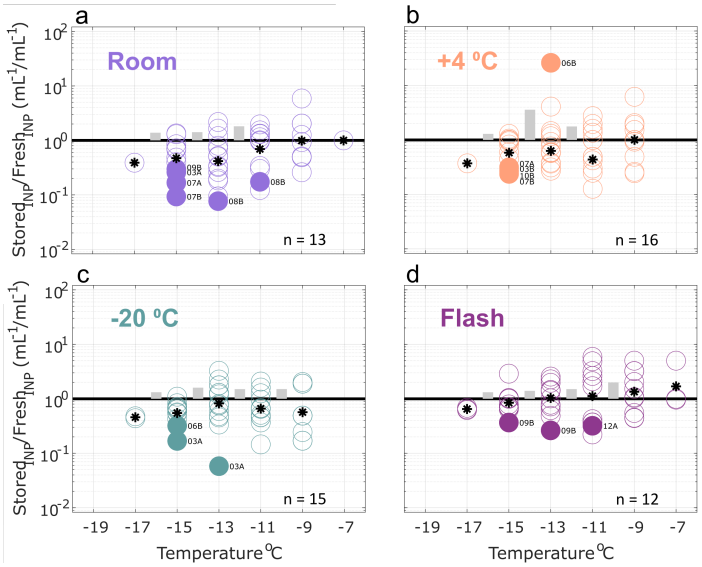

Figure 3.3: Ratio of INP concentrations measured in heated precipitation samples (stored : fresh), calculated in successive 2 °C increments between −19 and −7 °C. Four storage protocols were applied: (a) room temperature (21-23 °C), (b) refrigerated (+4 °C), (c) frozen (−20 °C) and (d) flash frozen in liquid nitrogen before storing frozen (−20 °C). All samples were processed at one or two time intervals between 1 and 166 d postcollection (see Supplementary Figs. 3.5-3.9). For samples processed at two intervals, both replicate samples are represented in the figure for a total of 14, 16, 18 and 12 samples in panels (a), (b), (c) and (d), respectively (see Table 3.3 for summary of sample and replicate numbers). Markers above the black 1 : 1 line indicate enhancement of INP concentrations in stored samples, and markers below indicate losses. In temperature intervals containing stored : fresh ratios from at least two sets of replicate samples, grey bars represent the average difference between replicates. Stored sample frozen well fractions that passed Fisher's exact test ($p < 0.01$) for significant differences from original fresh sample frozen well fractions at each of the five temperatures are indicated with filled markers, and the mean change in each temperature interval is marked with a star. Significant data are also labeled to indicate the sample number (01–15; see Table 3.1) and replicate ("A" or "B", and "U" indicates there were no replicates for the sample). Results show that, on average, INP concentrations decrease in stored samples and that both room temperature storage and refrigeration result in significant INP losses. Frozen and flash-frozen storage show comparable results, with fewer (3-4) of the observations exhibiting significant losses and enhancements in INP concentrations.

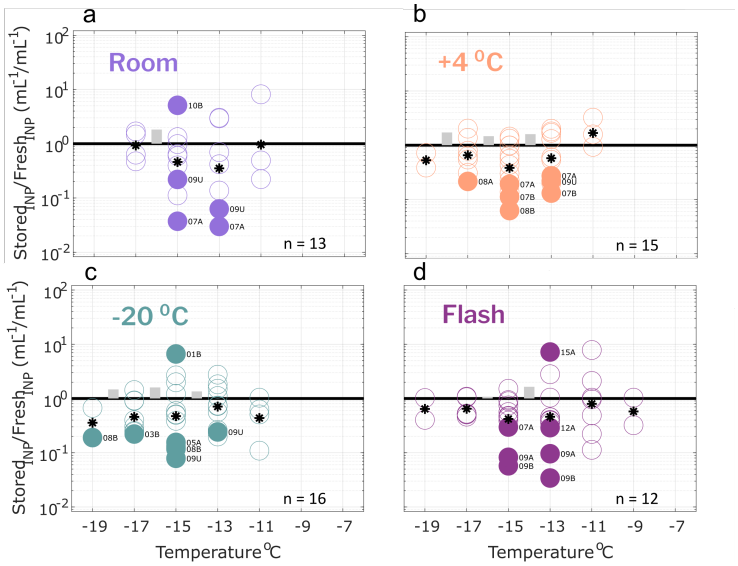

Figure 3.4: Ratio of INP concentrations measured in filtered (0.45μm) precipitation samples (stored : fresh), calculated in successive 2 °C increments between −19 and −7 °C. Same samples as in Fig. 2 but filtered with a 0.45 μm syringe filter prior to measurement (see Methods Sect. for details). All samples were processed at one or two time intervals between 1 and 166 d postcollection. For samples processed at two intervals, both replicate samples are represented in the figure for a total of 13, 15, 16 and 12 samples in panels (a), (b), (c) and (d), respectively (see Table 3.4) for summary of sample and replicate numbers). In temperature intervals containing stored : fresh ratios from at least two sets of replicate samples, grey bars represent the average difference between replicates. Results show significant losses of INPs in several filtered samples, regardless of storage protocol.

INP concentrations of stored replicate samples are compared with original fresh precipitation samples in Figs. 3.2-3.2, calculated in successive 2 °C increments between −7 and −19 °C. This temperature range was chosen for the analysis because most fresh precipitation samples exhibited freezing activity between −7 and −19 °C. Numbers of datapoints in Figs. 3.2-3.2 differ across the temperature intervals due to limits of detection (i.e., ratios were not calculated at temperatures where zero or all wells were frozen in the fresh and/or stored sample).

All stored:fresh ratios were calculated from cumulative INP distributions in 2 °C intervals, meaning that the INP concentration in each interval is inclusive of the concentration in all of the preceding (warmer) temperature intervals. The choice of the cumulative distribution was motivated by the fact that it is standard in INP studies to report INP concentrations in terms of

the cumulative distribution, and it is important to consider impacts of storage on cumulative INP distributions and any conclusions derived from them. Thus, in this study, deviations observed in a stored sample are not necessarily independent; i.e., the sensitivity of INPs to storage in one temperature interval could impact the observed changes in all of the following (colder) temperature intervals. For example, in fresh untreated precipitation samples (see Fig. 3.1), 32 % of the INP concentration calculated at -11 °C activated in one of the preceding (warmer) 2 °C temperature intervals. At -17 °C, this fraction is increased to 46 %.

To investigate correlations between sample storage time and INP enhancements or losses, duplicate samples were archived (when sufficient volume was available) so that each sample could be processed at two distinct points postcollection (see example Supplementary Fig. 3.5). For INPs with freezing temperatures ≥ -9 °C in samples stored at room temperature, time is moderately correlated with changes in INP concentrations ($R^2 = 0.58$). Supplementary Fig. 3.10 shows how losses of warm-freezing INPs in samples stored at +4 °C and room temperature impact the cumulative INP spectra for a select sample. Beyond these exceptions, little to no correlation between storage time and INP enhancements or losses was found for untreated, heated and filtered samples (see Supplementary Figs. 3.5–3.9). This indicates that most of the changes in INPs observed may occur on shorter timescales than those studied here, i.e., < 24 h.

Figure 3.2 shows the ratio of stored sample to fresh sample INP concentrations for untreated precipitation samples stored under four conditions: (a) room temperature (21- 23 °C), (b) refrigerated (+4 °C), (c) frozen (-20 °C) and (d) flash frozen with liquid nitrogen before storing at -20 °C. Markers above the 1:1 line indicate enhancements in INP concentration from the fresh sample, while markers below indicate losses. For each temperature interval containing data from at least two sets of replicate samples, the average differences in stored:fresh concentration ratios between replicates are represented with grey bars to indicate measurement variability. Replicate samples were processed for each storage protocol so that impacts of sample handling can be distinguished from storage impacts. For example, if settling occurs in bulk rain

samples that are then divided into smaller volumes prior to storage, INP concentrations may differ between replicates of the bulk sample. Thus, it is assumed that INP concentration changes that are greater than differences between replicates (grey bars in Figs. 4.2-4.4) can be attributed to storage impacts. We also assume that stored:fresh INP concentration ratios of 1:1 indicate insensitivity to storage, although it is possible that enhancements and losses of equal magnitude could also result in a 1:1 concentration ratio.

Finally, Fisher's exact test was applied to frozen and unfrozen well fractions between each stored sample and its corresponding fresh sample at each of the 2 °C temperature intervals. Stored sample frozen well fractions that were significantly different ($p < 0.01$) from fresh sample frozen well fractions are indicated with filled markers. The term "significant" henceforth is intended to describe INP losses or enhancements that correspond to frozen well fractions that are determined to be significantly different from corresponding fresh sample frozen well fractions, according to Fisher's exact test (i.e., filled markers in Figs. 3.2-3.4). Results in Fig. 3.2 show that significant enhancements or losses of INPs occurred in all storage protocols between -9 and -17 °C and that, on average, stored samples exhibit INP losses (as indicated by the mean change in each temperature interval). In frozen and flash-frozen samples, all enhancements and losses fall within $\pm$ 1 order of magnitude, whereas several significant INP losses beyond 1 order of magnitude are shown in room and refrigerated samples. INP concentration changes $\geq$ 1 order of magnitude are greater than changes in the ratios of the total insoluble particle population of 10–2000 nm during storage (see Supplementary Fig. 3.10). This indicates that the INPs in these samples are more sensitive to storage than the total insoluble particle population. Supplementary Fig. 3.13 illustrates the impacts of the four storage protocols on the full IN spectra of a select untreated precipitation sample at two time intervals, 27 and 64 d after collection.

Figure 3.3 shows the effects of storage on INP observations in heat-treated precipitation samples. Non-heat-labile INPs represented the majority (62 % on average at -15 °C; see Sect. 3.4.1) of the total INPs observed in the fresh samples (i.e., 38 % of the INPs in fresh samples were

heat-labile). Fewer significant losses of non-heat-labile INPs are observed for heat-treated samples stored at room temperature and at 4 °C compared with untreated samples. Again, slightly fewer (2-3) of the total frozen and flash-frozen samples exhibit significant losses and enhancements. All observations other than the one significantly enhanced sample in (b) fall within ranges of stored:fresh ratios observed in the total insoluble particle population (see Supplementary Fig. 3.11, within an order of magnitude). This demonstrates that non-heat-labile INPs are generally less sensitive to storage than the total INP population (Fig. 3.2).

Effects of storage protocol on INP concentrations of filtered precipitation samples are shown in Fig. 3.4 (0.45 μm syringe filter; see Sect. 3.4 for details). INPs $>$ 0.45 μm represented the majority (52 and 63 % on average at -11 and -15 °C, respectively; see Sect. 3.4.1) of total INPs measured in the fresh precipitation samples. A higher number of filter-treated samples exhibit significant losses across all four storage types when compared with the untreated samples. Furthermore, significant losses $>$ 1 order of magnitude are observed across all storage types indicating that INPs $<$ 0.45 μm are generally more sensitive to storage than the total INP population present in precipitation samples.

As the stored:fresh ratios follow a lognormal distribution (one-sample Kolmogorov–Smirnov test), the uncertainties associated with storage and 95 % confidence intervals were calculated in using the geometric mean and standard deviation of ratios of unique samples only between -9 and -17 °C (i.e., omitting any replicates; see Tables 3.4-3.6).

3.5 Discussion

The challenge in selecting a storage protocol for atmospheric samples (e.g., precipitation, cloud water, ambient atmosphere) is that the INP population composition is unknown and diverse, and the impact of any given technique on the different species may vary. Many types of aerosols can serve as INPs, including dusts, metals and metal oxides, organic and glassy aerosols,

Table 3.4: Estimate of uncertainty associated with storage impacts for INPs with activation temperatures between −9 and −17 °C measured in stored, untreated precipitation samples. Confidence intervals were derived from the lognormal distribution of changes observed in INP concentrations due to storage (see Fig. 3.2 and details in Sect. 3.3.2). Temperature intervals where datapoints were too few to derive confidence intervals are indicated with "NA". Changes in INP concentration corresponding to enhancements or losses greater than 1 order of magnitude (losses ≥ −90 % or enhancements ≥ +900 %) in bold.
∗For INPs with freezing temperatures ≥ −9 °C, changes in INP concentrations are moderately correlated with time in samples stored at room temperature or at +4 °C (see Sect. 3.3.2). Change factors for room temperature and refrigerated storage protocols are derived from samples stored in ranges of 27-76 and 8-46 d, respectively.

Storage protocol	Mean change −9 °C (%)	95 % CI low (%)	95 % CI high (%)	Mean change −11 °C (%)	95 % CI low (%)	95 % CI high (%)	Mean change −13 °C (%)	95 % CI low (%)	95 % CI high (%)	Mean change −15 °C (%)	95 % CI low (%)	95 % CI high (%)
Room temperature (21-23 °C)	−26	−82	+200	−51	**−97**	+850	−77	**−98**	+220	−77	**−99**	**+1000**
Refrigeration (+4 °C)	−42	−74	+32	−74	**−99**	+400	−46	**−95**	+520	−56	**−95**	+290
Freezing (−20 °C)	−48	**−95**	+430	−16	**−90**	+580	+24	−80	+650	−50	**−90**	+150
Flash freezing (−20 °C)	−21	**−90**	+520	−41	**−95**	+560	−33	**−91**	+390	NA	NA	NA

Table 3.5: Estimate of uncertainty associated with storage impacts for INPs with activation temperatures between −9 and −17 °C measured in stored, heated precipitation samples. Confidence intervals were derived from the lognormal distribution of changes observed in INP concentrations due to storage (see Fig. 3.3 and details in Sect. 3.3.2). Temperature intervals where datapoints were too few to derive confidence intervals are indicated with "NA". Changes in INP concentration corresponding to enhancements or losses greater than 1 order of magnitude (losses ≥ −90 % or enhancements ≥ +900 %) in bold.

Storage protocol	Mean change −9 °C (%)	95 % CI low (%)	95 % CI high (%)	Mean change −11 °C (%)	95 % CI low (%)	95 % CI high (%)	Mean change −13 °C (%)	95 % CI low (%)	95 % CI high (%)	Mean change −15 °C (%)	95 % CI low (%)	95 % CI high (%)
Room temperature (21-23 °C)	+32	−74	+550	−17	−86	+380	−65	**−95**	+155	−58	**−93**	+150
Refrigeration (+4 °C)	−56	**−91**	**+940**	−74	**−99**	**+1600**	−58	**−99**	**+6000**	−60	−87	+27
Freezing (−20 °C)	−55	**−91**	+130	−53	−87	+69	−42	**−93**	+390	−34	**−70**	+47
Flash freezing (−20 °C)	+36	−76	+660	+31	−88	**+1300**	−9.0	−81	+340	+1.0	−60	+150

Table 3.6: Estimate of uncertainty associated with storage impacts for INPs with activation temperatures between −9 and −17 °C measured in stored, heated precipitation samples. Confidence intervals were derived from the lognormal distribution of changes observed in INP concentrations due to storage (see Fig. 3.4 and details in Sect. 3.3.2). Temperature intervals where datapoints were too few to derive confidence intervals are indicated with "NA". Changes in INP concentration corresponding to enhancements or losses greater than 1 order of magnitude (losses ≥ −90 % or enhancements ≥ +900 %) in bold.

Storage protocol	Mean change −11 °C (%)	95 % CI low (%)	95 % CI high (%)	Mean change −13 °C (%)	95 % CI low (%)	95 % CI high (%)	Mean change −15 °C (%)	95 % CI low (%)	95 % CI high (%)	Mean change −17 °C (%)	95 % CI low (%)	95 % CI high (%)
Room temperature (21-23 °C)	NA	NA	NA	−80	**−99**	+360	−72	**−96**	+130	−7.0	−68	+170
Refrigeration (+4 °C)	NA	NA	NA	−48	**−94**	+300	−65	**−97**	+250	−7.0	-68	+170
Freezing (−20 °C)	NA	NA	NA	−31	−89	+330	−54	**−98**	+870	−32	−78	+110
Flash freezing (−20 °C)	−26	−83	+230	−65	**−98**	+650	−68	**−96**	+140	NA	NA	NA

bioaerosols, organic and mineral soil dust, and combustion products (Kanji et al., 2017). The aim of this study was to identify a storage protocol that best preserves the concentrations and characteristics of the general INP population observed in precipitation samples collected in a coastal environment. To this end, the impacts of four storage protocols on 15 untreated, heated and filtered precipitation samples collected between 22 September 2015 and 22 November 2019 in La Jolla, CA, were investigated by comparing measured INP concentrations between fresh and stored replicates. The fractions of INPs > 0.45 μm observed in this study varied between 52 % and 63 % at -11 and -15 °C, respectively. Excluding the five heat-treated samples in which INP concentrations were enhanced (e.g., 1.9-13 times between -9 and -11 °C), the average fraction of non-heat-labile INPs varied between 40 % and 62 % at -11 and -15 °C, respectively. INP enhancements in heat-treated samples are unexpected, as heat treatments are typically applied assuming that heat destroys proteinaceous (e.g., biological) INPs. The causes of INP enhancements in heat-treated samples are unknown and have only been reported in coastal precipitation samples (Martin et al., 2019) and nascent sea spray aerosol (McCluskey et al., 2018). Possible sources include the redistribution of dissolved IN-active molecules onto particles (McCluskey et al., 2018) and the release of IN-active content from cells (McCluskey et al., 2018; Wilson et al., 2015). These findings demonstrate that in samples influenced by marine sources, a superposition of both positive and negative $\triangle$ INP in samples could result in the observed changes in INP concentrations post heat treatment.

Additionally, the INP freezing temperatures and concentrations observed in this study compare with INPs observed in studies of marine and coastal environments (Fig. 3.1). As spectra in this regime (-5 to -20 °C and 10^{-5} to $\sim 10^{-1}$ L^{-1} air, respectively) cluster distinctly by source type (see Figs. 1-10 in Kanji et al., 2017), Fig. 3.1 indicates that the dominant sources to air masses sampled in this study were marine. Considering that data in this study compare well with marine and coastal INPs from a variety of marine-influenced air masses (DeMott et al., 2016; Yang et al., 2020), the findings herein are likely relevant to samples from other marine and coastal

environments.

While mean INP changes are within a factor of ~ 2 or less of fresh sample INP concentrations for all protocols except "Room temperature" (Table 3.4), none of the four storage protocols prevented significant losses or enhancements of INP concentrations in all samples (Fig. 3.2), indicating that INP concentration measurements on fresh precipitation are superior to measurements on stored samples. The 95 % confidence intervals in Table 3.4 span losses > 1 order of magnitude in all protocols across multiple temperature intervals. These uncertainties equal or exceed INP measurement uncertainties (1-2 orders of magnitude) at temperatures > -20 °C due to discrepancies between instruments (DeMott et al., 2017). If correspondence within 1 order of magnitude (or 2-3 °C) is desired, uncertainties associated with storage should also be considered in studies using samples from coastal or marine environments. Thus, uncertainty distributions provided in Tables 3.4-3.6 can be used to evaluate observed INP concentrations and responses to treatments in the context of potential changes due to storage. However, the degree to which INP sensitivity to storage varies by INP source (e.g., with soil-derived INP populations) remains to be tested.

Samples stored under freezing and flash-freezing conditions exhibited fewer changes overall compared to refrigerated samples. For example, at the INP activation temperature of -13 °C, in the rain sample that exhibited the highest sensitivity to storage, over 20 % of the original concentration was preserved in the frozen sample, whereas only 5 % of the original concentration was preserved in the refrigerated sample. These losses are more extreme than those of Stopelli et al. (2014), which demonstrated that INP concentrations of a snow sample refrigerated over 30 d decreased only two-fold from 0.027 to 0.013 L^{-1} at -10 °C.

Despite the range of enhancements and losses of heatsensitive INPs observed in fresh samples, non-heat-labile INPs were generally less sensitive to storage than the total INP population, and with the exception of samples stored at room temperature, all techniques yielded similar results with fewer enhancements or losses. Interestingly, INPs < 0.45 μm exhibited more

sensitivity to all storage conditions tested than the total INP population, with significant losses (Fisher's exact test, $p < 0.01$) observed in several samples leaving between 25 % and 3 % of the value observed in the original fresh sample. Losses of INPs < 0.45 μm in samples stored at room temperature and +4 °C were comparable to the losses of total INPs in untreated samples and are likely a result of chemical aging in solution. However, losses of INPs < 0.45 μm in samples stored at -20 °C (both frozen and flash frozen) exceeded losses observed in the corresponding untreated samples. This is surprising given that a large fraction of INPs in this study were resilient to heat treatments of +95 °C. Lacking the identities of INPs observed in this study, a clear mechanism for their losses remains elusive. However, we offer the following points for consideration. It is well known that as a solution freezes, some solute is incorporated into the crystal and some is rejected, leading to enrichment of the solution phase and aggregation of dissolved or colloidal organic matter (Butler, 2002). Thus, as precipitation samples are freezing, small organic INPs may be lost simply due to aggregation in channels of enriched solute. In coastal precipitation samples for example, INPs may be so "lost" as the increased salinity in solution-phase channels destabilizes small suspended particles, allowing them to coagulate and settle (Jackson and Burd, 1998). Another possibility is that as the solution phase is enriched during freezing, smaller INPs may be adsorbing onto the surface of larger particles. The size distributions of total insoluble particles in the frozen samples show that most samples exhibit losses between 0 and 500 nm after storage and enhancements in sizes $>$ 500 nm (see Supplementary Fig. 3.10). This effect is not observed for samples stored at room temperature or at +4 °C.

Changes in the total insoluble particle size distribution ($\pm$ 1 order of magnitude between 10 and 2000 nm; see Supplementary Figs. 3.10 and 3.11) may also have contributed to the observed INP concentration enhancements. Potential mechanisms for INP enhancements include increases in the number concentration of small particles due to breakup of loosely clumped masses of smaller particles, the redistribution of dissolved IN-active molecules onto particles (McCluskey et al., 2018), and the release of IN-active content from cells (McCluskey et al., 2018;

Wilson et al., 2015) during cell death and lysis post freezing (Mazur et al., 1984).

Previous studies on precipitation collected along the California coast have demonstrated the contribution of dust, marine and terrestrial bioparticles to INPs in precipitation (Levin et al., 2019; Martin et al., 2019). Considering that well-characterized IN-active dust and biological standards (Arizona test dust and Snomax®, respectively) are sensitive to storage conditions, it is possible that dust or biological INPs contributed to the observed INP changes. Perkins et al. (2020) found that the IN ability of Arizona test dust is degraded in most conditions, including aging in deionized water for 1 d, and results from Polen et al. (2016) show that the most efficient (i.e., warmest freezing) components of biological ice nucleators are also the most labile and sensitive to storage.

The observed distributions of INP concentration changes in stored precipitation samples have implications for the interpretation of heat and filtration treatment experiments. As heat denatures proteins, heat treatments are commonly used to infer contributions of proteinaceous or cellular contributions to INP populations, and filters are commonly applied to identify observed INP size ranges (e.g., McCluskey et al., 2018). For example, a typical analysis involves a comparison of the INP spectrum of an untreated sample to that of the heat-treated or filtered sample, and information about the sizes and biological composition of INPs is derived from this comparison. Our results demonstrate that these treatments may yield different results if treatments are applied to stored samples. Any losses of INPs due to filtering or heat application could be confounded by significant enhancements or losses caused by storage (up to >1 order of magnitude), resulting in inaccurate conclusions about INP characteristics. In this study, a large fraction (30 % to 48 %, on average) of INPs observed in fresh precipitation samples were $<$ 0.45 μm. Considering this and that INPs $<$ 0.45 μm exhibit significant losses across all storage types, there is a risk that filter treatments on stored samples in this study would lead to the underestimation of INPs $<$ 0.45 μm. Losses of heat-labile INPs in storage could also impact treatment outcomes on stored samples. Assuming negligible effects of storage on the heat-treated

sample but losses due to storage in the untreated sample (e.g., as was shown to be most likely for untreated samples stored at +4 °C), INP spectra of heat-treated samples could appear to indicate the entire INP population was heat-insensitive. This effect was observed in several samples across storage types (see Supplementary Fig. 3.12).

3.6 Conclusions

Based on all observations in this study, we provide the following recommendations for precipitation samples collected in coastal and marine environments for offline INP analyses:

1. Of the four storage protocols tested, none prevented changes in INP concentrations across all samples between -7 and -19 °C. However, whenever processing fresh samples is not possible, our results demonstrate that storage at -20 °C causes the least changes in INP concentrations.

2. Estimates of uncertainty attributed to storage impacts and 95 % confidence intervals for INP measurements obtained from stored samples are provided (see Tables 3.4-3.6).

3. Flash freezing with liquid nitrogen before storing at -20 °C did not improve conservation of INPs.

4. With the exception of warm-freezing INPs (freezing temperatures ≥ -9 °C) in samples stored at room temperature, we found little to no correlation between changes in INP concentrations and storage intervals on timescales between 1 and 166 d, indicating that most enhancements or losses are likely happening during freezing or on timescales < 24 h.

5. INPs that are insensitive to heat treatments are also less sensitive to storage. However, potential enhancements or losses due to storage (e.g., an average loss of 50 % for INPs with freezing temperatures gte -15 °C in samples stored at -20 °C) should be treated as additional uncertainty in measurements of INP concentration when comparing heat-treated with untreated INP spectra.

6. Due to the significant losses of INPs < 0.45 μm in storage, regardless of protocol, we recommend applying filtration treatments to fresh samples exclusively.

As measurements of INPs suspended in precipitation samples are used to infer in-cloud INP composition and concentration estimates, they represent important contributions to studies of links between aerosols, cloud processes and precipitation outcomes. This study derives bounds and correction factors for the impacts of storage on INPs and treatment outcomes from changes in INPs observed in coastal precipitation samples. However, it remains to be seen how INP sensitivity to storage varies by environment or INP composition. Further studies are needed to bracket storage effects on INP populations with various distributions of terrestrial and marine sources, as well as on heat-labile (biological) INPs, and INPs with colder activation temperatures. These studies could additionally benefit from analysis on how storage impacts differential INP spectra, which could reveal how sensitivity to storage varies by specific freezing temperature ranges. Bounds on the impact of storage will enable more meaningful intercomparisons of datasets and illuminate best practices for preserving INPs for offline analysis.

Data availability. The dataset supporting this paper is hosted by the UCSD Library Digital Collections (https://doi.org/10.6075/ J0M32T8B, Beall et al., 2020). The AR data were provided by Bin Guan via https://ucla.box.com/ARcatalog (last access: 27 July 2020).

Acknowledgements. This work was supported by the NSF through the NSF Center for Aerosol Impacts on Chemistry of the Environment (CAICE) CHE-1801971 and AGS-1451347. The National Weather Service Weather Prediction Center provided the surface analysis satellite composite products used in this study. Development of the AR detection algorithm and databases was supported by NASA.

Chapter 3, in full, is a reprint of the material as it appears in Atmospheric Measurement Techniques 2020. Beall, C. M., Lucero, D., Hill, T. C., DeMott, P. J., Stokes, M. D. and Prather, K. A.: Best practices for precipitation sample storage for offline studies of ice nucleation in marine and coastal environments, Atmos. Meas. Tech., 13(12), 6473–6486, doi:10.5194/amt-13-6473-2020, 2020. The dissertation author was the primary investigator and author of this

paper.

Financial support. This research has been supported by the National Science Foundation, Division of Chemistry (grant no. CHE- 1801971), and the National Science Foundation, Division of Atmospheric and Geospace Sciences (grant no. AGS-1451347).

3.7 References

Agresti, A. and Coull, B. A.: Approximate Is Better than "Exact" for Interval Estimation of Binomial Proportions, Am. Stat., 52, 119–126, https://doi.org/10.2307/2685469, 1998.

Beall, C. M., Stokes, M. D., Hill, T. C., DeMott, P. J., DeWald, J. T., and Prather, K. A.: Automation and heat transfer characterization of immersion mode spectroscopy for analysis of ice nucleating particles, Atmos. Meas. Tech., 10, 2613–2626, https://doi.org/10.5194/amt-10-2613-2017, 2017.

Beall, C. M., Lucero, D., Hill, T. C., DeMott, P. J., Stokes, M. D., and Prather, K. A.: Data from: Best practices for precipitation sample storage for offline studies of ice nucleation in marine and coastal environments, UC San Diego Library Digital Collections, https://doi.org/10.6075/J0M32T8B, 2020.

Budke, C. and Koop, T.: BINARY: an optical freezing array for assessing temperature and time dependence of heterogeneous ice nucleation, Atmos. Meas. Tech., 8, 689–703, https://doi.org/10.5194/amt-8-689-2015, 2015.

Butler, M. F.: Freeze Concentration of Solutes at the Ice/Solution Interface Studied by Optical Interferometry, Cryst. Growth Des., 2, 541–548, https://doi.org/10.1021/cg025591e, 2002.

Christner, B. C., Cai, R., Morris, C. E., McCarter, K. S., Foreman, C. M., Skidmore, M. L., Montross, S. N., and Sands, D. C.: Geographic, seasonal, and precipitation chemistry influence on the abundance and activity of biological ice nucleators in rain and snow, P. Natl. Acad. Sci. USA, 105, 18854–18859, https://doi.org/10.1073/pnas.0809816105, 2008.

Creamean, J. M., Suski, K. J., Rosenfeld, D., Cazorla, A., DeMott, P. J., Sullivan, R. C., White, A. B., Ralph, F. M., Minnis, P., Comstock, J. M., Tomlinson, J. M., and Prather, K. A.: Dust and biological aerosols from the Sahara and Asia influence precipitation in the Western U.S., Science, 340, 1572–1578, https://doi.org/10.1126/science.1227279, 2013.

Creamean, J. M., Mignani, C., Bukowiecki, N., and Conen, F.: Using freezing spectra characteristics to identify ice-nucleating particle populations during the winter in the Alps, Atmos. Chem. Phys., 19, 8123–8140, https://doi.org/10.5194/acp-19- 8123-2019, 2019.

DeMott, P. J., Prenni, a J., Liu, X., Kreidenweis, S. M., Petters, M. D., Twohy, C. H., Richardson, M. S., Eidhammer, T., and Rogers, D. C.: Predicting global atmospheric ice nuclei distributions and their impacts on climate, P. Natl. Acad. Sci. USA, 107, 11217– 11222, https://doi.org/10.1073/pnas.0910818107, 2010.

DeMott, P. J., Hill, T. C. J., McCluskey, C. S., Prather, K. A., Collins, D. B., Sullivan, R. C., Ruppel, M. J., Mason, R. H., Irish, V. E., Lee, T., Hwang, C. Y., Rhee, T. S., Snider, J. R., McMeeking, G. R., Dhaniyala, S., Lewis, E. R., Wentzell, J. J. B., Abbatt, J., Lee, C., Sultana, C. M., Ault, A. P., Axson, J. L., Diaz Martinez, M., Venero, I., Santos-Figueroa, G., Stokes, M. D., Deane, G. B., Mayol-Bracero, O. L., Grassian, V. H., Bertram, T. H., Bertram, A. K., Moffett, B. F., and Franc, G. D.: Sea spray aerosol as a unique source of ice nucleating particles, P. Natl. Acad. Sci. USA, 113, 5797–5803, https://doi.org/10.1073/pnas.1514034112, 2016.

DeMott, P. J., Hill, T. C. J., Petters, M. D., Bertram, A. K., Tobo, Y., Mason, R. H., Suski, K. J., McCluskey, C. S., Levin, E. J. T., Schill, G. P., Boose, Y., Rauker, A. M., Miller, A. J., Zaragoza, J., Rocci, K., Rothfuss, N. E., Taylor, H. P., Hader, J. D., Chou, C., Huffman, J. A., Pöschl, U., Prenni, A. J., and Kreidenweis, S. M.: Comparative measurements of ambient atmospheric concentrations of ice nucleating particles using multiple immersion freezing methods and a continuous flow diffusion chamber, Atmos. Chem. Phys., 17, 11227–11245, https://doi.org/10.5194/acp-17- 11227-2017, 2017.

Failor, K. C., Iii, D. G. S., Vinatzer, B. A., and Monteil, C. L.: Ice nucleation active bacteria in precipitation are genetically diverse and nucleate ice by employing different mechanisms, ISME J., 11, 2740–2753, https://doi.org/10.1038/ismej.2017.124, 2017.

Fleming, P. J. and Wallace, J. J.: How Not to Lie with Statistics: The Correct Way to Summarize Benchmark Results, Commun. ACM, 29, 218–221, https://doi.org/10.1145/5666.5673, 1986.

Guan, B. and Waliser, D. E.: Detection of atmospheric rivers: Evaluation and application of an algorithm for global studies, J. Geophys. Res.-Atmos., 120, 12514–12535, https://doi.org/10.1002/2015JD024257, 2015.

Guan, B., Waliser, D. E., and Ralph, F. M.: An Intercomparison between Reanalysis and Dropsonde Observations of the Total Water Vapor Transport in Individual Atmospheric Rivers, J. Hydrometeorol., 19, 321–337, https://doi.org/10.1175/JHM-D-17- 0114.1, 2018.

Hader, J. D., Wright, T. P., and Petters, M. D.: Contribution of pollen to atmospheric ice nuclei

concentrations, Atmos. Chem. Phys., 14, 5433–5449, https://doi.org/10.5194/acp-14-5433-2014, 2014.

Harrison, A. D., Whale, T. F., Rutledge, R., Lamb, S., Tarn, M. D., Porter, G. C. E., Adams, M. P., McQuaid, J. B., Morris, G. J., and Murray, B. J.: An instrument for quantifying heterogeneous ice nucleation in multiwell plates using infrared emissions to detect freezing, Atmos. Meas. Tech., 11, 5629–5641, https://doi.org/10.5194/amt-11-5629-2018, 2018.

Hegg, D. A. and Hobbs, P. V: Measurements of sulfate production in natural clouds, Atmos. Environ., 16, 2663–2668, https://doi.org/10.1016/0004-6981(82)90348-1, 1982.

Hill, T. C. J., Moffett, B. F., DeMott, P. J., Georgakopoulos, D. G., Stump, W. L., and Franc, G. D.: Measurement of ice nucleation-active bacteria on plants and in precipitation by quantitative PCR, Appl. Environ. Microbiol., 80, 1256–1267, https://doi.org/10.1128/AEM.02967-13, 2014.

Hill, T. C. J., DeMott, P. J., Tobo, Y., Fröhlich-Nowoisky, J., Moffett, B. F., Franc, G. D., and Kreidenweis, S. M.: Sources of organic ice nucleating particles in soils, Atmos. Chem. Phys., 16, 7195–7211, https://doi.org/10.5194/acp-16-7195-2016, 2016.

Hoose, C., Kristjánsson, J. E., Chen, J.-P., and Hazra, A.: A Classical-Theory-Based Parameterization of Heterogeneous Ice Nucleation by Mineral Dust, Soot, and Biological Particles in a Global Climate Model, J. Atmos. Sci., 67, 2483–2503, https://doi.org/10.1175/2010JAS3425.1, 2010.

Jackson, G. A. and Burd, A. B.: Aggregation in the Marine Environment, Environ. Sci. Technol., 32, 2805–2814, https://doi.org/10.1021/es980251w, 1998.

Joyce, R. E., Lavender, H., Farrar, J., Werth, J. T., Weber, C. F., D'Andrilli, J., Vaitilingom, M., and Christner, B. C.: Biological Ice-Nucleating Particles Deposited Year-Round in Subtropical Precipitation, Appl. Environ. Microbiol., 85, e01567-19, https://doi.org/10.1128/AEM.01567-19, 2019.

Kanji, Z. A., Ladino, L. A., Wex, H., Boose, Y., BurkertKohn, M., Cziczo, D. J., and Krämer, M.: Overview of Ice Nucleating Particles, Meteorol. Monogr., 58, 1.1–1.33, https://doi.org/10.1175/AMSMONOGRAPHS-D-16-0006.1, 2017.

Kulmala, M., Laaksonen, A., J.Charlson, R., and Korhonen, P.: Clouds without supersaturation, Nature, 388, 336–337, https://doi.org/10.1038/41000, 1997.

Levin, E. J. T., DeMott, P. J., Suski, K. J., Boose, Y., Hill, T. C. J., McCluskey, C. S., Schill, G. P., Rocci, K., Al-Mashat, H., Kristensen, L. J., Cornwell, G., Prather, K., Tomlinson, J., Mei, F., Hubbe, J., Pekour, M., Sullivan, R., Leung, L. R., and Kreidenweis, S. M.:

Characteristics of Ice Nucleating Particles in and Around California Winter Storms, J. Geophys. Res.-Atmos., 124, 11530–11551, https://doi.org/10.1029/2019JD030831, 2019.

Lim, Y. B., Tan, Y., Perri, M. J., Seitzinger, S. P., and Turpin, B. J.: Aqueous chemistry and its role in secondary organic aerosol (SOA) formation, Atmos. Chem. Phys., 10, 10521–10539, https://doi.org/10.5194/acp-10-10521-2010, 2010.

Lohmann, U.: A glaciation indirect aerosol effect caused by soot aerosols, Geophys. Res. Lett., 29, 11–14, https://doi.org/10.1029/2001GL014357, 2002.

Lohmann, U. and Feichter, J.: Global indirect aerosol effects: a review, Atmos. Chem. Phys., 5, 715–737, https://doi.org/10.5194/acp-5-715-2005, 2005.

Martin, A. C., Cornwell, G., Beall, C. M., Cannon, F., Reilly, S., Schaap, B., Lucero, D., Creamean, J., Ralph, F. M., Mix, H. T., and Prather, K.: Contrasting local and long-range-transported warm ice-nucleating particles during an atmospheric river in coastal California, USA, Atmos. Chem. Phys., 19, 4193–4210, https://doi.org/10.5194/acp-19-4193-2019, 2019.

Mason, R. H., Chou, C., McCluskey, C. S., Levin, E. J. T., Schiller, C. L., Hill, T. C. J., Huffman, J. A., DeMott, P. J., and Bertram, A. K.: The micro-orifice uniform deposit impactor–droplet freezing technique (MOUDI-DFT) for measuring concentrations of ice nucleating particles as a function of size: improvements and initial validation, Atmos. Meas. Tech., 8, 2449– 2462, https://doi.org/10.5194/amt-8-2449-2015, 2015.

Mazur, P.: Freezing of living cells: mechanisms and implications, Am. J. Physiol. Physiol., 247, C125–C142, https://doi.org/10.1152/ajpcell.1984.247.3.C125, 1984.

McCluskey, C. S., Hill, T. C. J., Sultana, C. M., Laskina, O., Trueblood, J., Santander, M. V, Beall, C. M., Michaud, J. M., Kreidenweis, S. M., Prather, K. A., Grassian, V., and DeMott, P. J.: A Mesocosm Double Feature: Insights into the Chemical Makeup of Marine Ice Nucleating Particles, J. Atmos. Sci., 75, 2405– 2423, https://doi.org/10.1175/JAS-D-17-0155.1, 2018.

McElfresh, C., Harrington, T., and Vecchio, K. S.: Application of a novel new multispectral nanoparticle tracking technique, Meas. Sci. Technol., 29, 65002, https://doi.org/10.1088/1361- 6501/aab940, 2018.

Michaud, A. B., Dore, J. E., Leslie, D., Lyons, W. B., Sands, D. C., and Priscu, J. C.: Biological ice nucleation initiates hailstone formation, J. Geophys. Res.-Atmos., 119, 12186–12197, https://doi.org/10.1002/2014JD022004, 2014.

Perkins, R. J., Gillette, S. M., Hill, T. C. J., and DeMott, P. J.: The Labile Nature of Ice Nucleation

by Arizona Test Dust, ACS Earth Sp. Chem., 4, 133–141, https://doi.org/10.1021/acsearthspacechem.9b00304, 2020.

Petters, M. D. and Wright, T. P.: Revisiting ice nucleation from precipitation samples, Geophys. Res. Lett., 42, 8758–8766, https://doi.org/10.1002/2015GL065733, 2015.

Polen, M., Lawlis, E., and Sullivan, R. C.: The unstable ice nucleation properties of Snomax® bacterial particles, J. Geophys. Res.-Atmos., 121, 11666–11678, https://doi.org/10.1002/2016JD025251, 2016.

Rangel-Alvarado, R. B., Nazarenko, Y., and Ariya, P. A.: Snow-borne nanosized particles: Abundance, distribution, composition, and significance in ice nucleation processes, J. Geophys. Res.-Atmos., 120, 11760–11774, https://doi.org/10.1002/2015JD023773, 2015.

Rogers, D. C., DeMott, P. J., Kreidenweis, S. M., and Chen, Y.: Measurements of ice nucleating aerosols during SUCCESS, Geophys. Res. Lett., 25, 1383, https://doi.org/10.1029/97GL03478, 1998.

Schnell, R. C.: Ice Nuclei in Seawater, Fog Water and Marine Air off the Coast of Nova Scotia: Summer 1975, J. Atmos. Sci., 34, 1299–1305, https://doi.org/10.1175/1520-0469(1977)034¡1299:INISFW¿2.0.CO;2, 1977.

Stopelli, E., Conen, F., Zimmermann, L., Alewell, C., and Morris, C. E.: Freezing nucleation apparatus puts new slant on study of biological ice nucleators in precipitation, Atmos. Meas. Tech., 7, 129–134, https://doi.org/10.5194/amt-7-129-2014, 2014.

Stopelli, E., Conen, F., Morris, C. E., Herrmann, E., Bukowiecki, N., and Alewell, C.: Ice nucleation active particles are efficiently removed by precipitating clouds, Sci. Rep., 5, 16433, https://doi.org/10.1038/srep16433, 2015.

Stopelli, E., Conen, F., Guilbaud, C., Zopfi, J., Alewell, C., and Morris, C. E.: Ice nucleators, bacterial cells and Pseudomonas syringae in precipitation at Jungfraujoch, Biogeosciences, 14, 1189–1196, https://doi.org/10.5194/bg-14-1189-2017, 2017.

Tan, I., Storelvmo, T., and Zelinka, M. D.: Observational constraints on mixed-phase clouds imply higher climate sensitivity, Science, 352, 224–227, https://doi.org/10.1126/science.aad5300, 2016. Vali, G.: Sizes of Atmospheric Ice Nuclei, Nature, 212, 384–385, https://doi.org/10.1038/212384a0, 1966.

Vali, G.: Freezing Nucleus Content of Hail and Rain in Alberta, J. Appl. Meteorol., 10, 73–78, 1971.

Vali, G.: Comments on "Freezing Nuclei Derived from Soil Particles," J. Atmos. Sci., 31,

1457–1459, https://doi.org/10.1175/1520- 0469(1974)031¡1457:CONDFS¿2.0.CO;2, 1974.

Vasebi, Y., Mechan Llontop, M. E., Hanlon, R., Schmale III, D. G., Schnell, R., and Vinatzer, B. A.: Comprehensive characterization of an aspen (Populus tremuloides) leaf litter sample that maintained ice nucleation activity for 48 years, Biogeosciences, 16, 1675–1683, https://doi.org/10.5194/bg-16-1675-2019, 2019.

Wex, H., Augustin-Bauditz, S., Boose, Y., Budke, C., Curtius, J., Diehl, K., Dreyer, A., Frank, F., Hartmann, S., Hiranuma, N., Jantsch, E., Kanji, Z. A., Kiselev, A., Koop, T., Möhler, O., Niedermeier, D., Nillius, B., Rösch, M., Rose, D., Schmidt, C., Steinke, I., and Stratmann, F.: Intercomparing different devices for the investigation of ice nucleating particles using Snomax® as test substance, Atmos. Chem. Phys., 15, 1463– 1485, https://doi.org/10.5194/acp-15-1463-2015, 2015.

Wex, H., Huang, L., Zhang, W., Hung, H., Traversi, R., Becagli, S., Sheesley, R. J., Moffett, C. E., Barrett, T. E., Bossi, R., Skov, H., Hünerbein, A., Lubitz, J., Löffler, M., Linke, O., Hartmann, M., Herenz, P., and Stratmann, F.: Annual variability of ice-nucleating particle concentrations at different Arctic locations, Atmos. Chem. Phys., 19, 5293–5311, https://doi.org/10.5194/acp-19-5293-2019, 2019.

Whale, T. F., Murray, B. J., O'Sullivan, D., Wilson, T. W., Umo, N. S., Baustian, K. J., Atkinson, J. D., Workneh, D. A., and Morris, G. J.: A technique for quantifying heterogeneous ice nucleation in microlitre supercooled water droplets, Atmos. Meas. Tech., 8, 2437–2447, https://doi.org/10.5194/amt-8-2437-2015, 2015.

Wilson, T. W., Ladino, L. A., Alpert, P. A., Breckels, M. N., Brooks, I. M., Browse, J., Burrows, S. M., Carslaw, K. S., Huffman, J. A., Judd, C., Kilthau, W. P., Mason, R. H., McFiggans, G., Miller, L. a., Nájera, J. J., Polishchuk, E., Rae, S., Schiller, C. L., Si, M., Temprado, J. V., Whale, T. F., Wong, J. P. S., Wurl, O., Yakobi-Hancock, J. D., Abbatt, J. P. D., Aller, J. Y., Bertram, A. K., Knopf, D. A., and Murray, B. J.: A marine biogenic source of atmospheric ice-nucleating particles, Nature, 525, 234–238, https://doi.org/10.1038/nature14986, 2015.

Wright, T. P., Hader, J. D., McMeeking, G. R., and Petters, M. D.: High relative humidity as a trigger for widespread release of ice nuclei, Aerosol Sci. Tech., 48, i–v, https://doi.org/10.1080/02786826.2014.968244, 2014.

Yang, J., Wang, Z., Heymsfield, A. J., DeMott, P. J., Twohy, C. H., Suski, K. J., and Toohey, D. W.: High ice concentration observed in tropical maritime stratiform mixed-phase clouds with top temperatures warmer than -8 °C, Atmos. Res., 233, 104719, https://doi.org/10.1016/j.atmosres.2019.104719, 2020.

3.8 Supplement

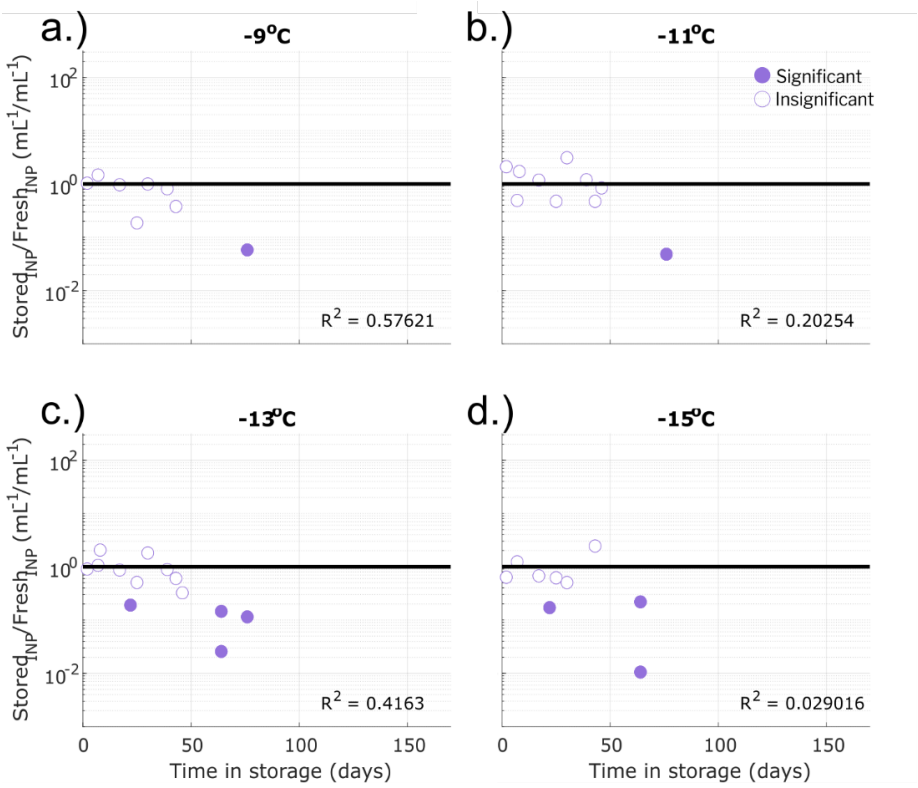

Figure 3.5: Changes in INP concentration in untreated precipitation samples stored between 1 and 76 days at room temperature (+21-23 °C). Stored sample frozen well fractions that passed Fishers Exact Test ($p < 0.01$) for significant differences from original fresh sample frozen well fractions are indicated with filled markers. R^2 values for linear fits are shown for each INP freezing temperature bin with >3 samples. Results show moderate correlation between storage time interval and INP losses for freezing temperatures ≥ -9 °C.

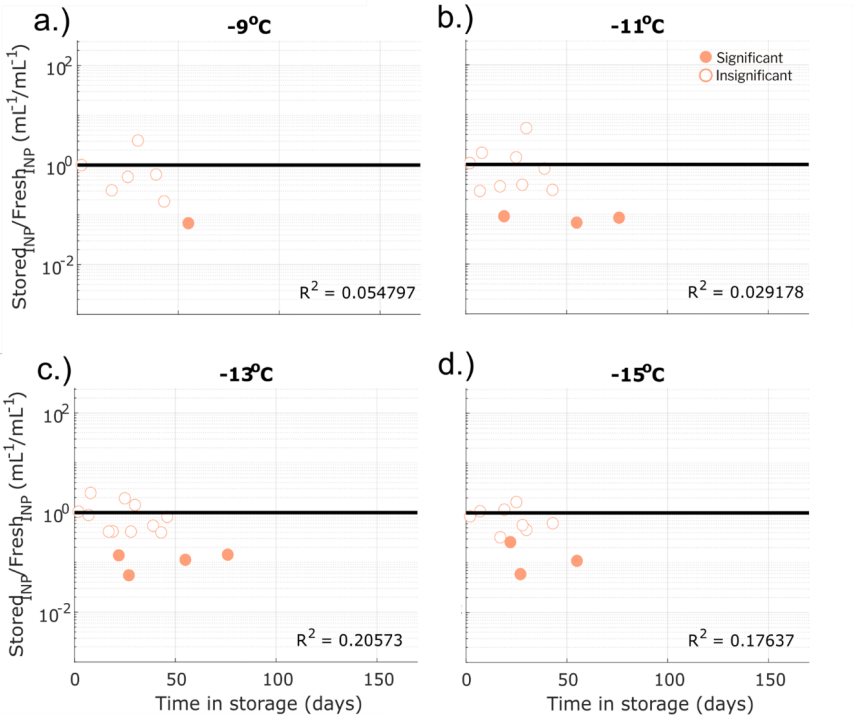

Figure 3.6: Changes in INP concentration in untreated precipitation samples stored between 1 and 76 days at +4 °C. Stored sample frozen well fractions that passed Fishers Exact Test ($p < 0.01$) for significant differences from original fresh sample frozen well fractions are indicated with filled markers. R^2 values for linear fits are shown for each INP freezing temperature bin with > 3 samples. Results show lack of correlation between storage time interval and changes in INP concentrations.

Table 3.7: Summary of previously reported precipitation sample storage conditions for offline analysis of INPs.

Publication	Storage temperature (°C)	Total storage time	Other details
1. Vali G. Sizes of Atmospheric Ice Nuclei. Nature. 1966;212(5060):384–5	unspecified	unspecified	

2. Vali G. Freezing Nucleus Content of Hail and Rain in Alberta. J Appl Meteorol. 1971 Jan 23;10(1):73–8.	−80	unspecified	
3. Christner BC, Morris CE, Foreman CM, Cai R, Sands DC. Ubiquity of Biological Ice Nucleators in Snowfall. Science (80-). 2008 Feb 29;319(5867):1214 LP – 1214.	variable	unspecified	Stored snow samples in coolers embedded in snowpack, then retrieved and archived in a −20 ºC freezer, unspecified storage time
4. Christner BC, Cai R, Morris CE, McCarter KS, Foreman CM, Skidmore ML, et al. Geographic, seasonal, and precipitation chemistry influence on the abundance and activity of biological ice nucleators in rain and snow. Proc Natl Acad Sci U S A. 2008;105(48):18854–9.	+4	18 hours	

5. Morris CE, Sands DC, Vinatzer BA, Glaux C, Guilbaud C, Buffière A, et al. The life history of the plant pathogen Pseudomonas syringae is linked to the water cycle. Isme J. 2008 Jan 10;2:321.	unspecified	unspecified	
6. Hill TCJ, Moffett BF, DeMott PJ, Georgakopoulos DG, Stump WL, Franc GD. Measurement of ice nucleation-active bacteria on plants and in precipitation by quantitative PCR. Appl Environ Microbiol. 2014;80(4):1256–67.	−20	unspecified	
7. Hader JD, Wright TP, Petters MD. Contribution of pollen to atmospheric ice nuclei concentrations. Atmos Chem Phys. 2014;14(11):5433–49.	−17	2 weeks	

8. Wright TP, Hader JD, McMeeking GR, Petters MD. High relative humidity as a trigger for widespread release of ice nuclei. Aerosol Sci Technol. 2014;48(11):i–v.	n/a	immediate processing	
9. Stopelli E, Conen F, Zimmermann L, Alewell C, Morris CE. Freezing nucleation apparatus puts new slant on study of biological ice nucleators in precipitation. Atmos Meas Tech. 2014;7(1):129–34.	+4	n/a	storage experiment on snow sample stored at +4 C over 30 days.
10. Michaud AB, Dore JE, Leslie D, Lyons WB, Sands DC, Priscu JC. Biological ice nucleation initiates hailstone formation. J Geophys Res Atmos. 2014;119(21):12,112-186,197.	-30	unspecified	thawing process prior to analysis: 18 hrs at +4 ºC.

11. Rangel-Alvarado RB, Nazarenko Y, Ariya PA. Snow-borne nanosized particles: Abundance, distribution, composition, and significance in ice nucleation processes. J Geophys Res Atmos. 2015;120(22):11,711-760,774.	−10 or −35	unspecified, many within 24 hours	
12. Santl-Temkiv T, Sahyoun M, Finster K, Hartmann S, Augustin-Bauditz S, Stratmann F, et al. Characterization of airborne ice-nucleation-active bacteria and bacterial fragments. Atmos Environ. 2015;109:105–17.	unspecified	unspecified	
13. Petters MD, Wright TP. Revisiting ice nucleation from precipitation samples. Geophys Res Lett. 2015;42(20):8758-66.	+4	0-35 days	

14. Stopelli E, Conen F, Morris CE, Herrmann E, Bukowiecki N, Alewell C. Ice nucleation active particles are efficiently removed by precipitating clouds. Sci Rep. 2015;5:16433.	n/a	processed immediately	
15. Hara K, Maki T, Kakikawa M, Kobayashi F, Matsuki A. Effects of different temperature treatments on biological ice nuclei in snow samples. Atmos Environ. 2016;140:415–9.	−10	unspecified	pre-concentrated samples prior to analysis
16. Stopelli E, Conen F, Guilbaud C, Zopfi J, Alewell C, Morris CE. Ice nucleators, bacterial cells and *Pseudomonas syringae* in precipitation at Jungfraujoch. Biogeosciences. 2017;14(5):1189-96.	n/a	processed immediately	

17. Failor KC, Schmale, D, Vinatzer BA, Monteil CL. Ice nucleation active bacteria in precipitation are genetically diverse and nucleate ice by employing different mechanisms. ISMEJ. 2017;11(12):2740-2573.	+4	unspecified	
18. Martin AC, Cornwell G, Beall CM, Cannon F, Reilly S, Schaap B, et al. Contrasting local and long-range-transported warm ice-nucleating particles during an atmospheric river in coastal California, USA. Atmos Chem Phys. 2019;19(7):4193-210.	−20	4 months	

19. Joyce RE, Lavender H, Farrar J, Werth JT, Weber CF, D'Andrilli J, et al. Biological Ice-Nucleating Particles Deposited Year-Round in Subtropical Precipitation. Stams AJM, editor. Appl Environ Microbiol. 2019 Dec 1;85(23):e01567-19.	+4	0 - 48 hours	
20. Creamean JM, Mignani C, Bukowiecki N, Conen F. Using freezing spectra characteristics to identify ice-nucleating particle populations during the winter in the Alps. Atmos Chem Phys. 2019;19(12):8123-40.	n/a	processed immediately	
21. David RO, Cascajo-Castresana M, Brennan KP, Rösch M, Els N, Werz J, et al. Development of the DRoplet Ice Nuclei Counter Zurich (DRINCZ): validation and application to field-collected snow samples. Atmos Meas Tech. 2019;12(12):6865-88.	−20	unspecified	snow thawed to room temperature (+20 ºC) before storing at −20 ºC

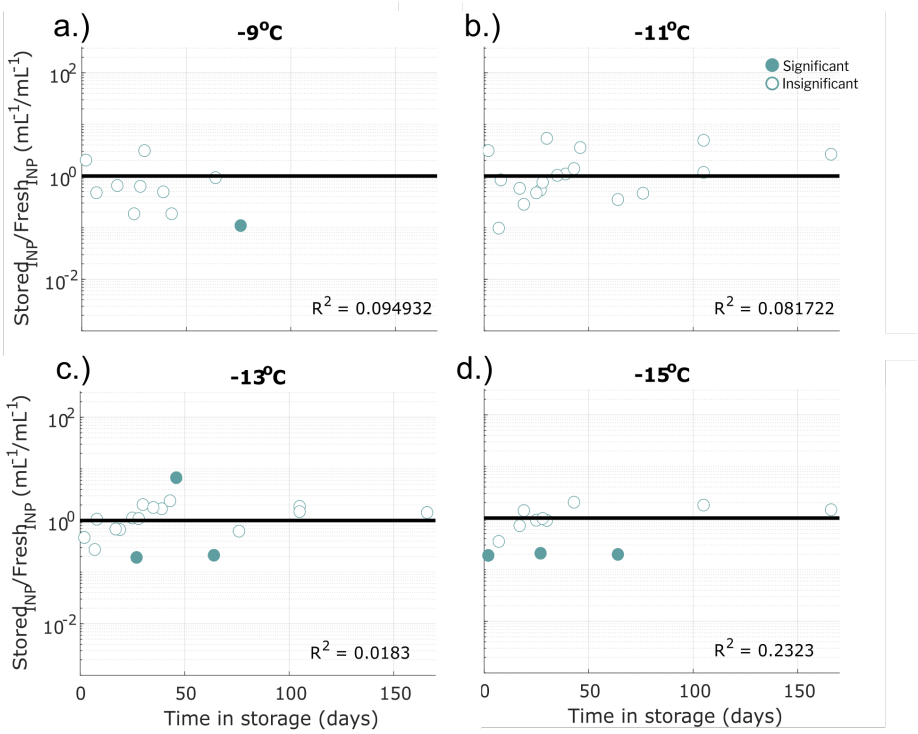

Figure 3.7: Changes in INP concentration in untreated precipitation samples stored between 1 and 76 days at -20 °C. Stored sample frozen well fractions that passed Fishers Exact Test ($p < 0.01$) for significant differences from original fresh sample frozen well fractions are indicated with filled markers. R^2 values for linear fits are shown for each INP freezing temperature bin with > 3 samples. Results show lack of correlation between storage time interval and changes in INP concentrations.

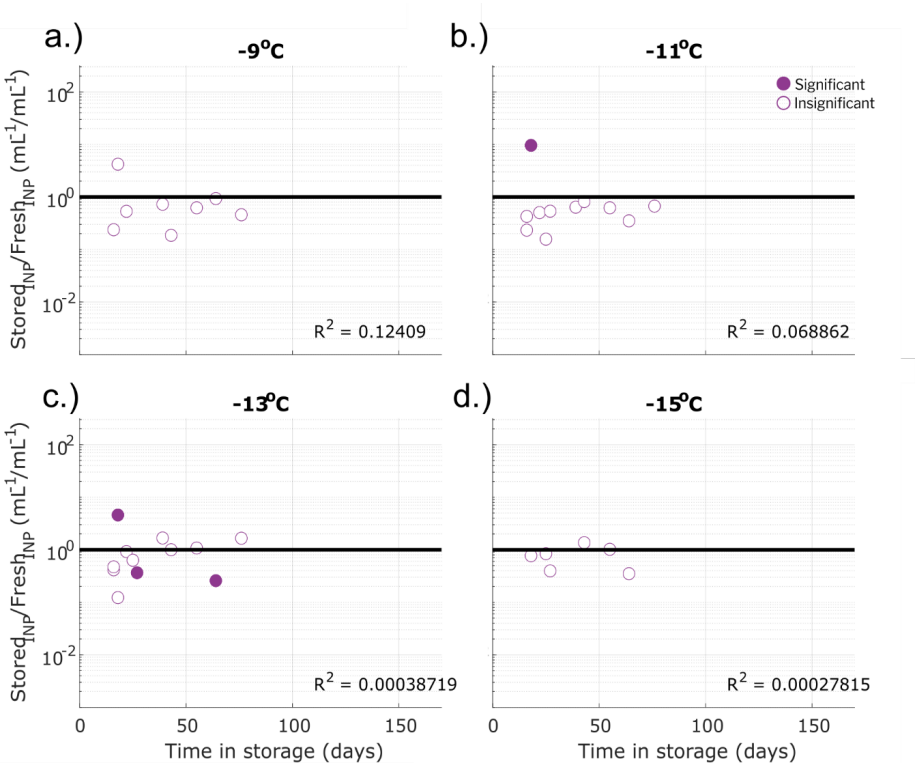

Figure 3.8: Changes in INP concentration in untreated precipitation samples stored between 1 and 76 days flash frozen with liquid nitrogen and stored at -20 °C. Stored sample frozen well fractions that passed Fishers Exact Test (p ¡ 0.01) for significant differences from original fresh sample frozen well fractions are indicated with filled markers. R2 values for linear fits are shown for each INP freezing temperature bin with >3 samples. Results show a lack of correlation between storage time interval and INP enhancements or losses.

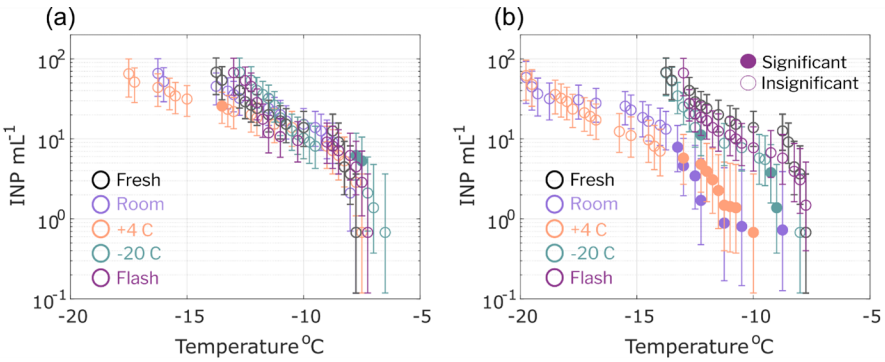

Figure 3.9: IN spectra of precipitation collected 1/19/2017, fresh and stored samples. IN spectra of stored samples are shown (a) 27 days and (b) 64 days after collection. Stored sample frozen well fractions that passed Fishers Exact Test ($p < 0.01$) for significant differences from original fresh sample frozen well fractions are indicated with filled markers. Results in (a), 27 days after collection, show INPs were generally insensitive to the various storage techniques. IN spectra of samples stored at room temperature and at +4 °C in (b) show significant losses in INP concentrations up to 1 order of magnitude from −10 to −20 ºC, indicating sensitivity to time in storage. Samples stored at −20 ºC or flash frozen were generally insensitive to storage and time interval.

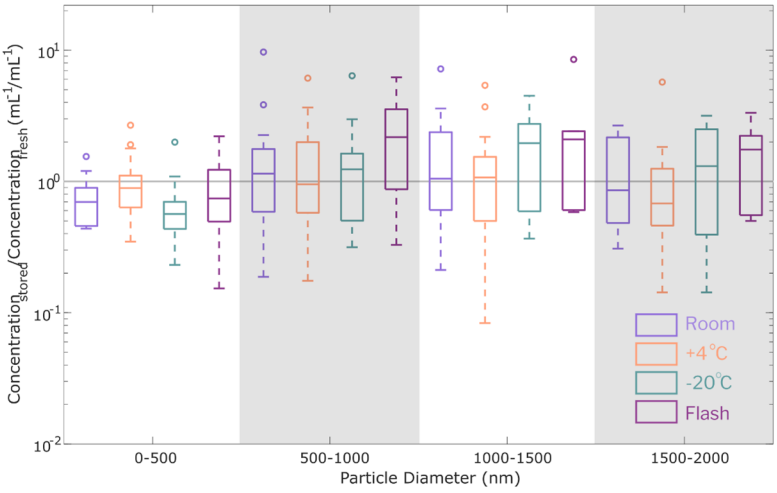

Figure 3.10: Distribution of total insoluble particle concentration ratios, stored:fresh, for 10 untreated precipitation samples (sampling periods 1-10, see Table 3.1).

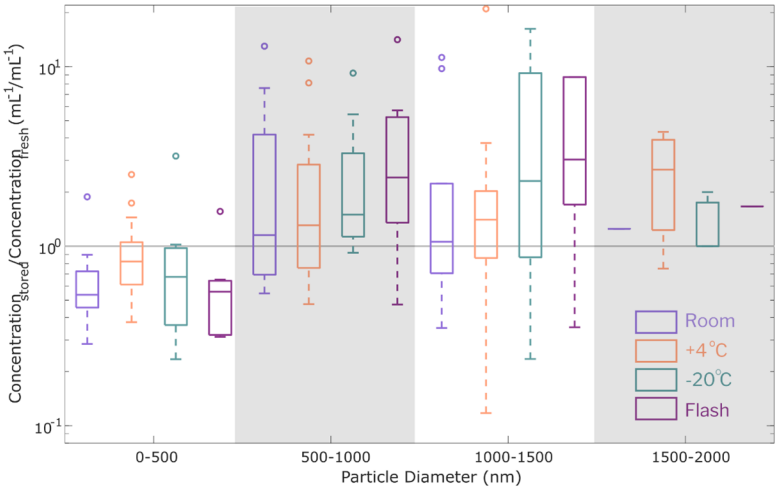

Figure 3.11: Distribution of total insoluble particle concentration ratios, stored:fresh, for 10 heat-treated precipitation samples (sampling periods 1-10, see Table 3.1).

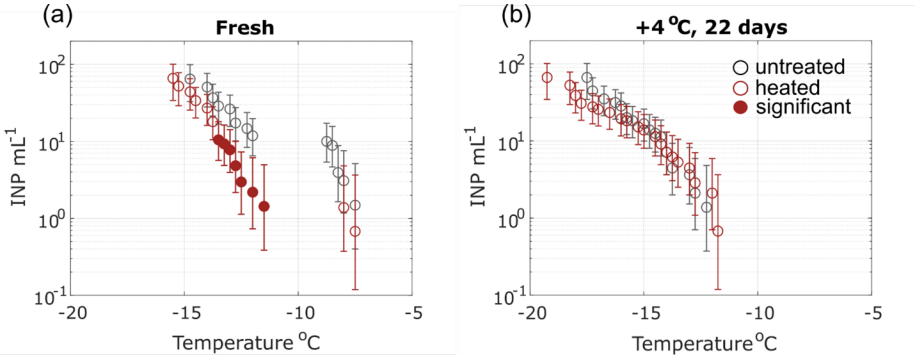

Figure 3.12: IN spectra of untreated and heat-treated precipitation collected 1/11/2017 for (a) a fresh sample and (b) a replicate stored at +4 °C for 22 days. Significant differences in frozen well fractions between the heat-treated and untreated sample (Fishers Exact Test, $p < 0.01$) are indicated with filled markers. Results in (a) indicate the presence of heat-labile (i.e. proteinaceous or cellular) INPs between −8 and −14 °C. However, results in (b) show a lack of heat-labile INPs and diminished concentrations overall, indicating losses of INPs in storage, including those that are heat-labile.).

Chapter 4

4 Cultivable halotolerant ice-nucleating bacteria and fungi in coastal precipitation

4.1 Abstract

Ice-nucleating particles (INPs) represent a rare subset of aerosol particles that initiate cloud droplet freezing at temperatures above the homogenous freezing point of water (–38 °C). Considering that the ocean covers 71 % of the Earth's surface and represents a large potential source of INPs, it is imperative that the identities, properties and relative emissions of ocean INPs become better understood. However, the specific underlying drivers of marine INP emissions remain largely unknown due to limited observations and the challenges associated with isolating rare INPs. By generating isolated nascent sea spray aerosol (SSA) over a range of biological conditions, mesocosm studies have shown that marine microbes can contribute to INPs. Here, we identify 14 (30 %) cultivable halotolerant ice-nucleating microbes and fungi among 47 total isolates recovered from precipitation and aerosol samples collected in coastal air in southern California. Ice-nucleating (IN) isolates collected in coastal air were nucleated ice from extremely warm to moderate freezing temperatures (–2:3 to –18 °C). While some Gammaproteobacteria

and fungi are known to nucleate ice at temperatures as high as –2 °C, *Brevibacterium* sp. is the first Actinobacteria found to be capable of ice nucleation at a relatively high freezing temperature (–2:3 °C). Air mass trajectory analysis demonstrates that marine aerosol sources were dominant during all sampling periods, and phylogenetic analysis indicates that at least 2 of the 14 IN isolates are closely related to marine taxa. Moreover, results from cell-washing experiments demonstrate that most IN isolates maintained freezing activity in the absence of nutrients and cell growth media. This study supports previous studies that implicated microbes as a potential source of marine INPs, and it additionally demonstrates links between precipitation, marine aerosol and IN microbes.

4.2 Introduction

Ice-nucleating particles (INPs) are rare aerosols, representing $\sim$ 1 in 10^5 or less of total particles in the free troposphere (Rogers et al., 1998) that induce freezing of cloud droplets at temperatures above the homogenous freezing point of water (–38 °C) and at relative humidities (RH) well below the homogenous freezing RH of aqueous solution droplets. They affect multiple climate-relevant properties of mixedphase and cold clouds. For example, in-cloud INP distributions can influence the ice-phase partitioning processes that determine clouds' reflectivity, lifetime and precipitation efficiency (Creamean et al., 2013; DeLeon-Rodriguez et al., 2013; Fröhlich-Nowoisky et al., 2016; Ladino et al., 2016). However, numerical representations of cloud ice processes challenge climate models across all scales (Curry et al., 2000; Furtado and Field, 2017; Kay et al., 2016; Klein et al., 2009; Prenni et al., 2007). It has been hypothesized that an enhanced understanding of marine and terrestrial INP populations lations could contribute to improved representation of ice processes in models (Seinfeld et al., 2016; Storelvmo, 2017; Kanji et al., 2017).

Despite recent evidence showing that sea spray aerosol (SSA) represents a source of

INPs (DeMott et al., 2016; McCluskey et al., 2016, 2018a, b), that these INPs can contribute significantly to total INP populations (particularly in remote marine regions where terrestrial aerosols are less abundant) (Burrows et al., 2013; Vergara-Temprado et al., 2017, 2018), and that specific parameterization of marine INPs can influence modeled radiative budgets (Wilson et al., 2015), little is known about the actual entities involved in forming marine INPs. Schnell and Vali (1975) were the first to associate phytoplankton blooms with increases in ice nucleation activity in seawater sampled shortly after a bloom in Bedford Basin, Nova Scotia. Recent mesocosm studies have linked SSA icenucleating (IN) activity specifically to the death phase of phytoplankton blooms. McCluskey et al. (2017) showed that increases in INP emissions corresponded to increased emissions of heterotrophic bacteria and the transfer of organic species in SSA, implicating microbes and biomolecules as contributors to marine INP populations. Marine microbes were further linked to INPs in McCluskey et al. (2018a): subsets of INPs in nascent SSA were found to be heat labile, with sizes greater than 0.2 μm, and INP emissions were found to be correlated with the increased emissions of cells or cellular material. An IN halotolerant strain of *Pseudomonas fluorescens* was detected in phytoplankton cultures derived from seawater (Fall and Schnell, 1985), and INPs have also been detected in seawater containing marine diatoms, green algae (Alpert et al., 2011; Junge and Swanson, 2008; Ladino et al., 2016; Parker et al., 1985) and sea-ice samples containing marine Antarctic bacteria (Junge and Swanson, 2008; Parker et al., 1985).

While indirect evidence indicates marine microbes and other biogenic entities as potential marine INPs, microbial contribution to marine INP populations has not yet been confirmed through direct observations (i.e., through isolation and identification in an atmospheric sample). Multiple factors make it difficult to determine INP origin, whether terrestrial or marine, including the low abundance of INPs and the diversity of aerosols that can ice nucleate (e.g., Kanji et al., 2017). However, cultivable IN microbes have been isolated from clouds and precipitation for decades (e.g., Sands et al., 1982; Failor et al., 2017; Morris et al., 2008), and the origins of

IN isolates can be determined by comparing sequences with reference isolates of known origin. There are several caveats to consider when inferring in-cloud INP concentrations or properties from precipitation samples (Petters and Wright, 2015), including "sweep-out" of additional INPs as the hydrometeor traverses the atmosphere below the cloud (Vali, 1974). However, previous studies have derived estimates of in-cloud INP concentrations and origins from the concentrations and identities of IN microbes from ground-level collections (Christner et al., 2008; Failor et al., 2017a; Joyce et al., 2019; Monteil et al., 2014) by assuming that particles in precipitation originate from the cloud rather than the atmospheric column through which the hydrometeor descended. This assumption is supported by Vali (1971), who found that sub-cloud scavenging of aerosol did not affect INPs observed in precipitation collected at the surface in comparisons of INP spectra from surface samples with samples collected at cloud base. Furthermore, Wright et al. (2014) estimated that sweep-out contributed between 1.2 % and 14 % of INPs suspended in a precipitation sample collected at the surface.

While evidence exists for relationships between IN microbes and precipitation in terrestrial systems, studies on the relationship between marine INPs, marine microbes and precipitation remain quite limited. Here, we report the identities and freezing temperatures of 14 cultivable halotolerant IN species derived from marine and coastal precipitation and aerosol samples. Over the course of 11 precipitation events during an El Niño season, 47 cultivable halotolerant bacteria and fungi were recovered from aerosol and precipitation samples collected in a coastal subtropical climate in southern California. Bacterial and fungal species were isolated, identified and tested for ice nucleation behavior from 0 to –25 °C using an immersion-mode droplet freezing assay technique. Precipitating cloud altitudes and isolate source regions were estimated using the High-Resolution Rapid Refresh (HRRR) atmospheric model and the FLEXible PARTicle (FLEXPART) dispersion model (Stohl et al., 1998), respectively. Finally, the effect of media on the observed IN behavior of isolates was investigated through cell-washing experiments.

4.3 Methods

4.3.1 Precipitation and aerosol sample collection methods

Precipitation and ambient aerosol samples were collected on the Ellen Browning Scripps Memorial Pier at Scripps Institution of Oceanography (SIO; 32.8662° N, 117.2544° W) from 6 March to 6 May 2016. Sampling took place in the surf 8 m above Mean Lower Low Water (MLLW), and samples were only collected during westerly winds. Aerosol samples were collected over 1.5–5 h periods on polycarbonate filters (45 mm diameter, 0.2 μm pore size; Whatman® Nuclepore, Chicago, Illinois, USA) placed in open-face Nalgene® analytical filter units (Waltham, Massachusetts, USA). Prior to sampling, filters were pretreated for decontamination by soaking in 10 % H_2O_2 for 10 min and rinsing them three times with ultrapure water. Background levels of INPs from the sample handling processes were estimated using INP concentrations in aerosol sample field blanks assuming the average sampling volume (2270 L). Estimated INP concentrations across the three field blanks ranged between 0 and 0.1 L^{-1} at –20 °C (see Fig. S1). After collection, aerosol filters were placed in 50 mL sterile plastic Falcon® tubes (Corning Life Sciences, Corning, NY, USA) and immersed in 12 mL of ultrapure water using sterile polypropylene forceps that were pretreated using the 10 % H_2O_2 process described above. The samples were then hand shaken for 20 min to resuspend particles from the filter. The precipitation samples were collected using a modified Teledyne ISCO fullsize portable sampler (Lincoln, Nebraska, USA), fitted with twenty-four 1 L polypropylene bottles. Prior to sampling, the bottles were immersed in 10 % hydrogen peroxide for 10 min and then rinsed three times with ultrapure water. The automated sampler would engage when triggered by precipitation of at least 0.13 cm h^{-1} and would sample using the first of 24 bottles for 30 min; thereafter, it would switch bottles at hourly intervals. Within 1–2 h of sample collection, INP concentrations were measured using the Scripps Institution of Oceanography Automated Ice Spectrometer (SIO-AIS) (Beall et al., 2017), an automated offline freezing assay technique for measurement of immersion-mode

INPs. To decrease the effect of interstitial particle sweep-out by falling raindrops on the measured INP concentration, precipitation from the first 30 min was discarded. Sweep-out effects have been estimated to contribute between 1.2 % and 14 % to measured concentrations of INP in a precipitation sample (Wright et al., 2014).

The INP measurement technique is described in detail in Beall et al. (2017). Briefly, the precipitation samples and aerosol sample suspensions were distributed in twentyfour to thirty 50 μL aliquots into a clean 96-well disposable polypropylene sample tray. An equal number and volume of aliquots of ultrapure water accompany each sample in the disposable tray as control for contamination from the loading and/or ultrapure water. The sample trays were then inserted into an aluminum block that is cooled until the samples are frozen. Cumulative INP number concentrations per temperature per volume are calculated using the fraction (f) of unfrozen wells per given temperature interval:

$$INP = \frac{-ln(f)}{V_d} \tag{4.1}$$

where V_d is the volume of the sample in each well. For aerosol filter samples, cumulative INP number concentrations are calculated using the ratio of the volume used for resuspension of the particles (V_{re}) to the volume of aerosol sampled (V_A):

$$INP = \frac{-ln(f) \cdot V_{re}}{V_d \cdot V_A} \tag{4.2}$$

The fraction of unfrozen wells (f) is adjusted for contamination by subtracting the number of frozen ultrapure water wells per temperature interval from both the total number of unfrozen wells and total wells of the sample. For this study, thirty 50 μL droplets were deposited into the droplet assay, The fraction of unfrozen wells (f) is adjusted for contamination by subtracting the number of frozen ultrapure water wells per temperature interval from both the total number of unfrozen wells and total wells of the sample. For this study, thirty 50 μL droplets were deposited

into the droplet assay yielding a detection limit of 0.675 INPs per milliliter of liquid.

Within 1–2 h of collection, precipitation and aerosol samples were also inoculated in 5 mL ZoBell growth media (ZoBell, 1947; 5 g peptone, 1 g yeast extract per 1 L of filtered (0.22 μm) autoclaved seawater) and grown under ambient conditions (21–24 °C). Seawater was collected at the Ellen Browning Scripps Memorial Pier and was filtered prior to autoclaving. INP concentrations in ZoBell enrichments were measured 1 d post inoculation and for several days thereafter to monitor for sustained IN activity.

4.3.2 Bacterial and fungal isolation and characterization

Precipitation and SSA microorganisms were cultivated using the ZoBell enrichment described above (ZoBell, 1947) (Fisher Scientific, Houston, Texas, USA). Isolation was performed by successive plating on ZoBell agar (BD Bacto™ Agar, Sparks, MD, USA). Liquid cultures were inoculated from single colonies and grown to the late exponential phase. DNA was extracted from liquid cultures of isolates after an overnight lysis with proteinase K (100 μg mL^{-1}) and lysozyme (5 mg mL^{-1}) (MilliporeSigma, Burlington, Massachusetts, USA) (Boström et al., 2004) using a QIAamp® kit (QIAGEN, Hilden, Germany). The V4 region of the 16S rRNA gene was amplified using 515F (5' GTGYCAGCMGCCGCGGTAA 3') and 926R (5' CCGYCAATTCMTTTRAGT 3') primers (Walters et al., 2015). The PCR reaction contained 0.5 ng μL^{-1} genomic DNA, 0.2 μM of each primer, and one KAPA HiFi HotStart ReadyMix (KAPA Biosystems, KK2601), and the thermocycler was set to the following program: 95 °C for 30 s; 25 cycles of 95 °C for 30 s, 55 °C for 30 s and 72 °C for 30 s; 72 °C for 5 min. PCR products were purified using a GenElute™ PCR clean-up kit (MilliporeSigma). The sequences of the amplified 16S rRNA gene fragments were determined by Sanger sequencing (Retrogen Inc., San Diego, CA). Taxonomic assignments were determined from 16S rRNA gene sequences using the SILVA Incremental Aligner (SINA) (Pruesse et al., 2012) and the Basic Local Alignment Search Tool (BLAST) (https://www.ncbi.nlm.nih.gov/, last access: 1 May 2019). SINA aligns sequences to the SILVA

database of rRNA genes using a combination of k-mer searching and partial order matching. Additionally, individual sequences were inspected using BLAST, and species identities were determined by >97 % sequence identity to reference rRNA sequences. The primers were specific to bacterial 16S rRNA gene sequences and were additionally able to capture some 18S fungal sequences. Primers specific to 18S rRNA were not used.

To assess for duplicate isolates within the sampling period, 16S rDNA sequences were compared. Sequences within the same genus were adjusted and aligned in DECIPHER (Alignseqs(), AdjustAlignment() with default settings) (Wright, 2015). DECIPHER uses an iterative process for multiple sequence alignment where two sequences are aligned and merged, and each successive sequence is added until all sequences are aligned. These sequence alignments were used to generate phylogenetic trees using ClustalW2 (the UPGMA method) (McWilliam et al., 2013) and visualized with the Interactive Tree Of Life (iTOL; Letunic and Bork, 2011). Alignments were not manually trimmed or adjusted prior to tree construction. Branch distances were used to evaluate sequence similarity. As the sequences resulting from rRNA amplification often covered unequal spans and had unequal lengths, their alignments often resulted in overestimates of tree distances (average mutations per base pair). This error was not seen in original taxonomic assignment where alignment of one sequence to a reference sequence in the database was more successful. To facilitate comparisons between organisms assigned to the same genus, identity assignments including divisions at distances ¿0:1 (e.g., 1, 2, 3 ...) were further subdivided by distances >0.01 (e.g., 1a, 1b, 1c ...). Nonzero distances < 0.01 were given sub-labels (e.g., 1a1, 1a2 ...). Zero distances were given identical labels. In consideration of overestimations of tree distances and the risk of overreporting the numbers of isolates found, we applied more conservative criteria for the removal of potential duplication of the same isolate instead of only considering 100 % identical sequences. Distances < 0.01 were determined to be possible duplicates if they were collected during the same sampling period unless the organisms had a different phenotype generally indicated by different pigmentation. Each duplicate was tested for its IN ability, and the

results are reported in Supplementary Table 4.2. If the duplicates had the same IN properties, only one representative isolate was retained, and the rest were discarded. Maximum likelihood phylogenetic trees were computed in MEGA7 (Tamura et al., 2013) after ClustalW alignment with reference sequences (https://www.ncbi.nlm.nih.gov/, last access: 18 May 2020).

4.3.3 Storm and aerosol source characterization methods

Cloud altitudes at the time of precipitation sample collection were estimated using the High-Resolution Rapid Refresh (HRRR) model. The altitudes and pressure levels of clouds were assumed to be located where the RH was $>$ 95 %–100 % in the model. The specific RH criteria applied to each sampling period are provided in Table S2. HRRR model output was compared with surface RH measurements from the SIO pier weather station during sampling periods, and the predicted RH was found to agree with observations with a root mean square error (RMSE) of $<$ 10 %–15 %, which aligns closely with previously reported RH accuracies over the continental USA (Benjamin et al., 2016). Three altitudes of the estimated cloud top, middle and bottom were used as release points for FLEXPART 10 d Lagrangian backward trajectories. Back trajectories were used to identify potential sources of INPs in the precipitation samples as well as to indicate potential sources of land-based contamination in aerosol and precipitation samples due to local wind patterns or land–sea breezes. Satellite composites from the National Weather Service Weather Prediction Center's North American Surface Analysis products were used for synoptic weather analysis to generally characterize meteorology during each rain event (see Supplementary Table 4.4).

4.3.4 Isolate IN activity measurement and controls

To measure the IN activity of each isolate, liquid cultures were grown to the late exponential phase. Growth was monitored by optical density (OD) (590 nm). INP concentrations

were measured as described in Sect. 4.3.1 in liquid cultures and compared to a ZoBell blank as a control. Isolate biomass was estimated from OD measurements using the distribution of OD to biomass conversion factors from Myers et al. (2013). As Myers et al. (2013) found, in a study of 17 diverse organisms, OD to biomass conversion factors ranged between 0.35 and 0.65 g DW OD^{-1} L^{-1} (where DW refers to dry weight); we assume that the INP per gram of biomass may be estimated from OD within a factor of 2. Thus, isolate INP concentrations as well as the upper and lower limits of the 95 % confidence intervals were scaled by $1/m$, where m is the mean, minimum or maximum value of the biomass conversion factor distribution from Myers et al. (2013), respectively (i.e., 0.5, 0.65 and 0.35 g DW OD^{-1} L^{-1}).

To investigate the effect of growth media on IN isolates, a subset of late exponential cultures were washed three times with filtered (0.22 μm) autoclaved seawater (FASW) by successive centrifugation and resuspension. The washing procedure removes everything that is water soluble as well as whole cells and insoluble molecules pellet upon centrifugation. INP measurements were taken as described within 2–4 h after the washing procedure and compared to sterile seawater controls (see Supplementary Fig. 4.6b, c).

As ZoBell growth media contained INPs at moderate to cold freezing temperatures (–13 to –25 °C; see Supplementary Fig. 4.6a), only isolates exhibiting INPs at significantly higher freezing temperatures (–2:3 to –15 °C) or at significantly higher concentrations than their respective ZoBell growth media sample were considered to be IN. The criterion for significance was chosen to be conservative: a data point along an isolate's measured IN spectrum was considered significant if there was no overlap between the 95 % binomial sampling confidence interval of the given data point (Agresti and Coull, 1998) and any ZoBell confidence interval within $\pm$2.2 °C, the maximum uncertainty in freezing temperature measurement due to heterogeneity in heat transfer rates across the instrument's droplet assay (Beall et al., 2017). This equates to a significance threshold of $p < 0.005$ (Krzywinski and Altman, 2013). The choice of $\pm$2.2 °C is likely conservative given that the average and maximum $\triangle T$ observed across the droplet assay when cooling from 0 to –25

°C in a study of 11 cooling cycles was 0.38 and 0.98 °C, respectively (and following this study, the addition of a second thermistor under the second sample tray decreased the observed $\triangle T$ to within thermistor uncertainty, $\pm$0.2 °C). The same criterion was applied to isolates washed and suspended in FASW as described above (Supplementary Fig. 4.6b, c). Many isolates were diluted with their respective media (ZoBell or FASW) to decrease opacity such that freezing events could successfully be detected by the camera; thus, their respective dilution factors were applied to both the INP concentrations measured in the isolate suspension and the INP concentrations measured in the FASW or ZoBell samples for the significance analysis (see Supplementary Figs. 4.6b, c and 4.7).

4.4 Results and discussion

4.4.1 Subtropical coastal storm properties and origins

Aerosol and rain samples were collected from a pier on the coast of La Jolla, California (32°52001.4" N, 117°15026.5" W) during an El Niño event spanning 11 precipitation sampling periods from 6 March to 7 May 2016 (Supplementary Table 4.4). Observations of INPs in precipitation generally fall within the bounds of previously reported INP concentrations from precipitation and cloud water samples (Fig. 1, gray shaded region, adapted from Petters and Wright, 2015). AIS measurement uncertainties are represented with 95 % binomial sampling intervals (Agresti and Coull, 1998). Observed freezing temperatures ranged from –6.5 to –22.0 °C, with concentrations up to the limit of testing at 10^5 INPs per liter of precipitation. Following the assumptions in Petters and Wright (2015) to estimate in-cloud INP concentrations from precipitation samples (i.e., condensed water content of 0.4 g m^{-3} air), observations of INP concentrations in fresh precipitation samples are additionally compared to studies on field measurements conducted in marine and coastal environments.

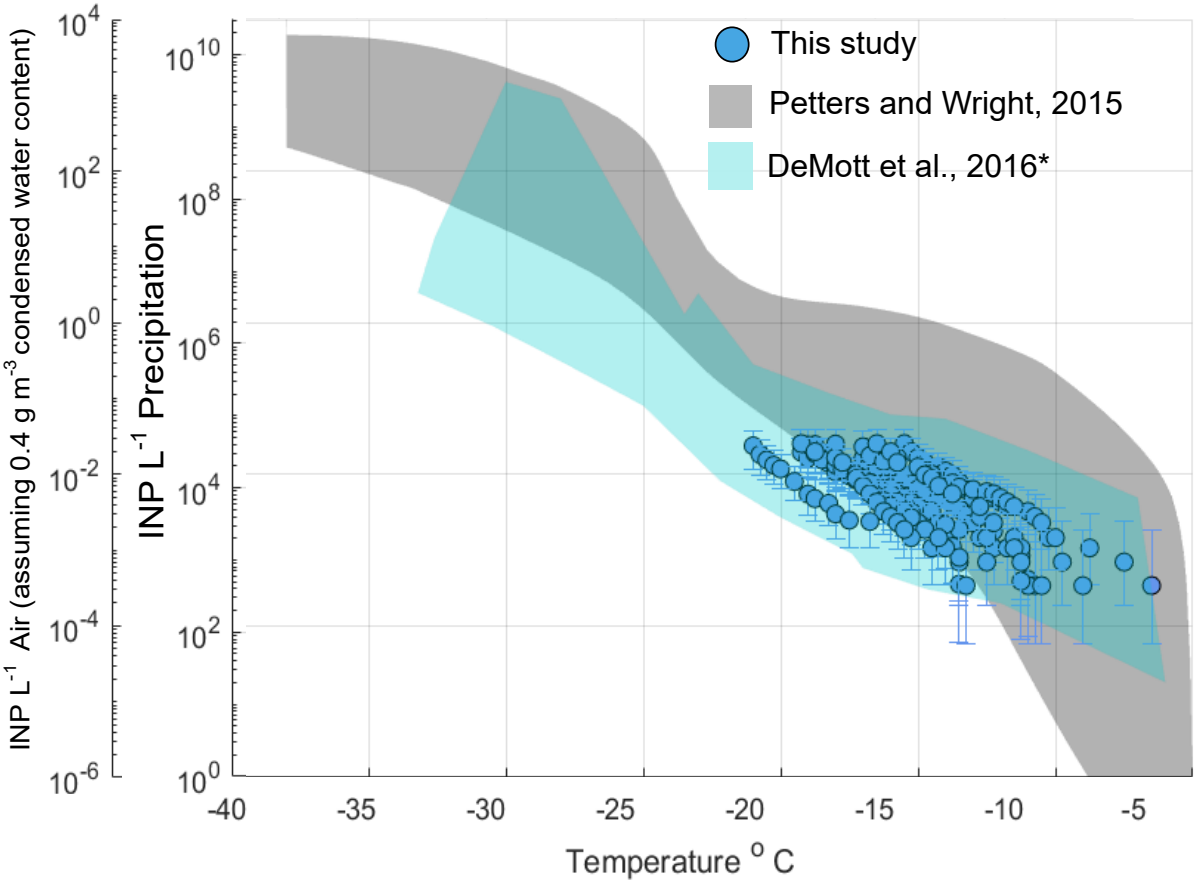

Figure 4.1: INP concentrations per liter precipitation and estimated in-cloud INP concentrations per volume of air in 11 precipitation samples collected at Scripps Institution of Oceanography Ellen Browning Scripps Memorial Pier (32.8662° N, 117.2544° W; La Jolla, California, USA) between March and May 2016. The gray shaded region indicates the spectrum of INP concentrations reported in nine previous studies on precipitation and cloud water samples collected from various seasons and locations worldwide, adapted from Fig. 1 in Petters and Wright (2015). The blue shaded region represents the composite spectrum of INP concentrations observed in a range of marine and coastal environments including the Caribbean, the eastern Pacific and the Bering Sea as well as laboratory-generated nascent sea spray (DeMott et al., 2016). ∗ DeMott et al. (2016) data have been updated with a complete dataset from the Ice in Clouds – Tropical (ICE-T) study, as shown in Yang et al. (2020).

Figure 4.1 shows that atmospheric INP concentration estimates compare well with INP concentrations observed in a range of marine and coastal environments, including the Caribbean, the eastern Pacific and the Bering Sea, as well as laboratory-generated nascent sea spray aerosol (DeMott et al., 2016). Observations of INPs in aerosol samples are shown in Supplementary Fig. 4.8 and are also comparable with those of DeMott et al. (2016).

The source regions of aerosols present in precipitating clouds were estimated using 10 d FLEXPART back trajectories (Fig. 4.2). For each of the 11 sampling periods, back trajectories show that the mid- to high-latitude Pacific Ocean was the primary source region for precipitating cloud layers. Periods 5 through 11 were additionally influenced by west coast continental sources (particularly periods 6 and 7). The 10 d back-trajectory simulations for aerosol samples similarly indicated that marine sources dominated (see Supplementary Fig. 4.5). Marine aerosols likely originated from regions near the coast (periods 2, 4–11, A1, A2 and A5) or in the mid-Pacific Ocean (periods 1 and 3), where trajectories descended below the marine boundary layer.

Cloud-bottom and cloud-top altitudes were estimated using the High-Resolution Rapid Refresh (HRRR) model, defined by the RH criteria in Table S2. Over the 11 precipitation sampling periods, cloud altitude ranged from 950 to 600 mbar, bottom to top, or from 500 to 4000 m, with temperatures ranging from 265 to 288 K.

4.4.2 Bacterial and fungal taxonomy

Cultivable bacteria and fungi were enriched from rain and aerosol samples in marine bacterial growth media, and strains were further isolated on marine agar. This resulted in a total of 47 isolates, 34 from rain samples and 13 from aerosol samples, with 29 unique genera as determined by $>$97 % sequence identity of 16S rDNA sequences to reference sequences using BLAST (Supplementary Table 4.2). The assignments by SINA agreed with the assignments by BLAST, although their sequence identities were lower in some cases (Supplementary Table 4.5). Many of the isolates derived from rain and aerosol were highly pigmented, as observed in other studies (Delort et al., 2017; Fahlgren et al., 2010, 2015; Hwang and Cho, 2011; Tong and Lighthart, 1997), presumably aiding their survival under high UV exposure (Supplementary Fig. 4.10). This pigmentation was especially prevalent in rain samples.

The taxonomy of the aerosol and rain isolates shows higher diversity in the precipitation samples (Supplementary Fig. 4.11 and Table 4.2), which may be due to artificial biases from low

aerosol isolate recovery or sweep-out of interstitial particles during raindrop descent. For example, sample handling may have decreased the isolate recovery rate from aerosol samples as cells were osmotically shocked during resuspension in ultrapure water (see Sect. 4.3.1). Decreased aerosol bacterial and fungal loads during rain events may have also contributed to lower isolate yield. INP concentration decreases in aerosol during precipitation events support this conclusion. For 3 of the 11 precipitation events featured in this study (see Supplementary Fig. 4.5), INP concentrations in aerosol were measured immediately before, during and after precipitation events. In each of the three events, INP concentrations in aerosol decreased below detection levels during precipitation and increased again soon after the end of the precipitation event (in under 24 h), although not beyond the concentrations observed prior to the precipitation event. Interestingly, these features (i.e., the observed decreased INP concentrations during precipitation events and the absence of increased INP concentrations within 24 h of precipitation events) are in opposition to multiple studies on INP concentrations during and after rainfall events in terrestrial systems (Bigg, 1958; Conen et al., 2017; Huffman et al., 2013; Prenni et al., 2013). Additionally, Levin et al. (2019) observed an increase in INP concentrations after precipitation events in a coastal environment, although this increase may have been related to a shift from marine to terrestrial aerosol sources as indicated by the back trajectories. Thus, results in this study indicate that the positive feedbacks between rainfall and surface INP emissions observed in terrestrial systems (Bigg et al., 2015; Morris et al., 2017) may not always apply to marine environments.

The rain samples had a high proportion of Actinobacteria, whereas Firmicutes and Proteobacteria were more dominant in aerosol. As Michaud et al. (2018) showed, Actinobacteria, as well as select Proteobacteria and Firmicutes, have an increased ability to be aerosolized from seawater in SSA emissions. Two isolates (one from rain and one from aerosol, 3.5 % of total isolates) are related to *Pantoea* sp., strains of which are known to possess IN proteins (e.g., Hill et al., 2014). *Pantoea* sp. and *Psychrobacter* sp. were the only bacterial taxa identified previously known to possess ice nucleation activity (Hill et al., 2014; Ponder et al., 2005). However,

both *Psychrobacter* sp. and *Idiomarina* sp. have been shown to be capable of inhibiting ice recrystallization, possibly through the production of antifreeze proteins (AFPs) which can both inhibit freezing at moderate temperatures and serve as INPs at colder temperatures (Wilson and Walker, 2010).

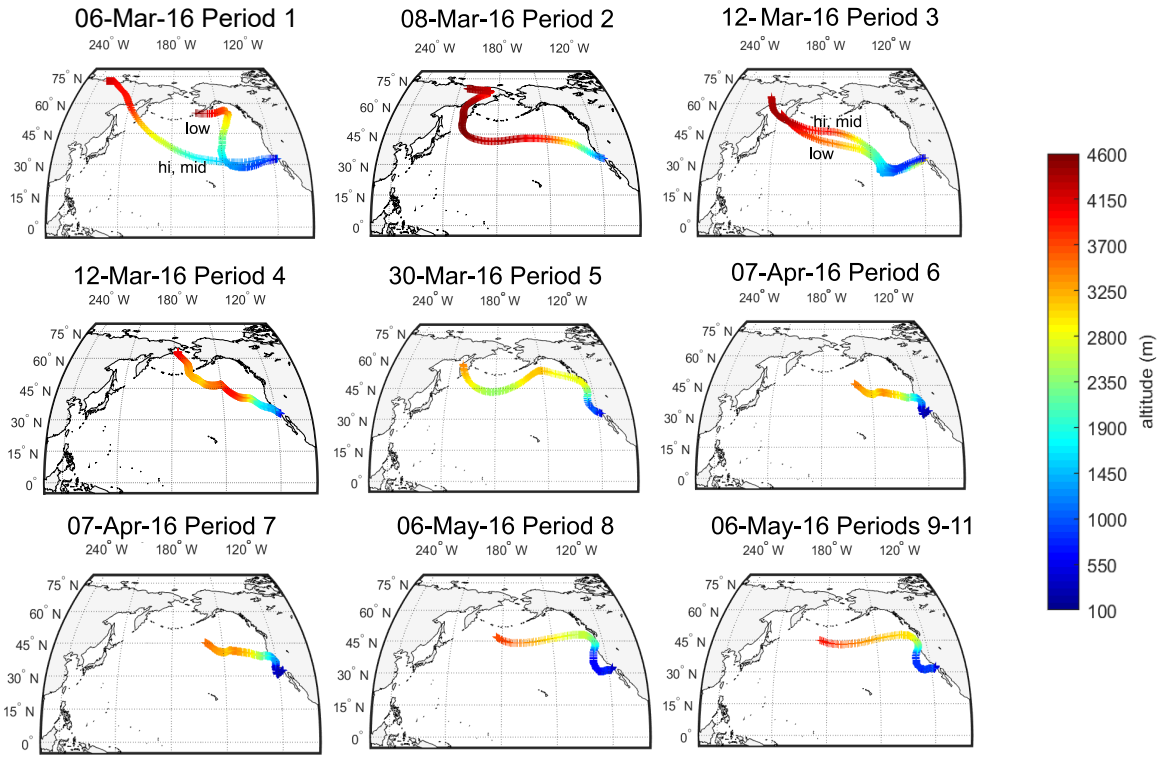

Figure 4.2: The 10 d back trajectories from cloud base, mid-cloud and cloud top during 11 precipitation sampling periods at the SIO pier (32.8662° N, 117.2544° W). FLEXPART back trajectories were used to estimate potential source regions of INPs to the clouds during precipitation events. Shown are the particle centroids of back trajectories from three release altitudes within each cloud (see Supplementary Table 4.3 for details on altitude selection criteria). If trajectories across the three selected release altitudes differed, they are labeled "hi" for cloud top, "mid" for halfway between base and top, and "low" for cloud bottom. Origins of particles in the 10 d simulation are shown to range from 4000 m over Russia to 2500–3500 m over the Sea of Okhostk, the Bering Sea and the North Pacific. FLEXPART results suggest a dominance of marine particle sources to clouds for sampling periods 1–11.

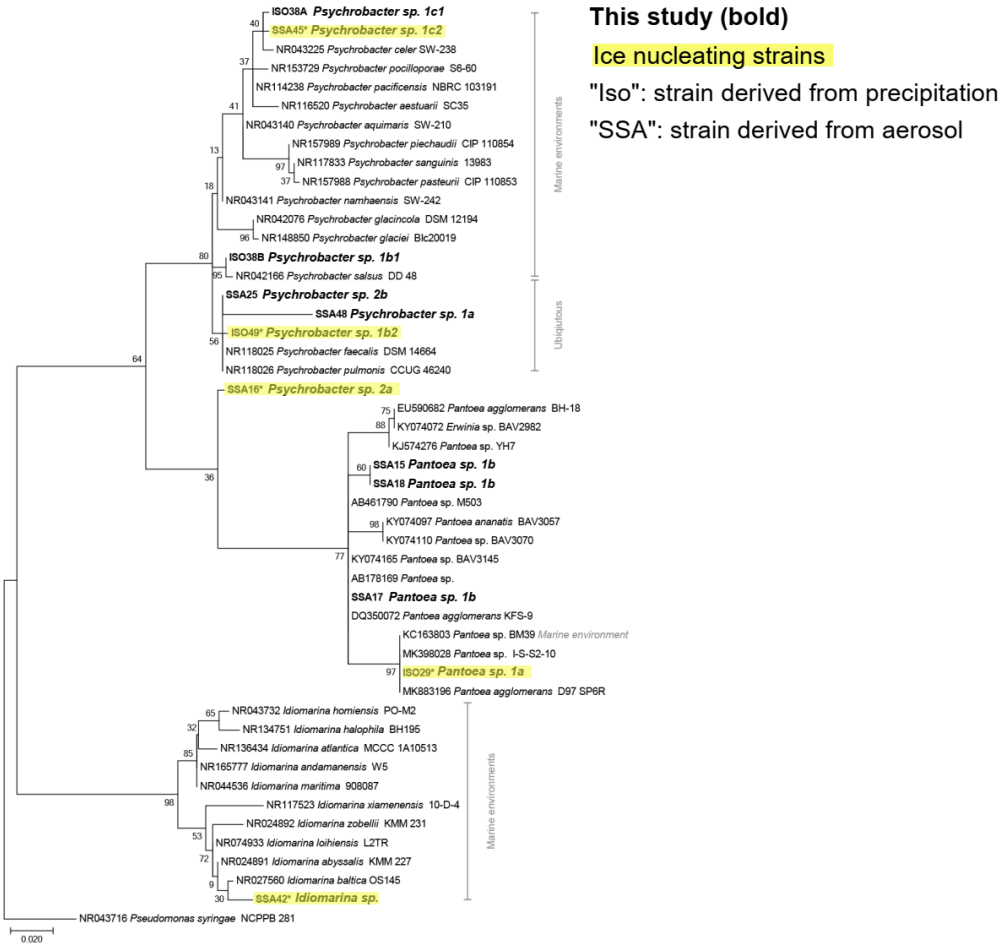

Figure 4.3: Maximum likelihood phylogenetic tree based on 420 nucleotides of the 16S rRNA gene sequences showing the phylogenetic relationships of isolates (in bold) related to Gammaproteobacteria reference sequences. The environmental source of the reference sequences (based on National Center for Biotechnology Information, NCBI, metadata) is indicated in gray. Isolates with ice-nucleating properties are shaded in yellow; bootstrap values ($n = 500$) are indicated at nodes; the scale bar represents changes per position..

The phylogenetic relationships between isolates and reference sequences (Fig. 4.3) show that at least 2 of the 14 IN isolates are closely related to marine taxa, *Idiomarina* sp. and *Psychrobacter* sp. 1c2, both of which were derived from coastal aerosol. Additionally, considering the aerosol transport simulation data (Fig. 4.2), the evidence of marine influence in precipitation INP spectra (Fig. 4.1) and the use of marine growth media, multiple other IN isolates derived

from the precipitation samples are also possibly marine. Furthermore, other IN isolates from precipitation samples cluster closely with marine reference sequences. For example, *Pantoea* sp. 1a and *Brevibacterium* sp. show high similarity to reference sequences derived from marine environments (Figs. 4.3, Supplementary Fig. 4.12). However, several of the species identified in this study are likely more ubiquitous and closely related to reference isolates found in terrestrial and freshwater systems (Bowers et al., 2009; Fröhlich-Nowoisky et al., 2016; SantlTemkiv et al., 2015; Vaïtilingom et al., 2012), including two of the IN isolates, *Psychrobacter* sp. 1b2 and *Paenibacillus* sp. 1.

4.4.3 Ice-nucleating properties of rain and SSA isolates

Of the 47 total isolates derived from precipitation and aerosol samples, 14 were found to be significantly ice nucleating according to the selection criterion described in Sect. 4.3.4.

Within the technique's temperature and detection limit of 0.675 INPs per milliliter of liquid between 0 and –25 °C, 11 precipitation isolates exhibited freezing temperatures between –2.3 and –24.3 °C, and 3 aerosol isolates exhibited freezing temperatures between –14.0 and –24.5 °C (Table 4.1). Prior to this study, *Lysinibacillus* sp. was the only known gram-positive species found to be capable of ice nucleation (Failor et al., 2017a). However, several IN isolates identified in this study are also gram-positive, including isolates of *Brevibacterium* sp., *Paenibacillus* sp., *Planococcus* sp., *Bacillus* sp., *Arthrobacter* sp. and *Cellulosimicrobium* sp.

Isolate INP spectra are shown in Fig. 4.4, normalized to biomass, (n_m g^{-1}; see Sect. 4.3.4 for details on biomass estimates). Also plotted in Fig. 4.4 are observations of a variety of marine and terrestrial bioaerosols from prior studies, including pollens, fungi, lichens, plankton, leaf litter and soil dusts (Conen et al., 2011; Conen and Yakutin, 2018; Després et al., 2012; Fröhlich-Nowoisky et al., 2015; Kunert et al., 2019; O'Sullivan et al., 2015; Wex et al., 2015). Results show that with the exception of *Brevibacterium* sp., isolates from this study are generally less efficient than most terrestrial IN biological particles, with lower concentrations and activation

Table 4.1: Identities of 14 cultivable halotolerant IN bacteria and fungi derived from aerosol and precipitation samples (see Supplementary Table 4.3 for precipitation and aerosol sample details).

Iso ID	Isolate	IN onset temperature (°C)	Precipitation or aerosol sample number
Iso2	*Cryptococcus* sp. 1	–9.3	1
Iso10B	*Paenibacillus* sp. 1	–14.8	2
Iso8	*Brevibacterium* sp. 1b	–2.3	4
Iso32B	*Planococcus* sp. 1	–12.3	7
Iso29	*Pantoea* sp. 1a	–17	8
Iso31	*Bacillus* sp. 1a1	–14.5	8
Iso21	*Cellulosimicrobium* sp. 1a1	–14	9
Iso23	Unknown	–13.3	9
Iso24A	*Metschikowia* sp.	–16.5	9
Iso27	*Cellulosimicrobium* sp. 1a3	–14.8	10
Iso49	*Psychrobacter* sp. 1b2	–13.8	11
SSA42	*Idiomarina* sp.	–14.3	A1
S SSA16	*Psychrobacter* sp. 1c2	–17.5	A2
SSA45	*Psychrobacter* sp. 2b	–14	A5

temperatures. Concentrations of INPs per milliliter in ZoBell suspension are additionally shown in Supplementary Fig. 4.14.

Fungal isolates *Cryptococcus* sp. and *Metschikowia* sp. represent two new asomycotic and basidiomycotic IN fungal species, respectively, with INP concentrations 7–8 orders of magnitude lower than the highest reported values for fungal isolates *F. armeniacum* and *F. acuminatum* (Kunert et al., 2019). While multiple other IN species of the Ascomycota and Basidiomycota phyla have been previously reported (e.g., Jayaweera and Flanagan, 1982; Kieft et al., 1988; Pouleur et al., 1992), very little is known regarding the distribution and source potential of fungal INPs. Moreover, multiple issues pose challenges to the differentiation of marine vs. terrestrial fungal species (Amend et al., 2019). Many fungi found in the sea are also found in

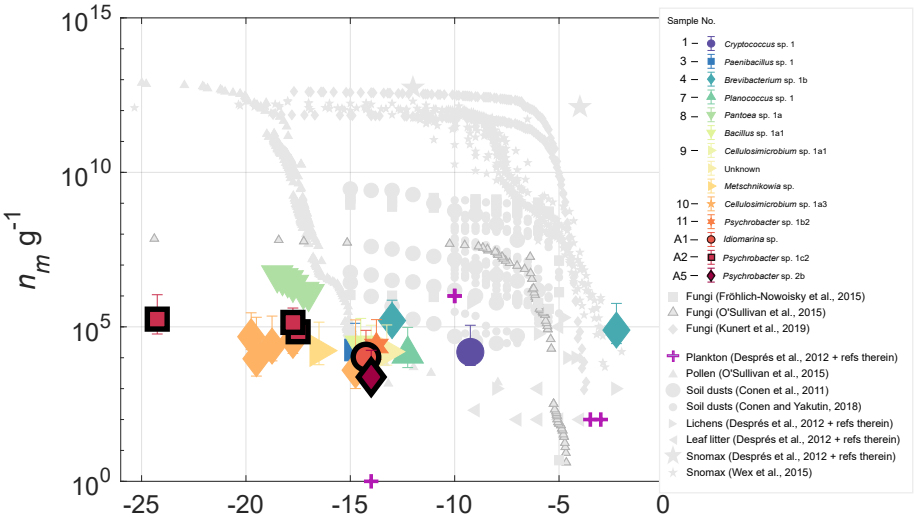

Figure 4.4: INP concentrations (g^{-1} biomass) for 14 halotolerant isolates derived from precipitation and aerosol samples. Also shown are INP observations of various biological particles from published studies. The sample numbers in the legend indicate the precipitation or aerosol sample from which the isolate was derived (see Supplementary Table 4.4). Data points corresponding to isolates from aerosol are outlined in black. Error bars indicate the 95 % confidence intervals and uncertainty associated with the biomass estimate (see Sect. 4.4.3 for details). Only freezing activity that was significantly enhanced ($p < 0.005$) above ZoBell growth media is shown. Results show that with the exception of *Brevibacterium* sp., isolates are generally less efficient ice nucleators than most biological INPs of terrestrial origin.

terrestrial environments, and strong correlations with abiotic environmental conditions (Orsi et al., 2013; Tisthammer et al., 2016) and gene expression data (Amend et al., 2012) suggest that some fungi are truly amphibious. Issues with amplicon sequencing pose additional challenges due to the co-amplification of other eukaryotes and large biases toward terrestrial species in internal transcribed spacer (ITS) rDNA primers, which were designed using sequence alignments from largely terrestrial representatives (Amend et al., 2019). However, future studies could take advantage of established marine fungi isolation and cultivation techniques to probe the INP source potential of various cultivable marine fungal species (e.g., Kjer et al., 2010; Overy et al., 2019).

To examine the IN properties of unique strains within samples, multiple sequence alignment of the 16S rDNA sequences was used to identity and remove duplicates. The relationship between 16S rDNA sequences of isolates within their genus is shown in Supplementary Fig.

4.15. Ice-nucleating precipitation and aerosol isolates exhibit moderate IN freezing temperatures ($<$ – 10 °C) (Fig. 4.4), with the exception of two warm freezing isolates: a fungal isolate from sampling period 1, *Cryptococcus* sp., which triggered freezing at –9.3 °C; and a bacterial isolate from sampling period 4, *Brevibacterium* sp., which triggered freezing at a relatively high freezing temperature of –2.3 °C. The freezing temperatures of all but *Brevibacterium* sp. 1b overlap with previously reported freezing temperatures of INPs produced in fresh SSA (–7 to –33 °C) and, in particular, with the freezing temperatures shown to be likely associated with microbes or cellular material in SSA (–8 to –22 °C). (DeMott et al., 2016; McCluskey et al., 2017). Isolate freezing temperatures also overlap with INP freezing temperatures in samples of the Arctic marine sea surface microlayer (Irish et al., 2017; Wilson et al., 2015). However, INP measurements were not performed repeatedly on isolate suspensions, so the extent to which the observed freezing behavior was affected by the isolate's growth phase remains unknown.

Of the known IN bacteria, only Gammaproteobacteria have been shown to nucleate ice at high temperatures (Morris et al., 2004). Brevibacterium sp. was the first Actinobacteria to be shown capable of IN near 2 °C. Considering that only IN microbes of continental origins, such as Pseudomonas syringae, have been reported to have freezing temperatures as high as –2 or –3 °C (e.g., Fröhlich-Nowoisky et al., 2016, and references therein) and that SSA is associated with 1000 times fewer ice-nucleating active sites per unit surface area compared with mineral dust (McCluskey et al., 2018b), one would not expect to find a marine IN isolate with an extremely warm freezing onset temperature. However, the presence of bacteria closely related to Brevibacterium sp. in marine environments suggests that a marine origin is possible (Supplementary Fig. 4.12, see also discussion in Sect. 4.4.2). Furthermore, the back-trajectory analysis for the sample from which Brevibacterium sp. was isolated indicates that the North Pacific region dominated the sampling period. Actinobacteria are common in marine environments (e.g., Bull et al., 2005) and have been identified in nascent SSA (Michaud et al., 2018). To explore the role of the growth media on the IN properties of isolates, controls were run on nine washed

isolates (Supplmentary Fig. 4.6 and Table 4.6, see Sect. 4.3.4). Five of the selected isolates were found to not be significantly IN above sterile ZoBell background, whereas four were chosen from the subset of significantly IN isolates. Interestingly, the observed INP concentrations of washed isolates above that of the FASW were inconsistently related to activity when grown in ZoBell media and were generally enhanced. Seven of the nine media-free isolates exhibited significant IN behavior, including four isolates that were not IN in ZoBell. Some of the observed differences in ice nucleation above background between isolates suspended in ZoBell and those suspended in FASW could be a result of the differences in the background INP concentrations present in the suspension media (i.e., concentrations of INPs in FASW are less than in ZoBell, thereby increasing the temperature range in which IN activity could be detected). Another possibility is that the isolates' IN behavior varied depending on multiple factors, including their viability, environment, stress and nutrient availability. As washing cells removes soluble molecules, the apparent IN activity of washed suspensions could indicate that the source of IN activity is membrane-associated or, alternatively, that expression of IN activity is sensitive to environmental factors. The difference in IN activity between ZoBell and FASW suspensions indicates that in situ measurements of IN bacteria will be necessary to determine the abundance of active IN microbes in the atmosphere.

One study of note, Failor et al. (2017), used similar cultivation and INP measurement techniques on precipitation samples and additionally identified multiple halotolerant IN species using marine growth media. However, the IN species identified in Failor et al. (2017) were limited to Gammaproteobacteria, whereas we find greater diversity among the IN isolate taxonomies, including Actinobacteria, Bacilli, Saccharomycetes and Tremellomycetes. Two of the halotolerant IN Gammaproteobacteria identified in Failor et al. (2017) were also found here (see also Fall and Schnell, 1985). Additionally, whereas Failor et al. (2017) reports high freezing temperatures between –4 and –12 °C for multiple halotolerant *Pseudomonas* spp., none of the *Pseudomonas* spp. isolated in our study exhibited detectable IN activity. IN observations for *Pantoea* sp. also

differ. The *Pantoea* sp. isolate in our study exhibited a moderate IN freezing temperature of –17 °C, but Failor et al. (2017) reported warm freezing activity between –4 and –10 °C. In addition to environmentdependent changes in isolate IN activity, the differences between the two studies could also be the result of inherent differences in IN activity between different strains of the same species (Morris et al., 2008).

Finally, the results from Failor et al. (2017) show discrepancies between IN behavior of isolates directly plated from precipitation samples and those from suspensions of purified strains, and we also find that IN behavior can vary between different types of isolate suspensions (i.e., ZoBell vs. FASW). Failor et al. (2017) suggests that changes in an isolate's IN activity may be explained in part by growth conditions not conducive for the expression of ice nucleation activity (INA) and that INA molecules may generally be produced in higher amounts in oligotrophic conditions, such as those found in the atmosphere.

4.5 Conclusions

Through isolation and identification of multiple IN microbes in precipitation and aerosol, this study provides the identities of multiple halotolerant IN microbes that are likely of marine origin. Furthermore, we isolated six new IN grampositive bacteria capable of ice nucleation. Prior to this study, *Lysinibacillus* sp. was thought to be the only gram-positive species capable of ice nucleation (Failor et al., 2017). Additionally, through cell-washing experiments in which soluble molecules and growth media are eliminated from isolate suspensions, we find that the IN activities of most isolates depend on growth conditions.

Due to the challenge of distinguishing between marine and terrestrial INPs in environmental samples, it is impossible to definitively claim marine or terrestrial origins for the 14 IN isolates measured in this study. In order to survive atmospheric transport and deposition in rainwater, cultivable isolates derived from precipitation must be tolerant of near-freshwater conditions.

However, marine origin is highly likely for multiple isolates for the following reasons: aerosol back trajectories and INP observations during sampling events indicate that marine sources were dominant (Figs. 4.1, 4.2), multiple isolate sequences show similarity to marine isolation sources in reference sequences (Figs. 4.3, 4.12), and isolate freezing temperatures are generally in agreement with previously documented nascent SSA IN freezing temperatures (DeMott et al., 2016; McCluskey et al., 2017, 2018a).

While cultivation methods preclude the quantification of atmospheric abundance and exclude a large fraction of uncultivable microorganisms, we captured several possible contributors to precipitation IN populations and, through isolation, maintained the ability to assess their IN activity and other characteristics. Considering the general rarity of atmospheric INPs (1 in 10^5 at –20 °C) (Rogers et al., 1998), the relatively lower concentrations of INPs in marine air masses (DeMott et al., 2016; McCluskey et al., 2018c) and the rarity of cultivable microbes, it is quite surprising that a substantial fraction of the cultivable microbial isolates from precipitation samples were found to be IN at temperatures above –17 °C (11 out of 34 total, or 32 %), and this suggests that there is a significant fraction of IN species in aerosols among the substantially larger uncultivable community.

Finally, as cultivable populations represent a small fraction of the total microbial community, future studies should combine INP measurements with state-of-the-art sequencing approaches to identify relationships between specific microbial communities and INP freezing activity. Furthermore, a combination of advanced fractionation methods to identify the putative ice-nucleating metabolites associated with specific microbial communities and computational networking could illuminate molecular and microbial linkages to ice nucleation and the mechanisms by which the entities work individually or in concert. Further study is also needed to understand the factors, such as atmospheric processing or nutrient limitation, that inhibit or enhance microbe IN behavior, as well as the factors that modulate the emissions of IN bacteria from the ocean surface.

Data availability. The 16S rRNA gene sequences from this study were deposited to Gen-

Bank under the accession numbers MW704027–MW704080. The dataset supporting this paper is hosted by the UC San Diego Library Digital Collections (https://doi.org/10.6075/J0GQ6W2Z) (Beall et al., 2020).

Acknowledgements. This work was supported by National Science Foundation (NSF) through the NSF Center for Aerosol Impacts on Chemistry of the Environment (CAICE grant nos. CHE-1801971, AGS-1451347 and IOS-1516156). This work was additionally supported by the U.S. Army Corps of Engineers (grant no. W912HZ- 15-2-0019). The authors gratefully acknowledge Kelsey Krug for her assistance with sample archiving; Jesse DeWald, John Beall and Matt Merrill for assistance with sample collection; and the NOAA Earth Systems Research Laboratory (ESRL) for providing the HighResolution Rapid Refresh model that was used in this study.

Chapter 4, in full, is a reprint of the material as it appears in Atmospheric Chemistry and Physics 2021. Beall, C. M., Michaud, J. M., Fish, M. A., Dinasquet, J., Cornwell, G. C., Stokes, M. D., Burkart, M. D., Hill, T. C., DeMott, P. J. and Prather, K. A.: Cultivable halotolerant ice-nucleating bacteria and fungi in coastal precipitation, Atmos. Chem. Phys., 21(11), 9031–9045, doi:10.5194/acp-21-9031-2021, 2021. The dissertation author was the primary investigator and author of this paper.

Financial support. This research has been supported by the National Science Foundation (grant nos. CHE-1801971, AGS- 1451347 and IOS-1516156) and the U.S. Army Corps of Engineers (grant no. W912HZ-15-2-0019).

4.6 References

Agresti, A. and Coull, B. A.: Approximate Is Better than “Exact” for Interval Estimation of Binomial Proportions, Am. Stat., 52, 119–126, https://doi.org/10.2307/2685469, 1998.

Alpert, P. A., Aller, J. Y., and Knopf, D. A.: Initiation of the ice phase by marine biogenic surfaces in supersaturated gas and supercooled aqueous phases, Phys. Chem. Chem. Phys., 13, 19882, https://doi.org/10.1039/c1cp21844a, 2011.

Amend, A. S., Barshis, D. J., and Oliver, T. A.: Coral-associated marine fungi form novel lineages and heterogeneous assemblages, ISME J., 6, 1291–1301, https://doi.org/10.1038/ismej.2011.193, 2012.

Amend, A., Burgaud, G., Cunliffe, M., Edgcomb, V. P., Ettinger, C. L., Gutiérrez, M. H., Heitman, J., Hom, E. F. Y., Ianiri, G., Jones, A. C., Kagami, M., Picard, K. T., Quandt, C. A., Raghukumar, S., Riquelme, M., Stajich, J., VargasMuñiz, J., Walker, A. K., Yarden, O., and Gladfelter, A. S.: Fungi in the Marine Environment: Open Questions and Unsolved Problems, edited by: Garsin, D. A., MBio, 10, e01189-18, https://doi.org/10.1128/mBio.01189-18, 2019.

Beall, C. M., Stokes, M. D., Hill, T. C., DeMott, P. J., DeWald, J. T., and Prather, K. A.: Automation and heat transfer characterization of immersion mode spectroscopy for analysis of ice nucleating particles, Atmos. Meas. Tech., 10, 2613–2626, https://doi.org/10.5194/amt-10-2613-2017, 2017.

Beall, C. M., Michaud, J. M., Fish, M. A., Dinasquet, J., Cornwell, G. C., Stokes, M., D., Burkart, M. D., Hill, T. C., DeMott, P. J., and Prather, K. A: Data from: Cultivable, halotolerant ice nucleating bacteria and fungi in coastal precipitation, in: Center for Aerosol Impacts on Chemistry of the Environment (CAICE), UC San Diego Library Digital Collections, https://doi.org/10.6075/J0GQ6W2Z, 2020.

Benjamin, S. G., Weygandt, S. S., Brown, J. M., Hu, M., Alexander, C. R., Smirnova, T. G., Olson, J. B., James, E. P., Dowell, D. C., Grell, G. A., Lin, H., Peckham, S. E., Smith, T. L., Moninger, W. R., Kenyon, J. S., and Manikin, G. S.: ANorth American Hourly Assimilation and Model Forecast Cycle: The Rapid Refresh, Mon. Weather Rev., 144, 1669–1694, https://doi.org/10.1175/MWR-D-15-0242.1, 2016.

Bigg, E. K.: A long period fluctuation in freezing nucleus concentrations, J. Meteorol., 15, 561–562, https://doi.org/10.1175/1520- 0469(1958)015¡0561:alpfif¿2.0.co;2, 1958.

Bigg, E. K., Soubeyrand, S., and Morris, C. E.: Persistent aftereffects of heavy rain on concentrations of ice nuclei and rainfall suggest a biological cause, Atmos. Chem. Phys., 15, 2313–2326, https://doi.org/10.5194/acp-15-2313-2015, 2015.

Boström, K. H., Simu, K., Hagström, Å., and Riemann, L.: Optimization of DNA extraction for quantitative marine bacterioplankton community analysis, Limnol. Oceanogr. Methods, 2, 365–373, 2004.

Bowers, R. M., Lauber, C. L., Wiedinmyer, C., Hamady, M., Hallar, A. G., Fall, R., Knight, R., and Fierer, N.: Characterization of airborne microbial communities at a high-elevation site and their potential to act as atmospheric ice nuclei, Appl. Environ. Microbiol., 75, 5121–5130, https://doi.org/10.1128/AEM.00447- 09, 2009.

Bull, A. T., Stach, J., Ward, A. C., et al. Marine actinobacteria: perspectives, challenges, future directions, Antonie Van Leeuwenhoek, 87, 65–79, https://doi.org/10.1007/s10482-004-6562-8, 2005.

Burrows, S. M., Hoose, C., Pöschl, U., and Lawrence, M. G.: Ice nuclei in marine air: biogenic particles or dust?, Atmos. Chem. Phys., 13, 245–267, https://doi.org/10.5194/acp-13-245-2013, 2013.

Carro-Calvo, L., Hoose, C., Stengel, M., and Salcedo-Sanz, S.: Cloud glaciation temperature estimation from passive remote sensing data with evolutionary computing, J. Geophys. Res., 121, 13591–13608, https://doi.org/10.1002/2016JD025552, 2016.

Christner, B. C., Cai, R., Morris, C. E., McCarter, K. S., Foreman, C. M., Skidmore, M. L., Montross, S. N., and Sands, D. C.: Geographic, seasonal, and precipitation chemistry influence on the abundance and activity of biological ice nucleators in rain and snow., P. Natl. Acad. Sci. USA, 105, 18854–18859, https://doi.org/10.1073/pnas.0809816105, 2008.

Conen, F. and Yakutin, M. V.: Soils rich in biological icenucleating particles abound in ice-nucleating macromolecules likely produced by fungi, Biogeosciences, 15, 4381–4385, https://doi.org/10.5194/bg-15-4381-2018, 2018.

Conen, F., Morris, C. E., Leifeld, J., Yakutin, M. V., and Alewell, C.: Biological residues define the ice nucleation properties of soil dust, Atmos. Chem. Phys., 11, 9643–9648, https://doi.org/10.5194/acp-11-9643-2011, 2011.

Conen, F., Eckhardt, S., Gundersen, H., Stohl, A., and Yttri, K. E.: Rainfall drives atmospheric ice-nucleating particles in the coastal climate of southern Norway, Atmos. Chem. Phys., 17, 11065– 11073, https://doi.org/10.5194/acp-17-11065-2017, 2017.

Creamean, J. M., Suski, K. J., Rosenfeld, D., Cazorla, A., DeMott, P. J., Sullivan, R. C., White, A. B., Ralph, F. M., Minnis, P., Comstock, J. M., Tomlinson, J. M., and Prather, K. A.: Dust and biological aerosols from the Sahara and Asia influence precipitation in the Western U.S, Science, 340, 1572–1578, https://doi.org/10.1126/science.1227279, 2013.

Curry, J. A., Hobbs, P. V., King, M. D., Randall, D. A., Minnis, P., Isaac, G. A., Pinto, J. O., Uttal, T., Bucholtz, A., Cripe, D. G., Gerber, H., Fairall, C. W., Garrett, T. J., Hudson, J., Intrieri, J. M., Jakob, C., Jensen, T., Lawson, P., Marcotte, D., Nguyen, L.,

Pilewskie, P., Rangno, A., Rogers, D. C., Strawbridge, K. B., Valero, F. P. J., Williams, A. G., and Wylie, D.: FIRE arctic clouds experiment, B. Am. Meteorol. Soc., 81, 5–29, https://doi.org/10.1175/1520- 0477(2000)081¡0005:FACE¿2.3.CO;2, 2000.

DeLeon-Rodriguez, N., Lathem, T. L., Rodriguez-R, L. M., Barazesh, J. M., Anderson, B. E., Beyersdorf, A. J., Ziemba, L. D., Bergin, M., Nenes, A., and Konstantinidis, K. T.: Microbiome of the upper troposphere: species composition and prevalence, effects of tropical storms, and atmospheric implications, P. Natl. Acad. Sci. USA, 110, 2575–80, https://doi.org/10.1073/pnas.1212089110, 2013.

Delort, A. M., Vaïtilingom, M., Joly, M., Amato, P., Wirgot, N., Lallement, A., Sancelme, M., Matulova, M., and Deguillaume, L.: Clouds: A Transient and Stressing Habitat for Microorganisms BT - Microbial Ecology of Extreme Environments, edited by: Chénard, C. and Lauro, F. M., 215–245, Springer International Publishing, Cham, 2017.

DeMott, P. J., Hill, T. C. J., McCluskey, C. S., Prather, K. A., Collins, D. B., Sullivan, R. C., Ruppel, M. J., Mason, R. H., Irish, V. E., Lee, T., Hwang, C. Y., Rhee, T. S., Snider, J. R., McMeeking, G. R., Dhaniyala, S., Lewis, E. R., Wentzell, J. J. B., Abbatt, J., Lee, C., Sultana, C. M., Ault, A. P., Axson, J. L., Diaz Martinez, M., Venero, I., Santos-Figueroa, G., Stokes, M. D., Deane, G. B., Mayol-Bracero, O. L., Grassian, V. H., Bertram, T. H., Bertram, A. K., Moffett, B. F., and Franc, G. D.: Sea spray aerosol as a unique source of ice nucleating particles, P. Natl. Acad. Sci., 113, 5797–5803, https://doi.org/10.1073/pnas.1514034112, 2016.

Després, V., Huffman, J. A., Burrows, S. M., Hoose, C., Safatov, A., Buryak, G., Fröhlich-Nowoisky, J., Elbert, W., Andreae, M., Pöschl, U., and Jaenicke, R.: Primary biological aerosol particles in the atmosphere: a review, Tellus B Chem. Phys. Meteorol., 64, 15598, https://doi.org/10.3402/tellusb.v64i0.15598, 2012.

Fahlgren, C., Hagström, Å., Nilsson, D., and Zweifel, U. L.: Annual Variations in the Diversity, Viability, and Origin of Airborne Bacteria, Appl. Environ. Microbiol., 76, 3015–3025, https://doi.org/10.1128/AEM.02092-09, 2010.

Fahlgren, C., Gómez-Consarnau, L., Zábori, J., Lindh, M. V, Krejci, R., Mårtensson, E. M., Nilsson, D., and Pinhassi, J.: Seawater mesocosm experiments in the Arctic uncover differential transfer of marine bacteria to aerosols, Environ. Microbiol. Rep., 7, 460– 470, https://doi.org/10.1111/1758-2229.12273, 2015.

Failor, K. C., Schmale, D. G., Vinatzer, B. A., and Monteil, C. L.: Ice nucleation active bacteria in precipitation are genetically diverse and nucleate ice by employing different mechanisms, ISME J., 11, 2740–2753, https://doi.org/10.1038/ismej.2017.124, 2017.

Fall, R. and Schnell, R. C.: Association of an ice-nucleating pseudomonad with cultures of the

marine dinoflagellate, Heterocapsa niei, J. Mar. Res., 43, 257–265, https://doi.org/10.1357/002224085788437370, 1985.

Fröhlich-Nowoisky, J., Hill, T. C. J., Pummer, B. G., Yordanova, P., Franc, G. D., and Pöschl, U.: Ice nucleation activity in the widespread soil fungus Mortierella alpina, Biogeosciences, 12, 1057–1071, https://doi.org/10.5194/bg-12-1057-2015, 2015.

Fröhlich-Nowoisky, J., Kampf, C. J., Weber, B., Huffman, J. A., Pöhlker, C., Andreae, M. O., Lang-Yona, N., Burrows, S. M., Gunthe, S. S., Elbert, W., Su, H., Hoor, P., Thines, E., Hoffmann, T., Després, V. R., and Pöschl, U.: Bioaerosols in the Earth system: Climate, health, and ecosystem interactions, Atmos. Res., 182, 346–376, https://doi.org/10.1016/j.atmosres.2016.07.018, 2016.

Furtado, K. and Field, P.: The Role of Ice Microphysics Parametrizations in Determining the Prevalence of Supercooled Liquid Water in High-Resolution Simulations of a Southern Ocean Midlatitude Cyclone, J. Atmos. Sci., 74, 2001–2021, https://doi.org/10.1175/JAS-D-16-0165.1, 2017.

Hill, T. C. J., Moffett, B. F., DeMott, P. J., Georgakopoulos, D. G., Stump, W. L., and Franc, G. D.: Measurement of ice nucleation-active bacteria on plants and in precipitation by quantitative PCR, Appl. Environ. Microbiol., 80, 1256–1267, https://doi.org/10.1128/AEM.02967-13, 2014.

Huffman, J. A., Prenni, A. J., DeMott, P. J., Pöhlker, C., Mason, R. H., Robinson, N. H., Fröhlich-Nowoisky, J., Tobo, Y., Després, V. R., Garcia, E., Gochis, D. J., Harris, E., MüllerGermann, I., Ruzene, C., Schmer, B., Sinha, B., Day, D. A., Andreae, M. O., Jimenez, J. L., Gallagher, M., Kreidenweis, S. M., Bertram, A. K., and Pöschl, U.: High concentrations of biological aerosol particles and ice nuclei during and after rain, Atmos. Chem. Phys., 13, 6151–6164, https://doi.org/10.5194/acp- 13-6151-2013, 2013.

Hwang, C. Y. and Cho, B. C.: Prokaryotic abundance and 16S rRNA gene sequences detected in marine aerosols on the East Sea (Korea), FEMS Microbiol. Ecol., 76, 327–341, https://doi.org/10.1111/j.1574-6941.2011.01053.x, 2011.

Irish, V. E., Elizondo, P., Chen, J., Chou, C., Charette, J., Lizotte, M., Ladino, L. A., Wilson, T. W., Gosselin, M., Murray, B. J., Polishchuk, E., Abbatt, J. P. D., Miller, L. A., and Bertram, A. K.: Ice-nucleating particles in Canadian Arctic sea-surface microlayer and bulk seawater, Atmos. Chem. Phys., 17, 10583–10595, https://doi.org/10.5194/acp-17-10583-2017, 2017.

Jayaweera, K. and Flanagan, P.: Investigations on biogenic ice nuclei in the Arctic atmosphere, Geophys. Res. Lett., 9, 94–97, https://doi.org/10.1029/GL009i001p00094, 1982.

Joyce, R. E., Lavender, H., Farrar, J., Werth, J. T., Weber, C. F., D'Andrilli, J., Vaitilingom, M., and Christner, B. C.: Biological Ice-Nucleating Particles Deposited Year-Round in Subtropical Precipitation, edited by: Stams, A. J. M., Appl. Environ. Microbiol., 85, e01567-19, https://doi.org/10.1128/AEM.01567-19, 2019.

Junge, K. and Swanson, B. D.: High-resolution ice nucleation spectra of sea-ice bacteria: implications for cloud formation and life in frozen environments, Biogeosciences, 5, 865–873, https://doi.org/10.5194/bg-5-865-2008, 2008.

Kanji, Z. A., Ladino, L. A., Wex, H., Boose, Y., BurkertKohn, M., Cziczo, D. J., and Krämer, M.: Overview of Ice Nucleating Particles, Meteorol. Monogr., 58, 1.1–1.33, https://doi.org/10.1175/AMSMONOGRAPHS-D-16-0006.1, 2017.

Kay, J. E., Wall, C., Yettella, V., Medeiros, B., Hannay, C., Caldwell, P., and Bitz, C.: Global climate impacts of fixing the Southern Ocean shortwave radiation bias in the Community Earth System Model (CESM), J. Clim., 29, 4617–4636, https://doi.org/10.1175/JCLI-D-15-0358.1, 2016.

Kieft, T. L.: Ice Nucleation Activity in Lichens, Appl. Environ. Microbiol., 54, 1678–1681, 1988. Kjer, J., Debbab, A., Aly, A. H., and Proksch, P.: Methods for isolation of marine-derived endophytic fungi and their bioactive secondary products, Nat. Protoc., 5, 479–490, https://doi.org/10.1038/nprot.2009.233, 2010.

Klein, S. A., McCoy, R. B., Morrison, H., Ackerman, A. S., Avramov, A., Boer, G. de, Chen, M., Cole, J. N. S., Del Genio, A. D., Falk, M., Foster, M. J., Fridlind, A., Golaz, J.-C., Hashino, T., Harrington, J. Y., Hoose, C., Khairoutdinov, M. F., Larson, V. E., Liu, X., Luo, Y., McFarquhar, G. M., Menon, S., Neggers, R. A. J., Park, S., Poellot, M. R., Schmidt, J. M., Sednev, I., Shipway, B. J., Shupe, M. D., Spangenberg, D. A., Sud, Y. C., Turner, D. D., Veron, D. E., Salzen, K. von, Walker, G. K., Wang, Z., Wolf, A. B., Xie, S., Xu, K.-M., Yang, F., and Zhang, G.: Intercomparison of model simulations of mixed-phase clouds observed during the ARM Mixed-Phase Arctic Cloud Experiment. I: single-layer cloud, Q. J. Roy. Meteorol. Soc., 135, 979–1002, https://doi.org/10.1002/qj.416, 2009.

Krzywinski, M. and Altman, N.: Error bars, Nat. Methods, 10, 921– 922, https://doi.org/10.1038/nmeth.2659, 2013.

Kunert, A. T., Pöhlker, M. L., Tang, K., Krevert, C. S., Wieder, C., Speth, K. R., Hanson, L. E., Morris, C. E., Schmale III, D. G., Pöschl, U., and Fröhlich-Nowoisky, J.: Macromolecular fungal ice nuclei in Fusarium: effects of physical and chemical processing, Biogeosciences, 16, 4647–4659, https://doi.org/10.5194/bg- 16-4647-2019, 2019.

Ladino, L. A., Yakobi-Hancock, J. D., Kilthau, W. P., Mason, R. H., Si, M., Li, J., Miller, L. A., Schiller, C. L., Huffman, J. A., Aller, J. Y., Knopf, D. A., Bertram, A. K., and Ab-

batt, J. P. D.: Addressing the ice nucleating abilities of marine aerosol: A combination of deposition mode laboratory and field measurements, Atmos. Environ., 132, 1–10, https://doi.org/10.1016/j.atmosenv.2016.02.028, 2016.

Letunic, I. and Bork, P.: Interactive Tree of Life v2: Online annotation and display of phylogenetic trees made easy, Nucleic Acids Res., 39, 475–478, https://doi.org/10.1093/nar/gkr201, 2011.

Levin, E. J. T., DeMott, P. J., Suski, K. J., Boose, Y., Hill, T. C. J., McCluskey, C. S., Schill, G. P., Rocci, K., Al-Mashat, H., Kristensen, L. J., Cornwell, G., Prather, K., Tomlinson, J., Mei, F., Hubbe, J., Pekour, M., Sullivan, R., Leung, L. R., and Kreidenweis, S. M.: Characteristics of Ice Nucleating Particles in and Around California Winter Storms, J. Geophys. Res.-Atmos., 124, 11530–11551, https://doi.org/10.1029/2019JD030831, 2019.

McCluskey, C. S., Hill, T. C. J., Malfatti, F., Sultana, C. M., Lee, C., Santander, M. V., Beall, C. M., Moore, K. A., Cornwell, G. C., Collins, D. B., Prather, K. A., Jayarathne, T., Stone, E. A., Azam, F., Kreidenweis, S. M., and DeMott, P. J.: A dynamic link between ice nucleating particles released in nascent sea spray aerosol and oceanic biological activity during two mesocosm experiments, J. Atmos. Sci., 74, 151–166, https://doi.org/10.1175/JAS-D-16-0087.1, 2017.

McCluskey, C. S., Hill, T. C. J., Sultana, C. M., Laskina, O., Trueblood, J., Santander, M. V, Beall, C. M., Michaud, J. M., Kreidenweis, S. M., Prather, K. A., Grassian, V., and DeMott, P. J.: A Mesocosm Double Feature: Insights into the Chemical Makeup of Marine Ice Nucleating Particles, J. Atmos. Sci., 75, 2405– 2423, https://doi.org/10.1175/JAS-D-17-0155.1, 2018a.

McCluskey, C. S., Ovadnevaite, J., Rinaldi, M., Atkinson, J., Belosi, F., Ceburnis, D., Marullo, S., Hill, T. C. J., Lohmann, U., Kanji, Z. A., O'Dowd, C., Kreidenweis, S. M., and DeMott, P. J.: Marine and Terrestrial Organic Ice-Nucleating Particles in Pristine Marine to Continentally Influenced Northeast Atlantic Air Masses, J. Geophys. Res.-Atmos., 123, 6196–6212, https://doi.org/10.1029/2017JD028033, 2018b.

McCluskey, C. S., Hill, T. C. J., Humphries, R. S., Rauker, A. M., Moreau, S., Strutton, P. G., Chambers, S. D., Williams, A. G., McRobert, I., Ward, J., Keywood, M. D., Harnwell, J., Ponsonby, W., Loh, Z. M., Krummel, P. B., Protat, A., Kreidenweis, S. M., and DeMott, P. J.: Observations of Ice Nucleating Particles Over Southern Ocean Waters, Geophys. Res. Lett., 45, 11911–989997, https://doi.org/10.1029/2018GL079981, 2018c.

McWilliam, H., Li, W., Uludag, M., Squizzato, S., Park, Y. M., Buso, N., Cowley, A. P., and Lopez, R.: Analysis Tool Web Services from the EMBL-EBI., Nucleic Acids Res., 41, 597–600, https://doi.org/10.1093/nar/gkt376, 2013.

Michaud, J. M., Thompson, L. R., Kaul, D., Espinoza, J. L., Richter, R. A., Xu, Z. Z., Lee, C., Pham, K. M., Beall, C. M., Malfatti, F., Azam, F., Knight, R., Burkart, M. D., Dupont, C. L., and Prather, K. A.: Taxon-specific aerosolization of bacteria and viruses in an experimental ocean-atmosphere mesocosm, Nat. Commun., 9, https://doi.org/10.1038/s41467-018-04409-z, 2018.

Monteil, C. L., Bardin, M., and Morris, C. E.: Features of air masses associated with the deposition of Pseudomonas syringae and Botrytis cinerea by rain and snowfall, 8, 2290–2304, https://doi.org/10.1038/ismej.2014.55, 2014.

Morris, C. E., Georgakopoulos, D. G., and Sands, D. C.: Ice nucleation active bacteria and their potential role in precipitation, J. Phys., IV France, 121, 87–103, https://doi.org/10.1051/jp4:2004121004, 2004.

Morris, C. E., Sands, D. C., Vinatzer, B. A., Glaux, C., Guilbaud, C., Buffière, A., Yan, S., Dominguez, H., and Thompson, B. M.: The life history of the plant pathogen Pseudomonas syringae is linked to the water cycle, ISME J., 2, 321–334, https://doi.org/10.1038/ismej.2007.113, 2008.

Morris, C. E., Soubeyrand, S., Bigg, E. K., Creamean, J. M., and Sands, D. C.: Mapping rainfall feedback to reveal the potential sensitivity of precipitation to biological aerosols, B. Am. Meteorol. Soc., 98, 1109–1118, https://doi.org/10.1175/BAMS-D-15- 00293.1, 2017.

Myers, J. A., Curtis, B. S., and Curtis, W. R.: Improving accuracy of cell and chromophore concentration measurements using optical density, BMC Biophys., 6, 4, https://doi.org/10.1186/2046-1682- 6-4, 2013.

Nemecek-Marshall, M., LaDuca, R., and Fall, R.: High-level expression of ice nuclei in a Pseudomonas syringae strain is induced by nutrient limitation and low temperature, J. Bacteriol., 175, 4062–4070, 1993.

Orsi, W., Biddle, J. F., and Edgcomb, V.: Deep Sequencing of Subseafloor Eukaryotic rRNA Reveals Active Fungi across Marine Subsurface Provinces, PLoS One, 8, e56335, https://doi.org/10.1371/journal.pone.0056335, 2013.

O'Sullivan, D., Murray, B. J., Ross, J. F., Whale, T. F., Price, H. C., Atkinson, J. D., Umo, N. S., and Webb, M. E.: The relevance of nanoscale biological fragments for ice nucleation in clouds, Sci. Rep., 5, 8082, https://doi.org/10.1038/srep08082, 2015.

Overy, D. P., Rämä, T., Oosterhuis, R., Walker, A. K., and Pang, K.-L.: The Neglected Marine Fungi, Sensu stricto, and Their Isolation for Natural Products' Discovery, Mar. Drugs, 17, 42, https://doi.org/10.3390/md17010042, 2019.

Parker, L., Sullivan, C., Forest, T., and Ackley, S.: Ice nucleation activity of antarctic marine microorganisms, Antarct. J., 20, 126– 127, 1985.

Petters, M. D. and Wright, T. P.: Revisiting ice nucleation from precipitation samples, Geophys. Res. Lett., 42, 8758–8766, https://doi.org/10.1002/2015GL065733, 2015.

Ponder, M. A., Gilmour, S. J., Bergholz, P. W., Mindock, C. A., Hollingsworth, R., Thomashow, M. F., and Tiedje, J. M.: Characterization of potential stress responses in ancient Siberian permafrost psychroactive bacteria, FEMS Microbiol. Ecol., 53, 103– 115, https://doi.org/10.1016/j.femsec.2004.12.003, 2005.

Pouleur, S., Richard, C., Martin, J., and Antoun, H.: Ice nucleation activity in Fusarium acuminatum and Fusarium avenaceum, Appl. Environ. Microbiol., 58, 2960–2964, 1992.

Prenni, A. J., Harrington, J. Y., Tjernström, M., DeMott, P. J., Avramov, A., Long, C. N., Kreidenweis, S. M., Olsson, P. Q., and Verlinde, J.: Can Ice-Nucleating Aerosols Affect Arctic Seasonal Climate?, B. Am. Meteorol. Soc., 88, 541–550, https://doi.org/10.1175/BAMS-88-4-541, 2007.

Prenni, A. J., Tobo, Y., Garcia, E., DeMott, P. J., Huffman, J. A., McCluskey, C. S., Kreidenweis, S. M., Prenni, J. E., Pöhlker, C., and Pöschl, U.: The impact of rain on ice nuclei populations at a forested site in Colorado, Geophys. Res. Lett., 40, 227–231, https://doi.org/10.1029/2012GL053953, 2013.

Pruesse, E., Peplies, J., and Glöckner, F. O.: SINA: Accurate high-throughput multiple sequence alignment of ribosomal RNA genes, Bioinformatics, 28, 1823–1829, https://doi.org/10.1093/bioinformatics/bts252, 2012.

Rogers, D. C., DeMott, P. J., Kreidenweis, S. M., and Chen, Y.: Measurements of ice nucleating aerosols during SUCCESS, Geophys. Res. Lett., 25, 1383, https://doi.org/10.1029/97GL03478, 1998.

Sands, D., Langhans, V. E., Scharen, A. L., and Smet, G.: The association between bacteria and rain and possible resultant meteorological implications, J. Hungarian Meteorol. Serv., 86, 148–152, 1982.

Santl-Temkiv, T., Sahyoun, M., Finster, K., Hartmann, S., AugustinBauditz, S., Stratmann, F., Wex, H., Clauss, T., Nielsen, N. W., Sorensen, J. H., Korsholm, U. S., Wick, L. Y., and Karlson, U. G.: Characterization of airborne ice-nucleation-active bacteria and bacterial fragments, Atmos. Environ., 109, 105–117, https://doi.org/10.1016/j.atmosenv.2015.02.060, 2015.

Schnell, R. C. and Vali, G.: Freezing nuclei in marine waters, Tellus, 27, 321–323,

https://doi.org/10.1111/j.2153- 3490.1975.tb01682.x, 1975.

Seinfeld, J. H., Bretherton, C., Carslaw, K. S., Coe, H., DeMott, P. J., Dunlea, E. J., Feingold, G., Ghan, S., Guenther, A. B., Kahn, R., Kraucunas, I., Kreidenweis, S. M., Molina, M. J., Nenes, A., Penner, J. E., Prather, K. A., Ramanathan, V., Ramaswamy, V., Rasch, P. J., Ravishankara, A. R., Rosenfeld, D., Stephens, G., and Wood, R.: Improving our fundamental understanding of the role of aerosol–cloud interactions in the climate system, P. Natl. Acad. Sci. USA, 113, 5781–5790, https://doi.org/10.1073/pnas.1514043113, 2016.

Stohl, A., Hittenberger, M., and Wotawa, G.: Validation of the Lagrangian particle dispersion model FLEXPART against large scale tracer experiment data, Atmos. Environ., 32, 4245–4264, 1998.

Storelvmo, T.: Aerosol Effects on Climate via Mixed-Phase and Ice Clouds, Annu. Rev. Earth Planet. Sci., 45, 199–222, https://doi.org/10.1146/annurev-earth-060115-012240, 2017.

Tamura, K., Stecher, G., Peterson, D., Filipski, A., and Kumar, S.: MEGA6: Molecular Evolutionary Genetics Analysis version 6.0, Mol. Biol. Evol., 30, 2725–2729, https://doi.org/10.1093/molbev/mst197, 2013.

Tisthammer, K. H., Cobian, G. M., and Amend, A. S.: Global biogeography of marine fungi is shaped by the environment, Fungal Ecol., 19, 39–46, https://doi.org/10.1016/j.funeco.2015.09.003, 2016.

Tong, Y. and Lighthart, B.: Solar Radiation Is Shown to Select for Pigmented Bacteria in the Ambient Outdoor Atmosphere, Photochem. Photobiol., 65, 103–106, https://doi.org/10.1111/j.1751- 1097.1997.tb01884.x, 1997.

Vaïtilingom, M., Attard, E., Gaiani, N., Sancelme, M., Deguillaume, L., Flossmann, A. I., Amato, P., and Delort, A. M.: Long-term features of cloud microbiology at the puy de Dôme (France), Atmos. Environ., 56, 88–100, https://doi.org/10.1016/j.atmosenv.2012.03.072, 2012.

Vali, G.: Freezing Nucleus Content of Hail and Rain in Alberta, J. Appl. Meteorol., 10, 73–78, 1971.

Vali, G.: Comments on "Freezing Nuclei Derived from Soil Particles," J. Atmos. Sci., 31, 1457–1459, https://doi.org/10.1175/1520- 0469(1974)031¡1457:CONDFS¿2.0.CO;2, 1974.

Vergara-Temprado, J., Murray, B. J., Wilson, T. W., O'Sullivan, D., Browse, J., Pringle, K. J., Ardon-Dryer, K., Bertram, A. K., Burrows, S. M., Ceburnis, D., DeMott, P. J., Mason, R. H., O'Dowd, C. D., Rinaldi, M., and Carslaw, K. S.: Contribution of feldspar and marine

organic aerosols to global ice nucleating particle concentrations, Atmos. Chem. Phys., 17, 3637–3658, https://doi.org/10.5194/acp-17-3637-2017, 2017.

Vergara-Temprado, J., Miltenberger, A. K., Furtado, K., Grosvenor, D. P., Shipway, B. J., Hill, A. A., Wilkinson, J. M., Field, P. R., Murray, B. J., and Carslaw, K. S.: Strong control of Southern Ocean cloud reflectivity by icenucleating particles, P. Natl. Acad. Sci. USA, 115, 2687–2692, https://doi.org/10.1073/pnas.1721627115, 2018.

Walters, W., Hyde, E. R., Berg-lyons, D., Ackermann, G., Humphrey, G., Parada, A., Gilbert, J. A., and Jansson, J. K.: Improved bacterial 16S rRNA gene (V4 and V4-5) and fungal internal transcribed spacer marker gene primers for microbial community surveys, mSystems, 1, e0009-15, https://doi.org/10.1128/mSystems.00009-15, 2015.

Wex, H., Augustin-Bauditz, S., Boose, Y., Budke, C., Curtius, J., Diehl, K., Dreyer, A., Frank, F., Hartmann, S., Hiranuma, N., Jantsch, E., Kanji, Z. A., Kiselev, A., Koop, T., Möhler, O., Niedermeier, D., Nillius, B., Rösch, M., Rose, D., Schmidt, C., Steinke, I., and Stratmann, F.: Intercomparing different devices for the investigation of ice nucleating particles using Snomax® as test substance, Atmos. Chem. Phys., 15, 1463– 1485, https://doi.org/10.5194/acp-15-1463-2015, 2015.

Wilson, S. L. and Walker, V. K.: Selection of low-temperature resistance in bacteria and potential applications, Environ. Technol., 31, 943–956, https://doi.org/10.1080/09593331003782417, 2010.

Wilson, T. W., Ladino, L. A., Alpert, P. A., Breckels, M. N., Brooks, I. M., Browse, J., Burrows, S. M., Carslaw, K. S., Huffman, J. A., Judd, C., Kilthau, W. P., Mason, R. H., McFiggans, G., Miller, L. A., Nájera, J. J., Polishchuk, E., Rae, S., Schiller, C. L., Si, M., Temprado, J. V., Whale, T. F., Wong, J. P. S., Wurl, O., Yakobi-Hancock, J. D., Abbatt, J. P. D., Aller, J. Y., Bertram, A. K., Knopf, D. A., and Murray, B. J.: A marine biogenic source of atmospheric ice-nucleating particles, Nature, 525, 234–238, https://doi.org/10.1038/nature14986, 2015.

Wright, E. S.: DECIPHER: harnessing local sequence context to improve protein multiple sequence alignment, BMC Bioinformatics 16, 322, https://doi.org/10.1186/s12859-015-0749-z, 2015.

Wright, T. P., Hader, J. D., McMeeking, G. R., and Petters, M. D.: High relative humidity as a trigger for widespread release of ice nuclei, Aerosol Sci. Technol., 48, i–v, https://doi.org/10.1080/02786826.2014.968244, 2014.

Wright E. S.: DECIPHER: harnessing local sequence context to improve protein multiple sequence alignment, BMC bioinformatics, 16, 322, https://doi.org/10.1186/s12859-015-0749-z, 2015.

Yang, J., Wang, Z., Heymsfield, A. J., DeMott, P. J., Twohy, C. H., Suski, K. J., and Toohey, D. W.: High ice concentration observed in tropical maritime stratiform mixed-phase clouds with top temperatures warmer than –8 °C, Atmos. Res., 233, 104719, https://doi.org/10.1016/j.atmosres.2019.104719, 2020.

ZoBell, C. E.: Marine Bacteriology, Annu. Rev. Biochem., 16, 565– 586, 1947.

4.7 Supplement

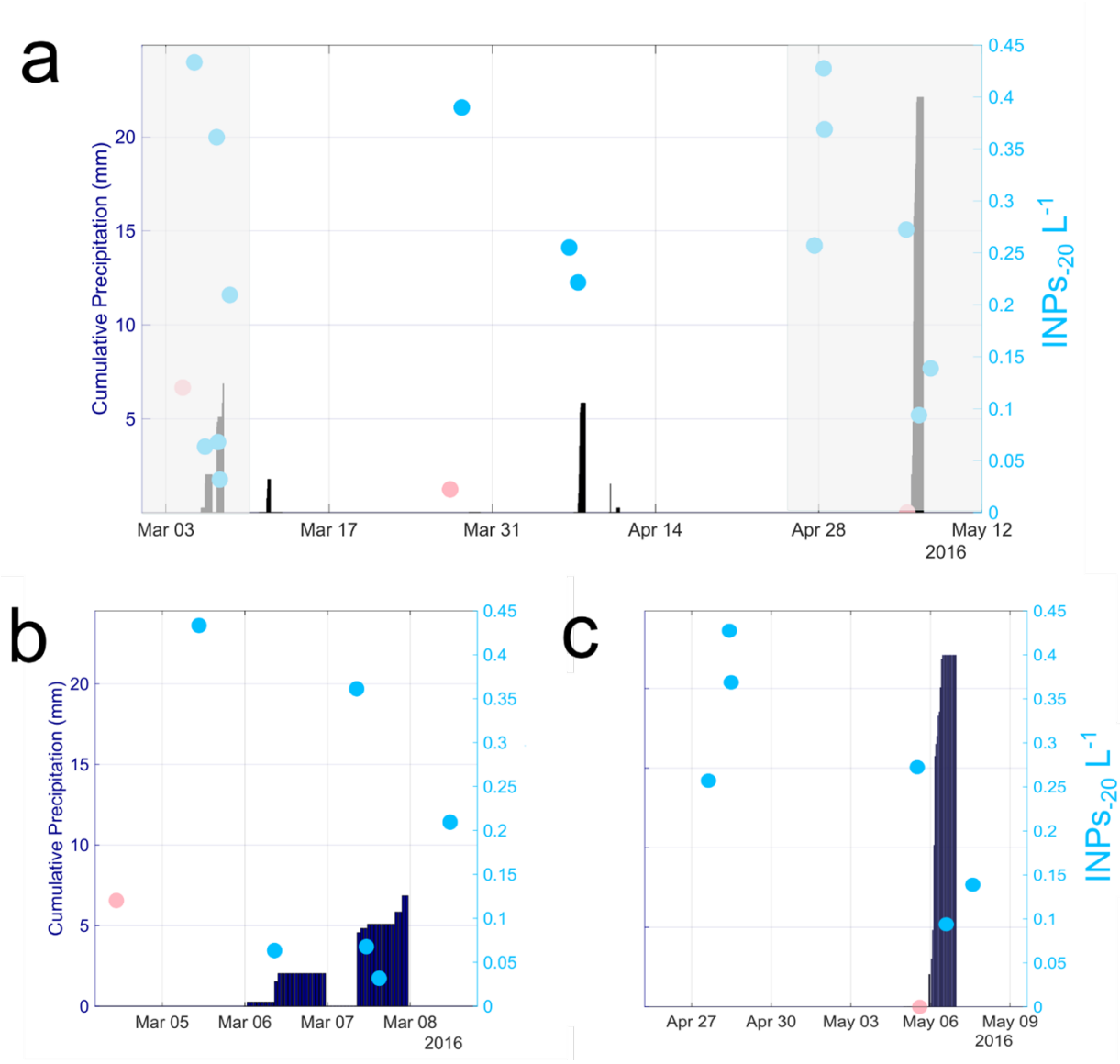

Figure 4.5: INP concentrations at -20 °C in aerosol collected at the Scripps Institution of Oceanography Pier (32°52'01.4"N 117°15'26.5"W) during and between precipitation events. INP concentrations in aerosol are represented by blue circles, and pink circles indicate background INP levels in field blanks. Dark blue bars indicate cumulative precipitation over a 24-hr period. (a) Highlighted in grey are three sampling days during which aerosol samples were available immediately before, during and after precipitation events. (b) Precipitation events over March 6 and 7, 2016 (left grey region in Fig. 4.9a) are magnified for better visibility. (c) The precipitation event from May 5 to May 6, 2016 (right grey region in Fig. 4.9a) is magnified for better visibility. For all three periods, INP concentrations in aerosol decrease during precipitation events, indicating sweepout of INPs by hydrometeors.

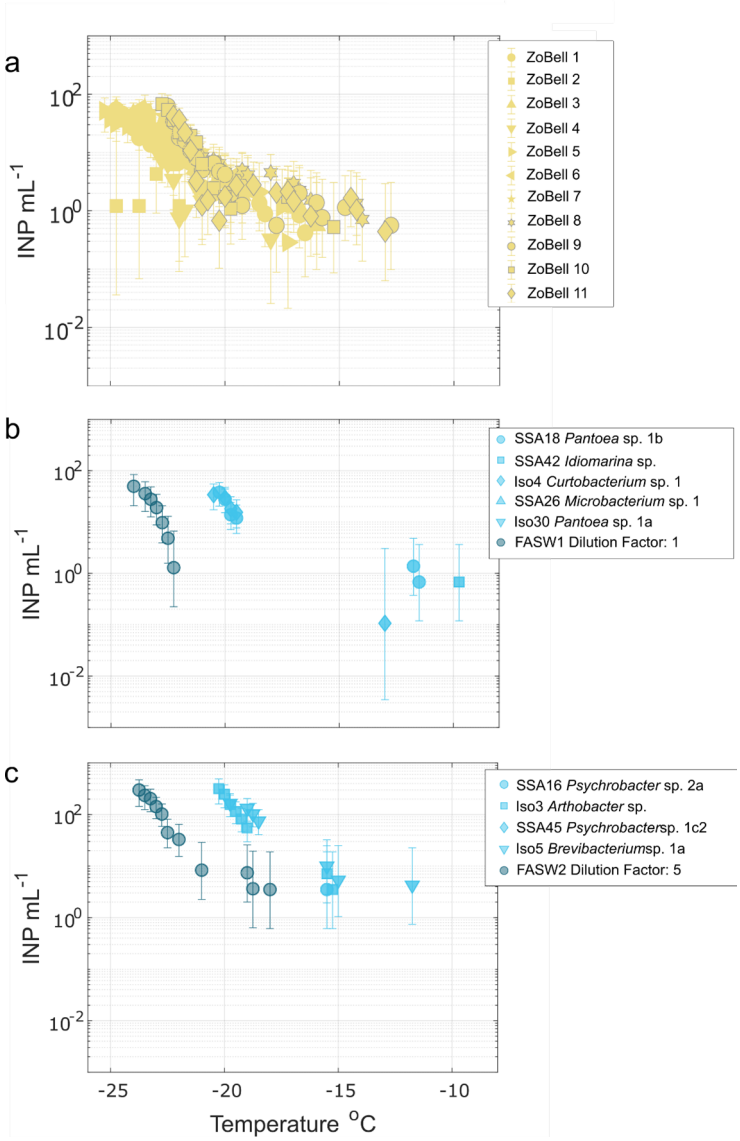

Figure 4.6: Controls of IN measurements. (a) IN activity of 11 ZoBell media blanks. (b) IN activity of selected media–free isolate with a dilution factor of 1 (undiluted). Filtered autoclaved seawater (FASW) was used for resuspension of the isolates for INP measurement. (c) IN activity of selected media–free isolates with a dilution factor of 5. Some isolates were diluted with FASW to decrease opacity such that freezing events could successfully be detected by the camera, and the IN spectra of the isolates and FASW are scaled by the same dilution factor for analysis of the isolate's ice nucleation ability beyond its media (Methods Sec. 4.3.4). Only INP concentrations that were significantly enhanced above FASW ($p < 0.005$, see Methods Sec. 4.3.4) are shown in (b) and (c).

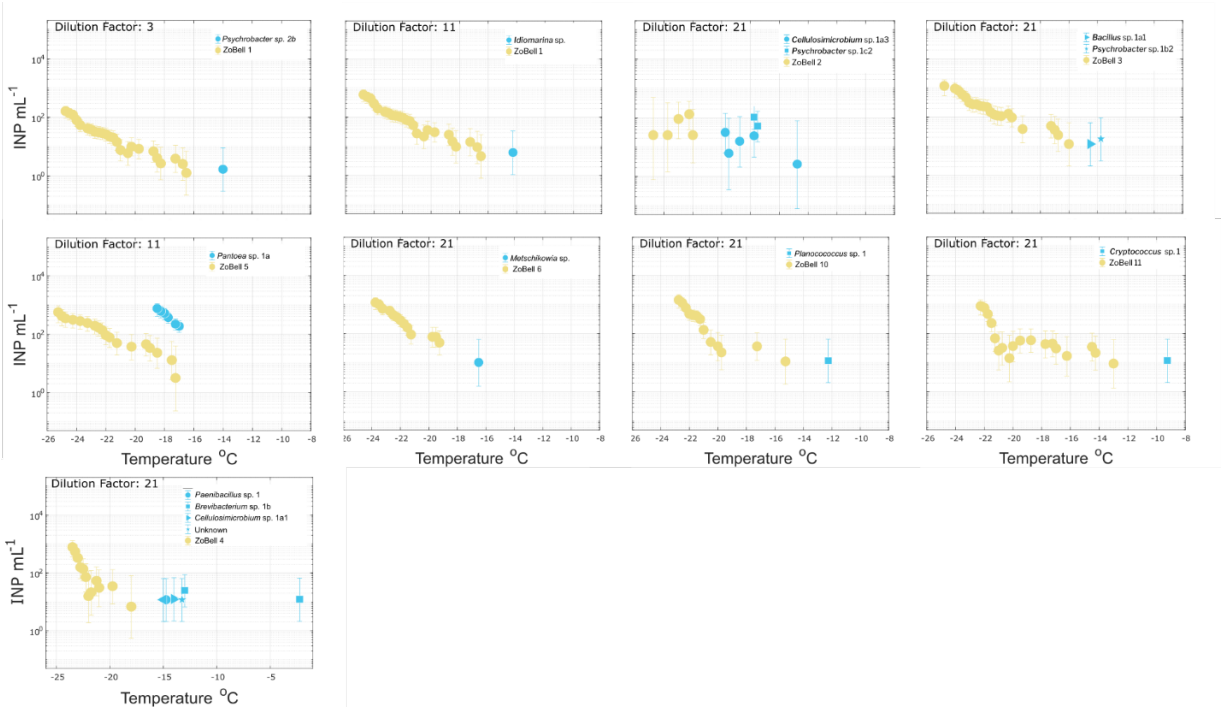

Figure 4.7: IN spectra of the 14 IN isolates and their respective ZoBell media samples, with IN spectra of both ZoBell and isolates scaled by the isolates' dilution factor. All isolates were diluted with additional ZoBell to decrease opacity such that freezing events could be detected with the camera. Only INP concentrations that were significantly enhanced above ZoBell ($p < 0.005$) are shown. See Methods section for description of the criterion applied to determine significant ice nucleation behavior above the background ZoBell levels.

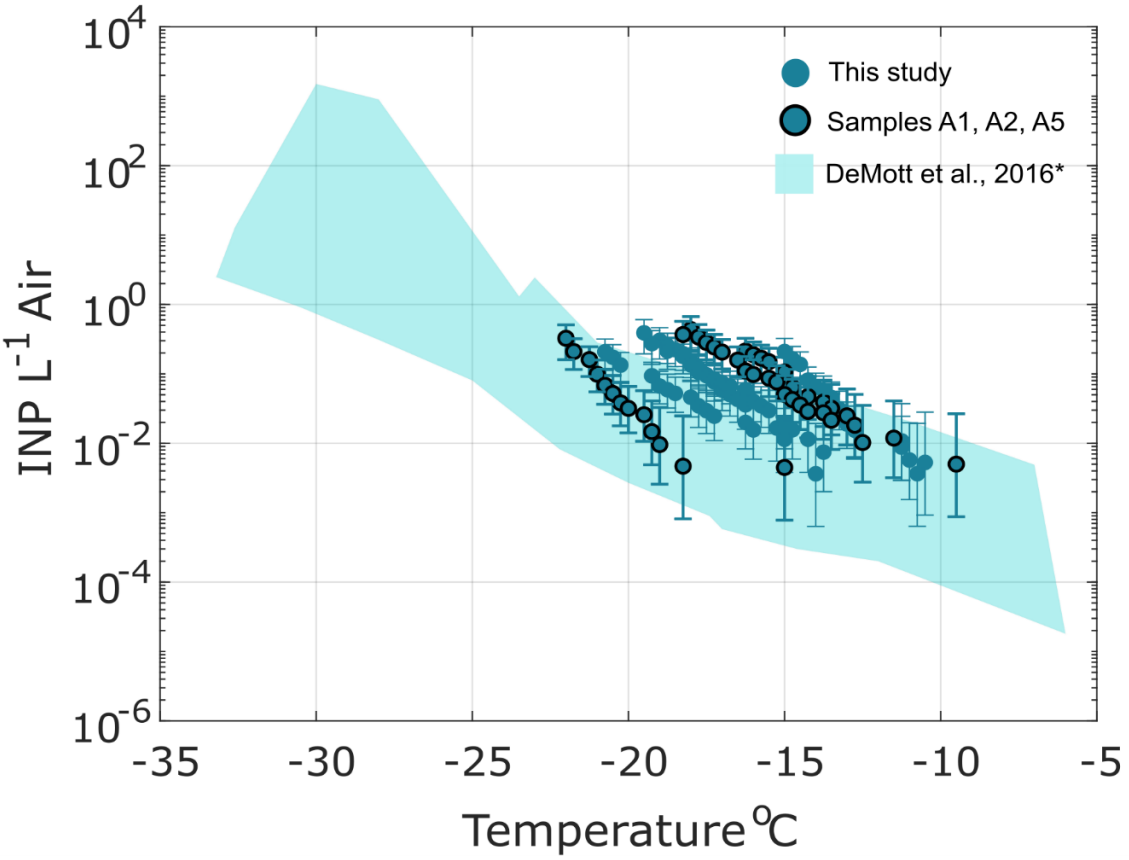

Figure 4.8: INP concentrations per liter air sampled for 7 aerosol samples collected at Ellen Browning Scripps Memorial Pier at Scripps Institution of Oceanography (SIO) (32.8662 °N, 117.2544 °W) between March and May 2016. The blue shaded region represents the composite spectrum of INP concentrations observed in a range of marine and coastal environments including the Caribbean, East Pacific and Bering Sea as well as laboratory-generated nascent sea spray (DeMott et al., 2016)*. INP spectra of the three samples from which IN isolates were derived (A1, A2, A5, see Table 1 and S1) are outlined in black. While the INPs observed in aerosol samples compare with INP concentrations in marine environments at warmer temperatures (DeMott et al., 2016), concentrations are enhanced at moderate to cold temperatures indicating terrestrial sources may have additionally contributed.
*DeMott et al., 2016 data has been updated with a completed dataset for the ICE-T study, as shown in (Yang et al., 2020).

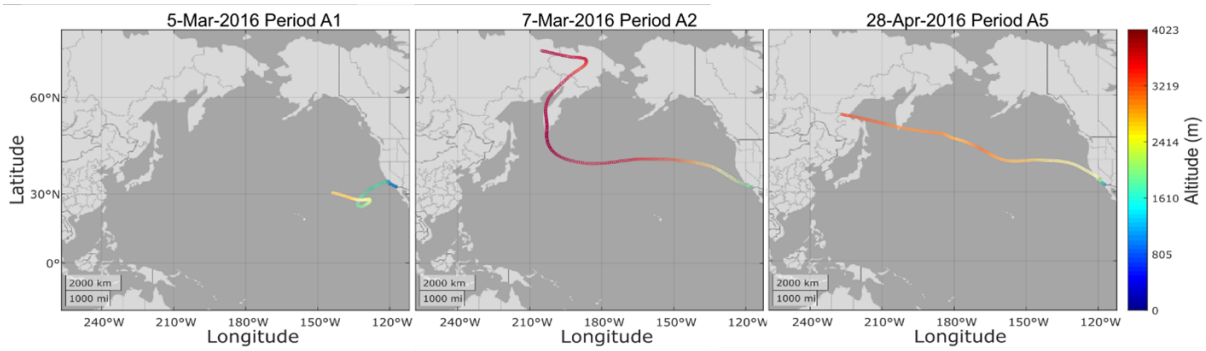

Figure 4.9: 10-day back-trajectories from the SIO Pier (32.8662 °N, 117.2544 °W, 8m above MLLW) during the 3 aerosol sampling periods from which IN isolates originated, A1, A2, and A5 (see Tables 1, S1). FLEXPART back-trajectories were used to estimate potential aerosol sources. Shown are the particle centroids of back-trajectories. Origins of particles in the 10-day simulation are shown to range from 4000 m over Russia to 3000 m over the Northeast Pacific. FLEXPART results suggest a dominance of marine particle sources to aerosol samples.

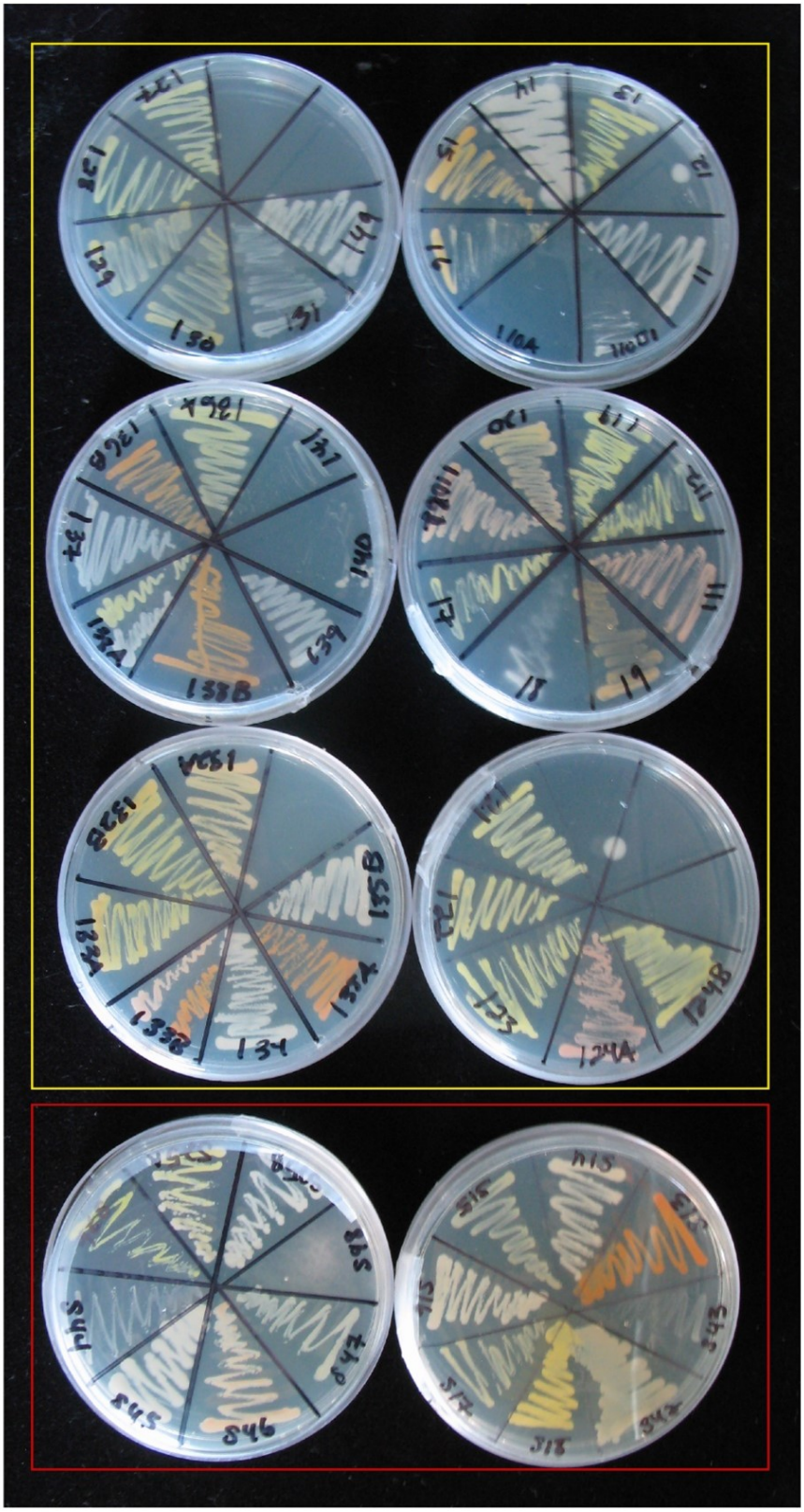

Figure 4.10: Image of aerosol (red box) and precipitation (yellow box) isolates on agar plates. Isolates derived from cultivation-based isolation.

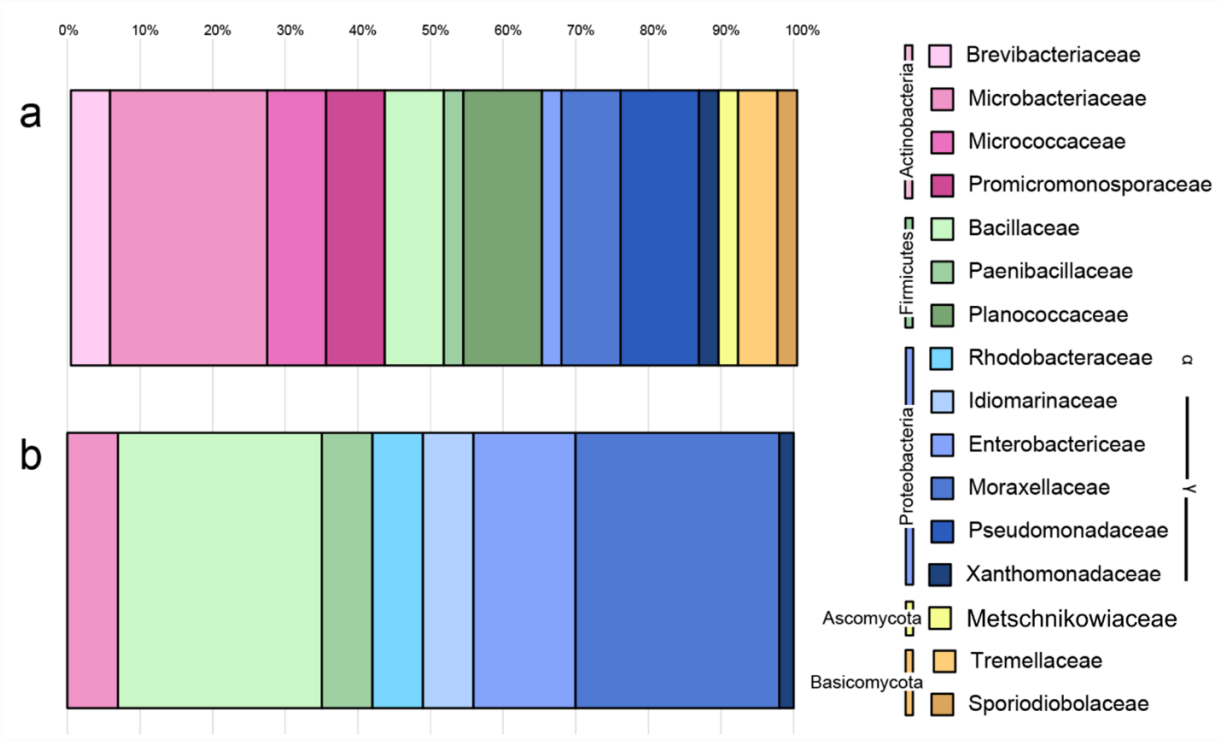

Figure 4.11: Taxonomic distributions of precipitation (a) and aerosol (b) isolates. 83% of the unique families and genera identified in aerosol were common to those found in precipitation.

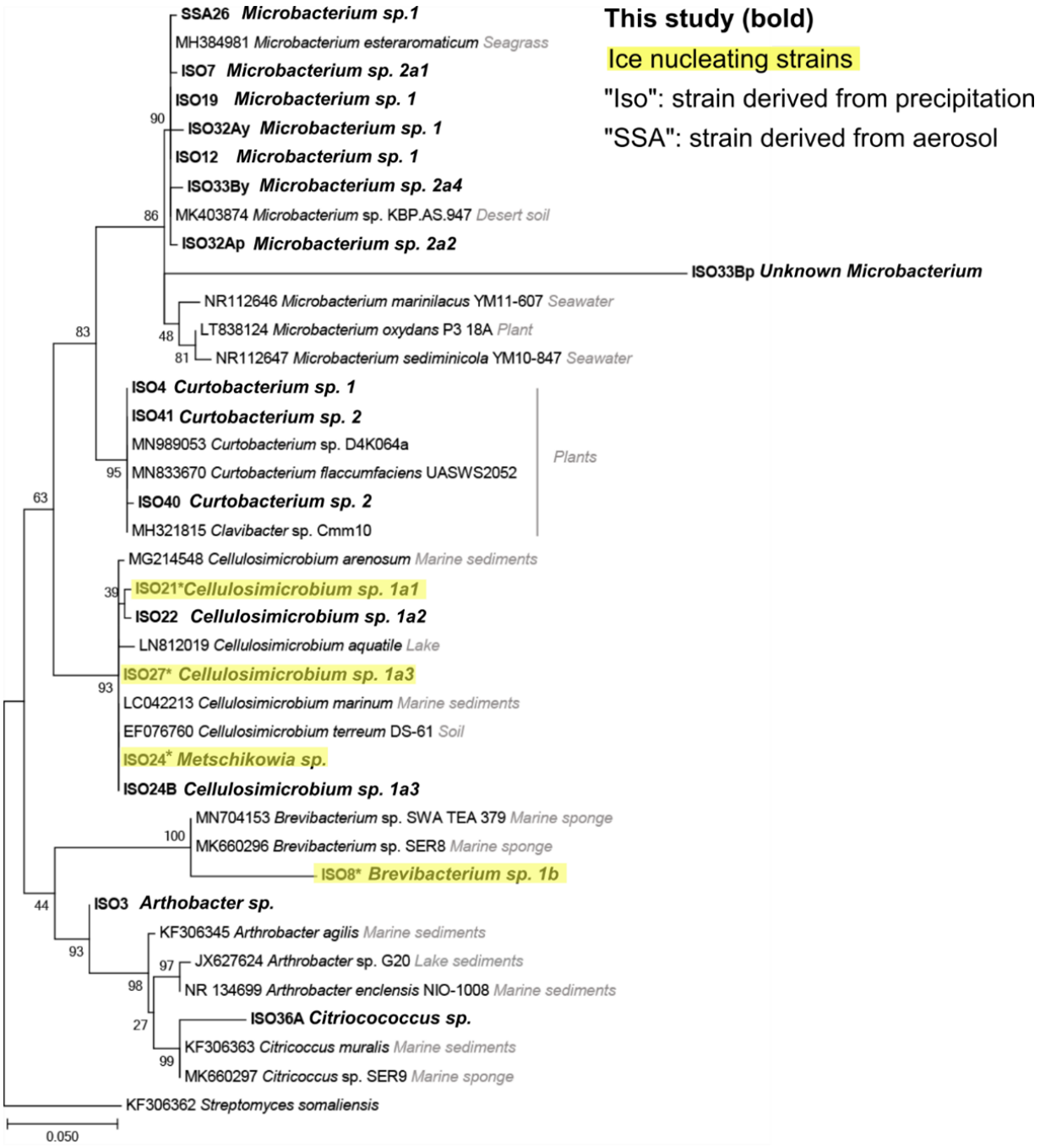

Figure 4.12: Phylogenetic relationships of isolates (in bold) related to Actinobacteria reference sequences. The environmental source of the reference sequences (based on NCBI metadata) is indicated in grey. Isolates with ice nucleating properties are shaded in yellow; bootstrap values ($n = 500$) are indicated at nodes; scale bar represents changes per positions.

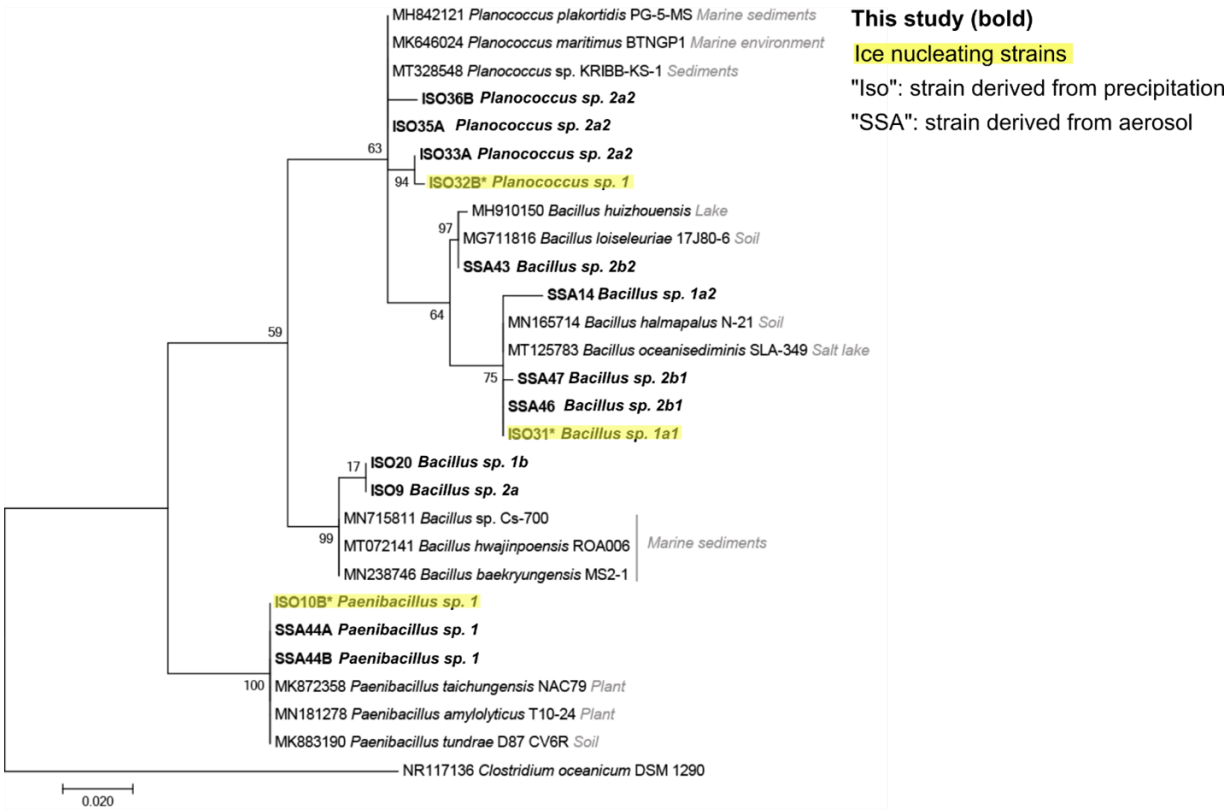

Figure 4.13: Phylogenetic relationships of isolates (in bold) related to Firmicutes reference sequences. The environmental source of the reference sequences based on NCBI metadata is indicated in grey. Isolates with ice nucleating properties are shaded in yellow; bootstrap values ($n = 500$) are indicated at nodes; scale bar represents changes per positions.

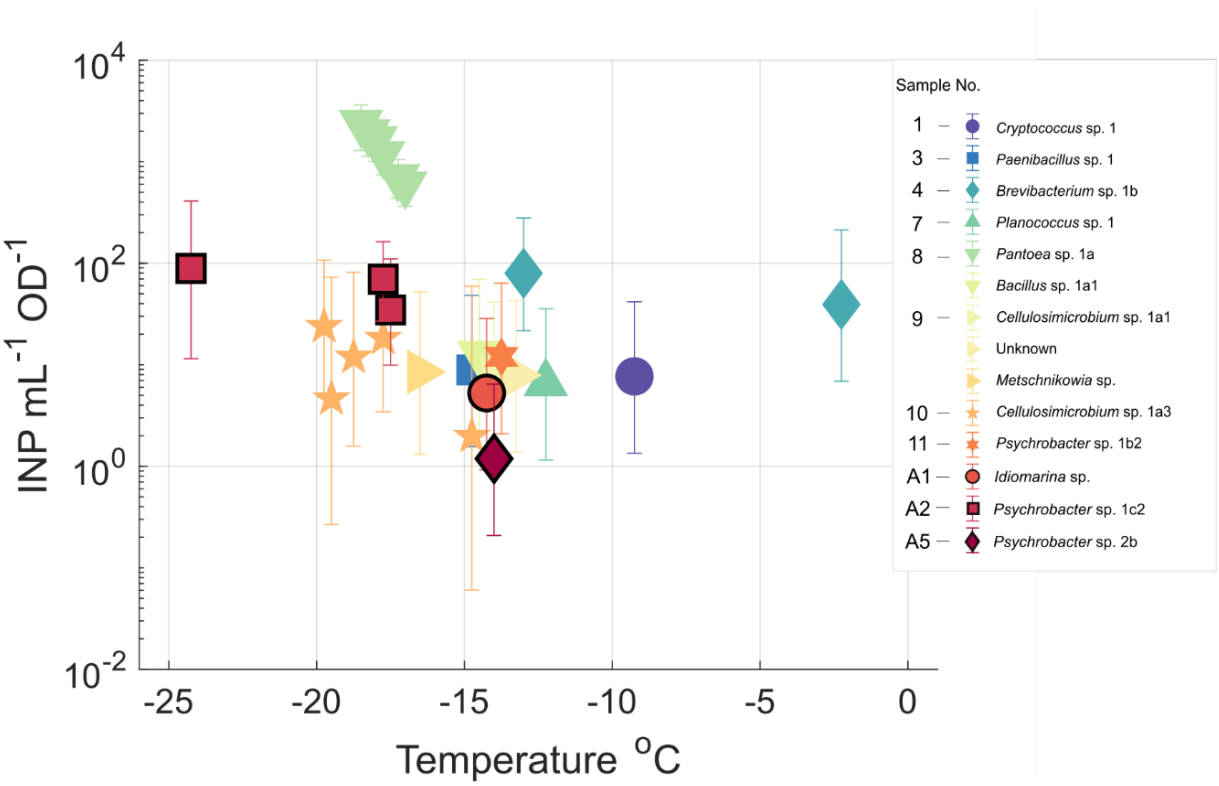

Figure 4.14: INP concentrations observed in 14 halotolerant isolates derived from precipitation and aerosol samples, normalized to culture OD (590 nm). Sample numbers in the legend indicate the precipitation or aerosol sample from which the isolate was derived (see Table 4.4). Datapoints corresponding to isolates from aerosol are outlined in black. Error bars indicate 95% confidence intervals (see Methods Sec. 4.3.4). Only freezing activity that was significantly enhanced ($p < 0.005$) above ZoBell growth media is shown.

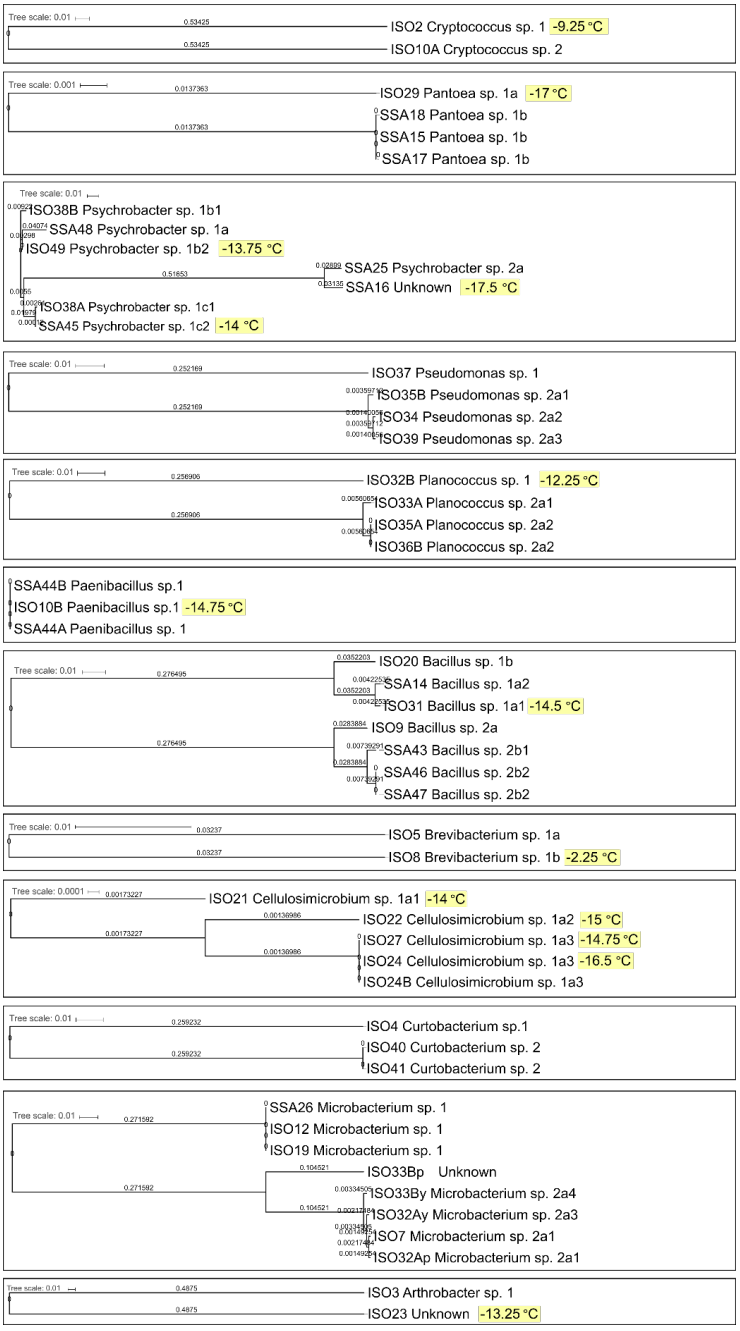

Figure 4.15: Relationship of isolates within the same OTUs using multiple sequence alignments of 16S rRNA gene sequences. Multiple sequence alignments were used to generate phylogenetic trees. The resulting branch distances were used to label isolates within the same OTU. Distances > 0.1 were given a new number. This division was further subdivided by distances > 0.01 which were given a unique letter. Distances < 0.01 were considered possible duplicates. 18S fungal sequences were obtained from 16S primers due to coamplification (see Methods Sec. 4.3.2). Freezing temperatures are shown in yellow boxes to indicate isolates with detected ice nucleation activity.

Table 4.2: Identity and characteristics of precipitation and aerosol isolates. Aerosol sampling period labels begin with "A" to distinguish from precipitation sampling periods 1-11 (see Table 4.4 for precipitation and aerosol sampling times). Taxonomy is denoted by results of BLAST from 16S rRNA gene sequences, percent identity to BLAST assignments, and membership to taxonomic divisions. Isolate identifiers derive from results of multiple sequence alignment analysis (Fig. 4.6). "IN onset temperature" refers to the first temperature at which isolates exhibited significant IN behavior above the background of the ZoBell media in which they were suspended. 18S fungal sequences were obtained from 16S primers due to coamplification (see Methods Sec. 4.3.2). Duplicate isolates that were derived from the same sampling period were not featured in Fig. 4.3a or Fig. 4.4a and were not counted toward the 14 total identified ice nucleating isolates, but each duplicate was tested for its IN ability and results are shown here.

Isolate ID	Isolate	Sampling Period	IN Onset Temperature °C	BLAST Identity	% Identity	Phylum	Class	Order	Family
Iso1	*Rhodoturula* sp.	1	n/a	*Rhodotorula mucilaginosa*	99%	Basidiomycota	Urediniomycetes	Sporidiales	Sporiodiobolaceae
Iso2	*Cryptococcus* sp. 1	1	-9.25	*Cryptococcus aureus*	100%	Basidiomycota	Tremellomycetes	Tremellales	Tremellaceae
Iso3	*Arthrobacter* sp.	2	n/a	*Arthrobacter sp. (A. luteolus, A.citreus)*	100%	Actinobacteria	Actinobacteria	Actinomycetales	Micrococcaceae
Iso5	*Brevibacterium* sp. 1a	2	n/a	*Brevibacterium sp. (B.linens)*	100%	Actinobacteria	Actinobacteria	Actinomycetales	Brevibacteriaceae
Iso4	*Curtobacterium* sp. 1	2	n/a	*Curtobacterium sp. (C. pusillum, C. flaccumfaciens, C. oceanosedimentum)*	100%	Actinobacteria	Actinobacteria	Actinomycetales	Microbacteriaceae
Iso6	*Lysobacter* sp.	2	n/a	*Lysobacter concretionis*	99%	Proteobacteria	Gammaproteobacteria	Xanthomonadales	Xanthomonadaceae
Iso10A	*Cryptococcus* sp. 2	3	n/a	*Cryptococcus sp. (C. flavescens, C. aureus)*	99%	Basidiomycota	Tremellomycetes	Tremellales	Tremellaceae
Iso10B	*Paenibacillus* sp. 1	3	-14.75	*Paenibacillus sp.*	100%	Firmicutes	Bacilli	Bacillales	Paenibacillaceae
Iso9	*Bacillus* sp. 2a	4	n/a	*Bacillus sp. (B. baekryungensis, B. hwajinpoensis)*	100%	Firmicutes	Bacilli	Bacillales	Bacillaceae
Iso8	*Brevibacterium* sp. 1b	4	-2.25	*Brevibacterium sp. (B. luteolum)*	97%	Actinobacteria	Actinobacteria	Actinomycetales	Brevibacteriaceae
Iso20	*Bacillus* sp. 1b	5	n/a	*Bacillus sp. (B. baekryungensis, B. hwajinpoensis)*	100%	Firmicutes	Bacilli	Bacillales	Bacillaceae
Iso12	*Microbacterium* sp. 1	5	n/a	*Microbacterium esteraromaticum*	100%	Actinobacteria	Actinobacteria	Actinomycetales	Microbacteriaceae
Iso19	*Microbacterium* sp. 1	5	n/a	*Microbacterium esteraromaticum*	100%	Actinobacteria	Actinobacteria	Actinomycetales	Microbacteriaceae
Iso7	*Microbacterium* sp. 2a1	5	n/a	*Microbacterium esteraromaticum*	100%	Actinobacteria	Actinobacteria	Actinomycetales	Microbacteriaceae
Iso36A	*Citricoccocus* sp.	6	n/a	*Citricoccocus sp. (C. muralis)*	97%	Actinobacteria	Actinobacteria	Actinomycetales	Micrococcaceae
Iso40	*Curtobacterium* sp. 2	6	n/a	*Curtobacterium sp.*	100%	Actinobacteria	Actinobacteria	Actinomycetales	Microbacteriaceae
Iso41	*Curtobacterium* sp. 2	6	n/a	*Curtobacterium flaccumfaciens*	100%	Actinobacteria	Actinobacteria	Actinomycetales	Microbacteriaceae
Iso35A	*Planococcus* sp. 2a2	6	n/a	*Planococcus sp.(P. maritimus, P. plakortidis, P. rifietoesis)*	100%	Firmicutes	Bacilli	Bacillales	Planococcaceae
Iso36B	*Planococcus* sp. 2a2	6	n/a	*Planococcus sp.*	100%	Firmicutes	Bacilli	Bacillales	Planococcaceae
Iso37	*Pseudomonas* sp. 1	6	n/a	*Pseudomonas sp. (P. synxantha, P. grimontii, P. extremaustralis)*	100%	Proteobacteria	Gammaproteobacteria	Pseudomondales	Pseudomonadaceae
Iso35B	*Pseudomonas* sp. 2a1	6	n/a	*Pseudomonas veronii*	100%	Proteobacteria	Gammaproteobacteria	Pseudomondales	Pseudomonadaceae
Iso34	*Pseudomonas* sp. 2a2	6	n/a	*Pseudomonas sp. (P. synxantha, P. grimontii, P. extremaustralis)*	100%	Proteobacteria	Gammaproteobacteria	Pseudomondales	Pseudomonadaceae
Iso39	*Pseudomonas* sp. 2a3	6	n/a	*Pseudomonas sp. (P. synxantha, P. mucidolens, P. grimontii)*	100%	Proteobacteria	Gammaproteobacteria	Pseudomondales	Pseudomonadaceae
Iso38B	*Psychrobacter* sp. 1b1	6	n/a	*Psychrobacter sp. (P. maritimus)*	100%	Proteobacteria	Gammaproteobacteria	Pseudomondales	Moraxellaceae
Iso38A	*Psychrobacter* sp. 1c1	6	n/a	*Psychrobacter sp.*	99%	Proteobacteria	Gammaproteobacteria	Pseudomondales	Moraxellaceae
Iso32Ap	*Microbacterium* sp. 2a2	7	n/a	*Microbacterium esteraromaticum*	99%	Actinobacteria	Actinobacteria	Actinomycetales	Microbacteriaceae
Iso33By	*Microbacterium* sp. 2a4	7	n/a	*Microbacterium esteraromaticum*	99%	Actinobacteria	Actinobacteria	Actinomycetales	Microbacteriaceae
Iso32B	*Planococcus* sp. 1	7	-12.25	*Planococcus maritimus*	99%	Firmicutes	Bacilli	Bacillales	Planococcaceae
Iso33A	*Planococcus* sp. 2a1	7	n/a	*Planococcus sp.*	99%	Firmicutes	Bacilli	Bacillales	Planococcaceae
Iso33Bp	Unknown	7	n/a	Unknown *Microbacterium sp.*	89%	Actinobacteria	Actinobacteria	Actinomycetales	Microbacteriaceae
Iso31	*Bacillus* sp. 1a1	8	-14.5	*Bacillus halmapalus*	100%	Firmicutes	Bacilli	Bacillales	Bacillaceae
Iso29	*Pantoea* sp. 1a	8	-17	*Pantoea sp. (P. agglomerans, P. ananatis)*	100%	Proteobacteria	Gammaproteobacteria	Enterobacteriales	Enterobacteriaceae
Iso30	*Pantoea* sp. 1a	8	-16.75	*Pantoea sp. (P. agglomerans , P. ananatis)*	100%	Proteobacteria	Gammaproteobacteria	Enterobacteriales	Enterobacteriaceae
Iso21	*Cellulosimicrobium* sp. 1a1	9	-14	*Cellulosimicrobium sp. (C. funkei, C.cellulans, C. marinum)*	100%	Actinobacteria	Actinobacteria	Actinomycetales	Promicromonosporaceae
Iso22	*Cellulosimicrobium* sp. 1a2	9	-15	*Cellulosimicrobium sp. (C. funkei, C.cellulans, C. marinum)*	99%	Actinobacteria	Actinobacteria	Actinomycetales	Promicromonosporaceae
Iso24B	*Cellulosimicrobium sp.* 1a3	9	n/a	*Cellulosimicrobium sp. (C. funkei, C.cellulans, C. marinum)*	100%	Actinobacteria	Actinobacteria	Actinomycetales	Promicromonosporaceae
Iso24A	*Metschnikowia* sp.	9	-16.5	*Metschnikowia sp. (M. zobellii, M. krissii, M. reukaufii)*	99%	Ascomycota	Saccharomycetes	Saccharomycetales	Metschnikowiaceae
Iso23	Unknown	9	-13.25	Unknown *Arthrobacter sp.*	86%	Actinobacteria	Actinobacteria	Actinomycetales	Micrococcaceae
Iso27	*Cellulosimicrobium* sp. 1a3	10	-14.75	*Cellulosimicrobium sp. (C. funkei, C.cellulans, C. marinum)*	100%	Actinobacteria	Actinobacteria	Actinomycetales	Promicromonosporaceae
Iso28	*Cellulosimicrobium* sp. 1a3	10	-14.5	*Cellulosimicrobium sp. (C. funkei, C.cellulans, C. marinum)*	100%	Actinobacteria	Actinobacteria	Actinomycetales	Promicromonosporaceae
Iso49	*Psychrobacter* sp. 1b2	11	-13.75	*Psychrobacter sp. (P. pulmonis, P. faecalis)*	99%	Proteobacteria	Gammaproteobacteria	Pseudomondales	Moraxellaceae
SSA42	*Idiomarina* sp.	A1	-14.25	*Idiomarina fontislapidosi*	100%	Proteobacteria	Gammaproteobacteria	Alteromonadales	Idiomarinaceae
SSA14	*Bacillus* sp. 1a2	A2	n/a	*Bacillus sp. (B. aquimaris, B. vietnamensis)*	100%	Firmicutes	Bacilli	Bacillales	Bacillaceae
SSA15	*Pantoea* sp. 1b	A2	n/a	*Pantoea sp. (P. ananatis, P. stewartii, P. agglomerans)*	100%	Proteobacteria	Gammaproteobacteria	Enterobacteriales	Enterobacteriaceae
SSA17	*Pantoea* sp. 1b	A2	n/a	*Pantoea sp. (P. ananatis, P. stewartii, P. agglomerans)*	100%	Proteobacteria	Gammaproteobacteria	Enterobacteriales	Enterobacteriaceae
SSA18	*Pantoea* sp. 1b	A2	n/a	*Pantoea sp. (P. ananatis, P. stewartii, P. agglomerans)*	100%	Proteobacteria	Gammaproteobacteria	Enterobacteriales	Enterobacteriaceae
SSA16	*Psychrobacter* sp. 2a	A2	-17.5	*Psychrobacter sp.*	93%	Proteobacteria	Gammaproteobacteria	Pseudomondales	Moraxellaceae
SSA43	*Bacillus* sp. 2b2	A3	n/a	*Bacillus sp. (B. muralis)*	100%	Firmicutes	Bacilli	Bacillales	Bacillaceae
SSA44A	*Paenibacillus* sp. 1	A4	n/a	*Paenibacillus sp. (P. tundrae, P. amyloyticus, P. agarideverons, P. taichungensis)*	100%	Firmicutes	Bacilli	Bacillales	Paenibacillus
SSA46	*Bacillus* sp. 2b1	A5	n/a	*Bacillus halmapalus*	100%	Firmicutes	Bacilli	Bacillales	Bacillaceae
SSA45	*Psychrobacter* sp. 1c2	A5	-14	*Psychrobacter sp.*	100%	Proteobacteria	Gammaproteobacteria	Pseudomondales	Moraxellaceae
SSA47	*Bacillus* sp. 2b1	A6	n/a	*Bacillus halmapalus*	100%	Firmicutes	Bacilli	Bacillales	Bacillaceae
SSA48	*Psychrobacter* sp. 1a	A6	n/a	*Psychrobacter sp. (P. pulmonis, P. faecalis)*	96%	Proteobacteria	Gammaproteobacteria	Pseudomondales	Moraxellaceae
SSA26	*Microbacterium* sp 1	A7	n/a	*Microbacterium esteraromaticum*	99%	Actinobacteria	Actinobacteria	Actinomycetales	Microbacteriaceae
SSA25	*Psychrobacter* sp. 2b	A7	n/a	*Psychrobacter sp. (P. pulmonis, P. faecalis)*	100%	Proteobacteria	Gammaproteobacteria	Pseudomondales	Moraxellaceae

Table 4.3: Cloud characteristics during 11 precipitation events over the sampling site: SIO Pier (32.8662 °N, 117.2544 °W). Cloud base and top altitudes were estimated using the RH product of the High-Resolution Rapid Refresh real-time atmospheric model, and three altitudes within the cloud were used as particle release points for FLEXPART back-trajectories (see Figure 6.1): cloud top, cloud base, and middle (halfway between). Regions where RH (Relative Humidity) ¿ 95% were considered for all events except Sampling Period 4 and 5, when a criterion of > 90 % was applied. The hourly products closest in time to the precipitation sampling period were used. When cloud depth and altitudes changed over the sampling period, the lowest cloud base and highest cloud altitude were selected as release points for FLEXPART back-trajectories.

	Local date	Local time start	Local time stop	UTC date	UTC time	RH criteria	Temp (K)	Pressure (mb)	Geopotential height (m)
1	3/6/2016	9:07	10:07	3/6/2016	17:07 – 18:07	>95%	283 – 274	950 – 750	800 – 2000
2	3/7/2016	18:30	19:30	3/8/2016	2:30 – 3:30	>95%	275 – 268	850 – 750	1700 – 3000
3	3/11/2016	16:20	17:20	3/12/2016	00:20 – 1:20	>95%	282 – 275	950 – 800	500 – 2200
4	3/12/2016	8:20	9:14	3/12/2016	16:20 – 17:14	> 90%	280 – 278	925 – 900	1000 – 1100
5	3/29/2016	23:35	0:35	3/30/2016	6:35 – 7:35	> 90%	270, 275	800, 900	2000, 700
6	4/7/2016	8:15	11:00	4/7/2016	15:15 – 18:00	> 95%	278 – 270	1000, 750 – 650	2200 – 4000
7	4/7/2016	12:07	13:07	4/7/2016	19:07 – 20:07	> 95%	275 – 265	750 – 600	2000 – 4000
8	5/5/2016	22:59	23:59	5/6/2016	6:00 – 7:00	> 95%	275 – 273	825 – 750	1100 – 2100
9	5/6/2016	2:59	3:59	5/6/2016	10:00 – 11:00	>95%	282 – 270	875 – 700	1000 – 3000
10	5/6/2016	4:59	5:59	5/6/2016	13:00 – 14:00	> 95%	275 – 273	825 – 675	2000 – 3000
11	5/6/2016	8:59	9:59	5/6/2016	17:00 – 18:00	> 95%	275 – 270	825 – 750	1800 – 2800

Table 4.4: Sampling periods for precipitation and aerosol samples collected on SIO Pier (32.8662 °N, 117.2544 °W). Synoptic weather conditions for each precipitation event were determined using National Weather Service Weather Prediction Center Surface Analysis Satellite Composite products.

Precipitation

Sampling Period	Local Date	Local Time	UTC Date	UTC time	Number of Isolates	General characteristics
1	3/6/2016	9:07 – 10:07	3/6/2016	17:07 – 18:07	2	frontal rain
2	3/7/2016	18:30 – 19:30	3/8/2016	2:30 – 3:30	4	convective, local updraft rain
3	3/11/2016	16:20 – 17:20	3/12/2016	00:20 – 1:20	2	frontal rain from decaying atmospheric river
4	3/12/2016	8:20 – 9:14	3/12/2016	16:20 – 17:14	2	warm, low cloud rain
5	3/29/2016	23:35 – 0:35	3/30/2016	6:35 – 7:35	4	scattered, low coastal clouds, lack of dynamical system
6	4/7/2016	8:15 – 11:00	4/7/2016	15:15 – 18:00	7	frontal rain from tropical moisture source
7	4/7/2016	12:07 – 13:07	4/7/2016	19:07 – 20:07	4	frontal rain from tropical moisture source
8	5/5/2016	22:59 – 23:59	5/6/2016	6:00 – 7:00	2	pre-frontal rain, meso-scale system
9	5/6/2016	2:59 – 3:59	5/6/2016	10:00 – 11:00	3	post-frontal rain, meso-scale system
10	5/6/2016	4:59 – 5:59	5/6/2016	13:00 – 14:00	1	post-frontal rain, meso-scale system
11	5/6/2016	8:59 – 9:59	5/6/2016	17:00 – 18:00	1	post-frontal rain, meso-scale system

Aerosol

Sampling Period	Local Date	Local Time	UTC Date	UTC time	Number of Isolates
A1	3/5/2016	10:40 – 12:15	3/5/2016	18:40 – 20:15	1
A2	3/7/2016	14:58 – 16:52	3/7/2016	22:58 – 23:52	5
A3	3/8/2016	11:34 – 14:42	3/8/2016	19:34 – 22:42	1
A4	3/28/2016	09:09 – 12:22	3/28/2016	16:09 – 19:22	1
A5	4/28/2016	11:45 – 13:22	4/28/2016	18:45 – 20:22	2
A6	5/5/2016	12:00 – 14:23	5/5/2016	19:00 – 21:23	2
A7	5/6/2016	14:15 – 16:37	5/6/2016	21:15 – 23:37	2

Table 4.5: Results of taxonomic assignment of SILVA Incremental Aligner (SINA) using the SILVA databases determined from 16S rRNA gene sequences.

Sequence_BLAST IDENTITY	sequence score	bp score	identity	quality	startpos	stoppos	ecolipos	bps	SILVA Lowest Common Ancestor Taxonomy
ISO1_Rhodotorula_mucliaginosa	0.984494	91	98.951	98	11889	27653	513	572	Eukaryota;Opisthokonta;Nucletmycea;Fungi;Dikarya;Basidiomycota;Pucciniomycotina;Microbotryomycetes;Sporidiobolales;
ISO2_Cryptococcus_aureus	0.994595	85	99.811	99	13141	26978	524	529	Eukaryota;Opisthokonta;Nucletmycea;Fungi;Dikarya;Basidiomycota;Agaricomycotina;Tremellomycetes;Trernellales;
ISO3_Arthrobacter_sp	0	97	100	100	13141	27150	524	366	Bacteria;Actinobacteria;Actinobacteria;Micrococcales;
ISO4_Curtobacterium_sp	0	92	100	100	13141	27638	524	381	Bacteria;Actinobacteria;Actinobacteria;Micrococcales;Microbacteriaceae;Curtobacterium;
ISO5_Brevibacterium_sp_linens	0.992084	98	98.9071	99	13143	27150	525	365	Bacteria;Actinobacteria;Actinobacteria;Micrococcales;Brevibacteriaceae;Brevibacterium;
ISO6_Lysobacter_sp	0.980307	101	95.1219	98	13128	27149	519	369	Bacteria;Proteobacteria;Gammaproteobacteria;Xanthomonadales;Xanthomonadaceae;Luteimonas;
Iso7_Microbacterium_esteraromaticum	0.99227	95	99.729	99	13141	27155	524	369	Bacteria;Actinobacteria;Actinobacteria;Micrococcales;Microbacteriaceae;Microbacterium;
ISO8_Brevibacterium_sp_luteolum	0.915246	71	93.266	91	10367	25293	508	294	Bacteria;Actinobacteria;Actinobacteria;Micrococcales;Brevibacteriaceae;Brevibacterium;
ISO9_Bacillus_sp	0.99212	95	99.455	99	13132	27152	521	367	Bacteria;Firmicutes;Bacilli;Bacillales;Bacillaceae;Bacillus;
ISO10A_Cryptococcus_sp	0.989263	99	99.4545	98	14958	28464	555	550	Eukaryota;Opisthokonta;Nucletmycea;Fungi;Dikarya;Basidiomycota;Agaricomycotina;Tremellomycetes;Trernellales;
ISO10B_Paenbacillus_sp	0	89	100	100	13141	27173	524	374	Bacteria;Firmicutes;Bacilli;Bacillales;Paenibacillaceae;Paenibacillus;
ISO12_Microbacterium_esteraromaticum	0	104	100	100	13870	28434	535	380	Bacteria;Actinobacteria;Actinobacteria;Micrococcales;Microbacteriaceae;Microbacterium;
SSA13_Paracoccus_marcusii	0	102	100	100	13874	28438	537	378	Bacteria;Proteobacteria;Alphaproteobacteria;Rhodobacterales;Rhodobacteraceae;Paracoccus;
SSA14_Bacillus_sp	0.992029	118	99.7215	99	14962	28438	557	359	Bacteria;Firmicutes;Bacilli;Bacillales;Bacillaceae;Bacillus;
SSA15_Pantoea_sp	0.981347	96	98.9848	98	13874	28475	537	394	Bacteria;Proteobacteria;Gammaproteobacteria;Enterobacteriales;Enterobacteriaceae;Pantoea;
SSA16_Psychrobacter_sp	0.919103	105	93.8548	91	14958	28431	555	357	Unclassified;
SSA17_Pantoea_sp	0	111	100	100	14286	28449	545	371	Bacteria;Proteobacteria;Gammaproteobacteria;Enterobacteriales;Enterobacteriaceae;Pantoea;
SSA18_Pantoea_sp	0.981347	96	98.9848	98	13874	28475	537	394	Bacteria;Proteobacteria;Gammaproteobacteria;Enterobacteriales;Enterobacteriaceae;Pantoea;
ISO19_Microbacterium_esteraromaticum	0	102	100	100	13861	28434	533	382	Bacteria;Actinobacteria;Actinobacteria;Micrococcales;Microbacteriaceae;Microbacterium;
ISO20_Bacillus_sp	0.994949	99	98.9529	99	13874	28451	537	381	Bacteria;Firmicutes;Bacilli;Bacillales;Bacillaceae;Bacillus;
ISO21_Cellulosimicrobium_sp	0.987932	118	99.4475	98	14962	28450	557	362	Bacteria;Actinobacteria;Actinobacteria;Micrococcales;Promicromonosporaceae;Cellulosimicrobium;
ISO22_Cellulosimicrobium_sp	0.753773	74	83.0409	75	14955	34478	553	535	Unclassified;
ISO23_Unknown	0.568338	33	67.8571	56	21333	26161	668	166	Unclassified;
ISO24_Cellulosimicrobium_sp	0	103	100	100	13870	28438	535	382	Bacteria;Actinobacteria;Actinobacteria;Micrococcales;Promicromonosporaceae;Cellulosimicrobium;
ISO24A_Metschikowia_sp	0.967483	76	95.8716	96	16525	28476	652	436	Eukaryota;Opisthokonta;Nucletmycea;Fungi;Dikarya;Ascomycota;Saccharomycotina;Saccharomycetes;Saccharomycetales;
ISO24B_Cellulosimicrobium_sp	0	103	100	100	13870	28438	535	382	Bacteria;Actinobacteria;Actinobacteria;Micrococcales;Promicromonosporaceae;Cellulosimicrobium;
SSA25_Psychrobacter_sp	0	100	100	100	13870	28450	535	382	Bacteria;Proteobacteria;Gammaproteobacteria;Pseudomonadales;Moraxellaceae;Psychrobacter;
SSA26_Microbacterium_esteraromaticum	0.97394	93	98.4962	97	13869	28476	535	399	Bacteria;Actinobacteria;Actinobacteria;Micrococcales;Microbacteriaceae;Microbacterium;
ISO27_Cellulosimicrobium_sp	0	102	100	100	13869	28438	535	383	Bacteria;Actinobacteria;Actinobacteria;Micrococcales;Promicromonosporaceae;Cellulosimicrobium;
ISO29_Pantoea_sp	0.968582	117	97.8022	96	14952	28438	552	364	Bacteria;Proteobacteria;Gammaproteobacteria;Enterobacteriales;Enterobacteriaceae;Pantoea;
ISO31_Bacillus_sp	0	118	100	100	14965	28434	559	355	Bacteria;Firmicutes;Bacilli;Bacillales;Bacillaceae;Bacillus;
ISO32Ap_Microbacterium_esteraromaticum	0.991482	89	99.7015	99	13874	26858	537	335	Bacteria;Actinobacteria;Actinobacteria;Micrococcales;Microbacteriaceae;Microbacterium;
ISO32Ay_Microbacterium_esteraromaticum	0.991369	88	99.7151	99	13146	26919	526	350	Bacteria;Actinobacteria;Actinobacteria;Micrococcales;Microbacteriaceae;Microbacterium;
ISO32B_Planococcus_sp_maritimus	0.992269	94	98.9218	99	13143	27163	525	371	Bacteria;Firmicutes;Bacilli;Bacillales;Planococcaceae;
ISO33A_Planococcus_sp	0.996495	101	99.2188	99	13860	28438	533	384	Bacteria;Firmicutes;Bacilli;Bacillales;Planococcaceae;
ISO33BpR_Unknown	0.75437	63	79.661	75	13146	25494	526	295	Unclassified;
ISO33By_Microbacterium_esteraromaticum	0.988208	95	99.4595	98	13151	27165	528	370	Bacteria;Actinobacteria;Actinobacteria;Micrococcales;Microbacteriaceae;Microbacterium;
ISO34_Pseudomonas_sp	0	100	100	100	13870	27655	535	372	Bacteria;Proteobacteria;Gammaproteobacteria;Pseudomonadales;Pseudomonadaceae;Pseudomonas;
ISO35A_Planococcus_sp	0	119	100	100	14978	28438	564	353	Bacteria;Firmicutes;Bacilli;Bacillales;Planococcaceae;
ISO35B_Pseudomonas_veronii	0.989209	92	99.6416	98	15875	26919	595	278	Bacteria;Proteobacteria;Gammaproteobacteria;Pseudomonadales;Pseudomonadaceae;Pseudomonas;
ISO36A_Citriococcus	0.946717	84	96.793	94	13151	26856	528	342	Bacteria;Actinobacteria;Actinobacteria;Micrococcales;Micrococcaceae;Citricoccus;
ISO36B_Planococcus_sp	0.983258	118	98.892	98	14961	28449	556	360	Bacteria;Firmicutes;Bacilli;Bacillales;Planococcaceae;
ISO37_Pseudomonas_sp	0	98	100	100	13146	27152	526	363	Bacteria;Proteobacteria;Gammaproteobacteria;Pseudomonadales;Pseudomonadaceae;Pseudomonas;
ISO38A_Psychrobacter_sp	0.996442	93	99.2063	99	13143	27638	525	378	Bacteria;Proteobacteria;Gammaproteobacteria;Pseudomonadales;Moraxellaceae;Psychrobacter;
ISO38B_Psychrobacter_sp	0	98	100	100	13128	27150	519	369	Bacteria;Proteobacteria;Gammaproteobacteria;Pseudomonadales;Moraxellaceae;Psychrobacter;
ISO39_Pseudomonas_sp	0.996323	115	99.7245	99	14948	28434	551	363	Bacteria;Proteobacteria;Gammaproteobacteria;Pseudomonadales;Pseudomonadaceae;Pseudomonas;
ISO40_Curtobacterium_sp	0.974701	108	98.3957	97	14965	28476	559	374	Bacteria;Actinobacteria;Actinobacteria;Micrococcales;Microbacteriaceae;Curtobacterium;
ISO41_Curtobacterium_sp	0.99151	92	99.7207	99	13143	26988	525	357	Bacteria;Actinobacteria;Actinobacteria;Micrococcales;Microbacteriaceae;Curtobacterium;
SSA42_Idiomarina_sp	0.991886	87	99.7159	99	13143	26976	525	352	Bacteria;Proteobacteria;Gammaproteobacteria;Alteromonadales;Idiomarinaceae;Idiomarina;
SSA43_Bacillus_sp	0.996471	92	99.4751	99	13141	27645	524	381	Bacteria;Firmicutes;Bacilli;Bacillales;Bacillaceae;Bacillus;
SSA44A_Paenbacillus_sp	0	96	100	100	13874	27638	537	366	Bacteria;Firmicutes;Bacilli;Bacillales;Paenibacillaceae;Paenibacillus;
SSA44B_Paenbacillus_sp	0	112	100	100	14973	27645	561	342	Bacteria;Firmicutes;Bacilli;Bacillales;Paenibacillaceae;Paenibacillus;
SSA45_Psychrobacter_sp	0.992322	95	99.1914	99	13132	27157	521	371	Bacteria;Proteobacteria;Gammaproteobacteria;Pseudomonadales;Moraxellaceae;Psychrobacter;
SSA46_Bacillus_sp	0	90	100	100	13143	27584	525	378	Bacteria;Firmicutes;Bacilli;Bacillales;Bacillaceae;Bacillus;
SSA47_Bacillus_sp	0.992261	95	99.7283	99	13134	27152	522	368	Bacteria;Firmicutes;Bacilli;Bacillales;Bacillaceae;Bacillus;
SSA48_Psychrobacter_sp	0.937055	78	95.9459	93	13151	25502	528	296	Bacteria;Proteobacteria;Gammaproteobacteria;Pseudomonadales;Moraxellaceae;Psychrobacter;
ISO49_Psychrobacter_sp	0.984997	98	98.9796	98	11887	27645	512	392	Bacteria;Proteobacteria;Gammaproteobacteria;Pseudomonadales;Moraxellaceae;Psychrobacter;
									57 species (93%)
									4 unclassified (7%)

Table 4.6: Summary of ice nucleation behavior of the 9 isolates that were tested for ice nucleation in the absence of media and resuspended in filtered autoclaved seawater (FASW). In comparison with ice nucleation behavior above ZoBell background levels, ice nucleation behavior was generally enhanced in media-free isolates, except in the case of SSA45, *Psychrobacter* sp. The first temperature at which ice nucleation is significant above background was determined by applying the criterion described in Methods. See Methods and Figure 4.10 for details of media-free freezing experiment.

		ZoBell		FASW	
Isolate	Species	Ice nucleation above background?	First Significant Freezing Temperature (°C)	Ice nucleation above background?	First Significant Freezing Temperature (°C)
Iso3	*Arthrobacter* sp. (*A. luteolus*, *A.citreus*)	no	n/a	yes	-15.25
Iso4	*Curtobacterium* sp. (*C. pusillum*, *C. flaccumfaciens*, *C. oceanosedimentum*)	no	n/a	yes	-13
Iso5	*Brevibacterium* sp. (*B. linens*)	no	n/a	yes	-11.75
Iso30	*Pantoea* sp. (*P. agglomerans*, *P. ananatis*)	yes	-16.75	yes	-15.5
SSA42	*Idiomarina fontislapidosi*	yes	-14.25	yes	-9.75
SSA16	*Psychrobacter* sp.	yes	-17.5	yes	-15.5
SSA18	*Pantoea* sp. (*P. ananatis*, *P. stewartii*, *P. agglomerans*)	no	n/a	yes	-11.5
SSA45	*Psychrobacter* sp.	yes	-14	no	n/a
SSA26	*Microbacterium esteraromaticum*	no	n/a	no	n/a

Chapter 5

Ice-Nucleating Particles Near Two Major Dust Source Regions

5.1 Abstract

Mineral dust and sea spray aerosol are important sources of ice nucleating particles (INPs), the small fraction of aerosol particles able to trigger cloud ice crystal formation and consequently, influence multiple climate-relevant cloud properties including lifetime, reflectivity and precipitation efficiency. Mineral dust is considered the dominant INP source in many parts of the world due to its ice nucleation efficiency and its sheer abundance, with global emission rates of up to 4700 Tg a^{-1}. However, INPs emitted from the ocean surface via sea spray aerosol frequently dominate INP populations in remote marine environments, including parts of the Southern Ocean where cloud-resolving model simulations have demonstrated that cloud reflectivity is likely strongly controlled by INPs. Here we report INP concentrations measured in aerosol and seawater samples during Air Quality and climate change in the Arabian BAsin (AQABA), a shipborne campaign that spanned the Red Sea, Gulf of Aden, Arabian Sea, Arabian Gulf and part of the Mediterranean. In aerosol samples collected within a few hundred kilometers of

the first and second ranked sources of dust globally, the Sahara and Arabian Peninsula, INP concentrations ranged from 0.2 to 11 L^{-1} at -20 °C with observed ice nucleation site densities (n_s) 1-3 orders of magnitude below levels predicted by mineral dust INP parameterizations. Over half of the samples (at least 14 of 26) were collected during dust storms with average dust mass concentrations between 150 and 490 μg m^{-3} (PM_{10}). The impacts of heat and peroxide treatments indicate that organics were responsible for the observed IN-activity at temperatures $\geq$ -15 °C with proteinaceous (heat-labile) INPs frequently observed at higher freezing temperatures $>$ -10 °C. Overall, results demonstrate that despite proximity to the Sahara and the Arabian Peninsula and the dominance of mineral dust in the aerosol sampled, existing mineral dust parameterizations alone would not skillfully represent the near-surface ns in the observed temperature regime (-6 to -25 °C). The decreased n_s and results demonstrating that organics dominated the observed IN activity $>$ -15 °C indicate that the IN-active organic species are limited compared to the mineral IN components of dust. Future efforts to develop or improve representations of dust INPs at modest supercooling ($>$ -15 °C) would benefit from a characterization of the specific organic species associated with dust INPs. An improved understanding of the organic species associated with increased IN-activity and their variability across dust source regions would directly inform efforts to determine whether n_s-based parameterizations are appropriate for skillful representation of dust INPs in this sensitive temperature regime, whether region-specific parameterizations are required, or whether an alternative to the n_s approach is necessary.

5.2 Introduction

Ice-nucleating particles (INPs) modulate the temperature and relative humidity at which ice particle formation occurs in the atmosphere and thus are a key factor that controls ice-phase partitioning in clouds. As initiators of ice formation and related phase-partitioning processes, INPs affect multiple cloud properties and exert a strong influence on cloud lifetime, reflectivity

and precipitation efficiency (e.g. Lohmann and Feichter, 2005; Vergara-Temprado et al., 2018).

Globally, desert dust is likely the most abundant aerosol type by mass (Kinne et al., 2006; Kok et al., 2021) and multiple studies have demonstrated that mineral (i.e., desert) dust is the dominant ice-nucleating (IN) species in many parts of the world based on observations (Ardon-Dryer and Levin, 2014; Boose et al., 2016; DeMott et al., 2015a; Price et al., 2018) and modeling of global INP distributions (Burrows et al., 2013; Hoose et al., 2010; Murray et al., 2012; Vergara-Temprado et al., 2017). Annual global dust emission rate estimates range between 400-4700 Tg a^{-1} (Huneeus et al., 2011; Kok et al., 2021). Of the global dust loading in the atmosphere (20-29 Tg), North African source regions are estimated to contribute $\sim$50% (11-15 Tg), and the Middle East and Central Asian source regions account for the bulk of the remainder, 30% (7.7 Tg) (Kok et al., 2021). Analysis of satellite products indicates that dust emissions rates are increasing over the Middle East at a rate of 15% a^{-1} (Klingmüller et al., 2016; Yu et al., 2018).

While Hoose and Möhler (2012) showed that mineral dust INPs generally activate ice crystals at freezing temperatures $<$ -15 °C, dust containing K-feldspar has been shown to nucleate ice at much higher temperatures, up to -4 °C (Atkinson et al., 2013; Harrison et al., 2016; Niedermeier et al., 2015; Wex et al., 2014; Whale et al., 2015; Zolles et al., 2015). Atkinson et al. (2013) found that feldspars represent up to $>$ 22% of Saharan and Asian dusts by mass. However, knowledge of the abundance and the available surface fraction of K-feldspar would be necessary to evaluate the IN efficiency of dust at temperatures $>$ -15 °C (Kanji et al., 2017).

Though mineral dust is considered to be the dominant INP source in many regions, multiple modeling and observational studies suggest that marine INPs are frequently dominant in remote ocean regions or in air masses with low concentrations of terrestrial aerosol (McCluskey et al., 2018b, 2018c; Vergara-Temprado et al., 2017; Wilson et al., 2015; DeMott et al., 2016). Using a global aerosol model to simulate marine organic and K-feldspar INP populations, Vergara-Temprado et al. (2017) showed that the relative contribution of marine organic vs. dust INPs in remote regions varies seasonally, and that marine organic INPs frequently outnumber K-feldspar

INPs (up to 100% of the simulated days in the Southern Ocean during summer). Results from a follow-on cloud-resolving model study showed that Southern Ocean cloud reflectivity is strongly modulated by INP concentrations, indicating that accurate estimates of the radiative energy budget in the Southern Ocean likely require improved and reliable representation of both dust and marine organic INPs (Vergara-Temprado et al., 2018). By generating isolated nascent sea spray over a range of biological conditions, mesocosm studies have shown that marine INPs are comprised of two classes: a dissolved organic carbon (DOC) type composed of IN active molecules and a particulate organic carbon (POC) type linked to the death phase of phytoplankton blooms (McCluskey et al., 2017, 2018a).

Parameterizations for both marine and mineral dust populations are commonly implemented in atmospheric models to estimate dust and marine INP concentrations. There are multiple existing mineral dust INP parameterizations used to estimate their concentrations in aerosolized desert dust, some based exclusively on laboratory measurements (e.g., Niemand et al., 2012; Ullrich et al., 2017), and others derived from a combination of laboratory and field measurements (DeMott et al., 2015). There are, additionally, multiple mineral-specific INP parameterizations including illite (Broadley et al., 2012), kaolinite (Welti et al., 2012), quartz (Harrison et al., 2019) and K-feldspar (Atkinson et al., 2013). The parameterizations by Ullrich et al. (2017, hereafter, "U17") and Niemand et al. (2012, "N12") were developed using dust samples from multiple deserts, and both found little variability in the IN activity between dusts from locations as disparate as the Sahara and Asia. DeMott et al. (2015, "D15") found agreement between their observations-based parameterization and N12, supporting the validity of laboratory-based parameterizations. Results in D15 also confirmed the conclusions of N12 and U17: that to first order, dusts from distinct regions can be parameterized as a single particle type. The D15 parameterization has been considered to be representative of dust that has undergone atmospheric photochemical and oxidative processes in transport (i.e., "aged" dust), because the parameterization was derived from observations made far (1000s of kilometers) from the dust emissions

sources (Boose et al., 2016).

By contrast, few studies report INP measurements near (e.g., $<$ 1 day of transport) a major dust source, and the lack of observations near dust source regions inhibit the evaluation of the ability of existing dust INP parameterizations to represent nascent dust populations (Boose et al., 2016; Gong et al., 2020; Price et al., 2018). INP observations are particularly lacking for the sensitive temperature regime $>$ -20 °C. Boose et al. (2016) found that D15 overpredicted INPs observed during Saharan dust events at a location within 100s of km of the Sahara (Izaña, Tenerife, Spain) by 2-3 orders of magnitude, suggesting that aging may lead to increased IN efficiency in mineral dust and that D15 may be less representative of nascent dust. These conclusions were supported by Conen et al. (2015), who found that concentrations of INPs at -20 °C measured during Saharan dust events were one order of magnitude higher at Jungfraujoch in the Swiss Alps than in Izaña, where dust events occurred 1-7 d prior to reaching Jungfraujoch. Gong et al. (2020) measured INPs in a variety of atmospheric and seawater sample types at Cabo Verde and determined mineral dust to be the dominant source of INPs observed in the atmosphere but found that INPs with freezing temperatures $>$ -10 °C were likely biological. At altitudes between 30 and 3500 m in the same region, Price et al. (2018) found that measured concentrations of INPs ranged two orders of magnitude at a given temperature, and that the observed concentrations related to the atmospheric dust loading.

Recently, multiple studies have provided new, much-needed observations of ambient atmospheric INPs in marine environments (DeMott et al., 2016; Hartmann et al., 2020; McCluskey et al., 2018b, 2018c; Yang et al., 2020) where data was historically lacking and consequently, an impediment to achieving predictive understanding of global INP distributions (Burrows et al., 2013). There are now two parameterizations available for the estimation of atmospheric concentrations of marine INPs emitted from the ocean surface: Wilson et al. (2015), which derives estimates of cumulative INPs from total organic carbon (TOC) concentrations in simulated SSA, and McCluskey et al. (2018), which estimates ice nucleation site density (n_s) from aerosol surface

area. Wilson et al. (2015) and McCluskey et al. (2018) derived marine INP parameterizations from field measurements of INPs in Atlantic and Arctic Ocean sea surface microlayer samples and pristine SSA samples over the North Atlantic Ocean, respectively.

Here, we report observations of INPs measured in air masses influenced by both desert dust and marine aerosol (Edtbauer et al., 2020) in close proximity to the two greatest global dust aerosol sources: the Sahara (#1) and the Arabian Peninsula (#2) (Kok et al., 2021). INP concentrations were measured in 26 aerosol samples collected during Air Quality and Climate Change in the Arabian BAsin (AQABA), a shipborne campaign which took place July – August 2017 on a transect that spanned the the central and eastern parts of Mediterranean, the Red Sea, the Gulf of Aden, the Arabian Sea and Arabian Gulf. Observed n_s were compared to dust and marine INP parameterizations, and the contributions of heat-labile (e.g., proteinaceous) and organic compounds to observed INP populations were assessed via heat and peroxide treatments. Finally, the potential INP source strengths of subsurface seawater (SSW) were assessed and compared with SSW INP measurements from prior studies of remote and coastal seawater.

5.3 Methods

5.3.1 Project overview

The AQABA campaign was conducted from 25 June to 3 September 2017 onboard the RV *Kommandor Iona*. The research voyage was conducted in two transects: the first leg beginning in La-Seyne-sur-Mer, France, heading through the Suez Canal, around the Arabian Peninsula and ending in Kuwait, and second leg a return transect via the same route (Supplementary Figs. 5.8-5.9). The campaign supported a large suite of on- and offline aerosol and gas-phase measurements (Bourtsoukidis et al., 2019, 2020; Celik et al., 2020; Edtbauer et al., 2020; Eger et al., 2019; Friedrich et al., 2021; Pfannerstill et al., 2019; Tadic et al., 2020; Wang et al., 2020).

5.3.2 Aerosol and trace gas measurements

Aerosol size distributions were measured using an Optical Particle Spectrometer (OPC, Grimm model 1.109) and a Fast Mobility Particle Spectrometer (FMPS, TSI model 3091). The OPC measures particles in size range 0.25 – 32 μm, and the FMPS measures particles with sizes between 5.6 nm and 560 nm. The inlet for the aerosol instrumentation was located at the top of a measurement container at a distance of $\sim$ 25 m from the INP filter sampling unit. To avoid condensation in inlet lines, aerosol samples were passed through a drying system, which reduced ambient relative humidity to an average value of $\sim$ 40 % in the measurement container. Two additional measurements provided aerosol data from which a filter flag intended to identify and eliminate stack emissions was derived: particle number concentrations as measured by a Condensation Particle Counter (CPC, TSI model 3787) and black carbon concentrations (Aethalometer, Magee AE33). The filter flag, based on short term variation in particle number concentration, black carbon concentration, wind direction and speed, was applied to all aerosol data so that samples contaminated by stack emissions could be identified.

Particle surface area concentrations were derived from FMPS and OPC measurements as follows. Geometric diameters were estimated from the measured mobility diameters (FMPS) and optical particle diameters (OPC). Aerosols were assumed dry at sampling conditions following the drying system described above. To convert optical particle diameters into geometric diameters, it was assumed that all coarse particles ($d_p > 3000$ nm) were composed of sea salt and dust with a mass ratio of 25% to 75%, and for the respective refractive indices and shapes the measured optical particle diameters were converted into geometric diameters. Fine particle ($d_p < 700$ nm) sizes were converted from dopt into dgeo using the optical properties calculated from the PM_1 chemical composition as measured by an Aerosol Mass Spectrometer (Aerodyne HR-ToF-AMS), assuming spherical particles. For particles in the intermediate size range (700 – 3000 nm), log-linear interpolation of optical and spherical properties was applied for conversion of optical into geometric particle diameters. The mobility diameters measured by the FMPS were considered

equivalent to the geometric diameter, assuming spherical particles. From the resulting particle size distributions, particle surface area was calculated for each size bin. Total particle surface concentrations were determined by integrating the surface area distribution for particles up to 10 μm. The overall uncertainty of derived particle surface area concentrations is estimated to be 30%.

The water-soluble fraction of total suspended particles (TSPs) was monitored with hourly resolution using a Monitor for AeRosols and Gases in Ambient Air, MARGA (Metrohm Applikon model S2, Herisau, Switzerland). Sea salt concentrations were estimated by scaling measured soluble Na^+ concentrations by 3.27 following Manders et al. (2009). Hourly composition data was linearly interpolated for 4 samples where 1-3 hours (of 7-24 hours total sampling time) was missing (Supplementary Fig. 5.10).

Nitric oxide (NO) concentrations were measured using a commercially available two-channel chemiluminescence monitor, CLD 790 SR (ECO Physics AG, Dürnten, Switzerland). During the AQABA campaign, the CLD 790 SR, MARGA, FMPS, OPC, HR-ToF-AMS, CPC and Aethalometer were operated within laboratory containers on the main deck of the research vessel. The NO measurements were used to prevent stack sampling during INP collection (see Sect. 5.2.4).

5.3.3 Dust mass concentrations from MERRA

Area-averaged hourly dust surface mass concentrations along the cruise track were obtained from the (0.5 x 0.625 °) Modern-Era Retrospective analysis for Research and Application, version 2 (MERRA-2; Gelaro et al., 2017). MERRA-2 uses the GEOS-5 Earth system model (Molod et al., 2015; Rienecker et al., 2011) with 72 vertical layers between the surface and 0.01 hPa (80 km) and the three-dimensional variational data assimilation Gridpoint Statistical Interpolation analysis system (Kleist et al., 2009; Wu et al., 2002). It simulates 5 types of aerosols (dust, sea salt, sulfate and black and organic carbon) using the Goddard Chemistry,

Aerosol, Radiation, and Transport (GOCART) model (Chin et al., 2002; Colarco et al., 2010). Dust emissions and deposition rates in MERRA-2 are estimated by summing the emissions and deposition rates across GOCART simulated dust particles between 0.1- 10 μm in size (dry diameter) (Gelaro et al., 2017). Dust emissions are constrained by wind-driven erosion over the source locations which are identified from the topographic depression map (Ginoux et al., 2001). Aerosol observations are derived from various satellite products and are jointly assimilated within GEOS-5 with meteorological observations (Buchard et al., 2017). MERRA-2 has been shown to successfully reproduce the interannual variability of north-Atlantic dust transport. Additionally, the improved aerosol assimilation scheme in MERRA-2 was shown to have a positive impact on the representation of long-range dust transport from the Sahara compared to prior versions (Buchard et al., 2017).

5.3.4 Measurement of ice-nucleating particles

Ambient aerosol sampling for offline measurement of INPs was conducted from 5 Jul – 31 Aug 2017 on the *Kommandor Iona*'s wheelhouse top (platform above the bridge), $\sim$ 25 m from the online aerosol measurements inlet and $\sim$ 35 m from the ocean surface (Supplementary Fig. 5.11). Sampling locations along the cruise transect corresponding to each aerosol sample are shown in Supplementary Figs. 5.8-5.9.

Aerosol samples were collected over 3-28 hour periods on polycarbonate filters (47 mm diameter, 0.2 μm pore-size, Whatman® Nucleopore, Chicago, Illinois, USA) placed in open-face Nalgene® Analytical Filter Units (Waltham, Massachusetts, USA). Aerosol sampling flow rates through the filter units were set to 10-13 Lpm using a MassStream™ mass flow controller (Bethlehem, PA, USA) connected inline with a rotary vane pump (Thomas QR-0100, Gardner Denver ©, Monroe, LA, USA). To decrease exposure to stack emissions, the pump was automated to switch off when online measurements of NO exceeded one standard deviation above the average background concentration for over 1 minute ($\sim$ 0.4 ± 0.8 ppb). Comparing the stack

contamination filter flag for aerosol measurements (Sect. 5.3.2) with INP sampling periods additionally indicates no influence of stack emissions on INP filter samples.

Prior to sampling, filters were cleaned by soaking in 10 % H2O2 for 10 minutes followed by rinsing three times with deionized water, the last rinse further "polished" by passage through a 0.1 μm pore-size syringe filter (Puradisc, Whatman, Maidstone, U.K). Filters were pre-loaded into filter units in a laminar flow hood to further minimize contamination from handling. After collection, each aerosol filter was placed in a 60 mm diameter sterile Petri dish (Life Science Products, Frederick, Colorado, USA) using pre-cleaned acetyl plastic forceps (Fine Science Tools, Foster City, California, USA), sealed with Parafilm and stored frozen (-20 °C). Samples were shipped in a dry shipper via Cryoport® High Vol Shipper at -180 °C and upon arrival at the laboratory were stored at -80 °C until processed, within 18 to 38 months of collection. To release collected particles, filters were immersed in 5-8 mL ultrapure water (Cat. Number W4502, Sigma-Aldrich®, St. Louis, MO, USA) and shaken for 20 minutes just prior to measurement. Eight samples were additionally diluted 100-fold to measure INP concentrations at lower freezing temperatures (Supplementary Fig. 5.12).

INP concentrations were measured using the SIO-Automated Ice Spectrometer (SIO-AIS), an immersion freezing droplet assay instrument that is described in detail in Beall et al. (2017). Briefly, the aerosol sample suspensions and SSW samples were distributed in 30 x 50-μL aliquots into clean 96-well polypropylene sample trays (OPTIMUM® ULTRA Brand, Life Science Products). An equal number and volume of aliquots of ultrapure water accompany each sample in the tray as a control. Trays were then inserted into an aluminum block that was cooled at -0.87 °C min^{-1} until the samples are frozen. Cumulative INP number concentrations per temperature per volume liquid are calculated using the fraction (f) of unfrozen wells per given temperature interval:

$$n_{INP,L} = \frac{-ln(f)}{V_d} \tag{5.1}$$

where V_d is the volume of the sample in each well. For aerosol filter samples, cumulative INP number concentrations are calculated using the ratio of the volume used for resuspension of the particles (V_{re}) to the volume of air sampled (V_A):

$$n_{INP} = \frac{-ln(f) \cdot V_{re}}{V_d \cdot V_A} \tag{5.2}$$

Prior to calculating n_{INP}, the fraction of unfrozen wells (f) was adjusted for contamination in the water used for suspension by subtracting the number of frozen ultrapure water wells per temperature interval from both the total number of unfrozen wells and total wells of the sample. The n_{INP} was additionally adjusted for background INPs from filters and sampling handling processes. Background INP concentrations were estimated using measured INP concentrations in aerosol sample field blanks, which were momentarily placed in the sampling apparatus before removal and unloading and storage of the filter. Seven field blank samples were collected, one every $\sim$ 7 days of the cruise (Supplementary Fig. 5.12). INP concentrations were measured in field blanks as described above, and the n_{INP} simulated using the mean air volume sampled (6680 L). Supplementary Fig. 5.13 shows the estimated n_{INP} across the 7 field blanks, which ranged between 3.0×10^{-4} and 3.0×10^{-2} L^{-1} at -20 °C. The freezing onset temperatures detected in the field blanks ranged between -6 and -27 °C. To correct n_{INP} measured in aerosol samples for background INP from sampling handling, a linear regression of the average INP concentration measured in field blank suspensions (mL^{-1} water) was used to estimate background concentrations of INP in samples at all temperatures between -14.5 °C and -27 °C. The estimated background INP concentration was then subtracted from the INP concentration measured in filter sample suspension volumes in this temperature range prior to calculating n_{INP}. The n_{INP} measured in one aerosol sample (f033) fell within the estimated INP background levels.

For this study, the detection limit was 0.68 INPs mL^{-1} liquid or $(0.1 - 2.4) \times 10^{-3}$ INP L^{-1} air for the maximum and minimum air volume sampled, respectively. The upper limit of detection (i.e., the point at which all droplets have frozen) is determined by several factors, including the

concentration of INPs in the sample, droplet volume, and the number of droplets measured. The upper limit of detection can be increased by performing dilutions. Thus, dilutions of 1:10 and 1:100 were performed on 8 samples (Supplementary Fig. 5.12).

The ice-active surface site density, n_s, is a metric used to define the ice-nucleating capabilities of an aerosol species (i.e., an aerosol sample of all the same particle type) (Kanji et al., 2017) as follows:

$$n_s = \frac{N_{ice}}{N_{tot} A(cm^2)} \tag{5.3}$$

where N_{ice} is the number of frozen droplets, N_{tot} is the total number of particles in a monodisperse aerosol population, and A is the surface area per particle.

The value of n_s can also be approximated for polydisperse aerosol samples containing multiple aerosol types:

$$n_s = \frac{N_{ice}}{A_{tot}(cm^2)} \tag{5.4}$$

where A_{tot} is the total surface area of the polydisperse aerosol sample. The difference between the n_s approximation (Eq. 5.4) and n_s (Eq. 5.3) is that many particle types are typically included in the n_s approximation, and in an ambient aerosol measurement most of these are not ice nucleating. Furthermore, the subset of INPs in the sample are likely also of different types, which likely have different n_s in the strict sense (Eq. 5.3). Nevertheless, the n_s approximation is a useful metric for comparing the ice-nucleating ability of different air masses and source regions and is often used for comparing data across studies of INPs measured in ambient air. It is extremely challenging to separate measurements of INPs and surface area by each particle type, and required, for example, combining online measurements of single particle chemistry, size distributions and INPs (Cornwell et al., 2019). All n_{INP} and n_s are reported normalized to a standard temperature of 273.15 K and pressure of 1013 hPa.

Heat and hydrogen peroxide treatments were applied to a subset of samples (12 of 26) to test for heat-labile biological (e.g., proteinaceous) and organic INP composition, respectively (McCluskey et al., 2018b; Suski et al., 2018). For each heat-treated sample, a 2 mL aliquot of the original ultrapure water suspension was heated to 95 °C for 20 minutes in a water bath and re-tested to assess the reduction in INP concentrations. For peroxide treatments, 1.6 mL of the original suspension was combined with 0.8 mL of 30% H2O2 (Sigma Aldrich ®, St. Louis, Missouri, USA) to achieve a final concentration of 10%, then the mixture was immersed in water, and heated to 95 °C for 20 min while being illuminated with two 26-W UVB fluorescent bulbs to generate hydroxyl radicals. To remove residual H_2O_2, to prevent otherwise significant freezing point depression, the solution was cooled and catalase (Cat. number IC10042910, MP Biomedicals, Santa Ana, California, USA) was added. Since catalase is itself decomposed by H_2O_2, while simultaneously catalyzing peroxide's disproportionation into water and oxygen, the enzyme was added in several 20 μL aliquots, allowing several minutes between each, until no effervescence resulted upon its addition. Fisher's Exact Test was applied to frozen and unfrozen well fractions between each untreated sample and its corresponding treated sample to test for significant differences ($p < 0.05$). Note that significant difference in frozen well fraction (Fig. 4, filled markers) is insufficient as a sole indicator of sensitivity in peroxide treated samples because samples are diluted 2:3 (by 33%) compared to untreated samples (see Methods Sect. 5.2.4). As INP concentrations can be corrected for the dilution by scaling (as opposed to frozen well fractions), the overlap in 95% binomial sampling confidence intervals (Agresti and Coull, 1998) between the untreated and peroxide-treated sample (error bars in Fig. 5.4) is an additional indicator of sensitivity for a given data point in the peroxide-treated sample spectrum within $\pm$ 0.2 °C, the uncertainty in the SIO-AIS temperature measurement (Beall et al., 2021). A lack of overlap in the 95% binomial sampling confidence interval within $\pm$ 0.2 °C equates to a significance threshold of $p < 0.005$ (Krzywinski and Altman, 2013).

INP concentrations were additionally measured in 10 SSW samples. For seawater sam-

pling, a water intake vertical steel pipe was positioned on the starboard of the ship approximately 2 m below the seawater level. The seawater was pumped into a 200 L stainless steel tank and continuously exchanged at a rate of 3000 L h^{-1}. SSW samples for INP analysis were collected in 15 mL sterile centrifuge tubes (Falcon™, ThermoFisher Scientific, Waltham, Massachusetts, USA) and stored frozen at -20 °C until they could be shipped in a dry shipper via Cryoport® (-180 °C) and ultimately stored at -80 °C as for aerosol samples. Heat and hydrogen peroxide treatments as described above were applied to five of these. To assess the contribution of submicron INPs to total measured INPs, 2 mL of SSW was filtered through a 0.2 μm sterile syringe-filter (Acrodisc® Pall®, Port Washington, New York, USA) and re-tested.

5.3.5 FLEXPART back trajectories

Aerosol 72-hour air mass back-trajectories for each sample were simulated using the FLEXible PARTicle dispersion model (FLEXPART) in backward mode (Stohl et al., 1998). NOAA Climate Forecast System (CFS) short-duration ($t < 6$ h) forecasts (Saha et al., 2014) were used as three-dimensional forcing datasets. Particle releases from 35 m above sea level (ASL) followed the vessel track using vessel position information from the European Common Automatic Weather Station (EUCAWS; http://eumetnet.eu/; last access Sept. 2021).

5.4 Results and discussion

5.4.1 Characteristics of INPs observed during AQABA

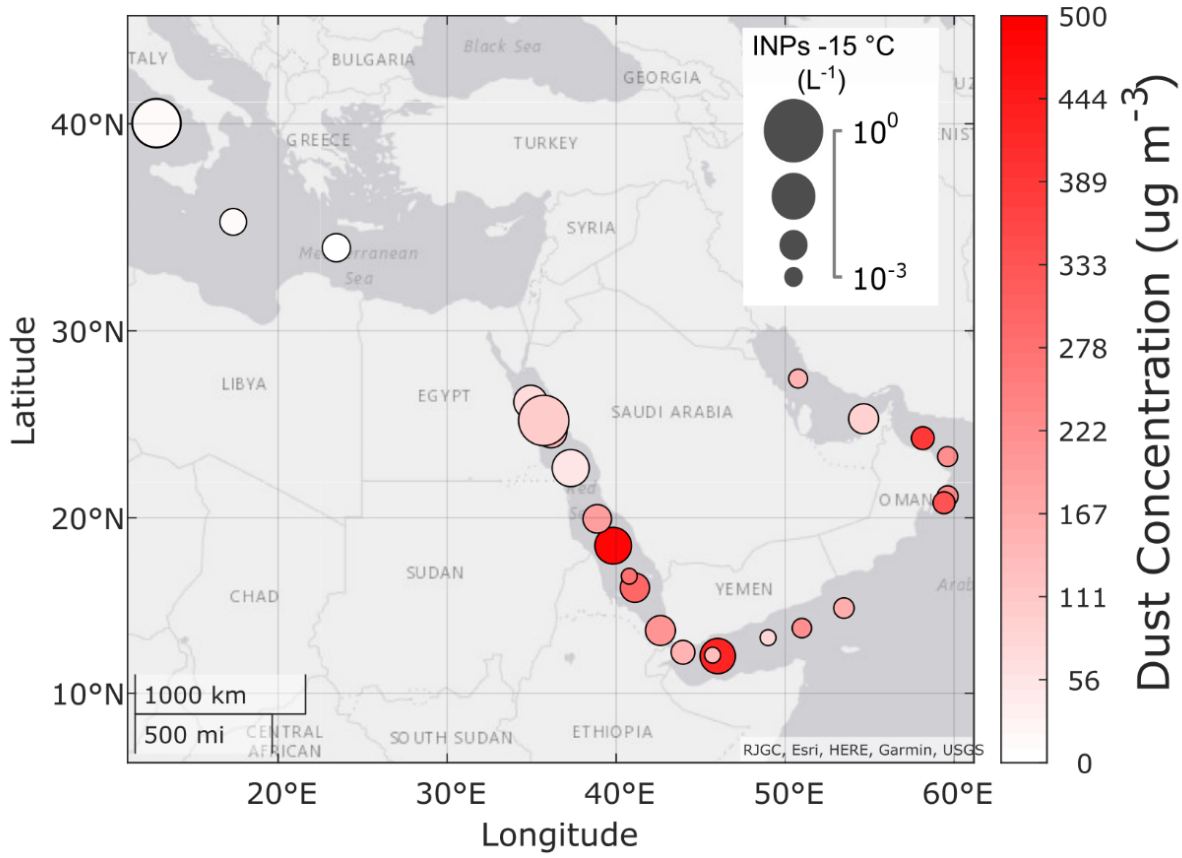

Figure 5.1: Map of the collection locations of 26 aerosol samples collected on the RV Kommandor Iona during Air Quality and climate change in the Arabian Basin (AQABA). Measured INP concentrations spanned three orders of magnitude at -15 °C, 10^{-3} to 0.5 L^{-1}. Marker sizes indicate abundance of INPs. Marker colors indicate the average ambient dust mass concentration during the sampling period from hourly MERRA-2 reanalysis data.

A total of 26 aerosol samples were collected July – August 2017 during AQABA for offline measurement of INPs. The INP concentrations (n_{INP}) measured in samples collected in the Mediterranean Sea, the Red Sea, the Gulf of Aden, Arabian Sea, Gulf of Oman, and Arabian Gulf spanned up to 3 orders of magnitude at -15 °C (Fig. 5.1). Average ambient dust

concentrations during each sampling period ranged from 2-490 μg m^{-3} (PM_{10})(Table 5.1). There is no agreed-upon standard for definition of extreme dust events in the literature, though the 24-hr average WHO or US EPA health standards for average PM_{10} are commonly used (Gandham et al., 2020; Khaniabadi et al., 2017). Using the US EPA health standard for PM_{10} as a threshold for extreme events (PM_{10}; 150 μg m^{-3}), 14 of the 26 samples were collected during dust events. This is conservative given the equivalent WHO guideline for PM_{10} is 50 μg m^{-3} (WHO, 2005), in which case 22 of the 26 sampling periods would be classified as dust events. Prior studies have reported comparable PM_{10} levels during dust events in the region (Gandham et al., 2020; Krasnov et al., 2016; Shahsavani et al., 2012).

Table 5.1: Summary of aerosol samples collected during AQABA. "—" indicates where data is missing.

Sample ID	Start datetime (UTC)	Stop datetime (UTC)	Latitude	Longitude	Sample Volume (L air)	Aerosol Surface Area (μm^2 cm^{-3})	Average Dust Concentration (μg m^{-3})	Average Sea Salt Concentration (μg m^{-3})
f006unt	05-Jul 05:46	05-Jul 11:37	26.224	35.025	3370	290	170	-
f007unt	05-Jul 16:40	05-Jul 19:51	26.291	34.933	2588	260	70	-
f008unt	06-Jul 07:09	06-Jul 14:08	25.225	35.775	5225	180	100	-
f009unt	07-Jul 05:50	07-Jul 15:07	25.011	35.947	6940	350	110	-
f010unt	08-Jul 16:33	09-Jul 05:59	23.623	36.931	8073	220	50	-
f013unt	14-Jul 12:26	14-Jul 16:13	18.687	39.672	2283	260	490	10
f014unt	15-Jul 05:10	15-Jul 11:49	16.552	40.834	4000	270	300	5
f016unt	18-Jul 07:04	18-Jul 14:52	11.939	45.334	4690	260	430	-
f018unt	22-Jul 10:20	22-Jul 18:44	20.941	59.474	5025	210	340	-
f019unt	23-Jul 04:48	23-Jul 13:34	21.410	59.691	5270	220	230	-
f020unt	25-Jul 17:15	26-Jul 04:02	23.976	58.809	6511	-	390	5
f023unt	04-Aug 04:05	04-Aug 11:56	28.084	50.284	4720	830	150	4
f024unt	05-Aug 05:57	05-Aug 13:53	25.432	53.853	5221	360	90	-
f025unt	07-Aug 09:26	07-Aug 16:46	23.814	59.186	4410	50	220	12
f030unt	13-Aug 07:08	14-Aug 11:06	15.970	54.705	15111	30	160	-
f031unt	14-Aug 15:03	15-Aug 09:03	14.003	52.357	12972	30	220	-
f032unt	15-Aug 09:42	15-Aug 15:07	13.354	49.432	3260	100	80	6
f033unt	16-Aug 09:30	16-Aug 13:17	12.208	45.706	2280	90	130	2
f034unt	16-Aug 13:27	17-Aug 07:04	12.177	45.429	8464	170	150	1
f035unt	17-Aug 07:30	17-Aug 14:55	13.308	42.974	4460	340	210	2
f036unt	18-Aug 06:36	18-Aug 15:03	16.290	41.038	6634	210	280	2
f037unt	19-Aug 07:05	20-Aug 07:04	18.699	39.609	18806	240	190	7
f038unt	21-Aug 07:22	21-Aug 16:01	24.112	36.554	6700	260	140	-
f040unt	26-Aug 16:02	27-Aug 07:04	33.803	24.814	9030	90	>10	3
f042unt	28-Aug 07:51	28-Aug 16:02	35.310	17.965	6396	160	10	2
f044unt	31-Aug 08:30	31-Aug 20:16	39.569	13.380	11296	210	10	-

FLEXPART aerosol 72-hour air mass back trajectories show that many of samples collected during extreme dust events (f013, f014, f016, f018 and f020) were influenced by emissions from North Africa and the Arabian Peninsula (Supplementary Figs 5.15-5.16). Other source regions included the Mediterranean (f006-f008), Northeast Egypt (f009-f010), Iran (f024) and Southern and Eastern Europe (f040, f042, f044).

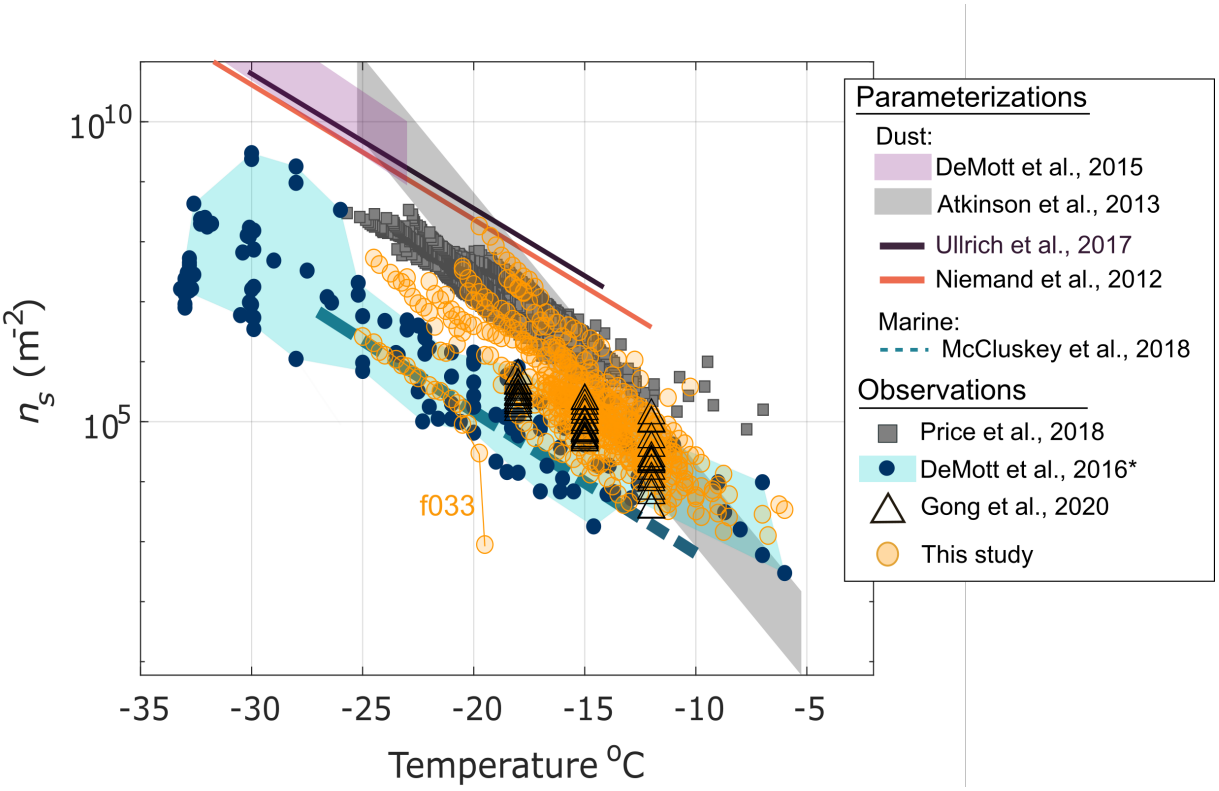

Figure 5.2: Ice nucleation site densities (n_s) as a function of temperature for 25 of 26 aerosol samples collected during AQABA. Gong et al. (2020) and Price et al. (2018) measured INPs in dust-dominant air masses in the tropical east Atlantic, with minor contributions from SSA. DeMott et al. (2016) measurements were collected across a range of locations and conditions within the marine boundary layer and includes air masses dominated by relatively pristine marine SSA. INP concentrations measured in sample f033 were below the detection limits imposed by field blanks (see Sect. 5.2.4, Supplementary Fig. 5.13). Sample f020 is not shown due to missing aerosol surface area data during the sampling period.
∗The DeMott et al. (2016) data shown have been updated with additional data from Yang et al. (2020).

In Figure 5.2, approximated ice nucleation site densities (n_s) are compared with multiple population-specific observations and parameterizations for dust and marine INPs. The AQABA

measurements are also compared with observations from dust-laden air over the Tropical Atlantic (Price et al., 2018). Overall, observations nearly bridge the full regime between M18, the parameterization for marine INPs (McCluskey et al., 2018b), and multiple dust INP parameterizations based on laboratory studies of surface dust. At higher temperatures between -5 and -12 °C, most observations show agreement with the composite spectrum of ns observed in a range of marine and coastal environments from DeMott et al. (2016) and Yang et al. (2019), and/or the Atkinson et al. (2013) K-feldspar parameterization. Between -10 and -20 °C, several samples agree with M18 marine INP parameterization within an order of magnitude, whereas two to three n_s spectra approach the U17 and N12 laboratory-derived dust INP parameterizations within an order of magnitude(Niemand et al., 2012; Ullrich et al., 2017), depending on temperature. Multiple samples ($\sim$8) additionally agreed with Price et al.'s (2018) observations of INPs between 30-3500 m above the dusty Tropical Atlantic, and most agree with the Gong et al. (2020) surface-level observations in the same region (Cabo Verde).

Considering the frequency of dust events encountered (Table 5.1), and the high probability that dust was the dominant aerosol source during most sampling periods, it is striking that most n_s spectra observed are 1-3 orders of magnitude lower than the values predicted by dust parameterizations. As noted in Gong et al. (2020), some deviations could be expected due to the difference between approximated n_s-based on total particle surface area in ambient measurements and true n_s based on surface area of a homogeneous aerosol population (see Methods Sect. 5.3.4). The FLEXPART back trajectories show that air masses for multiple samples originated from densely populated regions such as Southern and Eastern Europe (f040, f042, f044, Supplementary Fig. 5.16). The back trajectories also show that for samples f006-f008, f010, and f038, air masses were influenced by the populous region around the Nile River Delta. Agricultural soil dusts represent a potential constituent of the INPs observed from these regions. A range of n_s has been reported in studies of agricultural soil dusts, the lower end of which agrees with the n_s observed in the present study between -8 and -25 °C (Steinke et al., 2016; Tobo et al., 2014; O'Sullivan et

al., 2014).

Given the marine environment in which sampling occurred, a significant amount of sea spray aerosol (SSA) was also detected in many of the sampled air masses (Table 5.1), and likely present in others, for which no composition data were available. Edtbauer et al. (2020) reported the detection of high levels of dimethyl sulfide (DMS, up to 800 ppt) in the Gulf of Aden associated with a local phytoplankton bloom during AQABA (as evidenced by visible bioluminescence around the ship at night) as well as high levels of $DMSO_2$ and other marine biogenic VOCs from the Somalian upwelling region. As mentioned above, the ns for most samples between -6 and -18 °C agree with ns derived from observations across various locations within the marine boundary layer (Fig. 5.2). However, considering that SSA is associated with 1000 times fewer IN sites per unit surface area than dust (i.e. 1000× lower n_s) (McCluskey et al., 2018b) and the high relative abundance of dust compared to sea salt concentrations (Table 5.1), it is unlikely the observed INPs originated from SSA. As terrestrial INPs are nearly ubiquitous, detection of marine INP in ambient aerosol is challenging due to their low relative abundance and decreased efficiency compared to dust (DeMott et al., 2016; McCluskey et al., 2018b). Thus, while SSA contributed to the measured aerosol surface area (Table 5.1), it is unlikely that the INP observed in this study were marine in origin, or at least that this is indiscernible in the present study, or based on present parameterization of these populations.

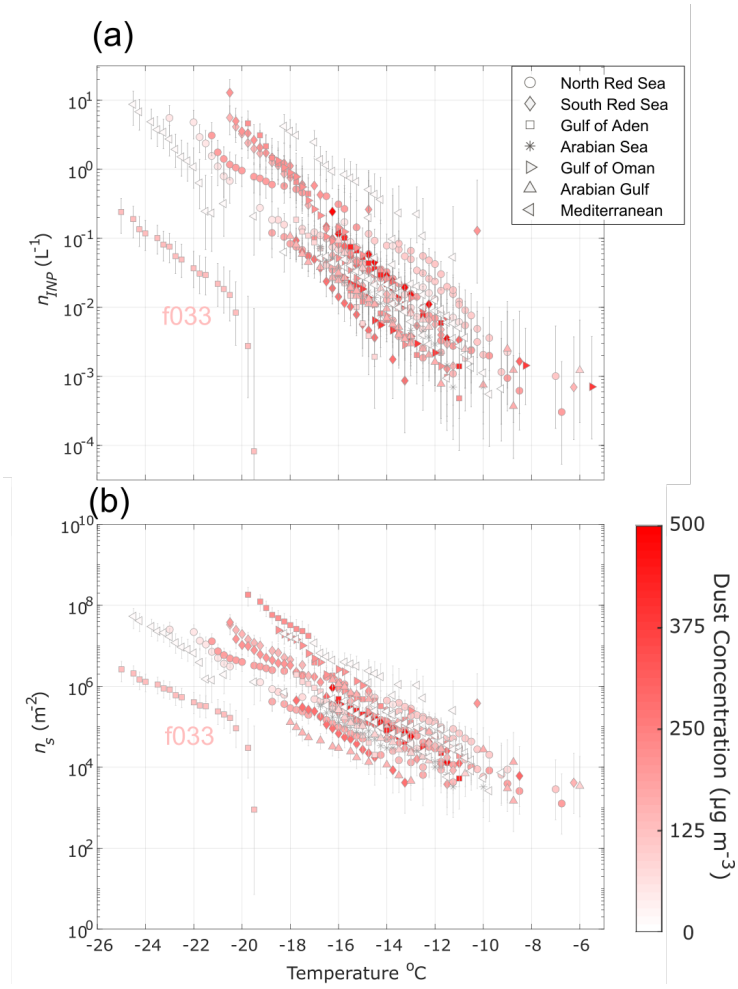

Figure 5.3: INP concentrations (n_{INP}) (a) and ice nucleation site densities (n_s) (b) as a function of temperature for 26 aerosol samples collected during AQABA. Markers are colored by the average ambient dust concentration for the respective sampling period. The ns measured in samples collected during low dust conditions are equal to or greater than (1-100×) the n_s measured during dust events between -9 and -18 °C. INP concentrations measured in sample f033 were below the detection limits imposed by field blanks (see Sect. 5.2.4, Supplementary Fig. 5.13). Sample f020 is not shown in (b) due to missing aerosol surface area data during the sampling period.

Heterogeneous aerosol composition in the sampled air masses likely contributed to some of the low n_s spectra observed due to the contribution of non-INPs to the measured aerosol surface area. However, the difference between n_s observed during the most extreme dust events, i.e., when the aerosol population was likely approaching homogeneity in composition, and the ns predicted from N12 and U17 was still greater than 2 orders of magnitude. Figure 5.3(a) and (b)

show overlap in n_{INP} and n_s observed in samples collected in low dust and high dust conditions, indicating that the INP populations observed during AQABA exhibited similar efficiencies despite variation in total aerosol composition and dust loading. No correlation was found between n_{INP} and aerosol surface area (Supplementary Fig. 5.14) or dust concentration. This result is in contrast to Price et al. (2018) who found the variability in n_{INP} to be largely determined by variability in dust loading or aerosol surface area. Yet the aerosol surface area concentrations compare very well, indicative of comparable dustiness between the two studies. Excluding three samples, Price et al. (2018) collected in an exceptionally optically thick dust layer: the average surface area was 227 ± 68 μm^2 cm^{-3} vs. 226 ± 26 μm^2 cm^{-3} for the present study. Furthermore, the sample with the highest n_s observed through -15 °C (f040) was collected when dust concentrations were the lowest (2 μg m^{-3}) (Fig. 5.3, Table 5.1). This is also in direct contrast to Price et al. (2018), who found that the highest n_s observed corresponded to the highest dust loading.

Gong et al. (2020) also observed n_s lower by more than 2 orders of magnitude compared to N12 and U17 despite that the large fraction of INPs observed in their study were supermicron (77-83% depending on temperature), and that the supermicron particles were mainly composed of mineral dust. The large differences between parametrized n_s for dust and n_s observed in Gong et al. (2020) and the present study between -12 and -25 °C demonstrate that the existing n_s-based parameterizations alone may not faithfully represent ns at moderate freezing temperatures, despite proximity to major source regions. Whereas DeMott et al. (2015a) found that for temperatures $<$ -20 °C, mineral dust particles from Saharan and Asian deserts may be parameterized as a common particle type, our findings suggest that characteristic n_s parameterizations for dust from different source regions may be needed for higher temperatures, or alternatively, that this temperature regime requires an alternative to an n_s -based parameterizations. Gong et al. (2019a) demonstrated that predicting n_{INP} from surface area size distributions alone may not be feasible in environments where the aerosol and/or INP composition are unknown and proposed a PDF-based approach to predicting INPs at a given freezing temperature.

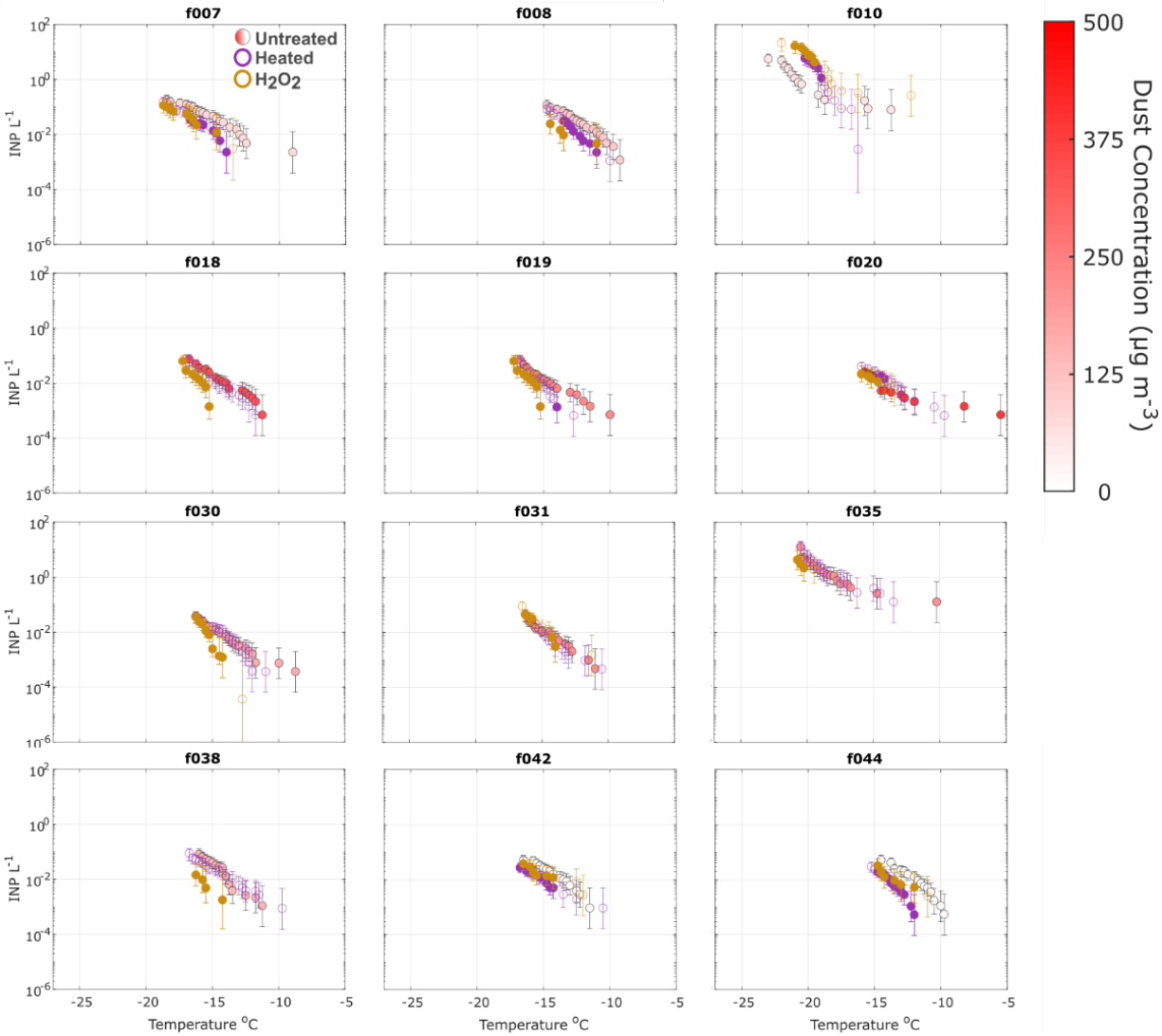

Figure 5.4: INPs in select aerosol samples that were treated with heat and H_2O_2 (Methods Sec. 5.3.4) to test for INP heat-lability and organic composition. Markers of untreated spectra are colored by the average dust concentration during the sampling period. Markers of heat-treated and H_2O_2-treated samples are filled to indicate significant INP concentration difference from untreated samples according to Fisher's Exact Test ($p < 0.05$). Sensitivity to H_2O_2 is evident forall samples $\geq$ -15 °C, indicative of stable organic INPs. Heat-lability is also evident at high to moderate temperatures in multiple samples, demonstrating that biological (e.g., proteinaceous) INPs also contributed to INPs observed during AQABA.

Offline treatments for testing heat lability and organic composition of INPs were performed on 12 samples via heat and H_2O_2 treatments, respectively (Fig. 5.4). Prior studies have shown that the IN active component of various types of mineral dusts are insensitive to heat treatments

(Conen et al., 2011; Hara et al., 2016; Hill et al., 2016; O'Sullivan et al., 2014). The IN activity of K-feldspar, the dominant IN component of mineral dust, was additionally found to be insensitive to digestion with peroxide (O'Sullivan et al., 2014). A small number of studies reported degradation of IN activity with peroxide treatment and/or heat treatment in Arizona Test Dust (ATD) that they attributed to organic material (Perkins et al., 2020; Yadav et al., 2019). Thus, we assume here that any degradation of IN activity due to heat and peroxide treatment are due to loss of heat-labile (e.g. proteinaceous) and heat-stable organic INPs, respectively.

Fisher's Exact Test was applied to frozen and unfrozen well fractions between each untreated sample and its corresponding treated sample to test for significant differences ($p < 0.05$). Sensitivity to peroxide in all samples demonstrate the consistent presence of stable organic INPs at temperatures $\geq$ -15 °C. The lack of peroxide sensitivity at temperatures below -15 °C indicates dominance by mineral dust INPs at lower temperatures. Heat sensitivity in five of the samples at the highest freezing temperatures indicated that biological INPs likely contributed to the warmest freezing INPs in some samples. Gong et al. (2020) similarly found heat-sensitivity in INPs at temperatures $>$ -10 °C. Four of the 12 samples exhibited heat sensitivity at relatively moderate temperatures 11 to -18 °C, including the two samples collected in the Mediterranean Sea. One sample (f010) exhibited increased INP concentrations in freezing temperatures below -18 °C after heat and peroxide treatments. This is an unexpected result given previous studies on treated soil dust measurements (Conen et al., 2011; Hill et al., 2016; O'Sullivan et al., 2014; Tobo et al., 2014), though an increase in IN activity after peroxide treatment has also been reported in a Himalayan dust sample (Paramonov et al., 2018). That the response of the heat and peroxide treated samples were nearly identical (Fig. 5.4) indicates that some heat-labile compounds were released from the surface during heating, uncovering a more IN active surface underneath in sample f010. Heating was common to both procedures (see Methods Sect. 5.3.4). This is an unexpected result given previous studies on treated soil dust measurements (Conen et al., 2011; Hill et al., 2016; O'Sullivan et al., 2014; Tobo et al., 2014)(Conen et al., 2011; Hill et al., 2016;

O'Sullivan et al., 2014; Tobo et al., 2014), though an increase in IN activity after peroxide treatment has also been reported in a Himalayan dust sample (Paramonov et al., 2018).

Given the frequency of dust storms and generally high concentrations of dust during most sampling periods, it is surprising that most samples exhibit peroxide sensitivity. Aridisols and entisols are the dominant soil types in North Africa and the Arabian Peninsula (Nortcliff, 2012). Both types are associated with the lowest levels of organic carbon, commonly used as a proxy for total soil organic matter, compared to other soil types (3 and 9 g kg^{-1}, respectively) (Yost and Hartemink, 2019).

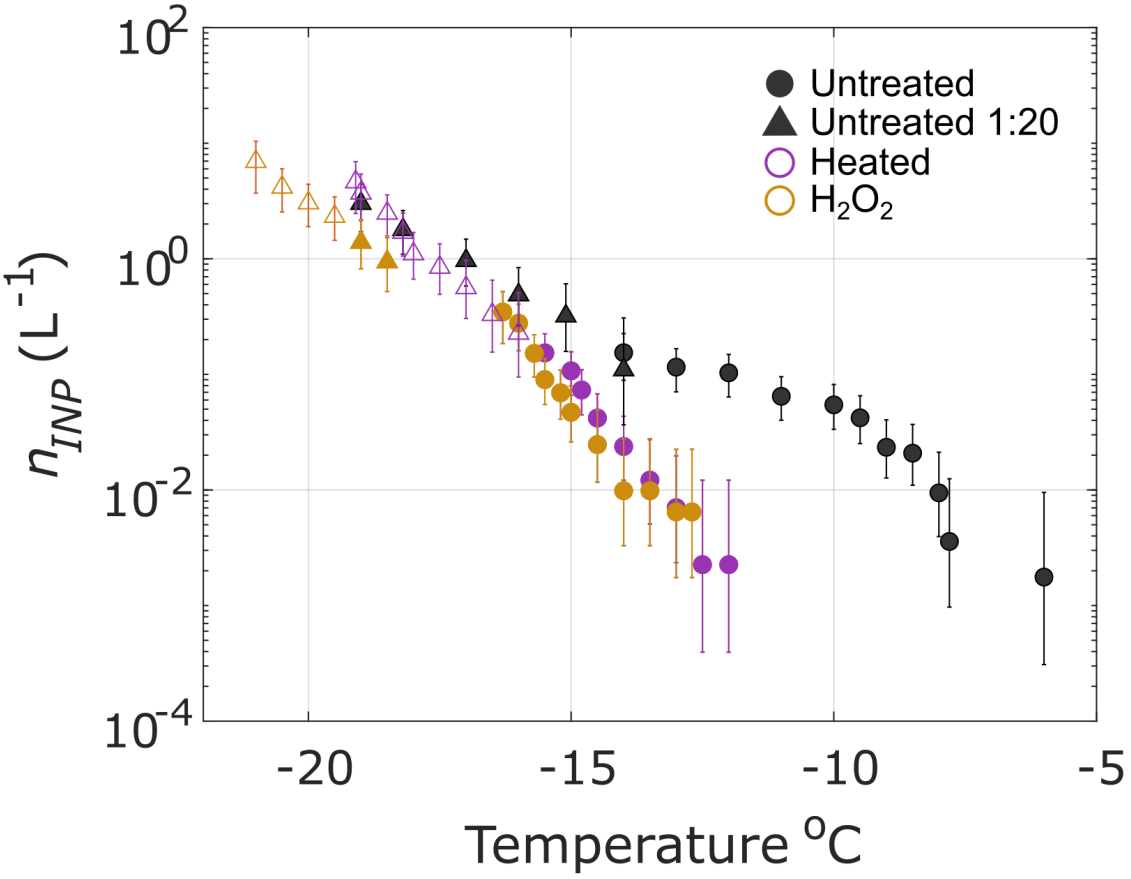

Figure 5.5: Measured concentrations of INPs in an aerosolized soil dust sample collected 50 km north of Cairo, Egypt, that was treated with heat and peroxide to test for INP heat-lability and organic composition, same as in Fig. 5.4 above (Methods Sect. 5.3.4) to test for INP heat-lability and organic composition. A 1:20 dilution of the sample is shown (triangles) and markers of heat-treated and H_2O_2-treated samples are filled to indicate significant INP concentration differences from untreated samples according to Fisher's Exact Test (p ¡ 0.05). Sensitivity to peroxide and heat treatments indicates biological INPs between -6 and -16 °C, and sensitivity to peroxide below -18 °C indicates stable organic INPs.

INP measurements of soil dusts in this region are scarce and have only been reported for a single surface dust soil sample, sample "SD", collected 50 km north of Cairo (Niemand et al., 2012). For comparison with this study, we measured INPs in untreated, heat-treated, and peroxide-treated subsamples of an archived aliquot of the SD sample described in Niemand et al. (2012) (Fig. 5.5). Sample SD exhibits sensitivity to both heat and peroxide at temperatures $>$ -16 °C, indicating biological composition of INPs at high freezing temperatures. Multiple AQABA

samples influenced by desert air mass sources show similar sensitivities at higher temperatures: f006, f007, f019, and f020. Several others exhibit only peroxide-sensitivity in this temperature range. Overall, the heat and peroxide sensitivity in the SD sample indicates that desert dusts may contribute biological and/or organic INPs at moderate to high-freezing temperatures, such as those observed in AQABA samples. Gong et al.'s (2020) results showing heat-sensitivity in INPs at temperatures $>$ -10 °C further demonstrate the contribution of biological INPs at high temperatures in dusty air masses near N. Africa.

Samples from air masses influenced by the Nile River Delta or Southern Europe (f007-8, f010, f038, f042, f044) show a higher fraction of heat-sensitive INPs (Fig. 5.4). Heat-sensitivity is indicative of biological INPs, which have been associated with agricultural soil dusts in prior studies (Hill et al., 2016; O'Sullivan et al., 2014). Hill et al. (2016) and O'Sullivan et al. (2014) showed peroxide sensitivity in agricultural soil dusts at temperatures $>$ -18 to -15 °C, respectively, a range which aligns with the peroxide sensitivity exhibited in the present study. Agricultural soil dusts are rich in organic and biological material (Conen et al., 2011, 2016; Ellerbrock et al., 2005; Kögel-Knabner et al., 2008; O'Sullivan et al., 2014) and contribute up to 20-25% of the global dust load (Ginoux et al., 2012). Furthermore, they are associated with IN efficiencies higher than that of mineral dust (Conen et al., 2011; Fornea et al., 2009; Isono and Ikebe, 1960; O'Sullivan et al., 2014; Steinke et al., 2016; Tobo et al., 2014). High onset temperatures up to -6 °C have been reported in multiple studies (Conen et al., 2011; Garcia et al., 2012; Hill et al., 2016; O'Sullivan et al., 2014), and the high efficiency of agricultural soil particles has been attributed to internally mixed organic matter (O'Sullivan et al., 2014; Tobo et al., 2014).

Organic material can condense or adsorb onto aerosols during photochemical and oxidative processes, representing another potential source of organics to the INPs observed during AQABA (Dall'Osto et al., 2010; Hinz et al., 2005; Krueger et al., 2004). Could aging explain a decreased n_s? Though dust aerosol was collected within $<$ 1 day's transport from source regions throughout this study, we cannot rule out the possibility of aging impacts lacking single particle chemistry

measurements (e.g., Sullivan et al., 2007). In addition to field observations of INP concentrations demonstrating that aging increased the IN efficiency of desert dust INPs (see Introduction; Boose et al., 2016; Conen et al. 2015), prior studies of the effects of aging on mineral dust INPs have yielded mixed and sometimes contradictory results, indicating that the impact of aging on IN properties likely depends on multiple factors including the ice nucleation pathway, the type of aging process, surface morphology and mineralogy (Perkins et al., 2020). Multiple studies have investigated the effects of various aging processes on Arizona Test Dust (ATD) as a proxy for diverse natural dust samples, including exposure to sulfuric acid, nitric acid vapor, and solution-phase processes (Cziczo et al., 2009; Eastwood et al., 2009; Knopf and Koop, 2006; Salam et al., 2007; Sullivan et al., 2010b, 2010a). Perkins et al. (2020) demonstrated the INP lability in ATD through multiple solution-phase aging processes (e.g., acid, salt), with up to 1000-fold reductions in INP abundance at freezing temperatures $>$ -10 °C. This result contrasts with the increase in IN activity attributed to aging reported in Boose et al. (2016) and Conen et al. (2015). Perkins et al. (2020) additionally reported that the lability of IN activity in ATD is temperature dependent, with large reductions evident at freezing temperature $>$ -10 °C, yet little to no change at temperatures below -15 °C. The decreased lability to heat and solution-phase processes with decreasing temperature was also reported in soil dust samples (Paramonov et al., 2018). In summary, it has proven difficult to determine any consistent impact of atmospheric processing on the IN activity of dust in model systems such as ATD, and few studies have reported on the impacts of aging on ambient desert dust, especially at the modest supercoolings explored in this study. Furthermore, in contrast to the Perkins et al.'s (2020) results showing that IN-lability was restricted to relatively high freezing temperatures in ATD, most of the n_s spectra in AQABA samples were 1000$\times$ lower than established dust parameterizations even at temperatures below -15 °C.

The cause of the decreased n_s observed here and in Gong et al. (2020) compared to dust n_s parameterizations remains elusive. Both studies were conducted in air masses dominated by dust

near major sources. In contrast, Price et al. (2018) found agreement near the region of the Gong et al. (2020) study. One obvious difference is that Price et al., 2018 conducted measurements at altitudes between 30 and 3500 m. A prior study that compared nINP in dusty air masses at the surface with n_{INP} collected with unmanned aircraft systems (UASs) between 0.5 and 3 km above sea level in samples found that median n_{INP} was increased by up to 10× above the surface and correlated to dust loading (Schrod et al., 2017). However, the results in the present study indicate that the dust loadings in the sampled air masses were comparable with Price et al. (2018) despite the difference in altitude. The decreased n_s compared to Price et al. (2018) is also unlikely to be related to differences in INP measurement. In all three studies, cold stage or droplet assay instruments for measurement of immersion mode INPs were used to measure INP concentrations in resuspensions of aerosol collected on filter samples. Recent studies that intercompared instruments designed for measurement of immersion mode INPs showed excellent agreement (i.e., within measurement uncertainty) in measurements of standardized dust and biological samples (DeMott et al., 2018) and when co-sampling ambient aerosol (DeMott et al., 2017). Moreover, the DeMott et al. (2018) intercomparison study demonstrated good agreement in multiple natural dust samples between the various measurement methods used to derive D15, N12 and U17 and the droplet assay methods applied in Gong et al. (2020), Price et al. (2018) and the present study.

In light of the evidence from this study that INPs observed were primarily influenced by organics associated with dust and especially so at higher temperatures, and the lack of relationship between dust loading, n_s, and n_{INP}, we offer the following points for consideration. Prior studies of aerosolized dust demonstrated that it is frequently enriched in organic matter by 6-20× and that wind erosion selectively removes the fine portion of the soil with relatively larger chemical concentrations, leaving behind the coarser portion with relatively lower chemical concentrations (Aryal et al., 2012; Delany and Zenchelsky, 1976; Van Pelt and Zobeck, 2007). Furthermore, a recent study that measured airborne concentrations of prokaryotic cells over the Red Sea

characterized the region as a “global hot spot”, with average concentrations of 154,812 $\pm$ 65,255 cells m^{-3}, 19$\times$ higher than that over the subtropical and tropical open ocean (Mayol et al., 2014; Yahya et al., 2019). Results from Yahya et al. (2019) additionally demonstrated that the relatively high microbial loading was highly likely to related to the high concentrations of dust, as 99.9% of the cells were attached to dust particles. However, organics are still limited compared to the mineral component of dust by mass, representing a small fraction of aridisols and entisols, the dominant soil types across North Africa and the Arabian Peninsula (Nortcliff, 2012; Yost and Hartemink, 2019). Organic and biological species have been shown to dominate IN-activity at temperatures $>$ $\sim$-15 °C in many studies (e.g., (Kanji et al., 2017; Ladino et al., 2019; O’Sullivan et al., 2018) , as was the case in the present study. Thus, a faithful representation of dust INPs that covers the full temperature spectrum will likely require at least two types of parameterizations: one for the IN-activity dominated by mineral activity $<\sim$-15 °C such as D15, U17 and N12, and another for the dust-associated organics $>\sim$-15 °C. Prior studies have reported a threshold temperature between -15 and -20 °C, above which mineral dusts dominate observed INP activity, and below which organic and biological INPs are dominant (Murray et al., 2012; Sanchez-Marroquin et al., 2021).

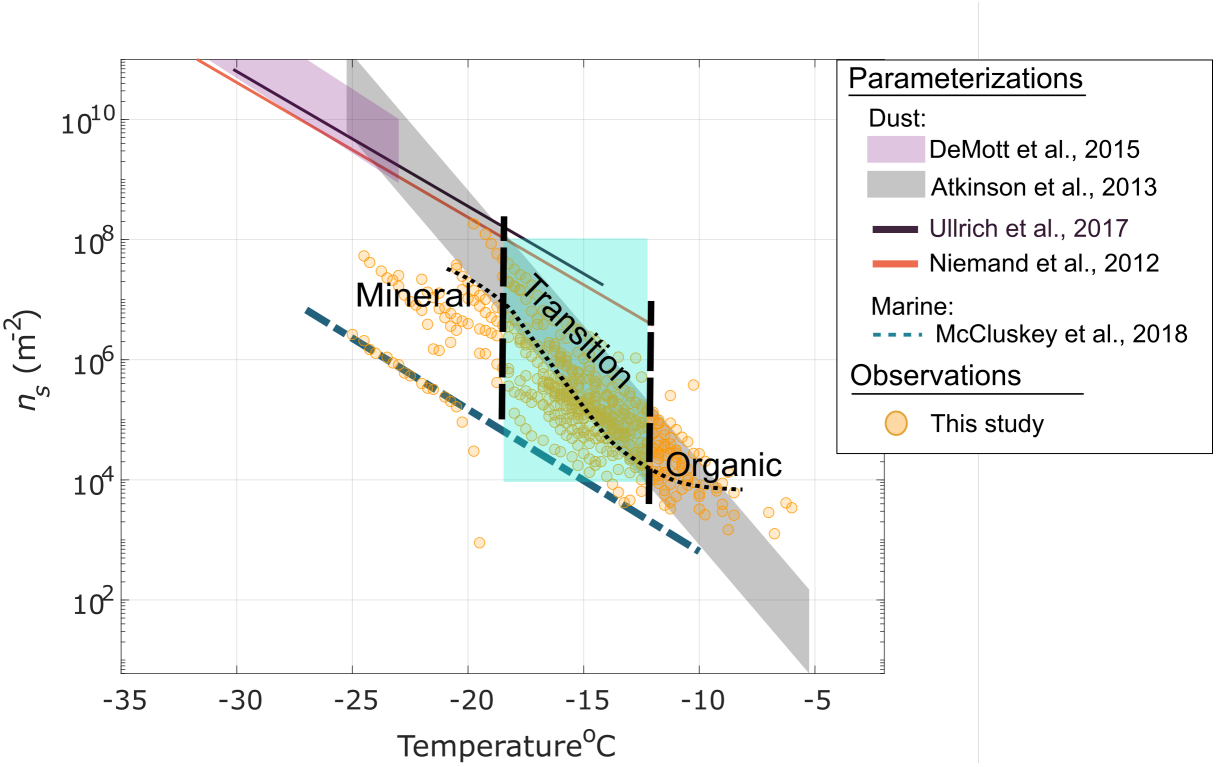

Figure 5.6: Potential ranges of mineral and organic-dominant INP activity observed during AQABA. Purple shaded region represents a possible ns transition between the two proposed regimes of the INP distribution.

DeMott et al. (2017) showed that the largest discrepancies (up to 3 orders of magnitude) between several instruments measuring n_s were associated with dust samples that exhibited a steep n_s activation curves versus temperature above -25 °C. Considering that a steep INP activation curve could cause large discrepancies, it is possible that the apparent decreased n_s observed in this study between -18 and -12 °C was related to a steep transition in n_s between the mineral and organic "modes" at modest supercooling (see Fig. 5.6). This study underscores the need to characterize the IN-active organic species associated with dust from major source regions and to investigate the extent to which biological and/or organic particles contribute to INP populations in dust-laden air masses at high to moderate freezing temperatures.

5.4.2 Seawater source potential

The n_{INP} values in 10 SSW samples collected during AQABA were used to characterize the INP source potential, or the number of INPs that likely contribute to INPs emitted through SSA via jet droplets (Wang et al., 2017). Results from prior studies have demonstrated that jet droplets are likely an efficient transfer method of INPs into SSA particles (Mitts et al., 2021; Wang et al., 2017). While it is unlikely that many of the INPs detected in aerosol samples were marine in origin (see Sect. 5.4.1), we measured the INP concentrations in SSW to test whether the seawater source strength was comparable to that of prior studies, or were possibly enriched with INPs due to biological activity or even dust deposition (Cornwell et al., 2020).

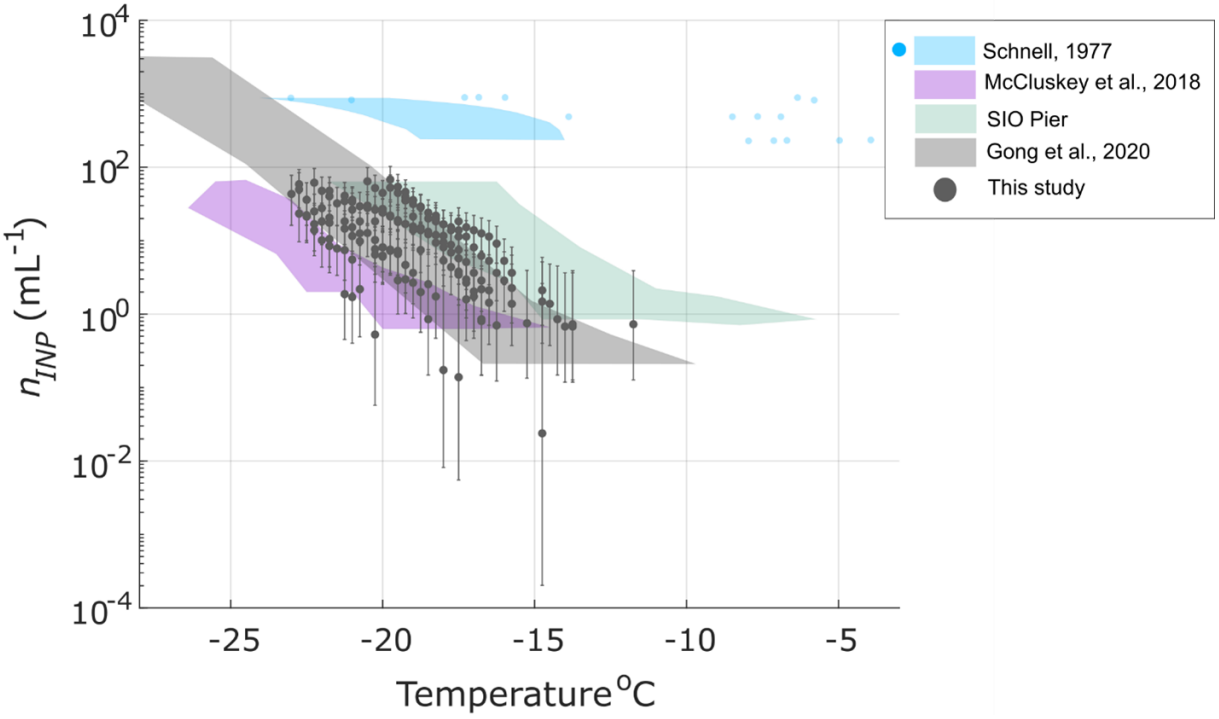

Figure 5.7: Measured INP concentrations in 10 SSW samples collected during AQABA. Also shown are the composite INP spectrum of coastal SSW samples collected on São Vincente Island, Cabo Verde (Gong et al., 2020), coastal SSW samples collected at the Ellen Browning Scripps Pier (green shading), and SSW samples collected in the Southern Ocean (McCluskey et al., 2018c). Schnell's (1977) SSW measurements are represented as a composite spectrum of 24 samples (blue shaded region) and 5 additional spectra (blue markers) from samples that exhibited higher freezing temperatures. All spectra presented are uncorrected for freezing point depression.

Supplementary Fig. 5.17 shows how the concentrations measured at -19 °C in 10 seawater samples varied by the sample collection location. Measured concentrations ranged between 1 and 50 INPs mL^{-1} and were highest between the Gulf of Oman and the Gulf of Aden. This region exhibited relatively high chlorophyll *a* during the cruise, with levels between 1 and 30 mg m^3 (Supplementary Fig. 5.18). In Fig. 5.7, INP concentrations were compared with SSW from the Ellen Browning Scripps Memorial Pier in coastal Southern California (SIO Pier), Cabo Verde in the Northeast Atlantic, the Southern Ocean (McCluskey et al., 2017), and the Northwest Atlantic (Schnell, 1977). AQABA INP concentration spectra spanned the regime between the SIO Pier

and McCluskey et al. (2017) datasets and agreed with Gong et al.'s (2020) observations in Cabo Verde as well as Schnell (1977).

Offline treatments for testing heat lability, organic composition, and size were applied to 5 of the 10 seawater samples (Methods Sect. 5.3.4). Heat and 0.2 μm filtering treatments suggest that a large fraction of the seawater INPs were heat sensitive and larger than 0.2 μm. These results are indicative of the particulate organic carbon (POC) type of marine INP defined in McCluskey et al. (2018a) (Supplementary Fig. 5.19). Heat-resilience but peroxide-sensitivity in sample s001 additionally indicates the presence of non-proteinaceous organic INPs, such as the dissolved organic carbon (DOC) type defined in McCluskey et al. (2018a). Considering the IN activity of SSW compared well with prior studies, the frequency of dust events during AQABA, and the lower n_s of SSA compared to mineral dust (McCluskey et al., 2018b), these results support our findings that dust was highly likely to be the dominant INP class observed in this study.

5.5 Conclusions

Observations from the two-month AQABA campaign in the Mediterranean, Red Sea, Arabian Sea and Arabian Gulf are among the first INP measurements made in close proximity to the two largest dust sources globally: the Sahara and the Arabian Peninsula (Kok et al., 2021). INP concentrations spanned three orders of magnitude (10^{-3} to 10^{0} L^{-1} at -15 °C).

In summary, INPs observed during AQABA were very likely dominated by mineral dust with some additional contributions possible from agricultural soil dusts from the Nile River Delta region and Southern or Eastern Europe. Despite proximity to major dust sources and a high frequency of dust events with mass concentrations up to 490 μg m^{-3} (PM_{10}), the observed n_s for most samples was lower by 1-3 orders of magnitude compared to n_s predicted by dust parametrizations N12 and U17 at T < -12 °C (Niemand et al., 2012; Ullrich et al., 2017) Many INPs measured in AQABA showed agreement with the A13 parameterization for K-feldspar

(Atkinson et al., 2013), an ice-active component of desert dust, with observations within the marine boundary layer (DeMott et al., 2016; Yang et al., 2020), and with the Price et al.'s (2018) measurements of INP concentrations in dust-laden air masses over the Tropical Atlantic. Peroxide sensitivity was evident in all samples tested (12/26), at temperatures $\geq$ -15 °C, demonstrating a consistent contribution of organic material to observed INPs. Heat-sensitivity further suggested the presence of biological (e.g., proteinaceous) INPs in a subset of aerosol samples tested, particularly at high freezing temperatures. While the dominant mineral dusts in the region are associated with the lowest concentrations of organic carbon globally (e.g., Yost and Hartemink, 2019 and references therein), aerosolized dust is known to be highly enriched in organic matter compared to soil dust (Aryal et al., 2012; Delany and Zenchelsky, 1976; Van Pelt and Zobeck, 2007) and is additionally associated with high microbial loading in the Red Sea (Yahya et al., 2019). A soil dust sample from North Africa exhibited heat and peroxide sensitivity between 5 and -21 °C, further demonstrating that the IN activity of mineral dust in this temperature regime could be associated with organic and/or biological material. Contrary to Price et al. (2018), who measured INP in the dust-laden Tropical Atlantic, no correlation was found between dust loading and n_{INP} or n_s. Results from this study and Gong et al. (2020) indicate that the existing n_s parameterizations alone do not skillfully represent mineral dust associated INPs at modest supercooling near major dust sources.

The source strengths of the Red Sea, Mediterranean Arabian Sea and Arabian Gulf bulk seawater were also evaluated. The maximum source potential was observed in the Arabian Sea (50 mL^{-1} at -19 °C) and was comparable to INP concentrations observed in coastal seawater collected from a pier in Southern California. Overall, the observed n_INP agreed with Gong et al.'s (2020) SSW measurements at Cabo Verde.

Considering that desert dust parameterizations overpredicted ns observed during AQABA despite proximity to major global emissions sources, this study demonstrates the need to evaluate the fidelity of dust INP parameterizations in nascent verses aged dust populations. The observed

discrepancies between measured and predicted n_s underscore a few challenges that inhibit evaluations of dust-specific INP parameterizations: limited observations at modest supercooling, few assured methods for distinguishing between different INP sources in ambient aerosol, a dearth of characteristic soil dust samples from major dust sources, and limited knowledge of the specific composition and characteristics of dust INPs at temperatures $>$ -15 °C.

In addition to providing observations at high to moderate freezing temperatures, future studies could apply the methods developed in Gong et al. (2020) to estimate the contribution of marine INPs to the aerosol sampled. Furthermore, given the combination of marine, dust and anthropogenically-influenced air masses encountered and the evidence of organic and biological INPs at modest supercooling in this study and Gong et al. (2020), future studies could benefit from advances in on-line Light-Induced Fluorescence (LIF) measurement techniques. Whereas the interpretation of fluorescence data from most LIF-based instruments has been limited by the lack of spectroscopic information, newer instruments support real-time spectrally-resolved size and fluorescence measurement information for single particles (Fennelly et al., 2018; Huffman et al., 2020; Könemann et al., 2019). This information could be used to "tag" different classes of organics and biological aerosols, enabling investigations of relationships between n_s, n_INP and organic signatures in, e.g., mineral dusts and agricultural soil dusts. Finally, the decreased n_s observed in this study further motivate comprehensive aerosol-ice nucleation closure studies, which aim to achieve closure between measured and predicted ambient INP concentrations by simultaneously characterizing ambient INPs and ice nucleation relevant properties of the total aerosol population, such as composition and aerosol chemical mixing state (Sullivan et al., 2007).

Data Availability: The data set supporting this manuscript is hosted by the UCSD Library Digital Collections (https://doi.org/10.6075/J0X0676P) (Beall et al., 2021).

Acknowledgements. The authors acknowledge collaborations with King Abdullah University of Science and Technology (KAUST), the Cyprus Institute (CyI) and the Kuwait Institute

for Scientific Research (KISR). We additionally thank Marcel Dorf and Claus Koeppel for the organization of the campaign, as well as Horst Fischer, Ivan Tadic and Uwe Parchatka for.provision of the NO data. Analyses and visualizations of dust mass concentrations and Chl a used in this paper were produced with the Giovanni online data system, developed and maintained by the NASA GES DISC. We would also like to thank Hays Ships Ltd. and the *Kommandor Iona's* crew for their attention to the safety and well-being of the researchers. Funding was provided by the Highly Cited Program at King Saud University and the Max Planck Society.

Chapter 5, in part, has been submitted for publication of the material as it may appear in Atmospheric Chemistry and Physics, 2021. Beall, C.M., Hill, Thomas C.J., DeMott, P.J., Könemann, T., Pikridas, M., Drewnick, F., Harder, H., Pöhlker, C., Lelieveld, J., Weber, B., Iakovides, M., Prokes, R., Sciare, J., Andreae, M.O., Stokes, M.D., Prather, K.A. The dissertation author was the primary investigator and author of this material.

5.6 References

Agresti, A. and Coull, B. A.: Approximate Is Better than "Exact" for Interval Estimation of Binomial Proportions, Am. Stat., 52(2), 119–126, doi:10.2307/2685469, 1998.

Ardon-Dryer, K. and Levin, Z.: Ground-based measurements of immersion freezing in the eastern Mediterranean, Atmos. Chem. Phys., 14(10), 5217–5231, doi:10.5194/acp-14-5217-2014, 2014.

Atkinson, J. D., Murray, B. J., Woodhouse, M. T., Whale, T. F., Baustian, K. J., Carslaw, K. S., Dobbie, S., O'Sullivan, D. and Malkin, T. L.: The importance of feldspar for ice nucleation by mineral dust in mixed-phase clouds, Nature, 498(7454), 355–358, doi:10.1038/nature12278, 2013.

Beall, C. M., Stokes, M. D., Hill, T. C., DeMott, P. J., DeWald, J. T. and Prather, K. A.: Automation and Heat Transfer Characterization of Immersion Mode Spectroscopy for Analysis of Ice Nucleating Particles, Atmos. Meas. Tech., (February), 1–25, doi:10.5194/amt-2016-412, 2017.

Beall, C. M., Michaud, J. M., Fish, M. A., Dinasquet, J., Cornwell, G. C., Stokes, M. D., Burkart,

M. D., Hill, T. C., DeMott, P. J. and Prather, K. A.: Cultivable halotolerant ice-nucleating bacteria and fungi in coastal precipitation, Atmos. Chem. Phys., 21(11), 9031–9045, doi:10.5194/acp-21-9031-2021, 2021.

Boose, Y., Sierau, B., Isabel García, M., Rodríguez, S., Alastuey, A., Linke, C., Schnaiter, M., Kupiszewski, P., Kanji, Z. A. and Lohmann, U.: Ice nucleating particles in the Saharan Air Layer, Atmos. Chem. Phys., 16(14), 9067–9087, doi:10.5194/acp-16-9067-2016, 2016.

Bourtsoukidis, E., Ernle, L., Crowley, J. N., Lelieveld, J., Paris, J.-D., Pozzer, A., Walter, D. and Williams, J.: Non-methane hydrocarbon (C_2–C_8) sources and sinks around the Arabian Peninsula, Atmos. Chem. Phys., 19(10), 7209–7232, doi:10.5194/acp-19-7209-2019, 2019.

Bourtsoukidis, E., Pozzer, A., Sattler, T., Matthaios, V. N., Ernle, L., Edtbauer, A., Fischer, H., Könemann, T., Osipov, S., Paris, J.-D., Pfannerstill, E. Y., Stönner, C., Tadic, I., Walter, D., Wang, N., Lelieveld, J. and Williams, J.: The Red Sea Deep Water is a potent source of atmospheric ethane and propane, Nat. Commun., 11(1), 447, doi:10.1038/s41467-020-14375-0, 2020.

Broadley, S. L., Murray, B. J., Herbert, R. J., Atkinson, J. D., Dobbie, S., Malkin, T. L., Condliffe, E. and Neve, L.: Immersion mode heterogeneous ice nucleation by an illite rich powder representative of atmospheric mineral dust, Atmos. Chem. Phys., 12(1), 287–307, doi:10.5194/acp-12-287-2012, 2012.

Buchard, V., Randles, C. A., da Silva, A. M., Darmenov, A., Colarco, P. R., Govindaraju, R., Ferrare, R., Hair, J., Beyersdorf, A. J., Ziemba, L. D. and Yu, H.: The MERRA-2 Aerosol Reanalysis, 1980 Onward. Part II: Evaluation and Case Studies, J. Clim., 30(17), 6851–6872, doi:10.1175/JCLI-D-16-0613.1, 2017.

Burrows, S. M., Hoose, C., Pöschl, U. and Lawrence, M. G.: Ice nuclei in marine air: biogenic particles or dust?, Atmos. Chem. Phys., 13(1), 245–267, doi:10.5194/acp-13-245-2013, 2013.

Celik, S., Drewnick, F., Fachinger, F., Brooks, J., Darbyshire, E., Coe, H., Paris, J.-D., Eger, P. G., Schuladen, J., Tadic, I., Friedrich, N., Dienhart, D., Hottmann, B., Fischer, H., Crowley, J. N., Harder, H. and Borrmann, S.: Influence of vessel characteristics and atmospheric processes on the gas and particle phase of ship emission plumes: in situ measurements in the Mediterranean Sea and around the Arabian Peninsula, Atmos. Chem. Phys., 20(8), 4713–4734, doi:10.5194/acp-20-4713-2020, 2020.

Chin, M., Ginoux, P., Kinne, S., Torres, O., Holben, B. N., Duncan, B. N., Martin, R. V, Logan, J. A., Higurashi, A. and Nakajima, T.: Tropospheric Aerosol Optical Thickness from the

GOCART Model and Comparisons with Satellite and Sun Photometer Measurements, J. Atmos. Sci., 59(3), 461–483, doi:10.1175/1520-0469(2002)059¡0461:TAOTFT¿2.0.CO;2, 2002.

Colarco, P., da Silva, A., Chin, M. and Diehl, T.: Online simulations of global aerosol distributions in the NASA GEOS-4 model and comparisons to satellite and ground-based aerosol optical depth, J. Geophys. Res. Atmos., 115(D14), doi:https://doi.org/10.1029/2009JD012820, 2010.

Conen, F., Morris, C. E., Leifeld, J., Yakutin, M. V and Alewell, C.: Biological residues define the ice nucleation properties of soil dust, Atmos. Chem. Phys., 11(18), 9643–9648, doi:10.5194/acp-11-9643-2011, 2011.

Conen, F., Rodríguez, S., Hüglin, C., Henne, S., Herrmann, E., Bukowiecki, N. and Alewell, C.: Atmospheric ice nuclei at the high-altitude observatory Jungfraujoch, Switzerland, Tellus, Ser. B Chem. Phys. Meteorol., 67(1), 1–10, doi:10.3402/tellusb.v67.25014, 2015.

Conen, F., Stopelli, E. and Zimmermann, L.: Clues that decaying leaves enrich Arctic air with ice nucleating particles, Atmos. Environ., 129, 91–94, doi:10.1016/j.atmosenv.2016.01.027, 2016.

Cornwell, G. C., McCluskey, C. S., Levin, E. J. T., Suski, K. J., DeMott, P. J., Kreidenweis, S. M. and Prather, K. A.: Direct Online Mass Spectrometry Measurements of Ice Nucleating Particles at a California Coastal Site, J. Geophys. Res. Atmos., 124(22), 12157–12172, doi:doi:10.1029/2019JD030466, 2019.

Cornwell, G. C., Sultana, C. M., Prank, M., Cochran, R. E., Hill, T. C. J., Schill, G. P., DeMott, P. J., Mahowald, N. and Prather, K. A.: Ejection of Dust From the Ocean as a Potential Source of Marine Ice Nucleating Particles, J. Geophys. Res. Atmos., 125(24), e2020JD033073, doi:https://doi.org/10.1029/2020JD033073, 2020.

Cziczo, D. J., Froyd, K. D., Gallavardin, S. J., Moehler, O., Benz, S., Saathoff, H. and Murphy, D. M.: Deactivation of ice nuclei due to atmospherically relevant surface coatings, Environ. Res. Lett., 4(4), 44013, doi:10.1088/1748-9326/4/4/044013, 2009.

Dall'Osto, M., Harrison, R. M., Highwood, E. J., O'Dowd, C., Ceburnis, D., Querol, X. and Achterberg, E. P.: Variation of the mixing state of Saharan dust particles with atmospheric transport, Atmos. Environ., 44(26), 3135–3146, doi:https://doi.org/10.1016/j.atmosenv.2010.05.030, 2010.

DeMott, P. J., Prenni, A. J., Mcmeeking, G. R., Sullivan, R. C., Petters, M. D., Tobo, Y. and Niemand, M.: Integrating laboratory and field data to quantify the immersion freezing ice nucleation activity of mineral dust particles, , 393–409, doi:10.5194/acp-15-393-2015,

2015.

DeMott, P. J., Hill, T. C. J., McCluskey, C. S., Prather, K. A., Collins, D. B., Sullivan, R. C., Ruppel, M. J., Mason, R. H., Irish, V. E., Lee, T., Hwang, C. Y., Rhee, T. S., Snider, J. R., McMeeking, G. R., Dhaniyala, S., Lewis, E. R., Wentzell, J. J. B., Abbatt, J., Lee, C., Sultana, C. M., Ault, A. P., Axson, J. L., Diaz Martinez, M., Venero, I., Santos-Figueroa, G., Stokes, M. D., Deane, G. B., Mayol-Bracero, O. L., Grassian, V. H., Bertram, T. H., Bertram, A. K., Moffett, B. F. and Franc, G. D.: Sea spray aerosol as a unique source of ice nucleating particles, Proc. Natl. Acad. Sci., 113(21), 5797–5803, doi:10.1073/pnas.1514034112, 2016.

DeMott, P. J., Hill, T. C. J., Petters, M. D., Bertram, A. K., Tobo, Y., Mason, R. H., Suski, K. J., Mccluskey, C. S., Levin, E. J. T., Schill, G. P., Boose, Y., Rauker, A. M., Miller, A. J., Zaragoza, J., Rocci, K., Rothfuss, N. E., Taylor, H. P., Hader, J. D., Chou, C., Huffman, J. A., Pöschl, U., Prenni, A. J. and Kreidenweis, S. M.: Comparative measurements of ambient atmospheric concentrations of ice nucleating particles using multiple immersion freezing methods and a continuous flow diffusion chamber, Atmos. Chem. Phys., 17(18), 11227–11245, doi:10.5194/acp-17-11227-2017, 2017.

DeMott, P. J., Möhler, O., Cziczo, D. J., Hiranuma, N., Petters, M. D., Petters, S. S., Belosi, F., Bingemer, H. G., Brooks, S. D., Budke, C., Burkert-Kohn, M., Collier, K. N., Danielczok, A., Eppers, O., Felgitsch, L., Garimella, S., Grothe, H., Herenz, P., Hill, T. C. J., Höhler, K., Kanji, Z. A., Kiselev, A., Koop, T., Kristensen, T. B., Krüger, K., Kulkarni, G., Levin, E. J. T., Murray, B. J., Nicosia, A., O'Sullivan, D., Peckhaus, A., Polen, M. J., Price, H. C., Reicher, N., Rothenberg, D. A., Rudich, Y., Santachiara, G., Schiebel, T., Schrod, J., Seifried, T. M., Stratmann, F., Sullivan, R. C., Suski, K. J., Szakáll, M., Taylor, H. P., Ullrich, R., Vergara-Temprado, J., Wagner, R., Whale, T. F., Weber, D., Welti, A., Wilson, T. W., Wolf, M. J. and Zenker, J.: The Fifth International Workshop on Ice Nucleation phase 2 (FIN-02): laboratory intercomparison of ice nucleation measurements, Atmos. Meas. Tech., 11(11), 6231–6257, doi:10.5194/amt-11-6231-2018, 2018.

Eastwood, M. L., Cremel, S., Wheeler, M., Murray, B. J., Girard, E. and Bertram, A. K.: Effects of sulfuric acid and ammonium sulfate coatings on the ice nucleation properties of kaolinite particles, Geophys. Res. Lett., 36(2), doi:https://doi.org/10.1029/2008GL035997, 2009.

Edtbauer, A., Stönner, C., Pfannerstill, E. Y., Berasategui, M., Walter, D., Crowley, J. N., Lelieveld, J. and Williams, J.: A new marine biogenic emission: methane sulfonamide (MSAM), dimethyl sulfide (DMS), and dimethyl sulfone ($DMSO_2$) measured in air over the Arabian Sea, Atmos. Chem. Phys., 20(10), 6081–6094, doi:10.5194/acp-20-6081-2020, 2020.
Eger, P. G., Friedrich, N., Schuladen, J., Shenolikar, J., Fischer, H., Tadic, I., Harder, H., Martinez, M., Rohloff, R., Tauer, S., Drewnick, F., Fachinger, F., Brooks, J., Darbyshire, E., Sciare, J., Pikridas, M., Lelieveld, J. and Crowley, J. N.: Shipborne measurements of $ClNO_2$ in the Mediterranean Sea and around the Arabian Peninsula during summer,

Atmos. Chem. Phys., 19(19), 12121–12140, doi:10.5194/acp-19-12121-2019, 2019.

Ellerbrock, R. H., Gerke, H. H., Bachmann, J. and Goebel, M.-O.: Composition of Organic Matter Fractions for Explaining Wettability of Three Forest Soils, Soil Sci. Soc. Am. J., 69(1), 57–66, doi:https://doi.org/10.2136/sssaj2005.0057, 2005.

Fennelly, M. J., Sewell, G., Prentice, M. B., O'Connor, D. J. and Sodeau, J. R.: Review: The Use of Real-Time Fluorescence Instrumentation to Monitor Ambient Primary Biological Aerosol Particles (PBAP), Atmosphere (Basel)., 9(1), doi:10.3390/atmos9010001, 2018.

Fornea, A. P., Brooks, S. D., Dooley, J. B. and Saha, A.: Heterogeneous freezing of ice on atmospheric aerosols containing ash, soot, and soil, J. Geophys. Res. Atmos., 114(D13), doi:https://doi.org/10.1029/2009JD011958, 2009.

Friedrich, N., Eger, P., Shenolikar, J., Sobanski, N., Schuladen, J., Dienhart, D., Hottmann, B., Tadic, I., Fischer, H., Martinez, M., Rohloff, R., Tauer, S., Harder, H., Pfannerstill, E. Y., Wang, N., Williams, J., Brooks, J., Drewnick, F., Su, H., Li, G., Cheng, Y., Lelieveld, J. and Crowley, J. N.: Reactive nitrogen around the Arabian Peninsula and in the Mediterranean Sea during the 2017 AQABA ship campaign, Atmos. Chem. Phys., 21(10), 7473–7498, doi:10.5194/acp-21-7473-2021, 2021.

Gandham, H., Dasari, H. P., Langodan, S., Karumuri, R. K. and Hoteit, I.: Major Changes in Extreme Dust Events Dynamics Over the Arabian Peninsula During 2003–2017 Driven by Atmospheric Conditions, J. Geophys. Res. Atmos., 125(24), e2020JD032931, doi:https://doi.org/10.1029/2020JD032931, 2020.

Garcia, E., Hill, T. C. J., Prenni, A. J., DeMott, P. J., Franc, G. D. and Kreidenweis, S. M.: Biogenic ice nuclei in boundary layer air over two U.S. High Plains agricultural regions, J. Geophys. Res. Atmos., 117(D18), doi:https://doi.org/10.1029/2012JD018343, 2012.

Gelaro, R., McCarty, W., Suárez, M. J., Todling, R., Molod, A., Takacs, L., Randles, C. A., Darmenov, A., Bosilovich, M. G., Reichle, R., Wargan, K., Coy, L., Cullather, R., Draper, C., Akella, S., Buchard, V., Conaty, A., da Silva, A. M., Gu, W., Kim, G.-K., Koster, R., Lucchesi, R., Merkova, D., Nielsen, J. E., Partyka, G., Pawson, S., Putman, W., Rienecker, M., Schubert, S. D., Sienkiewicz, M. and Zhao, B.: The Modern-Era Retrospective Analysis for Research and Applications, Version 2 (MERRA-2), J. Clim., 30(14), 5419–5454, doi:10.1175/JCLI-D-16-0758.1, 2017.

Ginoux, P., Chin, M., Tegen, I., Prospero, J. M., Holben, B., Dubovik, O. and Lin, S.-J.: Sources and distributions of dust aerosols simulated with the GOCART model, J. Geophys. Res. Atmos., 106(D17), 20255–20273, doi:https://doi.org/10.1029/2000JD000053, 2001.

Ginoux, P., Prospero, J. M., Gill, T. E., Hsu, N. C. and Zhao, M.: Global-scale attribution of

anthropogenic and natural dust sources and their emission rates based on MODIS Deep Blue aerosol products, Rev. Geophys., 50(3), doi:https://doi.org/10.1029/2012RG000388, 2012.

Gong, X., Wex, H., Müller, T., Wiedensohler, A., Höhler, K., Kandler, K., Ma, N., Dietel, B., Schiebel, T., Möhler, O. and Stratmann, F.: Characterization of aerosol properties at Cyprus, focusing on cloud condensation nuclei and ice-nucleating particles, Atmos. Chem. Phys., 19(16), 10883–10900, doi:10.5194/acp-19-10883-2019, 2019a.

Gong, X., Wex, H., van Pinxteren, M., Triesch, N., Fomba, K. W., Lubitz, J., Stolle, C., Robinson, T.-B., Müller, T., Herrmann, H. and Stratmann, F.: Ice nucleating particles measured in air, cloud and seawater at the Cape Verde Atmospheric Observatory (CVAO), , doi:10.1594/PANGAEA.906946, 2019b.

Gong, X., Wex, H., van Pinxteren, M., Triesch, N., Fomba, K. W., Lubitz, J., Stolle, C., Robinson, T.-B., Müller, T., Herrmann, H. and Stratmann, F.: Characterization of aerosol particles at Cabo Verde close to sea level and at the cloud level – Part 2: Ice-nucleating particles in air, cloud and seawater, Atmos. Chem. Phys., 20(3), 1451–1468, doi:10.5194/acp-20-1451-2020, 2020.

Hara, K., Maki, T., Kakikawa, M., Kobayashi, F. and Matsuki, A.: Effects of different temperature treatments on biological ice nuclei in snow samples, Atmos. Environ., 140, 415–419, doi:10.1016/j.atmosenv.2016.06.011, 2016.

Harrison, A. D., Whale, T. F., Carpenter, M. A., Holden, M. A., Neve, L., O'Sullivan, D., Vergara Temprado, J. and Murray, B. J.: Not all feldspars are equal: a survey of ice nucleating properties across the feldspar group of minerals, Atmos. Chem. Phys., 16(17), 10927–10940, doi:10.5194/acp-16-10927-2016, 2016.

Harrison, A. D., Lever, K., Sanchez-Marroquin, A., Holden, M. A., Whale, T. F., Tarn, M. D., McQuaid, J. B. and Murray, B. J.: The ice-nucleating ability of quartz immersed in water and its atmospheric importance compared to K-feldspar, Atmos. Chem. Phys., 19(17), 11343–11361, doi:10.5194/acp-19-11343-2019, 2019.

Hartmann, M., Adachi, K., Eppers, O., Haas, C., Herber, A., Holzinger, R., Hünerbein, A., Jäkel, E., Jentzsch, C., van Pinxteren, M., Wex, H., Willmes, S. and Stratmann, F.: Wintertime Airborne Measurements of Ice Nucleating Particles in the High Arctic: A Hint to a Marine, Biogenic Source for Ice Nucleating Particles, Geophys. Res. Lett., 47(13), e2020GL087770, doi:https://doi.org/10.1029/2020GL087770, 2020.

Hill, T. C. J., DeMott, P. J., Tobo, Y., Fröhlich-Nowoisky, J., Moffett, B. F., Franc, G. D. and Kreidenweis, S. M.: Sources of organic ice nucleating particles in soils, Atmos. Chem. Phys., 16(11), 7195–7211, doi:10.5194/acp-16-7195-2016, 2016.

Hinz, K.-P., Trimborn, A., Weingartner, E., Henning, S., Baltensperger, U. and Spengler, B.: Aerosol single particle composition at the Jungfraujoch, J. Aerosol Sci., 36(1), 123–145, doi:https://doi.org/10.1016/j.jaerosci.2004.08.001, 2005.

Hoose, C. and Möhler, O.: Heterogeneous ice nucleation on atmospheric aerosols: A review of results from laboratory experiments., 2012.

Hoose, C., Kristjánsson, J. E., Chen, J.-P. and Hazra, A.: A Classical-Theory-Based Parameterization of Heterogeneous Ice Nucleation by Mineral Dust, Soot, and Biological Particles in a Global Climate Model, J. Atmos. Sci., 67(8), 2483–2503, doi:10.1175/2010JAS3425.1, 2010.

Huffman, J. A., Perring, A. E., Savage, N. J., Clot, B., Crouzy, B., Tummon, F., Shoshanim, O., Damit, B., Schneider, J., Sivaprakasam, V., Zawadowicz, M. A., Crawford, I., Gallagher, M., Topping, D., Doughty, D. C., Hill, S. C. and Pan, Y.: Real-time sensing of bioaerosols: Review and current perspectives, Aerosol Sci. Technol., 54(5), 465–495, doi:10.1080/02786826.2019.1664724, 2020.

Huneeus, N., Schulz, M., Balkanski, Y., Griesfeller, J., Prospero, J., Kinne, S., Bauer, S., Boucher, O., Chin, M., Dentener, F., Diehl, T., Easter, R., Fillmore, D., Ghan, S., Ginoux, P., Grini, A., Horowitz, L., Koch, D., Krol, M. C., Landing, W., Liu, X., Mahowald, N., Miller, R., Morcrette, J.-J., Myhre, G., Penner, J., Perlwitz, J., Stier, P., Takemura, T. and Zender, C. S.: Global dust model intercomparison in AeroCom phase I, Atmos. Chem. Phys., 11(15), 7781–7816, doi:10.5194/acp-11-7781-2011, 2011.

Isono, K. and Ikebe, Y.: On the Ice-nucleating Ability of Rock-forming Minerals and Soil Particles; J. Meteorol. Soc. Japan. Ser. II, 38(5), 213–230, doi:10.2151/jmsj1923.38.5-213, 1960.

Kanji, Z. A., Ladino, L. A., Wex, H., Boose, Y., Burkert-Kohn, M., Cziczo, D. J. and Krämer, M.: Overview of Ice Nucleating Particles, Meteorol. Monogr., 58, 1.1-1.33, doi:10.1175/amsmonographs-d-16-0006.1, 2017.

Khaniabadi, Y. O., Daryanoosh, S. M., Amrane, A., Polosa, R., Hopke, P. K., Goudarzi, G., Mohammadi, M. J., Sicard, P. and Armin, H.: Impact of Middle Eastern Dust storms on human health, Atmos. Pollut. Res., 8(4), 606–613, doi:https://doi.org/10.1016/j.apr.2016.11.005, 2017.

Kinne, S., Schulz, M., Textor, C., Guibert, S., Balkanski, Y., Bauer, S. E., Berntsen, T., Berglen, T. F., Boucher, O., Chin, M., Collins, W., Dentener, F., Diehl, T., Easter, R., Feichter, J., Fillmore, D., Ghan, S., Ginoux, P., Gong, S., Grini, A., Hendricks, J., Herzog, M., Horowitz, L., Isaksen, I., Iversen, T., Kirkevåg, A., Kloster, S., Koch, D., Kristjansson, J.

E., Krol, M., Lauer, A., Lamarque, J. F., Lesins, G., Liu, X., Lohmann, U., Montanaro, V., Myhre, G., Penner, J., Pitari, G., Reddy, S., Seland, O., Stier, P., Takemura, T. and Tie, X.: An AeroCom initial assessment – optical properties in aerosol component modules of global models, Atmos. Chem. Phys., 6(7), 1815–1834, doi:10.5194/acp-6-1815-2006, 2006.

Kleist, D. T., Parrish, D. F., Derber, J. C., Treadon, R., Wu, W.-S. and Lord, S.: Introduction of the GSI into the NCEP Global Data Assimilation System, Weather Forecast., 24(6), 1691–1705, doi:10.1175/2009WAF2222201.1, 2009.

Klingmüller, K., Pozzer, A., Metzger, S., Stenchikov, G. L. and Lelieveld, J.: Aerosol optical depth trend over the Middle East, Atmos. Chem. Phys., 16(8), 5063–5073, doi:10.5194/acp-16-5063-2016, 2016.

Knopf, D. A. and Koop, T.: Heterogeneous nucleation of ice on surrogates of mineral dust, J. Geophys. Res. Atmos., 111(D12), doi:https://doi.org/10.1029/2005JD006894, 2006.

Kögel-Knabner, I., Guggenberger, G., Kleber, M., Kandeler, E., Kalbitz, K., Scheu, S., Eusterhues, K. and Leinweber, P.: Organo-mineral associations in temperate soils: Integrating biology, mineralogy, and organic matter chemistry, J. Plant Nutr. Soil Sci., 171(1), 61–82, doi:https://doi.org/10.1002/jpln.200700048, 2008.

Kok, J. F., Adebiyi, A. A., Albani, S., Balkanski, Y., Checa-Garcia, R., Chin, M., Colarco, P. R., Hamilton, D. S., Huang, Y., Ito, A., Klose, M., Li, L., Mahowald, N. M., Miller, R. L., Obiso, V., Pérez Garcı'a-Pando, C., Rocha-Lima, A. and Wan, J. S.: Contribution of the world's main dust source regions to the global cycle of desert dust, Atmos. Chem. Phys., 21(10), 8169–8193, doi:10.5194/acp-21-8169-2021, 2021.

Könemann, T., Savage, N., Klimach, T., Walter, D., Fröhlich-Nowoisky, J., Su, H., Pöschl, U., Huffman, J. A. and Pöhlker, C.: Spectral Intensity Bioaerosol Sensor (SIBS): an instrument for spectrally resolved fluorescence detection of single particles in real time, Atmos. Meas. Tech., 12(2), 1337–1363, doi:10.5194/amt-12-1337-2019, 2019.

Krasnov, H., Katra, I. and Friger, M.: Increase in dust storm related PM10 concentrations: A time series analysis of 2001–2015, Environ. Pollut., 213, 36–42, doi:https://doi.org/10.1016/j.envpol.2015.10.021, 2016.

Krueger, B. J., Grassian, V. H., Cowin, J. P. and Laskin, A.: Heterogeneous chemistry of individual mineral dust particles from different dust source regions: the importance of particle mineralogy, Atmos. Environ., 38(36), 6253–6261, doi:https://doi.org/10.1016/j.atmosenv.2004.07.010, 2004.

Krzywinski, M. and Altman, N.: Error bars, Nat. Methods, 10(10), 921–922,

doi:10.1038/nmeth.2659, 2013.

Ladino, L. A., Raga, G. B., Alvarez-Ospina, H., Andino-Enríquez, M. A., Rosas, I., Martínez, L., Salinas, E., Miranda, J., Ramírez-Díaz, Z., Figueroa, B., Chou, C., Bertram, A. K., Quintana, E. T., Maldonado, L. A., García-Reynoso, A., Si, M. and Irish, V. E.: Ice-nucleating particles in a coastal tropical site, Atmos. Chem. Phys., 19(9), 6147–6165, doi:10.5194/acp-19-6147-2019, 2019.

Lohmann, U. and Feichter, J.: Global indirect aerosol effects: a review, Atmos. Chem. Phys., 5(3), 715–737, doi:10.5194/acp-5-715-2005, 2005.

Manders, A. M. ., Schapp, M., Jozwicka, M., van Arkel, F., Weijers, E. . and Matthijsen, J.: The contribution of sea salt to PM 10 and PM in the Netherlands, 2009.

Mayol, E., Jiménez, M. A., Herndl, G. J., Duarte, C. M. and Arrieta, J. M.: Resolving the abundance and air-sea fluxes of airborne microorganisms in the North Atlantic Ocean, Front. Microbiol., 5, 557, doi:10.3389/fmicb.2014.00557, 2014.

McCluskey, C. S., Hill, T. C. J., Malfatti, F., Sultana, C. M., Lee, C., Santander, M. V, Beall, C. M., Moore, K. A., Cornwell, G. C., Collins, D. B., Prather, K. A., Jayarathne, T., Stone, E. A., Azam, F., Kreidenweis, S. M. and DeMott, P. J.: A Dynamic Link between Ice Nucleating Particles Released in Nascent Sea Spray Aerosol and Oceanic Biological Activity during Two Mesocosm Experiments, J. Atmos. Sci., 74(1), 151–166, doi:10.1175/JAS-D-16-0087.1, 2017.

McCluskey, C. S., Hill, T. C. J., Sultana, C. M., Laskina, O., Trueblood, J., Santander, M. V, Beall, C. M., Michaud, J. M., Kreidenweis, S. M., Prather, K. A., Grassian, V. and DeMott, P. J.: A Mesocosm Double Feature: Insights into the Chemical Makeup of Marine Ice Nucleating Particles, J. Atmos. Sci., 75(7), 2405–2423, doi:10.1175/JAS-D-17-0155.1, 2018a.

McCluskey, C. S., Ovadnevaite, J., Rinaldi, M., Atkinson, J., Belosi, F., Ceburnis, D., Marullo, S., Hill, T. C. J., Lohmann, U., Kanji, Z. A., O'Dowd, C., Kreidenweis, S. M. and DeMott, P. J.: Marine and Terrestrial Organic Ice-Nucleating Particles in Pristine Marine to Continentally Influenced Northeast Atlantic Air Masses, J. Geophys. Res. Atmos., 123(11), 6196–6212, doi:10.1029/2017JD028033, 2018b.

McCluskey, C. S., Hill, T. C. J., Humphries, R. S., Rauker, A. M., Moreau, S., Strutton, P. G., Chambers, S. D., Williams, A. G. and McRobert, I.: Observations of Ice Nucleating Particles Over Southern Ocean Waters, Geophys. Res. Lett., 989–997, doi:10.1029/2018GL079981, 2018c.

Mitts, B., Wang, X., Lucero, D., Beall, C., Deane, G., DeMott, P. and Prather, K.: Importance of

Supermicron Ice Nucleating Particles in Nascent Sea Spray, Geophys. Res. Lett., n/a(n/a), e2020GL089633, doi:https://doi.org/10.1029/2020GL089633, 2021.

Molod, A., Takacs, L., Suarez, M. and Bacmeister, J.: Development of the GEOS-5 atmospheric general circulation model: evolution from MERRA to MERRA2, Geosci. Model Dev., 8(5), 1339–1356, doi:10.5194/gmd-8-1339-2015, 2015.

Murray, B. J., O'Sullivan, D., Atkinson, J. D. and Webb, M. E.: Ice nucleation by particles immersed in supercooled cloud droplets., Chem. Soc. Rev., 41(19), 6519–54, doi:10.1039/c2cs35200a, 2012.

Niedermeier, D., Augustin-Bauditz, S., Hartmann, S., Wex, H., Ignatius, K. and Stratmann, F.: Can we define an asymptotic value for the ice active surface site density for heterogeneous ice nucleation?, J. Geophys. Res. Atmos., 120(10), 5036–5046, doi:https://doi.org/10.1002/2014JD022814, 2015.

Niemand, M., Möhler, O., Vogel, B., Vogel, H., Hoose, C., Connolly, P., Klein, H., Bingemer, H., Demott, P., Skrotzki, J. and Leisner, T.: A particle-surface-area-based parameterization of immersion freezing on desert dust particles, J. Atmos. Sci., 69(10), 3077–3092, doi:10.1175/JAS-D-11-0249.1, 2012.

Nortcliff, S.: World Soil Resources and Food Security. Edited by R. Lal and BA Stewart. Boca Raton, Fl, USA: CRC Press (2012), pp. 574,£82.00. ISBN-13: 978-1439844502., Exp. Agric., 48(2), 305–306, 2012.

O'Sullivan, D., Murray, B. J., Malkin, T. L., Whale, T. F., Umo, N. S., Atkinson, J. D., Price, H. C., Baustian, K. J., Browse, J. and Webb, M. E.: Ice nucleation by fertile soil dusts: relative importance of mineral and biogenic components, Atmos. Chem. Phys., 14(4), 1853–1867, doi:10.5194/acp-14-1853-2014, 2014.

O'Sullivan, D., Adams, M. P., Tarn, M. D., Harrison, A. D., Vergara-Temprado, J., Porter, G. C. E., Holden, M. A., Sanchez-Marroquin, A., Carotenuto, F., Whale, T. F., McQuaid, J. B., Walshaw, R., Hedges, D. H. P., Burke, I. T., Cui, Z. and Murray, B. J.: Contributions of biogenic material to the atmospheric ice-nucleating particle population in North Western Europe, Sci. Rep., 8(1), 13821, doi:10.1038/s41598-018-31981-7, 2018.

Paramonov, M., David, R. O., Kretzschmar, R. and Kanji, Z. A.: A laboratory investigation of the ice nucleation efficiency of three types of mineral and soil dust, Atmos. Chem. Phys., 18(22), 16515–16536, doi:10.5194/acp-18-16515-2018, 2018.

Perkins, R. J., Gillette, S. M., Hill, T. C. J. and DeMott, P. J.: The Labile Nature of Ice Nucleation by Arizona Test Dust, ACS Earth Sp. Chem., 4(1), 133–141, doi:10.1021/acsearthspacechem.9b00304, 2020.

Pfannerstill, E. Y., Wang, N., Edtbauer, A., Bourtsoukidis, E., Crowley, J. N., Dienhart, D., Eger, P. G., Ernle, L., Fischer, H., Hottmann, B., Paris, J.-D., Stönner, C., Tadic, I., Walter, D., Lelieveld, J. and Williams, J.: Shipborne measurements of total OH reactivity around the Arabian Peninsula and its role in ozone chemistry, Atmos. Chem. Phys., 19(17), 11501–11523, doi:10.5194/acp-19-11501-2019, 2019.

Price, H. C., Baustian, K. J., McQuaid, J. B., Blyth, A., Bower, K. N., Choularton, T., Cotton, R. J., Cui, Z., Field, P. R., Gallagher, M., Hawker, R., Merrington, A., Miltenberger, A., Neely III, R. R., Parker, S. T., Rosenberg, P. D., Taylor, J. W., Trembath, J., Vergara-Temprado, J., Whale, T. F., Wilson, T. W., Young, G. and Murray, B. J.: Atmospheric Ice-Nucleating Particles in the Dusty Tropical Atlantic, J. Geophys. Res. Atmos., 123(4), 2175–2193, doi:https://doi.org/10.1002/2017JD027560, 2018.

Rienecker, M. M., Suarez, M. J., Gelaro, R., Todling, R., Bacmeister, J., Liu, E., Bosilovich, M. G., Schubert, S. D., Takacs, L., Kim, G.-K., Bloom, S., Chen, J., Collins, D., Conaty, A., da Silva, A., Gu, W., Joiner, J., Koster, R. D., Lucchesi, R., Molod, A., Owens, T., Pawson, S., Pegion, P., Redder, C. R., Reichle, R., Robertson, F. R., Ruddick, A. G., Sienkiewicz, M. and Woollen, J.: MERRA: NASA's Modern-Era Retrospective Analysis for Research and Applications, J. Clim., 24(14), 3624–3648, doi:10.1175/JCLI-D-11-00015.1, 2011.

Saha, S., Moorthi, S., Wu, X., Wang, J., Nadiga, S., Tripp, P., Behringer, D., Hou, Y.-T., Chuang, H., Iredell, M., Ek, M., Meng, J., Yang, R., Mendez, M. P., van den Dool, H., Zhang, Q., Wang, W., Chen, M. and Becker, E.: The NCEP Climate Forecast System Version 2, J. Clim., 27(6), 2185–2208, doi:10.1175/JCLI-D-12-00823.1, 2014.

Salam, A., Lohmann, U. and Lesins, G.: Ice nucleation of ammonia gas exposed montmorillonite mineral dust particles, Atmos. Chem. Phys., 7(14), 3923–3931, doi:10.5194/acp-7-3923-2007, 2007.

Sanchez-Marroquin, A, West, J S, Burke, I T, McQuaid, J B, and Murray, B J: Mineral and biological ice-nucleating particles above the South East of the British Isles, 1, 176–191, https://doi.org/10.1039/D1EA00003A, 2021.

Schnell, R. C.: Ice Nuclei in Seawater, Fog Water and Marine Air off the Coast of Nova Scotia: Summer 1975, J. Atmos. Sci., 34(8), 1299–1305, doi:10.1175/1520-0469(1977)034¡1299:INISFW¿2.0.CO;2, 1977.

Shahsavani, A., Naddafi, K., Jafarzade Haghighifard, N., Mesdaghinia, A., Yunesian, M., Nabizadeh, R., Arahami, M., Sowlat, M. H., Yarahmadi, M., Saki, H., Alimohamadi, M., Nazmara, S., Motevalian, S. A. and Goudarzi, G.: The evaluation of PM10, PM2.5, and PM1 concentrations during the Middle Eastern Dust (MED) events in Ahvaz, Iran, from april through september 2010, J. Arid Environ., 77, 72–83,

doi:https://doi.org/10.1016/j.jaridenv.2011.09.007, 2012.

Steinke, I., Funk, R., Busse, J., Iturri, A., Kirchen, S., Leue, M., Möhler, O., Schwartz, T., Schnaiter, M., Sierau, B., Toprak, E., Ullrich, R., Ulrich, A., Hoose, C. and Leisner, T.: Ice nucleation activity of agricultural soil dust aerosols from Mongolia, Argentina, and Germany, J. Geophys. Res. Atmos., 121(22), 13,513-559,576, doi:https://doi.org/10.1002/2016JD025160, 2016.

Stohl, A., Hittenberger, M. and Wotawa, G.: Validation of the Lagrangian particle dispersion model FLEXPART against large scale tracer experiment data, Atmos. Environ., 32(24), 4245–4264, 1998.

Sullivan, R. C., Guazzotti, S. A., Sodeman, D. A. and Prather, K. A.: Direct observations of the atmospheric processing of Asian mineral dust, Atmos. Chem. Phys., 7(5), 1213–1236, doi:10.5194/acp-7-1213-2007, 2007.

Sullivan, R. C., Miñambres, L., DeMott, P. J., Prenni, A. J., Carrico, C. M., Levin, E. J. T. and Kreidenweis, S. M.: Chemical processing does not always impair heterogeneous ice nucleation of mineral dust particles, Geophys. Res. Lett., 37(24), doi:https://doi.org/10.1029/2010GL045540, 2010a.

Sullivan, R. C., Petters, M. D., DeMott, P. J., Kreidenweis, S. M., Wex, H., Niedermeier, D., Hartmann, S., Clauss, T., Stratmann, F., Reitz, P., Schneider, J. and Sierau, B.: Irreversible loss of ice nucleation active sites in mineral dust particles caused by sulphuric acid condensation, Atmos. Chem. Phys., 10(23), 11471–11487, doi:10.5194/acp-10-11471-2010, 2010b.

Sullivan, R. C., Petters, M. D., DeMott, P. J., Kreidenweis, S. M., Wex, H., Niedermeier, D., Hartmann, S., Clauss, T., Stratmann, F., Reitz, P., Schneider, J. and Sierau, B.: Irreversible loss of ice nucleation active sites in mineral dust particles caused by sulphuric acid condensation, Atmos. Chem. Phys., 10(23), 11471–11487, doi:10.5194/acp-10-11471-2010, 2010b.

Suski, K. J., Hill, T. C. J., Levin, E. J. T., Miller, A., DeMott, P. J. and Kreidenweis, S. M.: Agricultural harvesting emissions of ice-nucleating particles, Atmos. Chem. Phys., 18(18), 13755–13771, doi:10.5194/acp-18-13755-2018, 2018.

Tadic, I., Crowley, J. N., Dienhart, D., Eger, P., Harder, H., Hottmann, B., Martinez, M., Parchatka, U., Paris, J.-D., Pozzer, A., Rohloff, R., Schuladen, J., Shenolikar, J., Tauer, S., Lelieveld, J. and Fischer, H.: Net ozone production and its relationship to nitrogen oxides and volatile organic compounds in the marine boundary layer around the Arabian Peninsula, Atmos. Chem. Phys., 20(11), 6769–6787, doi:10.5194/acp-20-6769-2020, 2020.

Tobo, Y., DeMott, P. J., Hill, T. C. J., Prenni, A. J., Swoboda-Colberg, N. G., Franc, G. D. and

Kreidenweis, S. M.: Organic matter matters for ice nuclei of agricultural soil origin, Atmos. Chem. Phys., 14(16), 8521–8531, doi:10.5194/acp-14-8521-2014, 2014.

Ullrich, R., Hoose, C., Möhler, O., Niemand, M., Wagner, R., Höhler, K., Hiranuma, N., Saathoff, H. and Leisner, T.: A new ice nucleation active site parameterization for desert dust and soot, J. Atmos. Sci., 74(3), 699–717, doi:10.1175/JAS-D-16-0074.1, 2017.

Vergara-Temprado, J., Murray, B. J., Wilson, T. W., O'Sullivan, D., Browse, J., Pringle, K. J., Ardon-Dryer, K., Bertram, A. K., Burrows, S. M., Ceburnis, D., Demott, P. J., Mason, R. H., O'Dowd, C. D., Rinaldi, M. and Carslaw, K. S.: Contribution of feldspar and marine organic aerosols to global ice nucleating particle concentrations, Atmos. Chem. Phys., 17(5), 3637–3658, doi:10.5194/acp-17-3637-2017, 2017.

Vergara-Temprado, J., Miltenberger, A. K., Furtado, K., Grosvenor, D. P., Shipway, B. J., Hill, A. A., Wilkinson, J. M., Field, P. R., Murray, B. J. and Carslaw, K. S.: Strong control of Southern Ocean cloud reflectivity by ice-nucleating particles, Proc. Natl. Acad. Sci., 115(11), 2687 LP – 2692, doi:10.1073/pnas.1721627115, 2018.

Wang, N., Edtbauer, A., Stönner, C., Pozzer, A., Bourtsoukidis, E., Ernle, L., Dienhart, D., Hottmann, B., Fischer, H., Schuladen, J., Crowley, J. N., Paris, J.-D., Lelieveld, J. and Williams, J.: Measurements of carbonyl compounds around the Arabian Peninsula: overview and model comparison, Atmos. Chem. Phys., 20(18), 10807–10829, doi:10.5194/acp-20-10807-2020, 2020.

Wang, X., Deane, G. B., Moore, K. A., Ryder, O. S., Stokes, M. D., Beall, C. M., Collins, D. B., Santander, M. V, Burrows, S. M., Sultana, C. M. and Prather, K. A.: The role of jet and film drops in controlling the mixing state of submicron sea spray aerosol particles, Proc. Natl. Acad. Sci., 114(27), 6978–6983, doi:10.1073/pnas.1702420114, 2017.
Welti, A., Lüönd, F., Kanji, Z. A., Stetzer, O. and Lohmann, U.: Time dependence of immersion freezing: an experimental study on size selected kaolinite particles, Atmos. Chem. Phys., 12(20), 9893–9907, doi:10.5194/acp-12-9893-2012, 2012.

Wex, H., DeMott, P. J., Tobo, Y., Hartmann, S., Rösch, M., Clauss, T., Tomsche, L., Niedermeier, D. and Stratmann, F.: Kaolinite particles as ice nuclei: learning from the use of different kaolinite samples and different coatings, Atmos. Chem. Phys., 14(11), 5529–5546, doi:10.5194/acp-14-5529-2014, 2014.

Whale, T. F., Murray, B. J., O'Sullivan, D., Wilson, T. W., Umo, N. S., Baustian, K. J., Atkinson, J. D., Workneh, D. A. and Morris, G. J.: A technique for quantifying heterogeneous ice nucleation in microlitre supercooled water droplets, Atmos. Meas. Tech., 8(6), 2437–2447, doi:10.5194/amt-8-2437-2015, 2015.

Wilson, T. W., Ladino, L. a., Alpert, P. a., Breckels, M. N., Brooks, I. M., Browse, J., Burrows, S.

M., Carslaw, K. S., Huffman, J. A., Judd, C., Kilthau, W. P., Mason, R. H., McFiggans, G., Miller, L. a., Nájera, J. J., Polishchuk, E., Rae, S., Schiller, C. L., Si, M., Temprado, J. V., Whale, T. F., Wong, J. P. S., Wurl, O., Yakobi-Hancock, J. D., Abbatt, J. P. D., Aller, J. Y., Bertram, A. K., Knopf, D. a. and Murray, B. J.: A marine biogenic source of atmospheric ice-nucleating particles, Nature, 525(7568), 234–238, doi:10.1038/nature14986, 2015.
Wu, W.-S., Purser, R. J. and Parrish, D. F.: Three-Dimensional Variational Analysis with Spatially Inhomogeneous Covariances, Mon. Weather Rev., 130(12), 2905–2916, doi:10.1175/1520-0493(2002)130¡2905:TDVAWS¿2.0.CO;2, 2002.

Yadav, S., Venezia, R. E., Paerl, R. W. and Petters, M. D.: Characterization of Ice-Nucleating Particles Over Northern India, J. Geophys. Res. Atmos., 124(19), 10467–10482, doi:https://doi.org/10.1029/2019JD030702, 2019.

Yahya, R. Z., Arrieta, J. M., Cusack, M. and Duarte, C. M.: Airborne Prokaryote and Virus Abundance Over the Red Sea, Front. Microbiol., 10, 1112, doi:10.3389/fmicb.2019.01112, 2019.

Yang, J., Wang, Z., Heymsfield, A. J., DeMott, P. J., Twohy, C. H., Suski, K. J., and Toohey, D. W.: High ice concentration observed in tropical maritime stratiform mixed-phase clouds with top temperatures warmer than -8 °C, Atmos. Res., 233, 104719, https://doi.org/10.1016/j.atmosres.2019.104719, 2020.

Yost, J. L. and Hartemink, A. E.: Chapter Four - Soil organic carbon in sandy soils: A review, vol. 158, edited by D. L. Sparks, pp. 217–310, Academic Press., 2019.

Yu, Y., Kalashnikova, O. V, Garay, M. J., Lee, H. and Notaro, M.: Identification and Characterization of Dust Source Regions Across North Africa and the Middle East Using MISR Satellite Observations, Geophys. Res. Lett., 45(13), 6690–6701, doi:https://doi.org/10.1029/2018GL078324, 2018.

Zolles, T., Burkart, J., Häusler, T., Pummer, B., Hitzenberger, R. and Grothe, H.: Identification of Ice Nucleation Active Sites on Feldspar Dust Particles, J. Phys. Chem. A, 119(11), 2692–2700, doi:10.1021/jp509839x, 2015.

5.7 Supplement

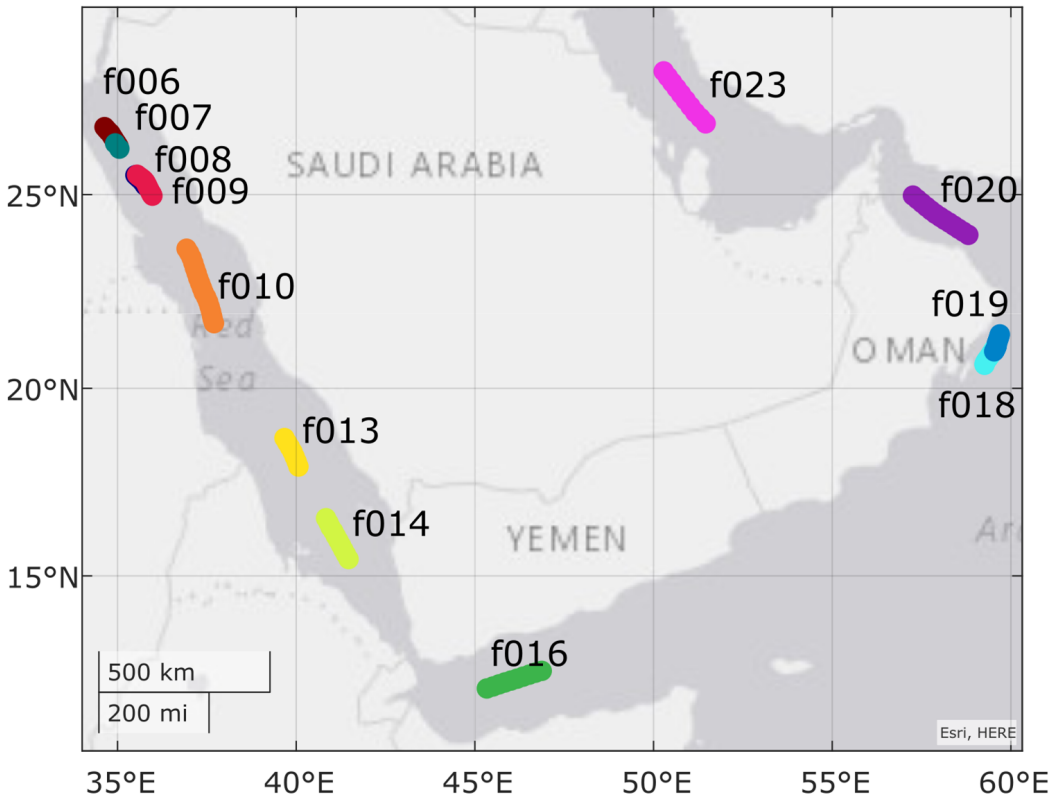

Figure 5.8: Locations where each aerosol sample was collected during Leg 1 (Malta to Kuwait).

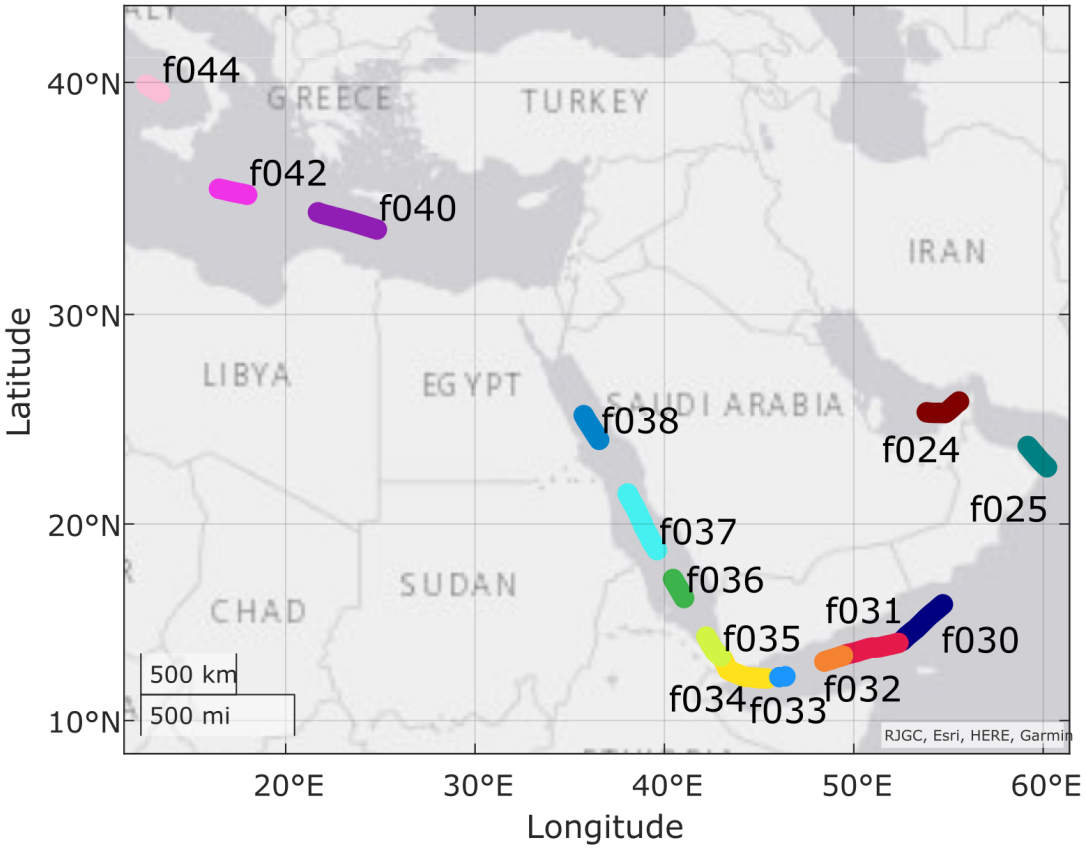

Figure 5.9: Locations where each aerosol sample was collected during Leg 2 (Kuwait to Toulon).

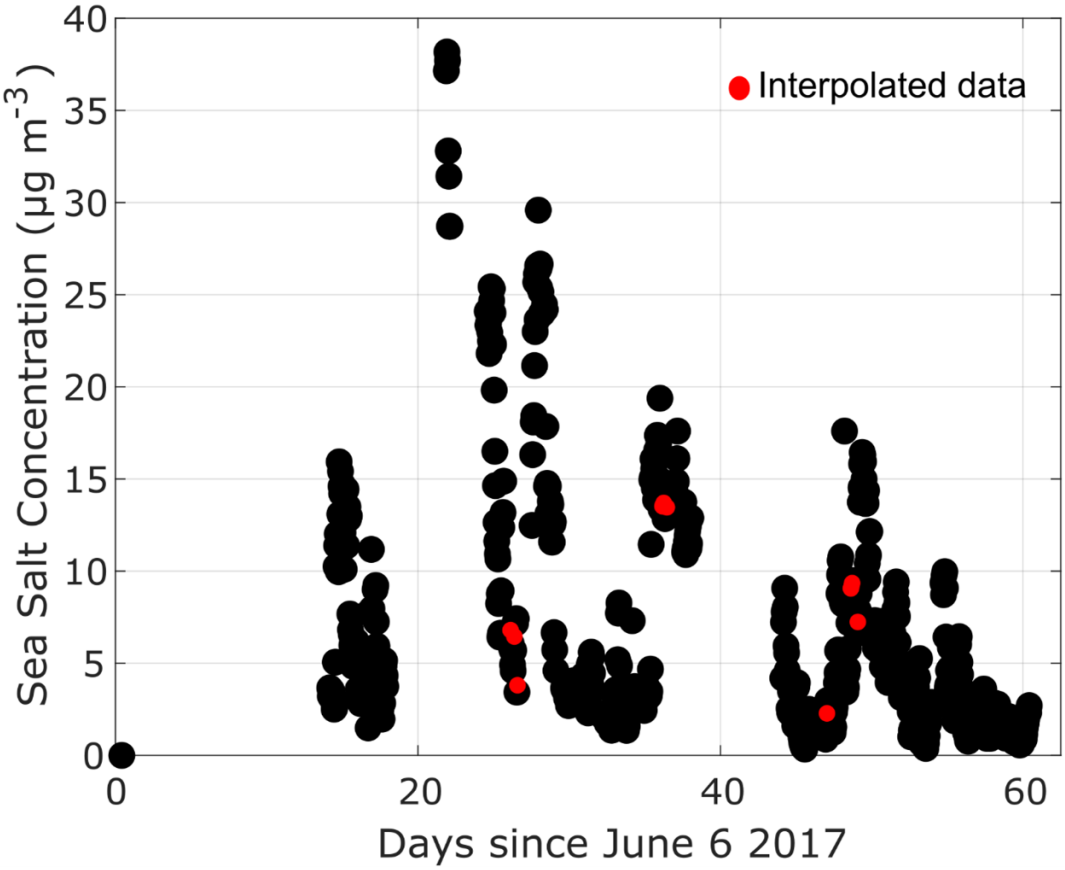

Figure 5.10: Time series of dust concentrations estimated from the Ca^{+} concentrations measured in the water-soluble fraction of total suspended particles. Red markers show where hourly composition data was linearly interpolated for four samples where data was partially missing (samples f020, f025, f036 and f037).

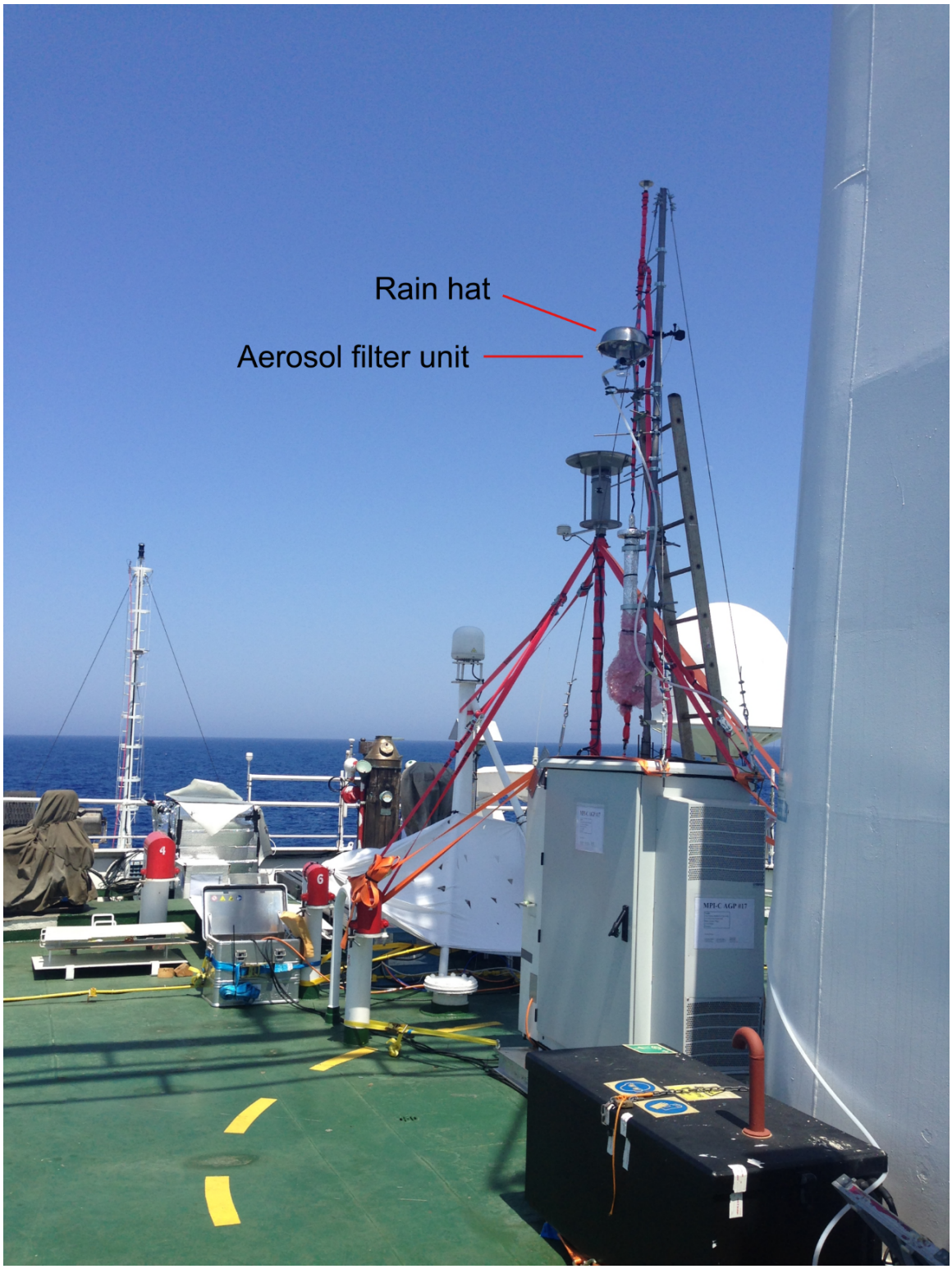

Figure 5.11: Aerosol sampling set-up on the RV *Kommandor Iona* wheelhouse top.

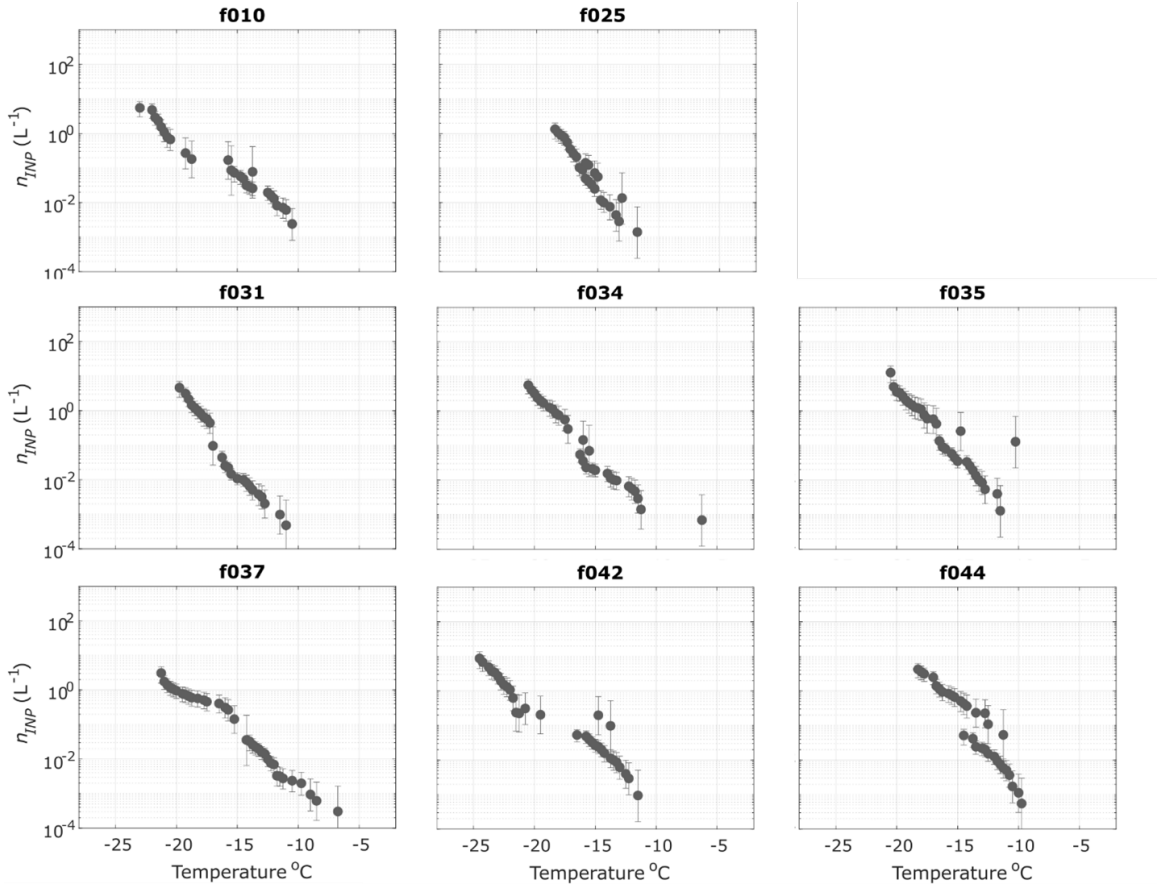

Figure 5.12: INP concentrations measured in 8 aerosol samples from which a dilution was performed (10-100X). The n_{INP} spectra from both the original suspension and the dilution are shown (see Methods Sect. 5.3.4).

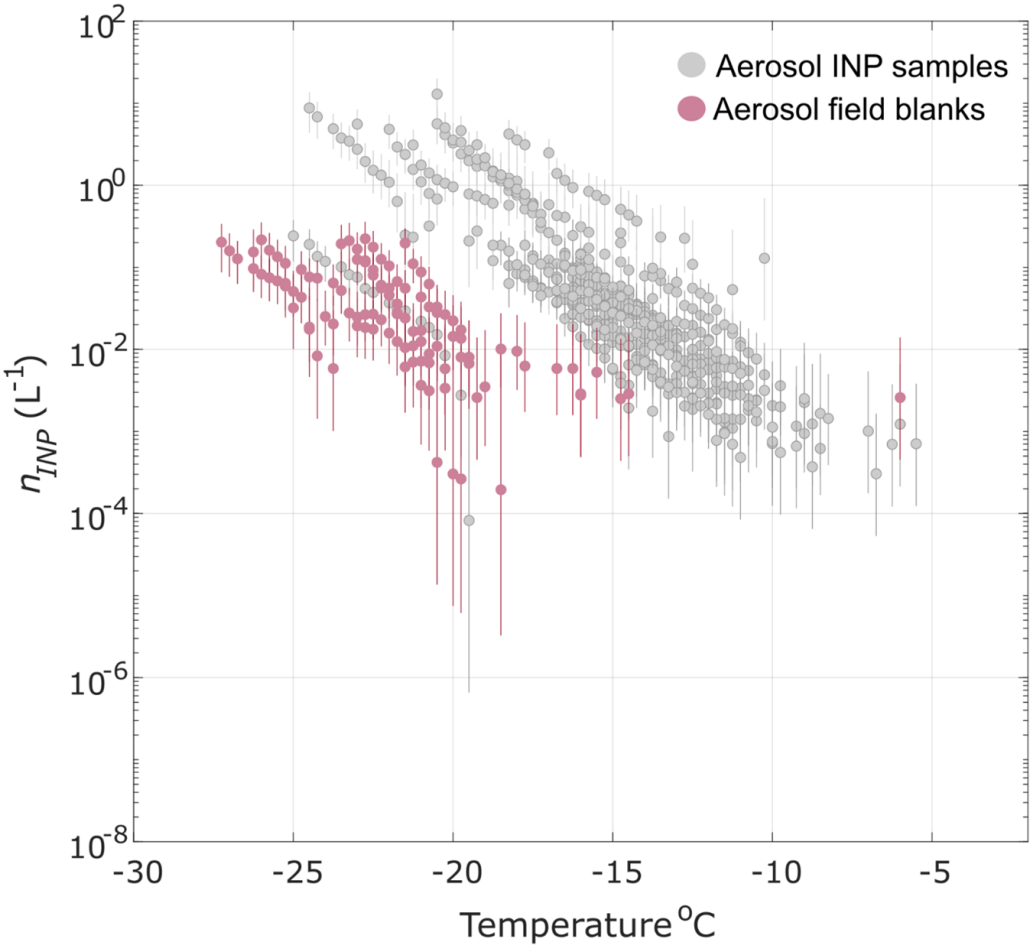

Figure 5.13: INP concentrations measured in 26 aerosol samples collected during AQABA and in simulated INP concentrations from 7 blank filter samples. The simulated blank filter INP concentrations were estimated for the mean volume sampled during AQABA (6680 L, see Methods Sect. 5.3.4). The freezing onset temperatures detected in 6 of the 7 field blanks ranged between -15 and -27 °C, with the exception of one field blank sample in which a single freezing event was detected at a relatively higher temperature -6 °C. This indicates the presence of a rare contaminant with a high freezing temperature from sampling handling processes, as this single freezing event represented 1/255 of total detected field blank freezing events. The INP concentrations measured in one aerosol sample (f033) fell within the range of background INP levels present in field blanks. Sample f033 was thus excluded from all other figures and analyses.

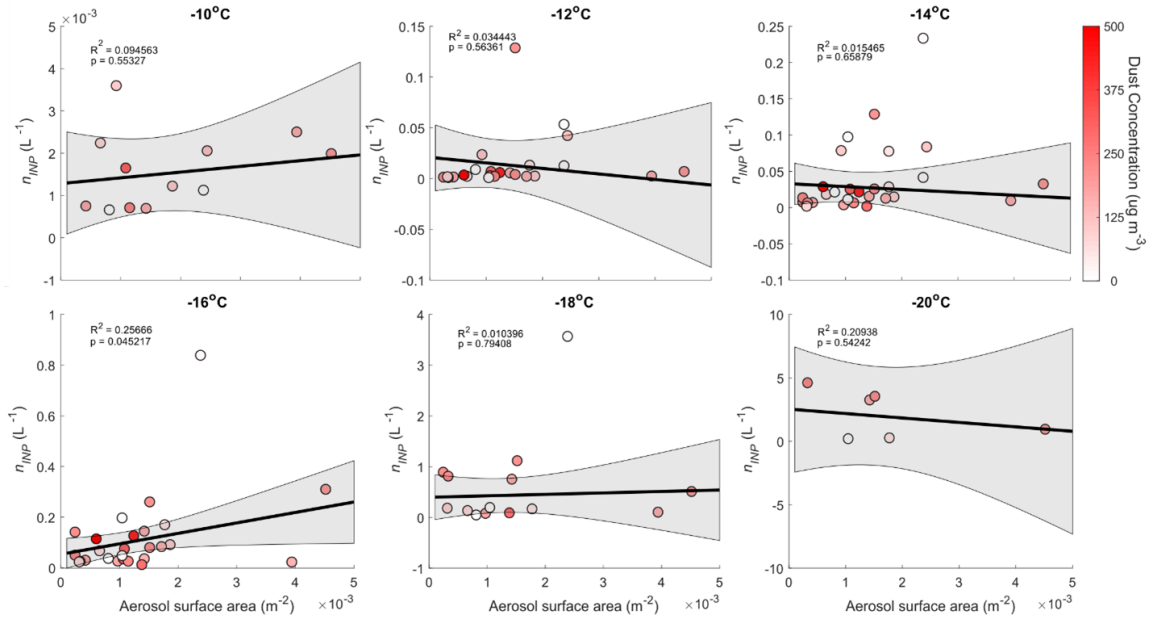

Figure 5.14: Linear regressions between total aerosol surface area and concentrations of INPs with freezing temperatures between -10 and -20 °C. Results show little to no correlation between INP concentrations and total aerosol surface area. R^2 and p values are also reported for each temperature. Shaded region is the 95% confidence interval for the best fit linear regression. Marker colors indicate the average ambient dust mass concentration during the sampling period. Dilutions of 8 filter samples are included in the regression analysis (Fig. 5.11).

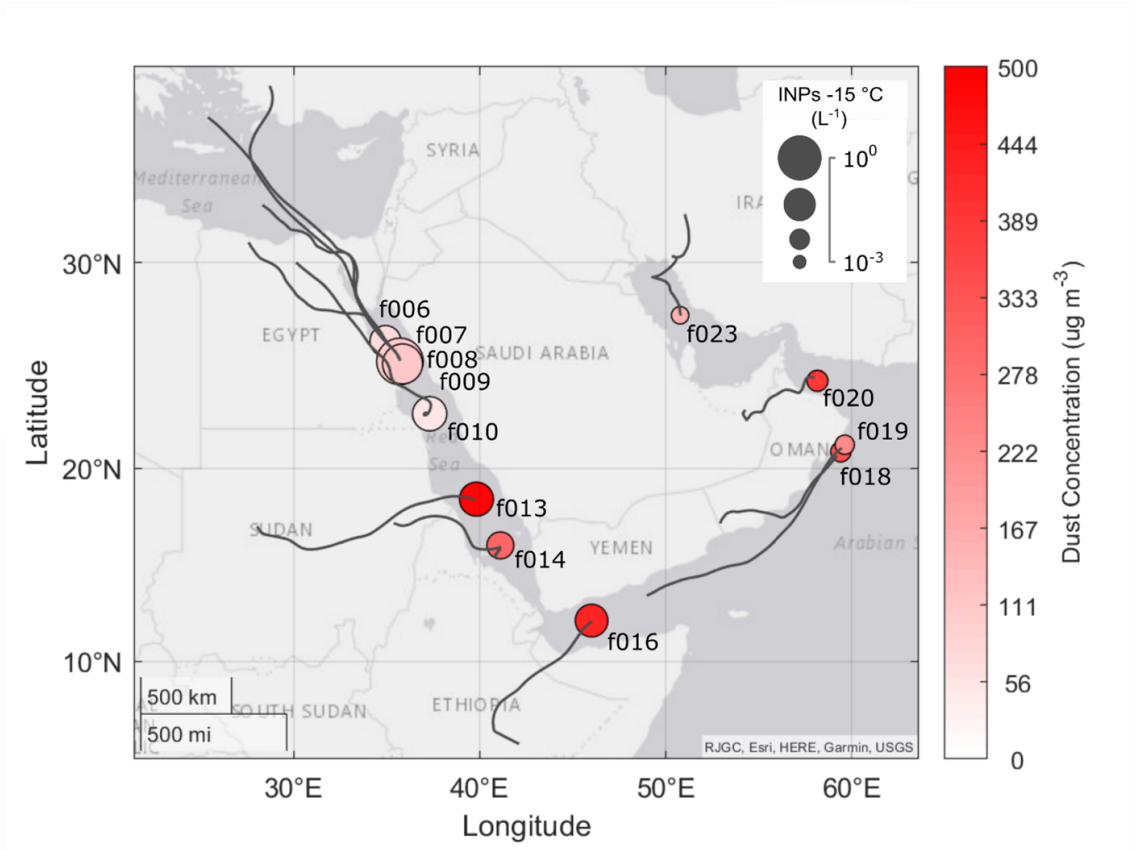

Figure 5.15: Aerosol 72-hour back trajectories for Leg 1 simulated by FLEXPART (Methods Sect. 5.2.5).

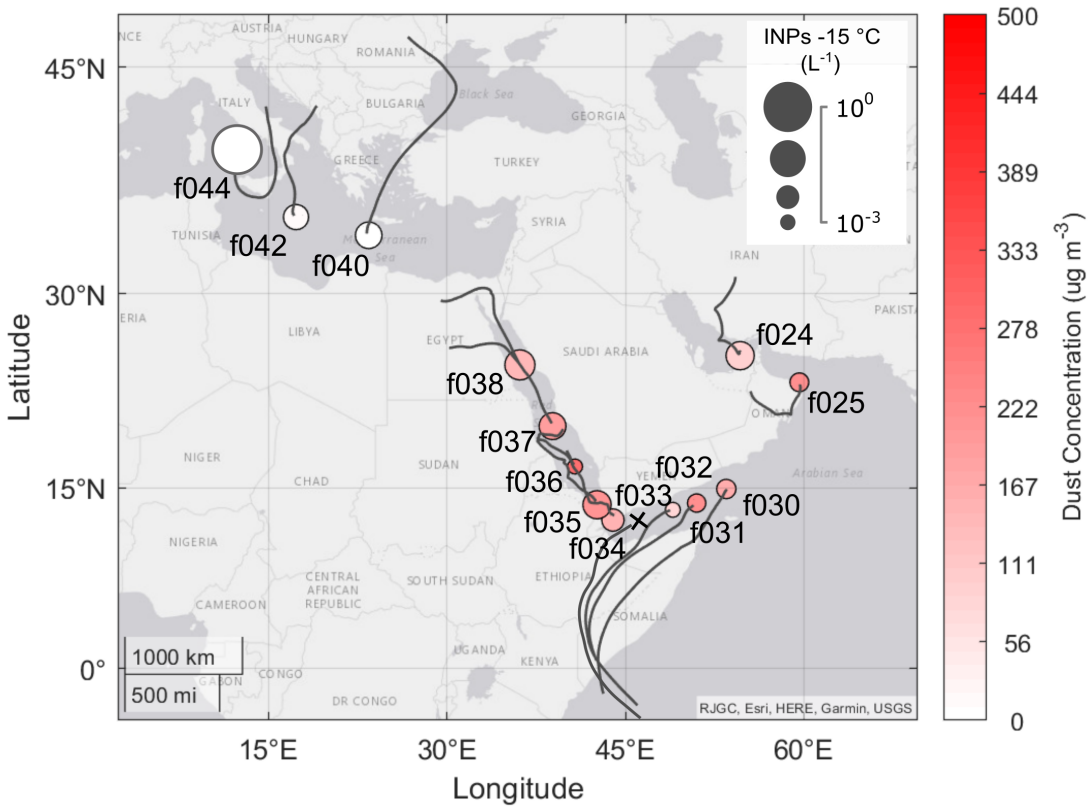

Figure 5.16: Aerosol 72-hour back trajectories for Leg 2 simulated by FLEXPART (Methods Sect. 5.2.5).

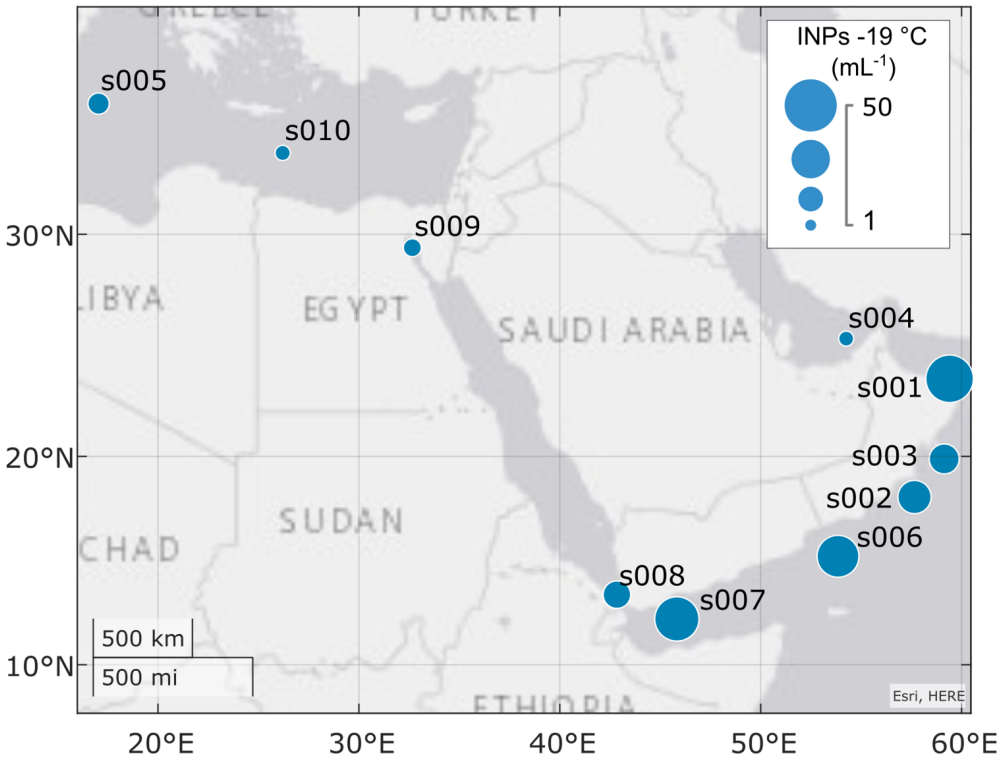

Figure 5.17: Map of the collection locations of 10 subsurface seawater (SSW) samples. Marker sizes indicate abundance of INPs.

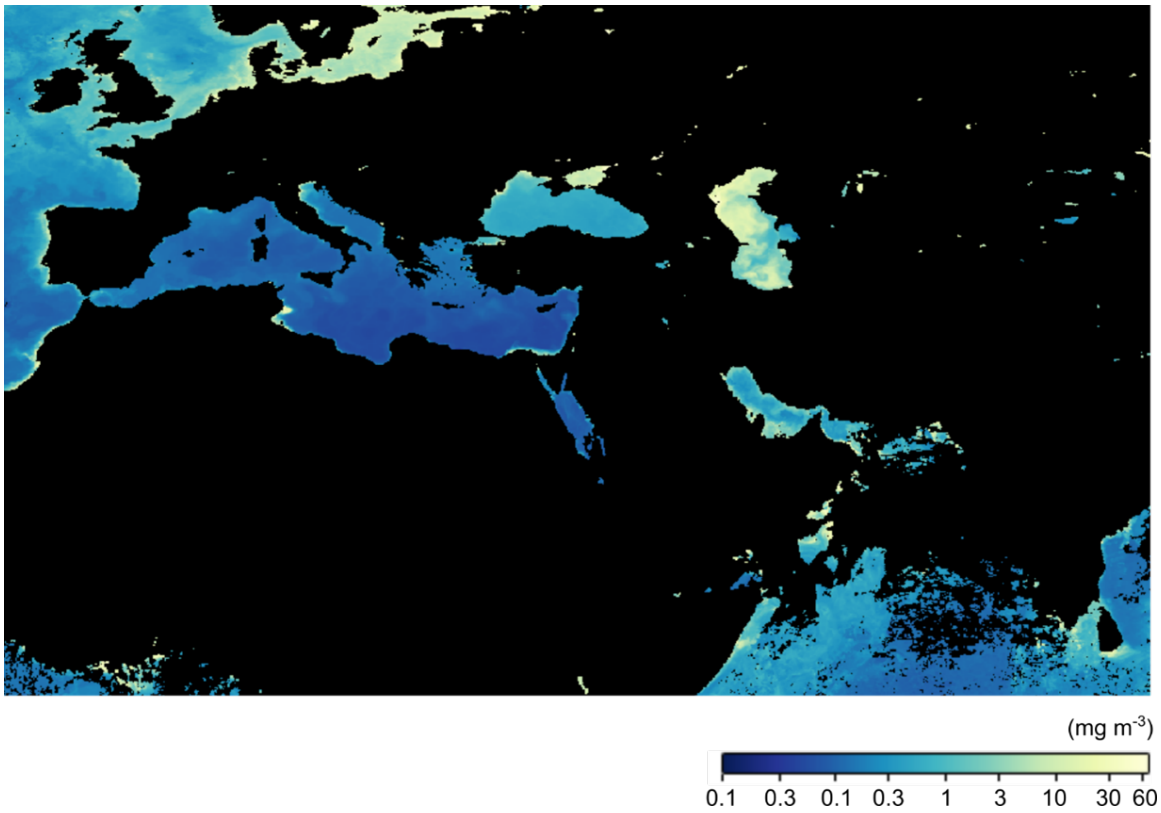

Figure 5.18: Average ocean surface chlorophyll a concentration from 1 August to 31 August 2017 (Moderate Resolution Imaging Spectroradiometre, https://oceandata.sci.gsfc.nasa.gov/MODIS-Aqua).

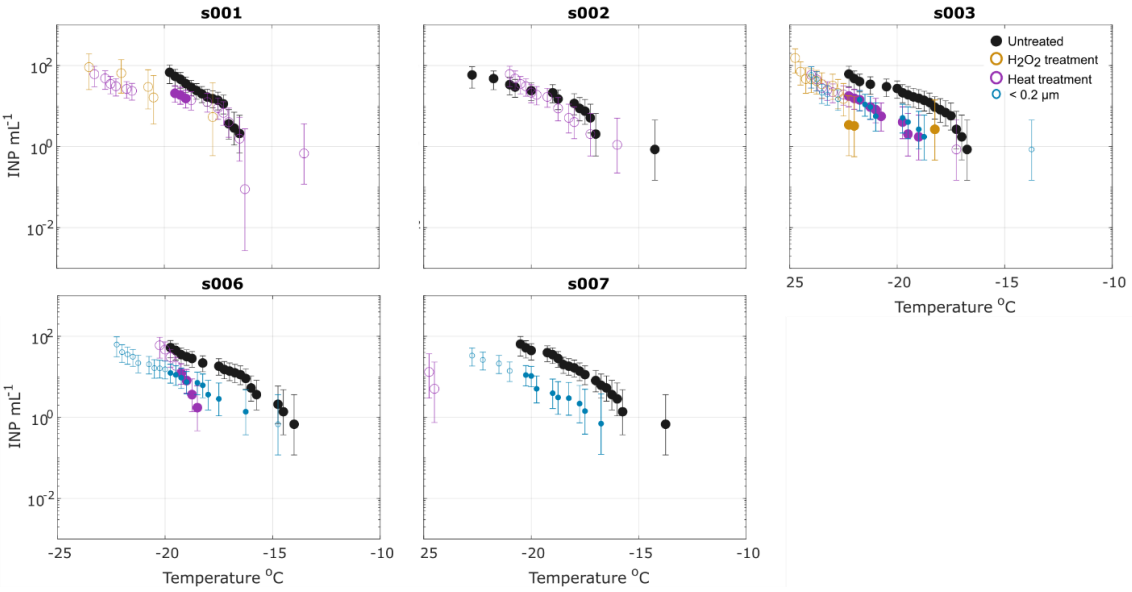

Figure 5.19: Measured concentrations of INPs in SSW samples that were treated with heat, hydrogen peroxide and a 0.2 μm filter (Methods Sect. 5.3.4). Results indicate the presence of organic, heat-labile and heat-stable INPs, and an abundance of INPs both larger and smaller than 0.2 μm.

Chapter 6

Toward Hydrometeor-Phase Evaluation of EAMv1 Arctic Mixed-Phase Cloud Representation Using $(GO)^2$-SIM

6.1 Abstract

The previous chapters addressed multiple challenges to advancing predictive understanding of immersion-mode INPs from the perspective of measurements and observations. In a pivot from the INP measurements-based topics of the previous chapters, here we consider some of the challenges of improving the representation of ice nucleation and other microphysical processes that modulate ice-phase partitioning in large-scale atmosphere models. While observational and experimental INP studies continue to develop and improve empirically-drived parameterizations for estimating INP concentrations in models, the extent to which improved INP representation could improve overall cloud-phase representation in models remains unknown due to several issues, many of which are related to the simplified cloud microphysics and low spatial resolution required for computational efficiency (see Introduction). Evaluation of simulated cloud phase

representation poses an additional challenge to improving representation of ice nucleation and other ice-phase partitioning processes in models. In this chapter, we describe a model output processing "pipeline" that facilitates hydrometeor phase evaluation of the DOE E3SM Atmospheric Model (EAMv1) using a forward ground-based radar simulator. Despite the overall improvements in EAMv1's representation of mean cloud state and cloud radiative forcing from v0 to v1, recent studies demonstrated that Arctic clouds are overrepresented and overly dominated by supercooled liquid with little ice production. While satellite data-based evaluations of simulated clouds in EAMv1 have illuminated biases in overall cloud representation, ground-based sensors offer finer spatiotemporal resolution and greater accuracy in observing the low-level stratiform cloud systems that are common in the Arctic. However, evaluations of model cloud properties with radar retrieval products are challenged by multiple issues, including discrepancies in scale and hydrometeor definition, and forward simulators overcome some of these challenges by estimating instrument observations from model variables. Here we introduce a capability to evaluate EAMv1 Arctic mixed-phase cloud representation against ARM ground-based cloud observations at North Slope Alaska (NSA) using $(GO)^2$-SIM, a forward ground-based radar simulator designed for hydrometeor-phase evaluation. Uniquely among forward ground-based radar simulators, $(GO)^2$-SIM distinguishes between frozen and liquid hydrometeors and exploits a combination of ground-based lidar and radar measurements that are advantageous for detection of liquid phase in low-level multilayered clouds. To take advantage of this simulator for model evaluation, we have prototyped an EAMv1 output processing "pipeline" that generates input variables needed to run $(GO)^2$-SIM on subcolumns. Using $(GO)^2$-SIM to apply phase-designation retrievals across the forward simulated and instrument observables, EAMv1 simulated stratiform cloud phase and vertical structures can be evaluated against NSA Ka-band Doppler radar and polarimetric lidar observations. This capability has potential to provide new observational constraints on EAM simulations of mixed-phase clouds, and in particular, constraints on cloud phase.

6.2 Introduction

In the latest version of the DOE E3SM Atmospheric Model (EAMv1), substantial updates to cloud physics, aerosol treatments and improved vertical resolution resulted in higher climate fidelity as well as significant model behavior changes, particularly for clouds and precipitation (Rasch et al., 2019; Xie et al., 2018). These behavior changes motivated multiple prior studies that aimed to provide an improved understanding of how modeled clouds respond to the new physics, aerosol schemes and increased resolution through sensitivity testing approaches and observations-based evaluations (Xie et al., 2018; Zhang et al., 2020, 2019b). Xie et al., (2018) demonstrated that improvements in mean cloud state, cloud radiative forcing and precipitation compared to EAMv0 was related to the following: the addition of the Cloud Layers Unified by Binormals (CLUBB) scheme for a unified treatment of Planetary Boundary Layer turbulence, shallow convection and cloud macrophysics, an updated cloud physics microphysics scheme (MG2), and the adoption of an ice nucleation scheme based on Classical Nucleation Theory (CNT) (Wang et al., 2014). Using satellite data to evaluate cloud representation in EAMv1, Zhang et al. (2019) found that EAMv1 underestimated clouds at high and mid-latitudes and overestimated clouds in the Arctic. Zhang et al. (2019) further found that when compared to CALIPSO observations, EAMv1 tends to produce too much supercooled liquid at the temperature range between -20 and -40 °C, less ice cloud fraction between 0 and -30 °C at high latitudes, and that these changes can be attributed to both the adoption of CNT in EAMv1 and a re-tuning of the ice deposition growth rate, which was reduced by a factor of 10 in EAMv1. Re-tuning refers the adjustment of variables required to maintain the top-of-atmosphere radiation budget as compared with the previous model version. For example, in EAMv1, the threshold relative humidity with respect to ice (RH_i) required for 100% cloud ice fraction was updated to improve representation of high-level clouds and longwave cloud radiative forcing.

As EAMv1 was found to be sensitive to the changes in physics and resolution, a substantial

re-tuning was performed during its development to achieve reasonable TOA energy flux and optimize model performance (Rasch et al., 2019; Xie et al., 2018). The re-tuning for EAMv1 primarily targeted parameterizations of cloud and precipitation processes (Zhang et al., 2019b). Due to poor scale-awareness of model physics, re-tuning was again required for the high-resolution configuration of EAMv1 (Xie et al., 2018), resulting in two different parameter settings for EAMv1 high and low-resolution models (HR and LR, respectively). Furthermore, Tang et al. (2019) results indicated that retuning may again be required for the refined region in variable-resolution configurations of EAMv1, as variables closely related to physical processes on the sub-grid scale (e.g. total precipitable water) exhibited sensitivity to the choice of the HR or LR parameter settings.

Given the demonstrated sensitivity to changes in physics and resolution, the consequences of differing tunings for the various model configurations (low, high and variable-resolution), and biases in the representation of ice and liquid, observations-based evaluations are critical to E3SM project goals to improve scale-awareness of parameterizations and develop a global cloud-resolving model with 3 km horizontal spacing. Ground-based cloud sensors offer a number of capabilities for model evaluation that differ from and complement those of satellite or aircraft-based observations. For example, space-borne lidar can adequately detect liquid clouds globally, but their signals cannot penetrate thick liquid layers (Hogan et al., 2004). Space-borne radar observations, however, can penetrate multilayer cloud systems, but are of coarser vertical resolution and limited value near the surface due to ground-interference and low sensitivity (Battaglia and Delanoë, 2013; Huang et al., 2012a, 2012b). Furthermore, many cloud microphysical properties such as ice particle properties and vertical velocities require multi-sensor observations (e.g. synthesis of radar, lidar and radiometer measurements) that are unavailable from satellites. Finally, aircraft-based field campaigns offer precious *in situ* measurements of cloud and aerosol properties such as size and number concentrations of hydrometeors, CCN and INPs, but as these data are quite limited in spatiotemporal scope, they are not appropriate for

evaluating biases on an e.g. seasonal or interannual time scale.

Ground-based cloud observations are well suited to address the gaps between satellite and in situ observations. The DOE Atmospheric Radiation Measurement (ARM) atmospheric observatories operate continuously and feature strategic combinations of cloud observing instruments that enable measurement of the unique cloud properties in their respective climate regimes. For example, at the ARM North Slope Alaska atmospheric observatory, measurements from vertically pointing polarimetic lidar and doppler radar can be used synergistically to detect water phase of the shallow and multilayered clouds (Lamer et al., 2018). This capability is particularly advantageous for the low-level mixed-phase clouds that exert a strong influence on the surface energy budget (Bennartz et al., 2013; Hofer et al., 2019; Nicolas et al., 2017) and are among the most frequently observed clouds in the spring and fall seasons (de Boer et al., 2009; Shupe et al., 2006, 2011; Zhang et al., 2019a). Despite their many advantages, ground-based cloud observations remain a mostly untapped resource in EAM evaluations due to multiple challenges including discrepancies in scale and hydrometeor definition (Wang et al., 2021). Forward radar simulators for ground-based observations have been developed to overcome some of these challenges by estimating instrument observables from model variables, enabling an apples-to-apples comparison of model output and measurements. The most commonly used simulator in EAM evaluations, the Cloud Feedback Model Intercomparison Project (CFMIP) Observation Simulator Project (COSP) converts model variables into radar observables (ground or satellite-based) to allow the comparison of model output with direct radar measurements rather than retrievals (Bodas-Salcedo et al., 2011; Swales et al., 2018). Wang et al. (2021) evaluated EAMv1-simulated 3D reflectivity over CONUS using ground-based radar observations and COSP and found that below 4 km, the EAMv1-simulated domain-mean reflectivity agreed with NEXRAD radar observations in magnitude but found disagreement in spatial variability, indicating that the model does not adequately represent mesoscale convective systems that dominate warm-season rainfall in the region. Above 4 km, the study found negative biases that increased with altitude, indicating that

EAMv1 accurately simulates some variability and reflectivity at the lower troposphere, but that these properties are underestimated at high levels. Wang et al. (2021) also found that modifying COSP microphysics assumptions to be more consistent with EAMv1 microphysics resulted in significant improvements in simulated subgrid reflectivity distributions when compared to the default COSP configuration. This result demonstrates the importance of consistency in microphysics assumptions between the model and subcolumn generator for accurate model evaluation. While forward simulators can resolve issues related to discrepancies in hydrometeor phase definition between observations and models, model output is commonly pre-processed using subcolumn generators that statistically downscale model output to address the discrepancy in scale between the model gridbox and observations (Lamer et al., 2018; Wang et al., 2021; Zhang et al., 2018).

In addition to COSP, there are two other existing forward radar simulators designed for evaluation of GCMs using ground-based observations: the ARM Cloud Radar Simulator and $(GO)^2$-SIM (Lamer et al., 2018; Zhang et al., 2018). The ARM Cloud Radar Simulator forward simulates ARM's vertically-pointing 35-GHz radar reflectivity from model variables, generating vertical reflectivity profiles from model output and ARM radar for comparison (Zhang et al., 2018). $(GO)^2$-SIM enables the evaluation of model hydrometeor phase occurrence by simulating Doppler radar (velocity and spectrum width) and lidar measurements (attenuated backscatter and depolarization) using 18 empirically-derived relationships between in-cloud water content and instrument observables (Lamer et al., 2018). This empirical approach to estimating instrument observables (e.g., lidar and radar backscatter power) differs from the ARM Cloud Radar Simulator and COSP simulators described above, which apply Mie scattering theory to estimate radar backscatter power and assume that all hydrometeors are spherical, including ice particles. $(GO)^2$-SIM additionally differs from existing radar forward simulators in that beyond estimating instrument observables, it also applies hydrometeor phase definitions from the Shupe (2007) multisensor phase classification retrieval.

Here, we describe an EAMv1 output processing "pipeline" to facilitate hydrometeor

phase evaluation using $(GO)^2$-SIM. This capability enables the estimation of biases in liquid, ice and mixed-phase frequency of occurrence in EAMv1 representation of Arctic large-scale stratiform clouds at default resolution (1 °) using $(GO)^2$-SIM, COSP, Ka-band Doppler radar and micropulse lidar measurements. These measurements are available from multiple ARM Atmospheric Observatories including North Slope Alaska (NSA), Eastern North Atlantic (ENA), and Tropical Western Pacific (TWP). Similar to Wang et al., (2021), we modified COSP microphysics assumptions for better integration with EAMv1. However, additional modifications were necessary to improve agreement between COSP and EAMv1 stratiform cloud liquid and ice fraction and to provide the necessary inputs for $(GO)^2$-SIM. As the deep convective cloud scheme in EAMv1 assumes simplified microphysics and neglects aerosol-cloud interactions and variables needed for $(GO)^2$-SIM, this hydrometeor phase evaluation capability is limited to large-scale stratiform cloud representation.

6.3 The EAMv1 to $(GO)^2$-SIM pipeline

6.3.1 EAMv1 description and configuration

EAMv1 is described in detail by Rasch et al. (2019) and Xie et al. (2018) provides additional details about the changes made in turbulence, cloud and convection parameterizations as well as model tuning. Turbulence, shallow cumulus clouds and cloud macrophysics are parameterized by the Cloud Layers Unified By Binormals (CLUBB) scheme (Golaz et al., 2002; Larson, 2017). CLUBB diagnoses cloud fraction and cloud liquid water from a joint double-Gaussian probability density function (PDF). Ice and liquid cloud fractions in CLUBB are the same and are analytically diagnosed by integrated oversaturated portions of the joint PDF (Guo et al., 2015). Ice phase processes, which are not explicitly included in the CLUBB PDF scheme, are treated via cloud microphysics. The transport of cloud ice mass mixing ratio is treated via the turbulence eddy diffusion scheme (Bogenschutz et al., 2013). The Zhang and McFarlane, 1995

(ZM) scheme is used for deep convection.

Microphysics for stratiform clouds is represented with the updated cloud microphysics scheme "Morrison and Gettelman version 2" (MG2) (Gettelman and Morrison, 2015). MG2 prognoses the mass and number concentration of cloud liquid, ice and precipitating hydrometeors. The coupled MG2 stratiform cloud microphysics and CLUBB higher-order turbulence parameterization explicitly provides values for hydrometeor mass and number as well as stratiform cloud fraction. A sub-time step of 5 minutes is used for the cloud microphysics for better coupling with CLUBB. As convective cloud fraction is not parameterized in the mass-flux based ZM scheme, it is diagnosed from the cloud mass flux for cloud radiation calculation, which is treated as a tunable parameter. The total cloud fraction in EAMv1 combines CLUBB, deep convective cloud fractions and ice cloud fraction assuming maximum overlap. Aerosol microphysics and interactions with stratiform clouds are treated with an updated version of the Modal Aerosol Module (MAM4; Liu et al., 2016) featuring improved representations of particle aging, secondary organic aerosol and cloud interactions as well as an additional aerosol type (marine organic aerosol).

EAMv1 simulations can be run using either a High-Resolution (HR, 0.25°) and Low-Resolution (LR, 1°) configuration with 72 vertical layers up to 60 km (0.1 hPa). In this study, the LR configuration is used with constrained large-scale circulation via the nudging technique (Lin et al., 2016; Ma et al., 2014; Zhang et al., 2014), in which horizontal winds are relaxed toward the Modern-Era Retrospective Analysis for Research and Applications, version 2 (MERRA2) reanalysis data (Gelaro et al., 2017). MERRA2 data are read in every 6 hr and linearly interpolated to the model time. The simulation was run for the time period from 1 January 2012 to 31 December 2016. EAMv1 output is regridded to geographic coordinates with a horizontal grid spacing of $\sim$100km using bilinear interpolation and sampled at 30-minute resolution.

6.3.2 $(GO)^2$-SIM description

$(GO)^2$-SIM was described in detail in Lamer et al. (2018). Briefly, $(GO)^2$-SIM is a ground-based instrument forward simulator for bulk microphysical models. It emulates radar Doppler spectral moments, lidar backscatter and depolarization and provides synthetic estimates of mixed-phase cloud occurrence in models that are comparable to estimates from observations using the same hydrometeor phase classification scheme. Compared to existing forward simulators (both for space-borne and ground-based instruments), $(GO)^2$-SIM creates an ensemble of forward simulations by slightly varying the scattering assumptions to estimate some of the uncertainty in these assumptions. Specifically, $(GO)^2$-SIM creates an ensemble of 576 forward simulations based on different combinations of 18 scattering assumptions that relate simulated in-cloud water content to hydrometeor-backscattered power as would be observed by vertically pointing micropulse lidar and Ka-band radar. The interquartile range of these statistics provides an estimate of the uncertainty in the scattering assumptions.

Beyond forward simulating Doppler radar and lidar measurements, $(GO)^2$-SIM includes a water classification module based on the Shupe (2007) multi-sensor phase classifier retrieval. $(GO)^2$-SIM objectively determines radar Doppler velocity and Doppler spectral width thresholds for hydrometeor classification using joint frequency of occurrence histograms of hydrometeor mixing ratios for a single species and forward simulated observable values. This is repeated for each forward simulation of the ensemble in order to provide a measure of uncertainty and to ensure that the choice of the empirical relationships used to convert hydrometeor water content to lidar extinction and radar reflectivity does not affect the phase classification. The water phase classification module can be applied directly to the forward simulator output and to Doppler radar and lidar observations to enable an "apples-to-apples" comparison of the occurrence of liquid, ice and mixed-phase.

Model variables required as input for the $(GO)^2$-SIM forward simulator are the following: mean grid box temperature and pressure, hydrometeor mixing ratios, areal fractions, mass-

weighted fall speeds and effective radii for four species: cloud liquid water, cloud ice, precipitating liquid water and precipitating ice. Following typical use of forward simulators for general circulation model (GCM) evaluation, subcolumns were generated to statistically downscale the 1° EAMv1 output variables for better comparison with NSA cloud observations (see next Section).

6.3.3 COSP description and configuration

The Cloud Feedback Model Intercomparison Project (CFMIP) Observations Simulator Package v2.0 was designed to facilitate "apples-to-apples" comparison of cloud-observing satellite data with model-simulated cloud properties (Bodas-Salcedo et al., 2011). However, for this study, we make use of COSP's subcolumn generator, the Subgrid Cloud Overlap Profile Sampler (SCOPS) rather than its satellite simulator capabilities (Webb et al., 2001). SCOPS addresses discrepancies in scale between observations (e.g. 10s of m) and the model grid-cell (e.g. 100 km) by generating subgrid distributions of modeled cloud and precipitation properties. Subcolumns are discrete samples, each of which is internally homogeneous but constructed such that a sufficiently large ensemble should reproduce the profile of bulk cloud properties within a model grid column (Swales et al., 2018; Webb et al., 2001). To this end, microphysics and cloud overlap assumptions in COSP are typically modified for consistency with the host model. For this study, "maximum-random" overlap in COSP is assumed for consistency with the overlap assumption in MG2. As noted above, this evaluation capability is limited to large-scale stratiform clouds due to limitations in the EAMv1 convective cloud scheme, so the modifications described below are consequently limited to large-scale stratiform clouds.

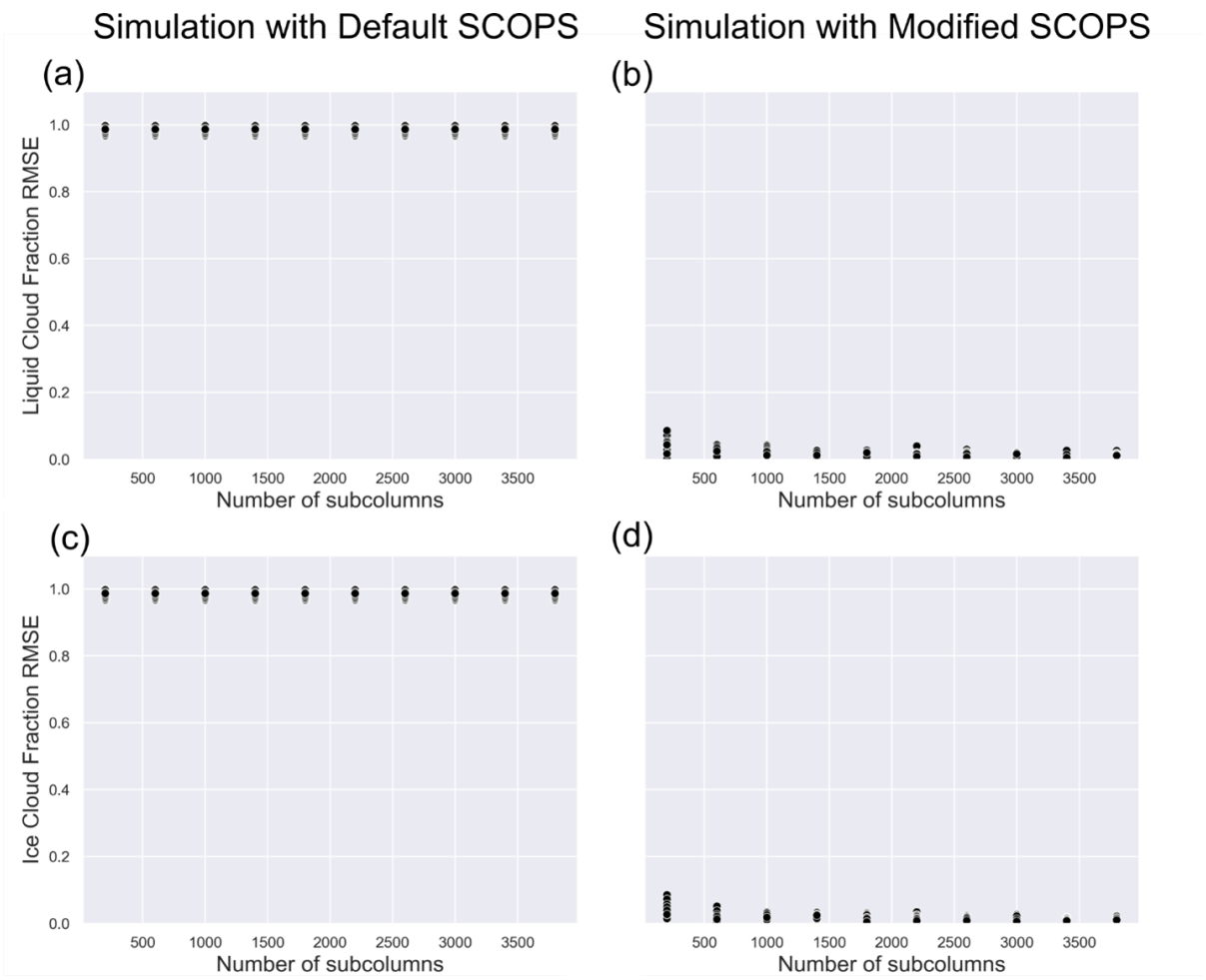

Figure 6.1: Maximum Root-Mean Square Error (RMSE) in COSP subcolumn ensemble stratiform liquid cloud fraction (a-b) and stratiform ice cloud fraction (c-d) from EAMv1 simulation 01-05-2012 00:00 – 23:30 in gridbox centered at 71°30' N 156°30' W. Each data point represents the maximum RMSE over the 72 levels from an instantaneous (30 minute) simulatsion output for varying numbers of COSP subcolumns. Modifications to SCOPS resulted in decreased RMSE in COSP output stratiform liquid and ice, demonstrating improved agreement between EAMv1 gridbox stratiform liquid and ice fraction and that of the COSP subcolumn ensemble.

When comparing the subcolumn ensemble stratiform liquid and ice cloud fraction with the corresponding values from EAMv1, we found that in its default configuration, SCOPS fails to reproduce distribution of liquid and ice within the gridcell (Fig. 6.1). In the default COSPv2.0 configuration, SCOPS derives subcolumn cloud type profile (i.e. stratiform, convective, and cloudless) from the model stratiform and convective cloud fraction and hydrometeor species are then homogenously distributed across the stratiform or convective subcolumns, respectively.

Table 6.1: Modification of SCOPS for better agreement with EAMv1 subgrid distributions of stratiform ice and liquid.

Table 1. Modification of SCOPS for better agreement with EAMv1 subgrid distributions of stratiform ice and liquid

Hydrometeor Type	Default	Modified
LSL	Ensemble of subcolumns reproduces total stratiform cloud fraction. Gridbox-mean stratiform liquid variables distributed homogenously across stratiform subcolumns.	Ensemble of subcolumns reproduces stratiform liquid and ice cloud fraction, respectively. Stratiform liquid variables distributed homogenously across stratiform liquid and mixed-phase subcolumns.
LSI	Ensemble of subcolumns reproduces total stratiform cloud fraction. Gridbox-mean stratiform ice variables distributed homogenously across stratiform subcolumns	Ensemble of subcolumns reproduces stratiform liquid and ice cloud fraction, respectively. Stratiform ice variables distributed homogenously across stratiform ice and mixed-phase subcolumns.

Consequently, the ensemble of subcolumns reproduces the total stratiform or convective cloud fraction within the model grid-box but does not reproduce the subgrid distribution of stratiform and convective cloud ice and liquid within the stratiform and/or convective clouds. For this study, we have modified SCOPS such that stratiform liquid and ice fraction variables from CLUBB are used to determine the stratiform cloud profile and phase of each subcolumn (i.e. cloudless, ice, liquid or mixed; see Table 6.1). Specifically, SCOPS was modified to define the phase and type of stratiform cloud subcolumns based on the given EAMv1 stratiform liquid and ice fraction. The COSP subcolumn generator for precipitation variables, PREC_SCOPS, was not modified for this study as its overlap assumptions and assumption about the fraction of cloud that precipitates agrees with EAMv1: in levels where cloud exists, 100% of the cloud precipitates and in levels where no cloud exists, the precipitation fraction is equal to the precipitating fraction in the level above.

To verify that the ensemble of subcolumns reproduced the grid-box mean stratiform ice and liquid cloud fraction and to determine the optimal number of subcolumns to generate, the Root Mean Square Error (RMSE) between the subcolumn ensemble stratiform ice and liquid cloud fractions and the grid-box mean stratiform ice and liquid cloud fractions were calculated

for increasing numbers of subcolumns (Fig. 6.1). Figure 6.1 shows that RMSE for both stratiform liquid and ice decreases with increasing numbers of subcolumns until ∼1000. For this study, we generate 2000 subcolumns for each EAMv1 gridcell via COSP.

Table 6.2: Modification of the hydrometeor assumptions used in COSP.

Table 2. Modification of the hydrometeor assumptions used in COSP.

Hydrometeor type[a]	Distribution type		Density[b] (kg m^{-3})		Particle mean diameter (μm)		Distribution width[c] (unitless)	
	Default	Modified	Default	Modified	Default	Modified	Default	Modified
LSL	Lognormal	Gamma	524 x D^3	-	6	12	0.3	0
LSI	Gamma	-	110.9 x D$^{2.91}$	500	40	-	2	0
LSR	Exponential	-	524 x D^3	-	*n/a*	-	*n/a*	-
LSS	Exponential	-	100	250	*n/a*	-	*n/a*	-

[a] LS: large-scale; L: cloud liquid; I: cloud ice; R: rain; S: snow.
[b] In COSP, density can either be defined by the mass-diameter relationship equation (1) $apm \times D^{bpm}$ or by a fixed value ρ
[c] Distribution width: ν $in\ N(D) = N_0 D^{(\nu-1)} e^{-\lambda D}$
n/a – not applicable

Of the three variables needed as input to (GO)^2-SIM, two were native to COSPv2.0: hydrometeor mass mixing ratio and effective radius. For mass-weighted fall speeds of stratiform cloud liquid, ice, rain and snow, the MG2 mass-weighted fall speed calculations for each hydrometeor species were implemented in COSP. The implemented mass-weighted fall speed calculations are dependent on COSP hydrometeor size distributions and several associated assumptions including distribution type, hydrometeor density, and mean particle diameter. These assumptions were modified for best agreement with MG2 (see Table 6.2) and are consistent with the modifications made in Wang et al., (2021). Wang et al., (2021) demonstrated that the modifications resulted in improved simulated radar reflectivity and its subgrid distribution, emphasizing the necessity of microphysical consistency between COSP and the host model.

6.4 Summary

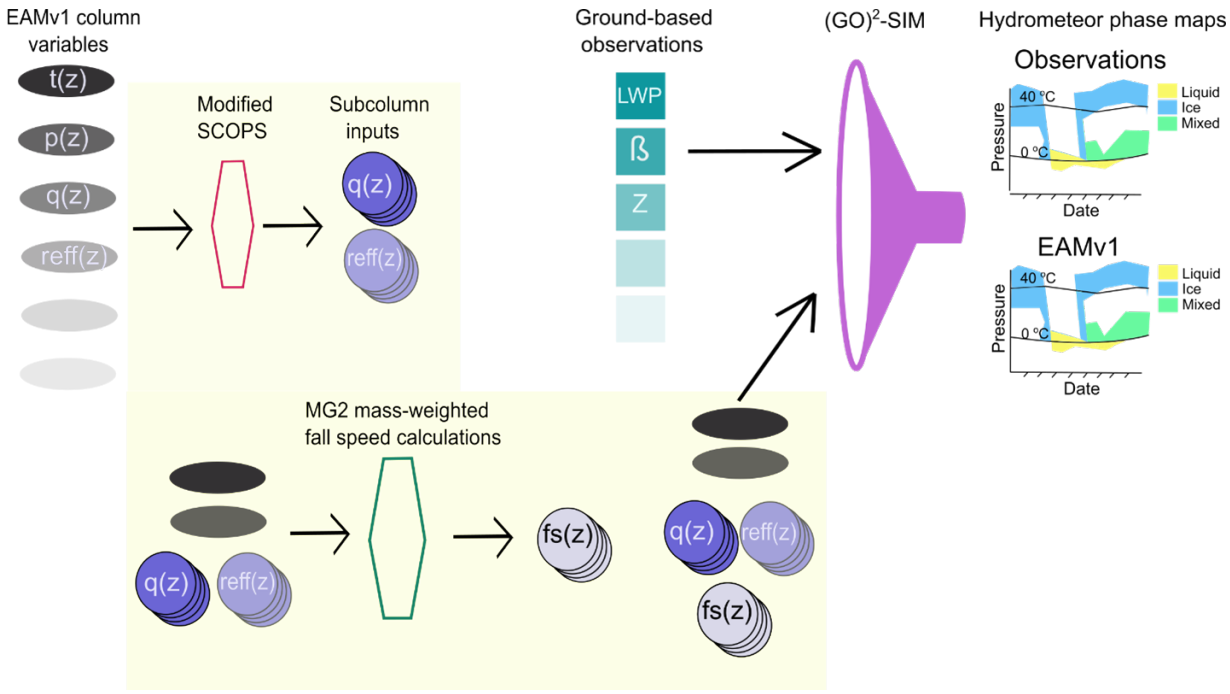

Figure 6.2: Schematic of the data processing pipeline between EAMv1 and (GO)^2-SIM (yellow shading).

Through a synthesis of EAMv1 with COSPv2.0 and (GO)^2-SIM, we present a capability to evaluate EAMv1 hydrometeor phase representation using ground-based Doppler radar and micropulse lidar observations. This capability has potential to illuminate biases and provide much-needed observational constraints for simulated phase-partitioning processes in Arctic mixed-phase clouds. Figure 6.2 shows a schematic of the EAMv1 output processing pipeline, which provides the following subcolumn-distributed variables as input to (GO)^2-SIM: stratiform mass-mixing ratios, effective radii, and mass-weighted fall speeds for cloud liquid, cloud ice, rain and snow.

In summary, EAMv1 gridbox-mean stratiform mixing ratios and effective radii are distributed onto subcolumns using the native COSPv2.0 subcolumn generator (SCOPS), which has been modified for better agreement with EAMv1 stratiform ice and liquid cloud fraction. Subcolumn mass-weighted fall speed calculations were additionally implemented in COSPv2.0

following the EAMv1 scheme for shallow convective and stratiform clouds (MG2). The data processing pipeline is integrated with the offline COSPv2.0 driver as a convenient single-step solution for distributing EAMv1 variables onto subcolumns and generating all the necessary inputs for $(GO)^2$-SIM. However, due to the simplified microphysics and neglect of aerosol-cloud interactions in EAMv1's deep convective cloud scheme (Rasch et al., 2019) this capability is currently limited to evaluation of large-scale stratiform clouds.

Using the EAMv1-to-$(GO)^2$-SIM pipeline, future evaluations of EAMv1 cloud representation can take advantage of multiple strengths of $(GO)^2$-SIM compared to other forward simulators for ground-based observations, including its hydrometeor phase definition module and its synthesis of polarimetric micropulse lidar and Ka-band Doppler radar measurements. This sensor combination is uniquely capable of sensing low-level, multi-layer clouds (Lamer et al., 2018) such as the mixed-phase stratocumulus clouds that are frequently observed in the Arctic (e.g., Shupe et al., 2006, 2011). Both polarimetic micropulse lidar and Ka-band Doppler radar are continuously operated at multiple ARM observatories spanning a wide range of climates, including the Eastern North Atlantic, Southern Great Plains, and Tropical West Pacific observatories as well as a temporary research facility operated at Ascension Island 2016-2017.

Finally, future studies can use $(GO)^2$-SIM supported estimates of biases in liquid, ice, rain and snow hydrometeor frequency of occurrence to provide new observational constraints on mixed-phase clouds. This evaluation capability is well-suited to support sensitivity studies in which selected microphysical parameters are perturbed across simulation ensembles, enabling comparison between ensemble members to better understand how various microphysical parameters, including INPs, affect phase representation.

Acknowledgements. Chapter 6, in part, is currently being prepared for submission for publication of the material. Beall, C.M., Lamer, K., Burrows, S.M., Ma, P., Stokes, M.D., Prather, K.A. The dissertation author was the primary investigator and author of this material.

6.5 References

Battaglia, A. and Delanoë, J.: Synergies and complementarities of CloudSat-CALIPSO snow observations, J. Geophys. Res. Atmos., 118(2), 721–731, doi:https://doi.org/10.1029/2012JD018092, 2013.

Bennartz, R., Shupe, M. D., Turner, D. D., Walden, V. P., Steffen, K., Cox, C. J., Kulie, M. S., Miller, N. B. and Pettersen, C.: July 2012 Greenland melt extent enhanced by low-level liquid clouds, Nature, 496(7443), 83–86, doi:10.1038/nature12002, 2013.

Bodas-Salcedo, A., Webb, M. J., Bony, S., Chepfer, H., Dufresne, J. L., Klein, S. A., Zhang, Y., Marchand, R., Haynes, J. M., Pincus, R. and John, V. O.: COSP: Satellite simulation software for model assessment, Bull. Am. Meteorol. Soc., 92(8), 1023–1043, doi:10.1175/2011BAMS2856.1, 2011.

de Boer, G., Eloranta, E. W. and Shupe, M. D.: Arctic mixed-phase stratiform cloud properties from multiple years of surface-based measurements at two high-latitude locations, J. Atmos. Sci., 66(9), 2874–2887, doi:10.1175/2009JAS3029.1, 2009.

Bogenschutz, P. A., Gettelman, A., Morrison, H., Larson, V. E., Craig, C. and Schanen, D. P.: Higher-order turbulence closure and its impact on climate simulations in the community atmosphere model, J. Clim., 26(23), 9655–9676, doi:10.1175/JCLI-D-13-00075.1, 2013.

Gelaro, R., McCarty, W., Suárez, M. J., Todling, R., Molod, A., Takacs, L., Randles, C. A., Darmenov, A., Bosilovich, M. G., Reichle, R., Wargan, K., Coy, L., Cullather, R., Draper, C., Akella, S., Buchard, V., Conaty, A., da Silva, A. M., Gu, W., Kim, G.-K., Koster, R., Lucchesi, R., Merkova, D., Nielsen, J. E., Partyka, G., Pawson, S., Putman, W., Rienecker, M., Schubert, S. D., Sienkiewicz, M. and Zhao, B.: The Modern-Era Retrospective Analysis for Research and Applications, Version 2 (MERRA-2), J. Clim., 30(14), 5419–5454, doi:10.1175/JCLI-D-16-0758.1, 2017.

Gettelman, A. and Morrison, H.: Advanced two-moment bulk microphysics for global models. Part I: Off-line tests and comparison with other schemes, J. Clim., 28(3), 1268–1287, doi:10.1175/JCLI-D-14-00102.1, 2015.

Golaz, J. C., Larson, V. E. and Cotton, W. R.: A PDF-based model for boundary layer clouds. Part I: Method and model description, J. Atmos. Sci., 59(24), 3540–3551, doi:10.1175/1520-0469(2002)059¡3540:APBMFB¿2.0.CO;2, 2002.

Guo, H., Golaz, J.-C., Donner, L. J., Wyman, B., Zhao, M. and Ginoux, P.: CLUBB as a unified cloud parameterization: Opportunities and challenges, Geophys. Res. Lett., 42(11), 4540–4547, doi:https://doi.org/10.1002/2015GL063672, 2015.

Hofer, S., Tedstone, A. J., Fettweis, X. and Bamber, J. L.: Cloud microphysics and circulation anomalies control differences in future Greenland melt, Nat. Clim. Chang., 9(7), 523–528, doi:10.1038/s41558-019-0507-8, 2019.

Hogan, R. J., Behera, M. D., O'Connor, E. J. and Illingworth, A. J.: Estimate of the global distribution of stratiform supercooled liquid water clouds using the LITE lidar, Geophys. Res. Lett., 31(5), doi:https://doi.org/10.1029/2003GL018977, 2004.

Huang, Y., Siems, S. T., Manton, M. J., Protat, A. and Delanoë, J.: A study on the low-altitude clouds over the Southern Ocean using the DARDAR-MASK, J. Geophys. Res. Atmos., 117(D18), n/a-n/a, doi:10.1029/2012JD017800, 2012a.

Huang, Y., Siems, S. T., Manton, M. J., Hande, L. B. and Haynes, J. M.: The structure of low-altitude clouds over the Southern Ocean as seen by CloudSat, J. Clim., 25(7), 2535–2546, doi:10.1175/JCLI-D-11-00131.1, 2012b.

Lamer, K., Fridlind, A. M., Ackerman, A. S., Kollias, P., Clothiaux, E. E. and Kelley, M.: $(GO)^2$-SIM: a GCM-oriented ground-observation forward-simulator framework for objective evaluation of cloud and precipitation phase, Geosci. Model Dev., 11(10), 4195–4214, doi:10.5194/gmd-11-4195-2018, 2018.

Larson, V. E.: CLUBB-SILHS: A parameterization of subgrid variability in the atmosphere, 2017.

Lin, G., Wan, H., Zhang, K., Qian, Y. and Ghan, S. J.: Can nudging be used to quantify model sensitivities in precipitation and cloud forcing?, J. Adv. Model. Earth Syst., 8(3), 1073–1091, doi:https://doi.org/10.1002/2016MS000659, 2016.

Liu, X., Ma, P.-L., Wang, H., Tilmes, S., Singh, B., Easter, R. C., Ghan, S. J. and Rasch, P. J.: Description and evaluation of a new four-mode version of the Modal Aerosol Module (MAM4) within version 5.3 of the Community Atmosphere Model, Geosci. Model Dev., 9(2), 505–522, doi:10.5194/gmd-9-505-2016, 2016.

Ma, P.-L., Rasch, P. J., Fast, J. D., Easter, R. C., Gustafson Jr., W. I., Liu, X., Ghan, S. J. and Singh, B.: Assessing the CAM5 physics suite in the WRF-Chem model: implementation, resolution sensitivity, and a first evaluation for a regional case study, Geosci. Model Dev., 7(3), 755–778, doi:10.5194/gmd-7-755-2014, 2014.

Nicolas, J. P., Vogelmann, A. M., Scott, R. C., Wilson, A. B., Cadeddu, M. P., Bromwich, D. H., Verlinde, J., Lubin, D., Russell, L. M., Jenkinson, C., Powers, H. H., Ryczek, M., Stone, G. and Wille, J. D.: January 2016 extensive summer melt in West Antarctica favoured by strong El Niño, Nat. Commun., 8(1), 15799, doi:10.1038/ncomms15799, 2017.

Rasch, P. J., Xie, S., Ma, P. L., Lin, W., Wang, H., Tang, Q., Burrows, S. M., Caldwell, P., Zhang, K., Easter, R. C., Cameron-Smith, P., Singh, B., Wan, H., Golaz, J. C., Harrop, B. E., Roesler, E., Bacmeister, J., Larson, V. E., Evans, K. J., Qian, Y., Taylor, M., Leung, L. R., Zhang, Y., Brent, L., Branstetter, M., Hannay, C., Mahajan, S., Mametjanov, A., Neale, R., Richter, J. H., Yoon, J. H., Zender, C. S., Bader, D., Flanner, M., Foucar, J. G., Jacob, R., Keen, N., Klein, S. A., Liu, X., Salinger, A. G., Shrivastava, M. and Yang, Y.: An Overview of the Atmospheric Component of the Energy Exascale Earth System Model, J. Adv. Model. Earth Syst., 11(8), 2377–2411, doi:10.1029/2019MS001629, 2019.

Shupe, M. D.: A ground-based multisensor cloud phase classifier, Geophys. Res. Lett., 34(22), doi:https://doi.org/10.1029/2007GL031008, 2007.

Shupe, M. D., Matrosov, S. Y. and Uttal, T.: Arctic mixed-phase cloud properties derived from surface-based sensors at SHEBA, J. Atmos. Sci., 63(2), 697–711, doi:10.1175/JAS3659.1, 2006.

Shupe, M. D., Walden, V. P., Eloranta, E., Uttal, T., Campbell, J. R., Starkweather, S. M. and Shiobara, M.: Clouds at Arctic atmospheric observatories. Part I: Occurrence and macrophysical properties, J. Appl. Meteorol. Climatol., 50(3), 626–644, doi:10.1175/2010JAMC2467.1, 2011.

Swales, D. J., Pincus, R. and Bodas-Salcedo, A.: The Cloud Feedback Model Intercomparison Project Observational Simulator Package: Version 2, Geosci. Model Dev., 11(1), 77–81, doi:10.5194/gmd-11-77-2018, 2018.

Tang, Q., Klein, S. A., Xie, S., Lin, W., Golaz, J.-C., Roesler, E. L., Taylor, M. A., Rasch, P. J., Bader, D. C., Berg, L. K., Caldwell, P., Giangrande, S. E., Neale, R. B., Qian, Y., Riihimaki, L. D., Zender, C. S., Zhang, Y. and Zheng, X.: Regionally refined test bed in E3SM atmosphere model version 1 (EAMv1) and applications for high-resolution modeling, Geosci. Model Dev., 12(7), 2679–2706, doi:10.5194/gmd-12-2679-2019, 2019.

Wang, J., Fan, J., Houze, R. A., Brodzik, S. R., Zhang, K., Zhang, G. J. and Ma, P. L.: Using radar observations to evaluate 3-D radar echo structure simulated by the Energy Exascale Earth System Model (E3SM) version 1, Geosci. Model Dev., 14(2), 719–734, doi:10.5194/gmd-14-719-2021, 2021.

Wang, Y., Liu, X., Hoose, C. and Wang, B.: Different contact angle distributions for heterogeneous ice nucleation in the Community Atmospheric Model version 5, Atmos. Chem. Phys., 14(19), 10411–10430, doi:10.5194/acp-14-10411-2014, 2014.

Webb, M., Senior, C., Bony, S. and Morcrette, J. J.: Combining ERBE and ISCCP data to assess clouds in the Hadley Centre, ECMWF and LMD atmospheric climate models, Clim. Dyn., 17(12), 905–922, doi:10.1007/s003820100157, 2001.

Xie, S., Lin, W., Rasch, P. J., Ma, P.-L., Neale, R., Larson, V. E., Qian, Y., Bogenschutz, P. A., Caldwell, P., Cameron-Smith, P., Golaz, J.-C., Mahajan, S., Singh, B., Tang, Q., Wang, H., Yoon, J.-H., Zhang, K. and Zhang, Y.: Understanding Cloud and Convective Characteristics in Version 1 of the E3SM Atmosphere Model, J. Adv. Model. Earth Syst., 10(10), 2618–2644, doi:https://doi.org/10.1029/2018MS001350, 2018.

Zhang, D., Vogelmann, A., Kollias, P., Luke, E., Yang, F., Lubin, D. and Wang, Z.: Comparison of Antarctic and Arctic Single-Layer Stratiform Mixed-Phase Cloud Properties Using Ground-Based Remote Sensing Measurements, J. Geophys. Res. Atmos., 124(17–18), 10186–10204, doi:https://doi.org/10.1029/2019JD030673, 2019a.

Zhang, G. J. and McFarlane, N. A.: Sensitivity of climate simulations to the parameterization of cumulus convection in the Canadian climate centre general circulation model, Atmosphere-Ocean, 33(3), 407–446, doi:10.1080/07055900.1995.9649539, 1995. Zhang, K., Wan, H., Liu, X., Ghan, S. J., Kooperman, G. J., Ma, P.-L., Rasch, P. J., Neubauer, D. and Lohmann, U.: Technical Note: On the use of nudging for aerosol–climate model intercomparison studies, Atmos. Chem. Phys., 14(16), 8631–8645, doi:10.5194/acp-14-8631-2014, 2014.

Zhang, M., Xie, S., Liu, X., Lin, W., Zhang, K., Ma, H.-Y., Zheng, X. and Zhang, Y.: Toward Understanding the Simulated Phase Partitioning of Arctic Single-Layer Mixed-Phase Clouds in E3SM, Earth Sp. Sci., 7(7), e2020EA001125, doi:https://doi.org/10.1029/2020EA001125, 2020.

Zhang, Y., Xie, S., Lin, W., Klein, S. A., Zelinka, M., Ma, P.-L., Rasch, P. J., Qian, Y., Tang, Q. and Ma, H.-Y.: Evaluation of Clouds in Version 1 of the E3SM Atmosphere Model With Satellite Simulators, J. Adv. Model. Earth Syst., 11(5), 1253–1268, doi:https://doi.org/10.1029/2018MS001562, 2019b.

Zhang, Y. Y., Xie, S., Klein, S. A., MaRchand, R. R., KolliaS, P., Clothiaux, E. E., Lin, W. Y., JohnSon, K. R., SWaleS, D., BodaS-Salcedo, A., Tang, S., Haynes, J. M., Collis, S., JenSen, M., BhaRadWaJ, N., Hardin, J. S. and Isom, Br. Y.: The ARM cloud radar simulator for global climate models bridging field data and climate models, Bull. Am. Meteorol. Soc., 99(1), 21–26, doi:10.1175/BAMS-D-16-0258.1, 2018.

Chapter 7

Conclusions

7.1 Summary

The objective of this dissertation is to address challenges to advancing the predictive understanding of INPs with instrumentation, methods development, observations of INPs near dust and marine aerosol sources and tools for observations-based evaluation of simulated cloud ice representation. As skillful representation of ice nucleation depends upon understanding derived from observations of clouds and INP populations, the majority of this dissertation focuses on measurements. First, applied statistics and finite-element-analysis based heat transfer simulations were used to develop automated instrumentation for the measurement of immersion-mode INPs and to quantify the uncertainty associated with freezing temperature measurements and common sample storage practices. The instrumentation and methods development herein supported subsequent studies in which INP observations, cultivation techniques and aerosol backtrajectory analyses were applied to identify ice-nucleating microbes in aerosol and precipitation samples and to provide INP observations within $<$ 1 day of transport from the largest dust source regions: North Africa and the Arabian Peninsula. However, an improved understanding of INP populations alone will not lead to improved representation in climate models. Ice nucleation and secondary

ice production processes occur on scales much finer ($\geq$ nanometers) than the size of the climate model gridbox (25 – 200 km). Furthermore, it is unknown whether an improved representation of INPs would benefit the cloud representation *a priori* given that the level of complexity required to properly represent ACI in general is unknown (e.g., how many moments is required for a microphysical parameterization?), and how this complexity depends on model resolution and cloud regime. In response to this challenge, the penultimate chapter of this dissertation presents a hydrometeor phase evaluation capability that will support the climate model sensitivity studies required to determine the potential for new INP representations to improve cloud representation. The conclusions from each chapter are summarized in more detail below.

In Chapter 2, a droplet assay for measurement of immersion-mode INPs was automated using a camera and custom LABVIEW software designed to extract droplet freezing data from live images of liquid samples. The heat transfer properties of the system were characterized using finite-element-analysis based heat transfer simulations. This modeling technique was proposed as a tool that could be useful for quantification of uncertainty in temperature measurement and for investigating sources of discrepancy between instruments. Results from the heat-transfer simulation showed a thermal gradient between the location of the thermistor probe and the sample aliquot of up to +1.8 °C, depending on temperature. Additionally, results demonstrated that the temperature difference between the headspace gas and the droplet assay well block of +8.4 °C results in a thermal gradient within the sample aliquot itself of up to +0.6 ºC, whereas a difference of +4.2 °C or less resulted in a thermal gradient within the error of the thermistor probes ($\pm$ 0.2 °C). A temperature correction was derived from the heat transfer simulation results and was used to inform uncertainty estimates in the chapters that follow. Finally, measurements of the standard test dust illite NX agreed well with 6 other droplet assay-based instruments.

In Chapter 3, the impacts of common storage practices on INP concentrations measured in coastal precipitation samples were quantified by comparison with fresh samples. We compared four conditions: 1.) storage at room temperature (+21-23 ºC), 2.) storage at +4 ºC 3.) storage

at -20 ºC, and 4.) flash freezing samples with liquid nitrogen prior to storage at -20 ºC. The sensitivities of INPs to heat and filtration treatments commonly used to probe INP size ranges and composition were also tested before and after storage. Through a study of 15 precipitation samples collected at a coastal location in La Jolla, CA, USA, we found INP concentration changes up to $>$ 1 order of magnitude caused by storage to concentrations of INPs with warm to moderate freezing temperatures (-7 to -19 ºC). Results demonstrate that storage can lead to both enhancements and losses of greater than one order of magnitude, with non-heat-labile INPs being generally less sensitive to storage regime, but significant losses of INPs smaller than 0.45 μm in all tested storage protocols. Correlations between total storage time (1-166 days) and changes in INP concentrations were weak across sampling protocols, with the exception of INPs with freezing temperatures $\geq$ -9 ºC in samples stored at room temperature. We provide the following recommendations for preservation of precipitation samples from coastal or marine environments intended for INP analysis: that samples be stored at -20 ºC to minimize storage artifacts, that changes due to storage are likely an additional uncertainty in INP concentrations, and that filtration treatments be applied only to fresh samples. The impacts of storage to INP analyses described in this chapter in part motivated the focus on fresh precipitation and SSA samples in the following chapter.

In Chapter 4, we identify 14 (30%) cultivable halotolerant ice-nucleating microbes and fungi among 47 total isolates recovered from precipitation and aerosol samples collected in La Jolla, CA, USA. Ice-nucleating isolates collected in coastal air nucleated ice from extremely high to moderate freezing temperatures (-2.3 to -18 °C). While some Gamma-proteobacteria and fungi are known to nucleate ice at temperatures as high as -2 °C, *Brevibacterium* sp. is the first Actinobacteria found to be capable of ice nucleation at a relatively high freezing temperature (-2.3 °C). Air mass trajectory analysis demonstrates that marine aerosol sources were dominant during all sampling periods, and phylogenetic analysis indicates that at least 2 of the 14 ice-nucleating isolates are highly likely marine, *Idiomarina* sp. and *Psychrobacter* sp. 1c2. The discovery of

cultivable ice-nucleating isolates will benefit future studies that aim to identify the predictors of biologically-enhanced INP emissions from the ocean surface as well as the extent to which environmental factors control the behavior of IN-active microbes in the atmosphere.

In Chapter 5, we report INP concentrations measured in aerosol and seawater samples during Air Quality and Climate Change Around the Arabian BAsin (AQABA), a shipborne campaign that spanned the Red Sea, Gulf of Aden, Arabian Sea, Arabian Gulf and Mediterranean. In aerosol samples collected within a few hundred kilometers of the first and second ranked sources of dust globally, the Sahara and Arabian Peninsula, INP concentrations ranged from 0.2 to 11 L^{-1} at -20 °C with observed ice nucleation site densities (n_s) 1-3 orders of magnitude below levels predicted by mineral dust INP parameterizations. Over half of the samples (at least 14 of 26) were collected during dust storms with average dust mass concentrations between 150 and 490 μg m^{-3}. The impacts of heat and peroxide treatments indicate that the observed INPs were organic in composition at temperatures $\geq$ -15 °C with proteinaceous (heat-labile) INPs frequently observed at higher freezing temperatures $>$ -10 °C. Overall, results from this study provide much-needed INP observations within $<$ 1 day of transport from the Sahara and the Arabian Peninsula and demonstrate that despite this proximity and the dominance of mineral dust in the aerosol sampled, existing mineral dust parameterizations alone would not skillfully represent the near-surface n_s in the observed temperature regime (-6 to -25 °C).

While Chapters 2-5 focus on critical challenges to advancing predictive understanding of INPs from the observational perspective, Chapter 6 begins to address challenges to improving INP representation from the modeling perspective using the DOE E3SM Atmosphere Model (EAMv1). In Chapter 6 we introduce a capability to evaluate EAMv1 Arctic mixed-phase cloud representation against ARM ground-based cloud observations at North Slope Alaska (NSA) using $(GO)^2$-SIM, a forward ground-based radar simulator designed for hydrometeor-phase evaluation. $(GO)^2$-SIM distinguishes between frozen and liquid hydrometeors and exploits a combination of ground-based lidar and radar measurements that are advantageous for detection of liquid phase in

low-level multilayered clouds. To take advantage of this simulator for model evaluation, we have prototyped a "pipeline" that generates input variables needed to run $(GO)^2$-SIM on subcolumns generated from EAMv1 simulations. Using $(GO)^2$-SIM to apply phase-designation retrievals across the forward simulated and instrument observables, EAMv1 simulated stratiform cloud phase and vertical structures can be evaluated against NSA KA-band Doppler radar and polarimetric lidar observations. This capability has potential to provide new observational constraints on EAM simulations of mixed-phase clouds and will support sensitivity studies that investigate the impacts of perturbed microphysical parameters on mixed-phase cloud representation. A brief discussion of how sensitivity studies based on hydrometeor phase evaluation could qualify the potential of improved INP parameterizations to improve cloud representation is included in the next section.

7.2 Directions for future and related research

As the largest source of uncertainty to estimates of radiative forcing, improving ACI representation is increasingly time critical (IPCC, 2021). The attainment of the accuracy and precision in climate forecasting required to derive quantitative, decision-useful information needed for climate change mitigation and adaptation efforts from climate models depends upon better constraint of the uncertainty associated with ACI. Results and innovations from this dissertation can be used to support future studies of ice nucleation, an important ACI that affects cloud phase, radiative properties, lifetime and precipitation outcomes, from both the modeling and observational perspective. Results herein address critical challenges to INP measurements and provide INP observations and identities in marine and dusty environments, yet many outstanding questions and observational gaps remain.

Results from Chapter 5 underscore the need for additional observations of natural desert dust in aerosol and soil dust at modest supercooling ($>$ -20 °C) to better characterize the IN

properties of dust in this sensitive temperature regime. Few parameterizations for desert dust exist for temperatures > -20 °C, and the results from Chapter 3 and Gong et al. (2020) demonstrate that the n_s-based parameterizations likely overrepresent INPs in some dusty air masses, particularly near major source regions. Future efforts to improve representations of dust INPs at modest supercooling (> -15 °C) would benefit from a characterization of the specific organic species associated with dust INPs. More generally, an improved understanding of the organic species associated with increased IN activity and their variability across dust source regions would directly inform efforts to determine whether n_s-based parameterizations are appropriate for faithful representation of dust INPs in this sensitive temperature regime, whether region-specific parameterizations are required, or whether an alternative to the n_s approach is necessary. For example, Gong et al. (2019) demonstrated that predicting n_{INP} from surface area size distributions alone may not be feasible in environments where the aerosol and/or INP composition are unknown and proposed a probability density function (PDF)-based approach to predicting INPs at a given freezing temperature.

While observations of desert dust INPs at modest supercooling are needed, observations of ambient INPs in this temperature regime are also lacking overall (see Fig. 1-10 in Kanji et al. (2017)). Though concentrations of INPs decrease roughly exponentially with increasing freezing temperature, it is possible for a relatively small number of INPs with high activation temperatures to significantly affect cloud radiative properties, lifetime and precipitation efficiency due to secondary freezing processes, such as the Hallet-Mossop, which is most efficient between ∼-3 and -8 °C (Hallet and Mossop, 1974). Future observational studies of ambient INPs could target the modest supercooling temperature range by sampling large air volumes and using offline immersion-mode droplet assay instruments such as those described in this dissertation. Although offline techniques lack the temporal resolution capabilities of online instruments for INP measurement, immersion-mode droplet assays are well-suited for detection of INPs at modest supercooling because sample air volumes are effectively unlimited, and, in contrast to online

instruments such as the CFDC, they can operate efficiently at modest supercooling (e.g., DeMott et al., 2017). However, as samples are commonly stored prior to measurement on offline instruments, future studies should also expand on the work described in Chapter 3 by investigating the extent to which common storage practices affect different aerosol samples, and these uncertainties should be included in estimates of uncertainty in INP concentration measurement. The uncertainties provided in Chapter 3 should also be considered in future studies of INPs measured in stored precipitation samples.

In addition to providing observations at high to moderate freezing temperatures, future studies should continue to develop methods for distinguishing between different INP sources in ambient aerosol. Cornwell et al., (2019) provides an example of how this can be done by combining online measurements of single particle chemistry, size distributions and INPs. Gong et al. (2020) describes how measurements of INP and salt concentrations in bulk seawater and aerosol can be used to estimate the fraction of marine INPs observed in ambient aerosol. The concept that INP concentrations in the bulk seawater may be representative of INPs in SSA is supported by mesocosm study results. Mitts et al. (2021) and Wang et al. (2017) showed that jet droplets that transfer INPs from seawater to SSA are likely the dominant INP emissions pathway. Future studies could also benefit from recent advances in Light-Induced Fluorescence (LIF) measurement techniques. Whereas the interpretation of fluorescence data from most LIF-based instruments has been limited by the lack of spectroscopic information, the Spectral Intensity Bioaerosol Sensor (SIBS) supports real-time spectrally-resolved size and fluorescence measurement information for single particles (Könemann et al., 2019). This information could be used to "tag" different classes of organics and biological aerosols, enabling investigations of relationships between n_s, INP concentrations and organic signatures in, e.g., mineral dusts and SSA.

To help advance predictive understanding of marine biological INP emissions, future studies can use the species identified in Chapter 4 to investigate the factors that determine

their emissions as an effective "tracer" for marine IN-active microbes (e.g., *Idiomarina* sp. and *Psychrobacter* sp.). As these isolates are cultivable, future studies should also investigate the specific properties or mechanisms through which these isolates modulate ice nucleation. Further study is also needed to understand the factors, such as atmospheric processing or nutrient limitation, that inhibit or enhance microbe IN behavior, as well as the factors that modulate the emissions of IN bacteria from the ocean surface. However, as cultivable populations represent a small fraction of the total microbial community, future studies should combine INP measurements with state-of-the-art sequencing approaches to identify relationships between specific microbial communities and INP freezing activity. Furthermore, a combination of advanced fractionation methods to identify the putative ice nucleating metabolites associated with specific microbial communities and computational networking could illuminate molecular and microbial linkages to ice nucleation and the mechanisms by which the entities work individually or in concert.

Finally, from the modeling perspective, future studies will need to determine the extent to which improved INP parameterizations could improve model representation of phase-partitioning processes, and whether ice production process representation could benefit from AI/ML techniques that supplement or replace parameterizations (see Introduction). Future studies of EAM can use the pipeline provided in Chapter 6 to apply $(GO)^2$-SIM to evaluate hydrometeor phase across different model configurations (e.g., high-resolution, low-resolution and regionally-refined) and cloud microphysics representations. This evaluation capability is also well-suited to support sensitivity studies in which selected microphysical parameters are perturbed across simulation ensembles, enabling comparison between ensemble members to better understand how various subgrid microphysical parameterizations, such as INP parameterizations, affect representation of cloud phase, lifetime and radiative properties.

7.3 References

Cornwell, G. C., McCluskey, C. S., Levin, E. J. T., Suski, K. J., DeMott, P. J., Kreidenweis, S. M. and Prather, K. A.: Direct Online Mass Spectrometry Measurements of Ice Nucleating Particles at a California Coastal Site, J. Geophys. Res. Atmos., 124(22), 12157–12172, doi:doi:10.1029/2019JD030466, 2019.

DeMott, P. J., Hill, T. C. J., Petters, M. D., Bertram, A. K., Tobo, Y., Mason, R. H., Suski, K. J., Mccluskey, C. S., Levin, E. J. T., Schill, G. P., Boose, Y., Rauker, A. M., Miller, A. J., Zaragoza, J., Rocci, K., Rothfuss, N. E., Taylor, H. P., Hader, J. D., Chou, C., Huffman, J. A., Pöschl, U., Prenni, A. J. and Kreidenweis, S. M.: Comparative measurements of ambient atmospheric concentrations of ice nucleating particles using multiple immersion freezing methods and a continuous flow diffusion chamber, Atmos. Chem. Phys., 17(18), 11227–11245, doi:10.5194/acp-17-11227-2017, 2017.

Gong, X., Wex, H., Müller, T., Wiedensohler, A., Höhler, K., Kandler, K., Ma, N., Dietel, B., Schiebel, T., Möhler, O. and Stratmann, F.: Characterization of aerosol properties at Cyprus, focusing on cloud condensation nuclei and ice-nucleating particles, Atmos. Chem. Phys., 19(16), 10883–10900, doi:10.5194/acp-19-10883-2019, 2019.

Gong, X., Wex, H., van Pinxteren, M., Triesch, N., Fomba, K. W., Lubitz, J., Stolle, C., Robinson, T.-B., Müller, T., Herrmann, H. and Stratmann, F.: Characterization of aerosol particles at Cabo Verde close to sea level and at the cloud level – Part 2: Ice-nucleating particles in air, cloud and seawater, Atmos. Chem. Phys., 20(3), 1451–1468, doi:10.5194/acp-20-1451-2020, 2020.

Hallet, J. and Mossop, S. C.: Production of secondary ice particles during the riming process, Nature, 249(5452), 26–28, doi:10.1038/249026a0, 1974.

IPCC: Climate Change 2021: The Physical Science Basis, Cambridge Univ. Press. Press., 2021.

Kanji, Z. A., Ladino, L. A., Wex, H., Boose, Y., Burkert-Kohn, M., Cziczo, D. J. and Krämer, M.: Overview of Ice Nucleating Particles, Meteorol. Monogr., 58, 1.1-1.33, doi:10.1175/amsmonographs-d-16-0006.1, 2017.

Könemann, T., Savage, N., Klimach, T., Walter, D., Fröhlich-Nowoisky, J., Su, H., Pöschl, U., Huffman, J. A. and Pöhlker, C.: Spectral Intensity Bioaerosol Sensor (SIBS): an instrument for spectrally resolved fluorescence detection of single particles in real time, Atmos. Meas. Tech., 12(2), 1337–1363, doi:10.5194/amt-12-1337-2019, 2019.

Mitts, B., Wang, X., Lucero, D., Beall, C., Deane, G., DeMott, P. and Prather, K.: Importance of Supermicron Ice Nucleating Particles in Nascent Sea Spray, Geophys. Res. Lett., n/a(n/a),

e2020GL089633, doi:https://doi.org/10.1029/2020GL089633, 2021.

Wang, X., Deane, G. B., Moore, K. A., Ryder, O. S., Stokes, M. D., Beall, C. M., Collins, D. B., Santander, M. V, Burrows, S. M., Sultana, C. M. and Prather, K. A.: The role of jet and film drops in controlling the mixing state of submicron sea spray aerosol particles, Proc. Natl. Acad. Sci., 114(27), 6978–6983, doi:10.1073/pnas.1702420114, 2017.